

Development of alternative
thermomechanical processing techniques
to improve forging outcomes of cast
peritectic TiAl alloys

Sean Peters

Advanced Forming Research Centre
Design, Manufacturing and Engineering Management
School of Engineering
University of Strathclyde

2023

Abstract

The aim of this research was to investigate and develop alternative thermomechanical processing techniques to improve the forging outcomes, at industrially viable temperatures, of two cast, peritectic solidifying, consolidated titanium aluminide alloys; 45XD (Ti-45Al-2Nb-2Mn-1B at.%) and 4822 (Ti-48Al-2Nb-2Cr at.%).

This study differed from existing work on TiAl alloy composition-processing-microstructure relationships with an emphasis on controlling the initial microstructure to optimise primary processing (i.e., ingot breakdown) efficiency and produce a microstructure that improves the outcome of secondary processing (i.e., isothermal closed die forging, or hot rolling), ideally approaching a strain rate sensitivity of ≥ 0.3 . For these alloys, consolidation by hot isostatic pressing (HIP) followed by primary compression alone does not remove the casting segregation or the anisotropic behaving lamellar content that hinders secondary processing; alternative processes are required.

For 45XD, this study found that integrating HIP and homogenisation stages into one step, using HIP equipment, proved beneficial to the forging outcome in comparison to the traditional two step approach. Achieving an elementally homogeneous and refined fully lamellar microstructure enabled high levels of globularisation, and dynamic recrystallised material from 50 % primary compression at 1100 °C and 0.001 s⁻¹. This aided secondary compression, returning the highest strain rate sensitivity of 0.32.

For 4822, this study investigated the impact of cyclic heat treatment (CHT) and cooling rate on HIP and homogenised material, as well as its subsequent effect on forging outcomes. For the first time, industrially relevant induction heating equipment was applied to conduct the five cycles to the single α phase temperatures (1370 °C) necessary for lamellar grain refinement. The compression results showed that CHT, irrespective of cooling, proved successful with uniform 50 % primary compression at 1100 °C and 0.001 s⁻¹, compared to the shearing instability of HH material. This led to secondary compression of CHT material returning material high in dynamic recrystallised content and free of lamellar morphologies, with a strain rate sensitivity of 0.25.

Declaration of Authenticity and Author's Rights

'This thesis is the result of the author's original research. It has been composed by the author and has not been previously submitted for examination which has led to the award of a degree.'

'The copyright of this thesis belongs to the author under the terms of the United Kingdom Copyright Acts as qualified by University of Strathclyde Regulation 3.50. Due acknowledgement must always be made of the use of any material contained in, or derived from, this thesis.'

Signed: Sean Peters

Date: 31/07/2023

Previously Published Material

Integrating HIP and homogenisation heat treatment and its effect on the workability of a conventional peritectic TiAl alloy. Published in the journal, *Intermetallics*, <https://doi.org/10.1016/j.intermet.2023.107884>.

Improving forging outcomes of cast titanium aluminide alloy via cyclic induction heat treatment. Published in the journal, *Metals*, <https://doi.org/10.3390/met13081420>.

Acknowledgements

My name is on the front of this document, but despite trying, I cannot take all the credit for getting it to this point.

Firstly, I would like to thank Paul, Dorothy and Marcos for giving me the opportunity in the first place to work and develop as a researcher at the Advanced Forming Research Centre (AFRC). I am particularly grateful to Paul for giving me, my papers, and this document, so much of his time and sound advice over the years. Thank you and I wish you all the best for your retirement.

I would like to acknowledge the Tier one members of the AFRC for their support of this project and regular interrogation at technical board meetings throughout my PhD. Thanks go to TIMET, for material as well as technical support and direction from Yvon Millet. Again, I wish you all the best for your retirement.

A special thanks must go to my fellow AFRC colleagues; Jacqueline, Ryan, Kornelia and Adam, throughout the pandemic your efforts at the AFRC, whilst the rest of us worked from home, really kept this project on track despite all the uncertainty, thank you. Thanks, must also go to Aurik for his advice, time and expertise, it really was appreciated.

My final and most sincere thanks go to my partner Izzy and all of my family, as well as the Garnsey's. You have all given me the time and space to get to this point without a "proper job" or a solid understanding of what I actually do. As a thank you, you don't have to read it all, there will be no test. Izzy, thank you, I look forward to what we get up to next.

Table of contents

Abstract	2
Declaration of Authenticity and Author's Rights.....	3
Previously Published Material	4
Acknowledgements	5
Table of contents.....	6
List of figures	9
List of tables	14
Abbreviations and symbols	16
1 Introduction.....	20
1.1 Intermetallics and titanium aluminide	20
1.2 Background and justification for this study.....	21
2 Literature Review	23
2.1 Titanium aluminide	23
2.2 Crystallography, phases and alloying of titanium aluminide	24
2.2.1 Phase diagram – effect of aluminium	24
2.2.2 Crystal structures of phases in titanium aluminide.....	25
2.2.3 Alloying of titanium aluminide	25
2.3 Titanium aluminide alloys and their microstructures	29
2.3.1 Microstructures	29
2.4 Composition- processing-microstructure relationships of titanium aluminide	34
2.4.1 Titanium aluminide stock production	34
2.4.2 Thermal mechanical processing of titanium aluminide	37
2.5 The low-pressure turbine blade	57
2.5.1 4822.....	58
2.5.2 45XD	58
2.5.3 TNM.....	59
2.5.4 Other alloys of interest and their uses.....	59
2.6 Summary of the knowledge gap.....	61
2.7 Aims and Objectives	61
3 Experimental Methods.....	63
3.1 Materials and their pre-compression processing.....	63
3.1.1 As received material (ASR)	63

3.1.2 Hot isostatic pressing (HIP)	64
3.1.3 Determining the impact of heat treatment on the HIP microstructure of 45XD pre-compression	65
3.1.4 Traditional HIP and homogenisation (THH)	66
3.1.5 Integrated HIP and homogenisation (IHH).....	66
3.1.6 Intermediate heat treatment for 45XD.....	67
3.1.7 Cyclic induction heat treatment for 4822	67
3.2 Compression testing	70
3.2.1 Primary compression	70
3.2.2 Secondary compression	70
3.2.3 Compression behaviour analysis.....	70
3.3 Microstructural Characterisation.....	72
3.3.1 Specimen preparation and microscopy	72
3.3.2 Data processing.....	72
4 Thermomechanical processing trials of 45XD.....	75
4.1 The impact of HIP and heat treatment on the microstructure and subsequent compression behaviour of 45XD.....	75
4.1.1 Introduction	75
4.1.2 Results and discussion	76
4.1.3 Summary	91
4.2 Identifying the homogenisation temperature for 45XD in respect to compression behaviour and microstructural outcome.....	92
4.2.1 Introduction	92
4.2.2 Results and discussion	93
4.2.3 Summary	98
4.3 The effect of multi-stage forge processing on the forging outcome of consolidated 45XD.....	99
4.3.1 Introduction	99
4.3.2 Results and discussion	101
4.3.3 Summary	109
4.4 Integrating HIP and homogenisation heat treatment and its effect on the primary processing of 45XD	111
4.4.1 Introduction	111
4.4.2 Results and discussion	113
4.4.3 Summary	123
4.5 Effect of prior processing on secondary compression behaviour of 45XD	124

4.5.1 Introduction.....	124
4.5.2 Results and discussion.....	125
4.5.3 Summary	130
4.6 Conclusions and industrial relevance for 45XD.....	131
4.7 Future work recommendations for 45XD.....	134
5 Thermomechanical processing trials of 4822.....	135
5.1 The impact of HIP, homogenisation and integrating the two processes on 4822 cast ingot material and its subsequent response to primary compression	135
5.1.1 Introduction.....	135
5.1.2 Results and discussion.....	136
5.1.3 Summary	149
5.2 Effect of induction cyclic heat treatment on the microstructure of HIP and homogenised 4822 and its forging outcomes.....	151
5.2.1 Introduction.....	151
5.2.2 Results and discussion.....	152
5.2.3 Summary	172
5.3 Conclusions and industrial relevance for 4822	173
5.4 Future work recommendations for 4822	174
6 Contributions to knowledge.....	175
7 References.....	177

List of figures

Figure 1: Specific strength versus temperature diagram for structural materials [8]	23
Figure 2: Ti-Al phase diagram[3]	24
Figure 3: titanium aluminide phase diagram [10].....	24
Figure 4: Left, α_2 -Ti ₃ Al hexagonal D0 ₁₉ structure a=0.5782 nm, c=0.4629 nm. Right, γ -TiAl tetragonal L1 ₀ structure a=0.4005 nm, c=0.4070 nm [11].	25
Figure 5: Example of phase diagram and working at different temperatures to achieve different microstructures for TiAl alloy 4822 [25].	29
Figure 6: Near-gamma microstructure[25].....	29
Figure 7: Near fully lamellar microstructure[25]	30
Figure 8: Fully lamellar microstructure [25]	30
Figure 9: Duplex microstructure [25].....	31
Figure 10: β solidifying microstructure[31].....	32
Figure 11: diagram displaying processing routes possible for titanium aluminide	34
Figure 12: Diagram displaying PAM process, with homogenization step and ingot drawing[44].....	34
Figure 13: Diagram displaying VAR process, with method of Ti inclusion [44]	35
Figure 14: Diagram displaying ISM process and pouring for centrifugal casting, also used for casting melt from the VAR processes [44].....	35
Figure 15: Ordered B2 and disordered body centred cubic unit cell structure [3].....	39
Figure 16: Phase diagram of TNM type alloying system[65]	40
Figure 17: Angle of compression to lath of lamellar grain.....	43
Figure 18: a) Rolls Royce UltraFan, (b) Turbine section[14]	57
Figure 19: (a) Low pressure turbine blade (LPT), (b) Turbine assembly [14].....	57
Figure 20: Turbocharger turbine wheel [22].....	59
Figure 21: Phase fraction diagram determined from CALPHAD for 45XD	63
Figure 22: Phase fraction diagram determined from CALPHAD for 4822	64
Figure 23: (a) Ingot of 45XD alloy of \varnothing 146 x 245 mm and 18kg. (b) Ingot of 4822 alloy of \varnothing 140 x 233 mm and 15kg. Courtesy of TIMET.....	64
Figure 24: 45XD Ti-Al phase diagram calculated from data received from Computherm.....	65
Figure 25: Idealised temperature-time profile of the traditional and integrated HIP and homogenisation heat treatment, including consolidation (HIP), homogenisation (HMG), and integrating the two for 45XD before primary compression (COMP.).....	67
Figure 26: Compression sample ready for ACCHT or FCCHT with glass-based coating, -C= centre, -F1= one face, -F2= the opposite face to F1 for post heat treatment analysis	69
Figure 27: (a) Idealised temperature-time profile of air-cooling cyclic and furnace cooling cyclic heat treatment, including consolidation (HIP), homogenisation (HMG), and five cycles of induction cyclic heat treatment (CHT) of 4822 before primary compression (COMP.) (b) Induction cyclic heat treatment set-up with pyrometer temperature monitoring.	69
Figure 28: (a)Image of electrical discharge machined primary compression sample, (b) diagram indicating EDM pattern of primary compression samples (0.001 s ⁻¹ only, faster strain rates only have the red dashed cut) giving two cylindrical samples ready for secondary compression and central cut for microstructural analysis	70
Figure 29: (a) BSE image of as- received (ASR) cast microstructure of 45XD from the centre of the received ingot, equivalent of position C in Figure 26, at 500x magnification, where	

black areas correspond to γ phase, white β_0 and grey α_2 . (b) Calculation of phase diagram (CALPHAD) of 45XD alloy from ICP analysis in Table 6.....	75
Figure 30: BSE images of 45XD alloy in the HIP condition respectively, at 500x, where black areas correspond to γ phase, white β_0 and grey α_2 . Lamellar grain and boundary examples outlined in red blue arrow identifies γ_{eq} , yellow arrows identify β_{eq} examples and red arrow identifies an α_2 lath.....	76
Figure 31: SEM micrographs (BSE) at 500x magnification of 45XD alloy before compression, heat treated for 2 hours at different temperatures with either FC or AC cooling rates; 1130 °C FC(a) and AC(e), 1200 °C FC(b) and AC(f), 1270 °C FC(c) and AC(g), 1350 °C FC(d) and AC(h). Where black areas correspond to γ phase, white β_0 and grey α_2 , respectively.	77
Figure 32: Flow stress-true strain curves for each 45XD material condition through 50% compression at 1100°C, 0.001s ⁻¹ , over 760 seconds.....	80
Figure 33: SEM micrographs (BSE) at 1000x magnification of 45XD alloy after compression, in the HIP condition (a) and heat treated for 2 hours at different temperatures with either FC or AC cooling rates; 1130 °C FC(b) and AC(c), 1200 °C FC(d) and AC(e), 1270 °C FC(f) and AC(g), 1350 °C FC(h) and AC(i). Where black areas correspond to γ phase, white β_0 and grey α_2 , respectively.	82
Figure 34: EBSD used to give maps of, (left) band contrast, (middle) phase map; blue is γ , red is α_2 , yellow is β_0 , (Right) X-DRX; red is the recrystallised fraction, blue is deformed, of 45XD alloy in the HIP condition (a- c), and heat treated for 2 hours at different temperatures with either FC or AC cooling rates; 1130 °C FC (d-f) and AC(g-i), 1200 °C FC(j-l) and AC(m-o), 1270 °C FC (p-r), and AC (s-u), 1350 °C FC (v-x) and AC(y-ai), at 1600x magnification, after 50% compression at 1100 °C, 0.001 s ⁻¹	85
Figure 35: Plots calculating the DRX fraction from the GOS approach on the left, grain area frequency density on the right, for each material condition after 50% primary compression at 1100 °C and 0.001 s ⁻¹ , HIP (a, b), and heat treated for 2 hours at different temperatures with either FC or AC cooling rates; 1130 °C FC (c, d) and AC (e, f), 1200 °C FC(g, h) and AC(i, j), 1270 °C FC (k, l), and AC (m, n), 1350 °C FC (o-p) and AC (q, r).	90
Figure 36: (a) SEM used to give BSE images at 500x magnification (left) where black areas correspond to γ phase, white β_0 and grey α_2 , and EBSD phase maps at 1600x magnification, (right); where blue is γ , red is α_2 , yellow is β_0 , of 45XD alloy in the HIP condition (a- b), and heat treated for 2 hours at ; 1270 °C FC (c-d), and 1300 °C FC (e-f).	93
Figure 37: Flow stress-true strain curves for each 45XD material condition through 50% compression at 1100°C, 0.001s ⁻¹ , over 760 seconds.....	95
Figure 38: (a), SEM micrograph in BSE mode at 1000x magnification of 45XD alloy in the 1300 FC condition after compression, where black areas correspond to γ phase, white β_0 and grey α_2 , respectively. EBSD used to give maps of, (b) band contrast, (c) phase map; blue is γ , red is α_2 , yellow is β_0 , (d) X-DRX; red is the recrystallised fraction, blue is deformed, at 1600x magnification.	96
Figure 39: Trend line between pre-compression (a) lamellar content and (b) equiaxed content and globularised fraction returned from primary compression at 0.001 s ⁻¹ . This scatter plot includes material described in chapter 4.1 and 4.2.....	97
Figure 40: relationship between pre-compression average lamellar grain size and DRX fraction returned from primary compression at 0.001 s ⁻¹ . This scatter plot includes material described in chapter 4.1 and 4.2.....	97

Figure 41: BSE images of 45XD alloy in the (a), HIP condition, at 1000x magnification, where black areas correspond to γ phase, white β_0 and grey α_2 . (b) Phase map from EBSD at 1600x, blue areas correspond to γ phase, yellow to β_0 and red to α_2 101

Figure 42: Flow stress-true strain chart of 45XD following different intermediate steps showing the both blows (a), first blow is of material in a similar HIP condition, and (b) a zoomed in view of the second blow of hot compression at 1100°C, 0.001s⁻¹, 25 - 50%. 102

Figure 43: SEM micrograph (BSE) of 45XD alloy after 50% compression in (a), the HIP+50% condition, (b), 25% + RT + 25%, (c), 25% + 1200-AC+25%, (d), 25% + Dwell + 25%, (e), 50% + 1200-AC,, all at 500X magnification, where black areas correspond to γ phase, white β_0 and grey α_2 , respectively. 104

Figure 44: EBSD used to give maps of, (left) band contrast, (middle) phase map; blue is γ , red is α_2 , yellow is β_0 , (Right) X-DRX; red is the recrystallised fraction, blue is deformed, of 45XD alloy after 50% compression in (a-c), the HIP condition plus intermediate stages (d-f), 25% + RT + 25%, (g-i), 25% + 1200-AC+25%, (j-l), 25% + Dwell + 25%, post compression stages are (m-o), 50% + 1200-AC, all at 1600X magnification. 107

Figure 45: Plots calculating the DRX fraction from the GOS approach on the left, grain area frequency density on the right, for each material condition after 50% primary compression at 1100 °C and 0.001 s⁻¹ (a-b), the HIP condition plus intermediate stages (c-d), 25% + RT + 25%, (e-f), 25% + 1200-AC+25%, (g-h), 25% + Dwell + 25%, post compression stages are (i-j), 50% + 1200-AC, 109

Figure 46: (a) SEM image of HIP microstructure to identify phases and lamellar (lam) and equiaxed (eq) microstructures, as indicated dark grey/black areas correspond to γ phase, white β_0 and light grey α_2 , (b) phase fraction diagram determined from CALPHAD, with main crystal structures (including metallic boride (MB)) 111

Figure 47: BSE images of 45XD alloy in the HIP (a), THH (d), IHH (g) condition at 500x magnification. Black areas correspond to γ phase, white β_0 and grey α_2 . EBSD phase fraction maps HIP (b), THH (d), IHH (h) condition at 1600x magnification 114

Figure 48: Primary stress-stain curves (a), compression at 1100 °C to 50 % at 0.001, 0.005 and 0.01 s⁻¹ over 760, 152, and 76 seconds respectively. Calculation of strain rate sensitivity (m) for each material for primary compression (b)..... 116

Figure 49: EBSD used to give maps of, (left) band contrast, (middle) phase map; blue is γ , red is α_2 , yellow is β_0 , (right) X-DRX; red is the recrystallised fraction, blue is deformed, of 45XD alloy after 50% compression in the HIP (a, b, c), THH (d, e, f), IHH (g, h, i) condition at 500x magnification..... 118

Figure 50: Plots calculating the DRX fraction from the GOS approach on the left, grain area frequency density on the right, for each material condition after 50 % primary compression at 1100 °C and 0.001 s⁻¹, (a, b) HIP, (c, d) THH, (e, f) IHH..... 121

Figure 51: Band contrast (BC) (a), phase fraction (b) and X-DRX map (c) of 45XD alloy in the THH+HT condition. This is THH material, primary compressed at 1100 °C, 0.001 s⁻¹ followed by intermediate heat treatment of 1200 °C, 2 hours followed by air-cooling. 125

Figure 52: SEM micrograph (BSE) of 45XD alloy after 50% compression, in the following conditions (a), HIP, (b), THH, (c), IHH, (d), THH+HT, all at 250X magnification, where black areas correspond to γ phase, white β_0 and grey α_2 , respectively..... 126

Figure 53: Secondary stress-stain curves (a), secondary compression at 1100 °C to 50 % at 0.001, 0.01 and 0.1 s⁻¹ over 870, 87 and 8.7 seconds respectively. Calculation of strain rate sensitivity (m) for each material for secondary compression (b). 128

<i>Figure 54: relationship between strain rate sensitivity of secondary compression and, (a) primary compression DRX fraction, (b) primary compression lamellar grain size, (c) primary compression lamellar content, (d) secondary compression relationship between β_0 and α_2 phase fraction and strain rate sensitivity.</i>	129
Figure 55: (a) relationship between pre-compression lamellar grain size (μm) and dynamic recrystallised fraction (X-DRX) returned (b) relationship between X-DRX returned from primary compression and its relationship with secondary strain rate sensitivity (m) (c) primary and secondary compression relationship between lamellar grain size (μm) and strain rate sensitivity (m), from work without intermediate and post working heat treatment in 4.1, 4.2, 4.4 and 4.5.	132
Figure 56: (a) OM image of as- received (ASR) cast microstructure of 4822 at 5x magnification, (b) Calculation of phase diagram (CALPHAD) of 4822 alloy from ICP analysis in Table 22.	135
Figure 57: OM images of 4822 alloy in the HIP (a, b), THH (c, d), IHH (e, f), condition at 5x magnification (a, c, e,) and 20x magnification (b, d, f,) before compression.	137
Figure 58: Primary stress-stain curves, compression at 1100 °C to 50% at 0.001 s ⁻¹ over 760 seconds.	138
Figure 59: Unstable material flow shown by images of compression samples (a, c, f). Of material in the 4822 alloy in the HIP (a, b), THH (c, d), IHH (e, f) condition at 5x OM magnification, after 50% primary compression at 1100°C, 0.001 s ⁻¹ .	141
Figure 60: EBSD used to give maps of, (left) band contrast, (middle) phase map; blue is γ , red is α_2 , yellow is β_0 , (right) X-DRX; red is the recrystallised fraction, blue is deformed, of 4822 alloy in the HIP (a, b, c), THH (d, e, f), IHH (g, h, i) condition at 500x magnification, after 50% primary compression at 0.001 s ⁻¹ .	142
Figure 61: Plots calculating the DRX fraction from the GOS approach on the left, grain area frequency density on the right, for each material condition after 50% primary compression at 1100 °C and 0.001 s ⁻¹ , (a, b) HIP, (c, d) THH, (e, f) IHH	144
Figure 62: Secondary stress-stain curves (a), secondary compression at 1100 °C to 50 % at 0.001, 0.01 and 0.1 s ⁻¹ over 870, 87 and 8.7 seconds respectively. Calculation of strain rate sensitivity (m) for each material for secondary compression (b).	145
Figure 63: EBSD used to give maps of, (left) band contrast, (middle) phase map; blue is γ , red is α_2 , yellow is β_0 , (right) X-DRX; red is the recrystallised fraction, blue is deformed, of 4822 alloy in the HIP (a, b, c), THH (d, e, f), IHH (g, h, i) condition at 1600x magnification, after 50% secondary compression at 1100 °C, 0.001 s ⁻¹ .	147
Figure 64: EBSD used to give maps of, (left) band contrast, (middle) phase map; blue is γ , red is α_2 , yellow is β_0 , (right) X-DRX; red is the recrystallised fraction, blue is deformed, of 4822 alloy in the HIP (a, b, c), THH (d, e, f), IHH (g, h, i) condition at 1600x magnification, after 50% secondary compression at 1100 °C, 0.1 s ⁻¹ . Adiabatic shear (ABS) example outlined in red.	149
Figure 65: (a)HIP and Homogenised microstructure of 4822 under 5X magnification OM (b) Phase fraction diagram for 4822 cast alloy determined from CALPHAD.	151
Figure 66: Recorded temperature-time profile of (AC) air cooled cyclic heat treatment and (FC) furnace cooled cyclic heat treatment from LAND instruments pyrometer.	153
Figure 67: OM images of 4822 alloy in the ACCHT (a, c, e), FCCHT (b, d, f), condition at 20x magnification. (a, b) at Face 1, (c, d) at the centre, (e, f) at Face 2.	154

Figure 68: (a) Lamellar grain size, (b) Compression sample ready for ACCHT or FCCHT with glass-based coating, -C= centre, -F1= one face, -F2= the opposite face to F1 for post heat treatment analysis	156
Figure 69: Primary stress-stain curves of the three material conditions under compression at 1100 °C to 50% at 0.001s ⁻¹ over 760 seconds.	158
Figure 70: OM image at the Face 1 of 4822 alloy in the ACCHT condition at 5x magnification after water quench from the compression thermal cycle at 1100 °C, with a 5-minute soak.	159
Figure 71: OM image at the Face 1 of 4822 alloy in the ACCHT condition at 5x magnification	159
Figure 72: OM images at P1 (centre) of 4822 alloy in the HH (a, b), ACCHT (c, d), FCCHT (e, f) condition at 5x magnification (a, c, e) and 20x magnification (b, d, f) after 50% primary compression at 1100 °C, 0.001 s ⁻¹	161
Figure 73: EBSD used to give maps to identify grains of similar orientation (a, d, g) , phase fraction (b, e, h) and X-DRX maps (c, f, i) of 4822 alloy in the HH (a, b, c), ACCHT (d, e, f), FCCHT (g, h, i) condition at P1 (centre) 500x magnification, after 50% primary compression at 1100 °C, 0.001 s ⁻¹	162
Figure 74: (a) Remnant lamellar grain area analysis of maximum, minimum and inter-quartile range of each material condition at P1 and P2 after 50% primary compression at 1100 °C and 0.001 s ⁻¹ . (b) positioning of analysis	163
Figure 75: Plots calculating the DRX fraction from the GOS approach on the left, grain area frequency density on the right, for each material condition at P1 after 50% primary compression at 1100 °C and 0.001 s ⁻¹ , (a, b) HH, (c, d) ACCHT, (e, f) FCCHT	164
Figure 76: Secondary stress-stain curves (a) of the three material conditions under compression at 1100 °C to 50% at 0.001s ⁻¹ over 800 seconds, 0.01s ⁻¹ over 80 seconds, 0.1s ⁻¹ over 8 seconds. Calculation of strain rate sensitivity (m) for each material for secondary compression (b).	166
Figure 77: EBSD used to give maps of, (left) band contrast, (middle) phase map; blue is γ , red is α_2 , yellow is β_0 , (right) X-DRX; red is the recrystallised fraction, blue is deformed, of 4822 alloy in the HH (a, b, c), ACCHT (d, e, f), FCCHT (g, h, i) condition at 1600x magnification, after 50% secondary compression at 1100 °C, 0.001 s ⁻¹	169
Figure 78: SEM-BSE used to give details of microstructural morphologies, (left) 0.001 s ⁻¹ , (middle) 0.01 s ⁻¹ , (right) 0.1 s ⁻¹ ; of 4822 alloy in the HH (a, b, c), ACCHT (d, e, f), FCCHT (g, h, i) condition at 1000x magnification, after 50% secondary compression at 1100 °C.	171

List of tables

Table 1: Effect of alloying elements in Titanium Aluminides	27
Table 2: Alloys in use as low pressure turbine blade material	58
Table 3: Average chemical composition of supplied 45XD ingot, analysed via ICP at three points by TIMET	63
Table 4: Average chemical composition of supplied 4822 ingot, analysed via ICP at four points by TIMET	64
Table 5: Heat treatment sample identification, temperature (°C)- cooling rate together with the phase the heat treatment is working within	66
<i>Table 6: Average chemical composition of supplied 45XD ingot, analysed via ICP at three points by TIMET</i>	<i>75</i>
Table 7: breakdown of lamellar grain content and size, as well as lamellar and equiaxed morphology and respective phase composition for 45XD in different conditions before compression from BSE image processing.....	79
Table 8: maximum flow stress seen for each 45XD material condition with 50% compression at 1100 °C, 0.001 s ⁻¹	81
Table 9: breakdown of phase composition for 45XD in all material conditions at P1 after compression from BSE image processing and EBSD mapping.	86
Table 10: Remnant lamellar morphologies of all 45XD material conditions at P1 and P2 after 50% compression, 1100 °C, 0.001 s ⁻¹	87
Table 11: breakdown of lamellar grain content and size, as well as lamellar and equiaxed morphology and respective phase composition for 45XD in different conditions before compression from BSE image processing and EBSD mapping.	94
Table 12: maximum flow stress seen for each 45XD material condition with 50% compression at 1100 °C, 0.001 s ⁻¹	95
Table 13: breakdown of lamellar grain content and size, as well as lamellar and equiaxed morphology and respective phase composition for 45XD in different conditions after 50% compression at 1100 °C, 0,001 s ⁻¹ from BSE image processing and EBSD mapping.	96
<i>Table 14: Sample identification and expectations for each test, all material is in the HIP (hot isostatic pressed) condition first, then described sequentially for simplicity. Any compression is described per blow (%), any heat treatment is described by temperature (°C)- cooling rate. Any dwell is for 30 minutes at compression temperature. RT is where the sample is returned to room temperature.....</i>	<i>99</i>
Table 15: Breakdown of microstructural analysis; lamellar grain size and content, phase and DRX fraction including grain area fraction ≤50µm ² , for 45XD following different processing sequences through hot compression at 1100°C, 0.001s ⁻¹ , to 50%.....	106
Table 16: Phase morphology fraction and lamellar content in the three material conditions before compression	115
<i>Table 17: Peak flow stress and strain rate sensitivity, measured at peak flow stress, strain of 0.04, for each material condition over primary compression</i>	<i>116</i>
Table 18: Phase, morphology, DRX and grain area <50 µm ² fraction for each material after 50% primary compression at 1100 °C and 0.001, 0.005 and 0.01 s ⁻¹ calculated from a combination of BSE and EBSD analysis.	119

Table 19: Sample identification, all material is in the HIP (hot isostatic pressed) condition first, then further processing is described sequentially for simplicity. All material is primary compressed to 50%, any heat treatment is described by temperature (°C), time, cooling rate.....	124
Table 20: Phase, morphology, DRX and grain area <50 µm ² fraction for each material after 50% primary compression at 1100 °C and 0.001 s ⁻¹ calculated from a combination of BSE and EBSD analysis.	125
<i>Table 21: peak flow stress and strain rate sensitivity for each material condition over secondary compression.....</i>	<i>129</i>
Table 22: Average chemical composition of supplied 4822 ingot, analysed via ICP at three points by TIMET.	135
Table 23: Microstructural details of 4822 material conditions investigated pre-compression from optical microscopy analysis.....	138
Table 24: Peak flow stress for each material condition over primary compression.	139
Table 25: Phase, morphology, DRX and grain area <50 µm ² fraction for each material after 50% primary compression at 1100 °C and 0.001, 0.005 and 0.01 s ⁻¹ calculated from a combination of OM and EBSD analysis.	143
Table 26: Compression behaviour values, peak flow stress and strain rate sensitivity for each material condition over secondary compression at 1100 °C to 50% at 0.001s ⁻¹ over 800 seconds, 0.01s ⁻¹ over 80 seconds, 0.1s ⁻¹ over 8 seconds.	146
Table 27: Phase, morphology, DRX and grain area <50 µm ² fraction for each material after 50% secondary compression at 1100 °C and 0.001, 0.01 and 0.1 s ⁻¹ calculated from a combination of BSE and EBSD analysis.	148
Table 28: CHT details for both FC and AC from pyrometer temperature monitoring.....	153
Table 29: Microstructural details of 4822 material conditions investigated pre-compression from optical microscopy analysis.....	155
Table 30: Compression behaviour values for each material condition over 760s compression at 1100 °C and 0.001 s ⁻¹	159
Table 31: Microstructural details of 4822 material conditions investigated after cyclic heat treatment and water quench from the compression thermal cycle at 1100 °C, with a 5-minute soak.....	159
Table 32: Morphology fraction for each material after 50% primary compression at 1100 °C and 0.001 s ⁻¹ calculated from OM and EBSD analysis.....	163
Table 33: Compression behaviour values, peak flow stress and strain rate sensitivity for each material condition over secondary compression at 1100 °C to 50% at 0.001s ⁻¹ over 800 seconds, 0.01s ⁻¹ over 80 seconds, 0.1s ⁻¹ over 8 seconds.	167
Table 34: Morphology fraction for each material after 50% secondary compression at 1100 °C, 0.001, 0.01 and 0.1 s ⁻¹ calculated from OM and EBSD analysis.	170

Abbreviations and symbols

45XD Ti-45Al-2Nb-2Mn-1 at%. XD is exothermic dispersion of boride.

4822 Ti-47.2-48Al-2Nb-2Cr at%

%_{eq} fraction of equiaxed morphology

%_{lam} fraction lamellar morphology

%_{α2} fraction of alpha 2

%_{β0} fraction of ordered beta

%_γ fraction of gamma

%_{γf} fraction of feathery gamma

1' Primary

2'' Secondary

25% + Dwell + 25% 25% compression of material in the HIP condition followed by a dwell at compression temperature followed by another 25% compression.

25% + RT + 25% 25% compression of material in the HIP condition followed by cooling to room temperature and then returning to compression temperature and another 25% compression.

25% + 1200AC + 25% 25% compression of material in the HIP condition followed by a heat treatment for 2 hour, 1200 °C with air cooling then returning to compression temperature and another 25% compression.

50% + 1200AC 50% compression of material in the HIP condition followed by post compression 2 hour, 1200 °C heat treatment with air cooling.

AC Air cooling

ACCHT Air cooled cyclic heat treatment

AFRC Advanced forming research centre

ASR As received

ASTM American Society for Testing and Materials

at% atomic percentage

BCC Body centred cubic

BSE Back scatter electron

C Centre of cyclic heat-treated work piece

CALPHAD Calculated phase diagram

CHT	Cyclic heat treatment
DRV	Dynamic recovery
DRX	Process of dynamic recrystallisation
EBM	Electron beam melting
EBSD	Electron back scatter diffraction
EDM	Electron discharge machining
EIGA	Electrode induction melting gas atomisation
eq	equiaxed morphology
F1	Face 1 of cyclic heat-treated work piece
F2	Face 2 of cyclic heat-treated work piece
FC	Furnace cooling
FCCHT	Furnace cooled cyclic heat treatment
FCT	Face centred tetragonal
GE	General Electric
GOS	Grain orientation spread
HCP	Hexagonal close packed
HEXRD	High energy x-ray diffraction
HH	HIP and HMG
HIP	hot isostatic pressing
HIP 50%	50% compression of material in the HIP condition
HMG	homogenisation
HT	Heat treatment
ICP	Inductively coupled plasma spectroscopy for elemental identification
IHH	Integrated HIP and HMG
IM	Ingot based metallurgy
ISM	Induction skull melting
IWQ	Ice water quench
lam	lamellar morphology
LPT	Low pressure turbine blade
m	Strain rate sensitivity

MDRX	meta-dynamic recrystallisation
OM	Optical microscopy
P1	Position 1, centre of compression test piece
P2	Position 2, outside 1mm of compression test piece
PAM	Plasma arc melting
PIGA	Plasma melting induction guiding gas atomisation
PM	Powder based metallurgy
RFL	Refined fully lamellar
SEM	Scanning electron microscopy
SRX	Static recrystallisation
THH	Traditional HIP and HMG
TiAl	Titanium aluminide
TIMET	Titanium metals corporation
TNB	Titanium, Niobium and boron. Group of TiAl alloys
TNM	Titanium, niobium and molybdenum. Group of titanium aluminide alloys
TZM	Titanium, zirconium and molybdenum. For high temperature forging dies.
VAR	Vacuum arc remelting
WQ	water quench
X-DRX	Dynamic recrystallised fraction
α	disordered alpha phase
α_2	Alpha 2 phase of D019 long range structure, chemical formula; Ti ₃ Al
β	Disordered beta phase, chemical formula; Ti
β_0	Ordered beta phase, of B2 long range structure, chemical formula; Ti
γ	Gamma phase of L10 structure, chemical formula; TiAl
γ_f	Feathery gamma microstructure
γ_{f-gb}	Feathery gamma microstructure formed at lamellar grain boundary
γ_{f-int}	Feathery gamma microstructure formed within lamellar grain
δ	Penetration depth effect of induction heating on work piece
ϵ	Strain
$\dot{\epsilon}$	Strain rate

ϵ_c	Critical strain
μ_r	magnetic permeability
σ	Stress
σ_{pfs}	Peak flow stress
σ_{ss}	Steady-state flow stress

1 Introduction

1.1 Intermetallics and titanium aluminide

Intermetallic compounds were defined in 1967 by Schulze as “intermetallic compounds as solid phases containing two or more metallic elements, with optionally one or more non-metallic elements, whose crystal structure differs from that of the other constituents” [1]. They show both metallic and ionic bonding characteristics between dissimilar atoms such as Fe-Al or Ti-Al over Fe-Fe or Ti-Ti bonding respectively. This leads to large, long range ordered crystal structures. This order brings with it properties that lend intermetallic compounds to applications as varied as superconductors and metallic glasses to non-conducting composites [2].

With ever increasing demands on automotive and aerospace engine manufacturers to develop systems with improved efficiency and reduced environmental footprint, advanced designs are based on higher service temperatures, lighter weight, and higher operation speeds. With properties such as high temperature stability, oxidation and corrosion resistance, high strength, and creep resistance, while also having a low density, intermetallic titanium aluminide (TiAl) alloys began being incorporated into aerospace designs in the latter half of the 20th century [3].

The difficulty, as with most intermetallics, is their inherent brittle nature at low temperatures. This leads to high processing costs due to the elevated temperatures required to achieve acceptable workability. If further applications of titanium aluminide are to be made, then the processing and production of high integrity titanium aluminide alloys requires further research and greater understanding.

1.2 Background and justification for this study

This project is a collaboration between Tier One members of the Advanced Forming Research Centre (AFRC), a recognised Centre of Excellence in innovative manufacturing technologies, research and development, metal forming and forging research. TIMET, as a global producer of titanium alloys and Tier One member of the AFRC, provided titanium aluminide cast ingot material for the project.

Titanium aluminide (TiAl) alloys fill an important gap between high temperature and high-density superalloys and low temperature and low-density titanium and aluminium alloys. This is particularly important when considering high temperature applications such as automotive and aerospace engine components [4]. Titanium aluminides compare favourably to nickel-based superalloys in terms of their high elastic modulus and low density, and to titanium alloys in terms of high temperature stability and oxidation resistance [5]. The interest in this study is in investigating methods to ease their production, and therefore expand their possible uses in the aeroengine and in other industries. With drives towards improved efficiency being seen across the transport sector, advanced materials are essential if we are to meet our climate change goals.

One major obstacle to further application identified is in the processing of a material with an inherent brittle nature at low temperatures (<800 °C). TiAl alloys show both metallic and ionic bonding character giving defined long-range ordered, therefore brittle, phases. For TiAl, they are based on γ (TiAl), α_2 (Ti₃Al) and β_0 /B2 (Ti). Their brittle nature leads to wrought processing techniques being largely avoided due to the high processing and equipment costs involved in multiple processing steps working at elevated temperatures which are necessary to achieve acceptable workability, as reviewed by *Appel et al.* [6]. Therefore, reducing processing steps and/or improving forging outcomes would be of industrial interest.

There are also challenges created by the initial casting process, casting of TiAl alloys such as 4822 (Ti-47.2-48Al-2Nb-2Cr at%) and 45XD (Ti-45Al-2Nb-2Mn-1 at%) used in this study, follow a peritectic solidification pathway resulting in solidification porosity and elemental segregation, which promotes the formation of brittle phases and large grained lamellar microstructures.

This results in a material that shows:

- Ease of fracture and flow localisation during processing
- Plastic anisotropy due to large grain sizes
- Slow recrystallisation due to elemental segregation

A review by *Kim, S.L., and Kim, Y. W.*, discussed several “pathways” to making improvements to and expanding the use of titanium aluminides [7]. The “pathway” starts with identifying a component, a target application or end use. This target then requires clear specific properties. This is followed by

investigation and understanding of the composition-processing-microstructure relationship of that material and the “Data, Knowledge and Information” collected over the past 30 years. A final target microstructure can then be identified to provide these properties.

A similar methodology has been followed in this study, by identifying processes of interest capable of producing components and new applications for the material. These target processes, such as isothermal closed die forging and hot rolling, require high integrity forged titanium aluminide stock, high in dynamic recrystallised material and free of anisotropic grain morphologies.

The aim of this PhD research is to investigate and develop alternative thermomechanical processing techniques to improve the forging outcomes, at industrially viable temperatures, of two cast, peritectic solidifying, consolidated titanium aluminide alloys; 45XD (Ti-45Al-2Nb-2Mn-1B at%) and 4822 (Ti-48Al-2Nb-2Cr at.%).

To start the project, a literature review will identify promising ingot processing techniques that may improve the efficiency of the initial ingot breakdown stage, referred to as primary compression. These processes and primary compression will look to produce high integrity, forged titanium aluminide stock ready for secondary processing by high deformation processes, such as closed-die forging and hot rolling, potentially expanding the list of possible applications.

2 Literature Review

2.1 Titanium aluminide

Titanium aluminide materials fill an important gap between high temperature and high-density superalloys against low temperature and low-density titanium and aluminium alloys. Titanium aluminide provides the compromise between these materials, as shown in Figure 1. The difficulty, as mentioned earlier, is in the processing and application of a material with a brittle nature, hence the drive to near net shape processing routes and application away from potential damage in service. The following chapters describe the current theory behind the processing, microstructure and properties of current titanium aluminides [8].

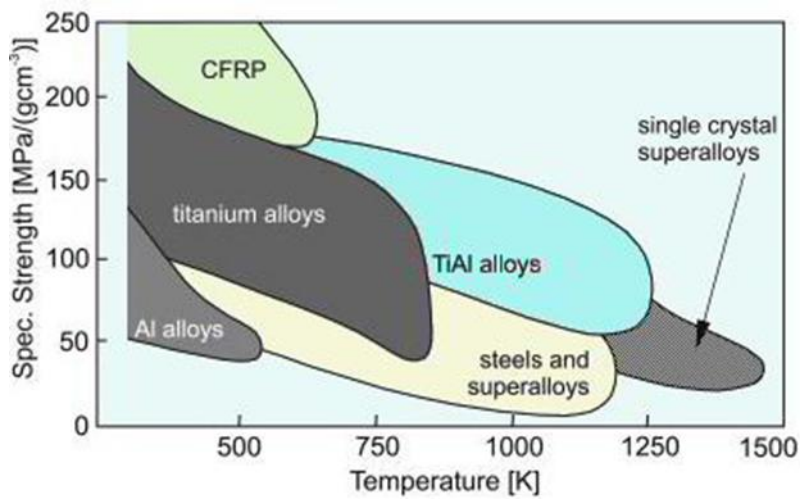


Figure 1: Specific strength versus temperature diagram for structural materials [8]

2.2 Crystallography, phases and alloying of titanium aluminide

2.2.1 Phase diagram – effect of aluminium

Titanium aluminide (TiAl) is an intermetallic compound that contains, at its most basic, titanium and aluminium. There are three intermetallic titanium aluminides, γ -TiAl, α_2 -Ti₃Al and α -TiAl₃. These are prevalent at different concentrations of aluminium respectively as shown in Figure 2 [3].

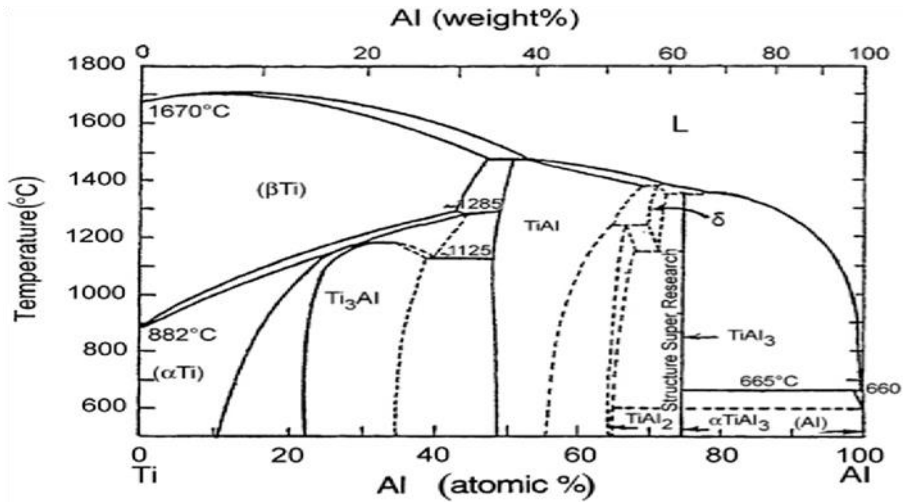


Figure 3: Ti-Al phase diagram[3].

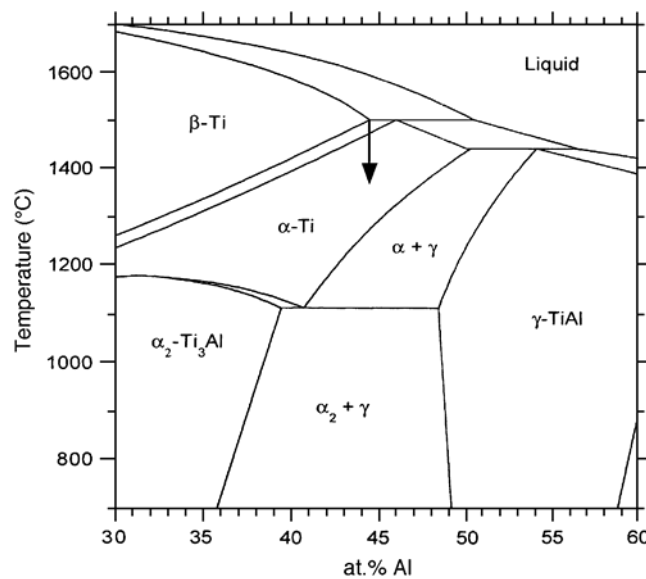


Figure 2: titanium aluminide phase diagram [10].

From an engineering point of view single phase alloys are of limited interest due to their brittle nature at all temperatures throughout their solidification pathway [5]. The dual phase γ + α_2 alloys of an aluminium content of 45-48 at% have been of interest for a number of years due to the phase fraction at this aluminium concentration providing the ductility required for hot working [9]. A more detailed phase diagram showing this region is shown in Figure 3 [10].

2.2.2 Crystal structures of phases in titanium aluminide

The α_2 -Ti₃Al and γ -TiAl phases give different structures, α_2 -Ti₃Al being hexagonal D0₁₉, while γ -TiAl has a tetragonal L1₀ structure, as shown in Figure 4 respectively, together with available slip planes and lattice parameters [11]. The traditional titanium phases of hexagonal (HCP) α and body centred-cubic (BCC) β structures are only present at high temperatures and, if alloyed accordingly in titanium aluminide alloys, ordered β , β_0 /B2 which will be discussed later in section 2.3.1.5. This phase is important when considering wrought processing routes [12].

α_2 -Ti₃Al hexagonal D0₁₉ structure
a=0.5782 nm, c=0.4629 nm

γ -TiAl tetragonal L1₀ structure
a=0.4005 nm, c=0.4070 nm

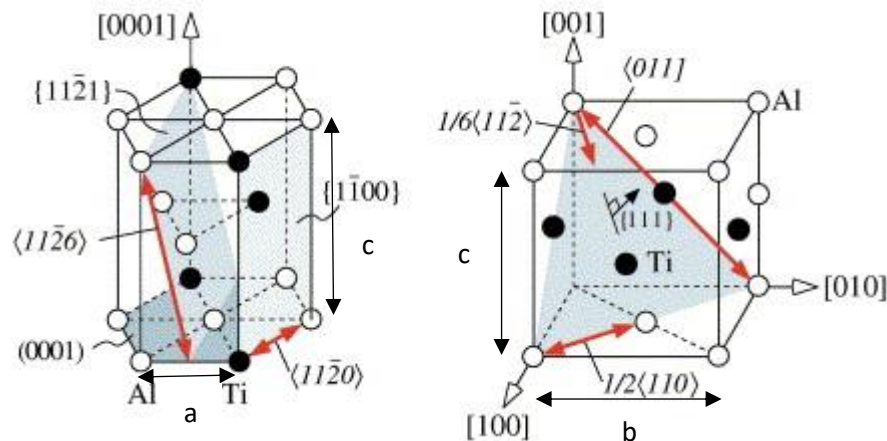


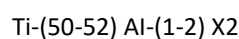
Figure 4: Left, α_2 -Ti₃Al hexagonal D0₁₉ structure a=0.5782 nm, c=0.4629 nm. Right, γ -TiAl tetragonal L1₀ structure a=0.4005 nm, c=0.4070 nm [11].

2.2.3 Alloying of titanium aluminide

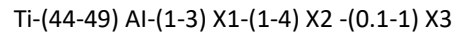
Alloying of titanium aluminide has been one method of improving properties. Extensive research has given four distinct generations of titanium aluminide alloy up until now, by applying different combinations and ratios of elements to enhance properties such as ductility. This ductility from alloying arises from improving four aspects of the intermetallic structure; enabling more slip modes, removing or at least changing the long range order, introduction of ductile phases that allow deformation, and changes in solidification during thermomechanical processing to give a more controlled or refined microstructure [3].

Moving away from single phase γ alloys to dual phase γ + α_2 of various aluminium concentrations, with small additions of additional elements typified the first generation of titanium aluminide alloys described by *Kim and Dimiduk* [13]. The 4822 (Ti—48Al-2Nb-2Cr at%) alloy characterises this first generation, being the first titanium aluminide alloy applied to a commercial aero engine, these flying from 2012 in General Electric (GE) turbine engines [14].

First-generation single-phase alloys have a general formula described by.

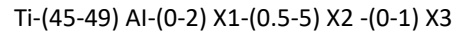


and dual phase alloys as.



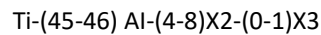
X1 covering manganese, chromium; X2 being niobium, tantalum, tungsten, molybdenum and X3 describing silicon, carbon, boron, nitrogen, and yttrium.

The second generation described by *Appel et al.* [15] restructured the formula for titanium aluminide alloys, these all being dual phase systems.

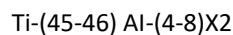


The roles of these alloying elements were retained, alloys include 45XD (Ti-45Al-2Nb-2Mn-at% -0.8TiB₂ vol%), this likely to be applied to future Rolls-Royce turbine engines [14].

The third generation of titanium aluminide alloys are dominated by those described as TNM (Titanium, niobium, molybdenum) or TNB (titanium, niobium, boron) alloys, these are higher in X2 alloying elements, particularly niobium, than earlier alloys which gives distinctive and useful β solidifying properties, which will be discussed in later chapters. These alloys, again dual phase at room temperature, follow the formula [16];



The removal of boron from the formulation and the increased significance placed on the grain refinement offered by massive transformation via post-solidification heat treatments, was the focus of the European IMPRESS project [17]. This gave the fourth generation of titanium aluminides, with an alloy of configuration;



In the IMPRESS project all of X2 was niobium, Ti- 46Al-8Nb (at.%). The project team took this new alloy from raw material and produced turbine blades for both aero and stationary gas turbine engines [18].

X1, X2 and X3 elements all play differing roles in the solid solution and are common throughout the generations providing a compromise between properties of ductility and toughness compared to temperature stability and oxidation resistance.

Table 1: Effect of alloying elements in Titanium Aluminides

Element	General alloying effect	Position in alloy formula	α , β or neutral stabiliser
Al	Increases oxidation resistance and lowers density	NA	α
Nb	Increases oxidation and creep resistance	X2	β
Ta	Increases oxidation and creep resistance, tendency for hot cracking	X2	β
W	Increases Oxidation and creep resistance	X2	β
B	Grain refiner	X3	α
C	Increases creep and oxidation resistance	X3	α
Cr	Increases ductility if added in small amounts; increases oxidation resistance in high conc.	X1	β
Mn	Increases ductility	X1	β
Mo	Increases strength, and creep and oxidation resistance.	X2	β
Si	Improves high temp mech properties	X3	β
Y	Grain refinement in lamellar structures	X3	β

To explain the mechanisms and the effects of these elements, we must break down these groups further in terms of how they alter the binary Ti-Al phase diagram. In titanium metallurgy, α and β stabilisers refer to elements which increase or decrease the α/β phase transformation temperature, or transus, of pure titanium, α increasing this temperature, β decreasing. The α and β phases are not present in TiAl alloys at room temperature but they still impact on these alloys during solidification, as will be discussed in 2.3.

X1 elements vanadium, manganese and chromium are applied to improve ductility of two-phase alloys, as they are found to reduce the strain caused by the tetragonal distorted face centred cubic structure of the γ phase, this caused by the atomic radii difference in titanium versus aluminium. X1 elements reduce the c/a ratio of the unit cell. This is by substitution at aluminium sites in the unit cell, leading to a weakening of the Ti-Al bonding due to changes in the electronic structure of the unit cell. In turn, this alters the bonding in the unit cell to become more isotropic and reduces the lattice resistance to dislocations along the $\frac{1}{2}$ (110) direction, shown in Figure 4b, when compared to binary titanium aluminide [19].

These additions do, however, reduce the oxidation resistance of the alloy, preventing the formation of protective aluminium oxide at high temperatures, hence the need for X2 alloying elements [20]. The X2 atoms, niobium, tantalum, tungsten, molybdenum, do not inhibit the formation of protective layers, in particular aluminium oxide, Al_2O_3 , providing increased oxidation resistance.

Smaller X3 element additions are made for reasons including oxidation and creep resistance, castability as well as more regular microstructure refinement. Additions of boron and yttrium offer grain refinement, boron and its effect on solidification and microstructure will be discussed later in greater depth [21]. Rarely applied elements such as carbon and silicon have shown improvements in creep properties, reductions in melt viscosity and improved high temperature properties [22–24].

2.3 Titanium aluminide alloys and their microstructures

2.3.1 Microstructures

Here, the focus will be on the dual phase alloys over the out-of-favour single phase alloys [13]. The titanium aluminide alloys of concern in this study are dual phase alloys, existing in the $\gamma+\alpha_2$ region at room temperature. However, it is the processing and cooling from higher temperature phases in heat treatment, or solidification from casting, which gives the materials microstructure and therefore its properties. This section describes the microstructures of titanium aluminide alloys, how alloying with boron impacts these and the effect of the solidification pathway the material has followed.

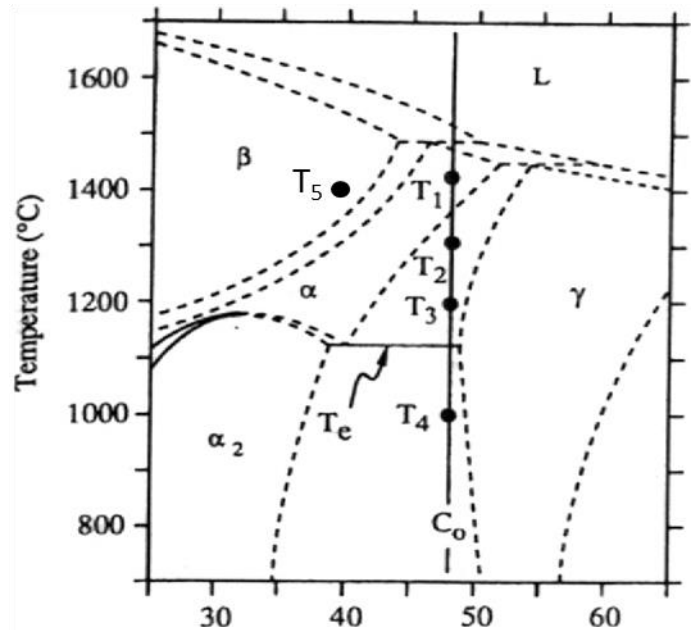
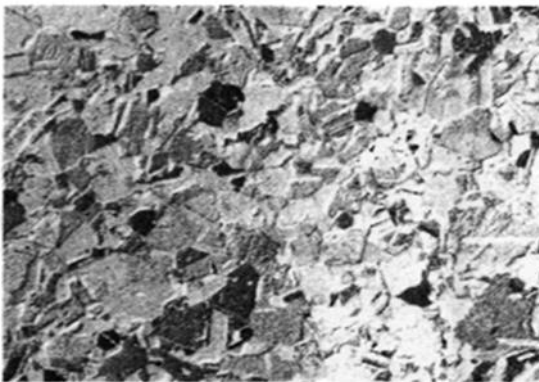


Figure 5: Example of phase diagram and working at different temperatures to achieve different microstructures for TiAl alloy 4822 [25].

2.3.1.1 Near-gamma



T4
Figure 6: Near-gamma microstructure[25]

Near-gamma is composed of equiaxed grains of γ with smaller α_2 deposits, as in Figure 6, this forms via heating in the $\gamma+\alpha_2$ phase field, as shown by point T4 in Figure 5 [25]. This microstructure lends itself to positive tensile properties at room temperature but poor fracture and creep resistance, moving the microstructure to the background in terms of research attention.

2.3.1.2 Near fully lamellar

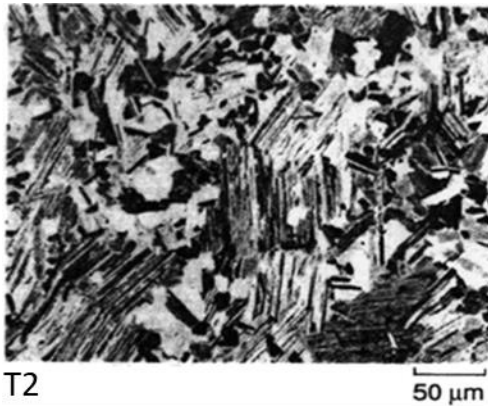


Figure 7: Near fully lamellar microstructure [25]

Colonies consist of near-lamellar grains of $\alpha_2 + \gamma$ plates with the presence of small equiaxed γ grains.

This microstructure is formed high in the $\alpha + \gamma$ region at point T2, the $\alpha_2 + \gamma$ plates and the equiaxed γ ratio as well as the size of the grains is controlled via the cooling rate and composition of the alloy [26]. The image at Figure 7 is 4822 (Ti-48 Al-2 Nb-2 Cr at%), an alloy which applies a near fully lamellar microstructure to give its mechanical properties in service. These at room temperature are more ductile and tougher than the more widely used fully lamellar microstructure, discussed below, however when in comparison at higher temperatures they are inferior [27].

2.3.1.3 Fully lamellar

Fully lamellar microstructures, like that of the near fully lamellar structure, consist of $\gamma + \alpha_2$ lamellae with the equiaxed γ deposits being absent. Formed from casting solidification or via heat treatments above the α transus, at point T1 on Figure 5, time spent at this temperature leads to α grain growth and so large lamellar grain sizes upon further cooling, described below. The solidifying route of the fully lamellar microstructure does not follow a eutectic pathway, but can follow two different routes depending on the aluminium concentration of the alloy [28]. Route 2 is the pathway followed by the alloys of concern in this study upon solidification or heat treatment.

Route 1; $\alpha \rightarrow \alpha_2 \rightarrow \alpha_2 + \gamma$

Route 2; $\alpha \rightarrow \alpha + \gamma \rightarrow \alpha_2 + \gamma$

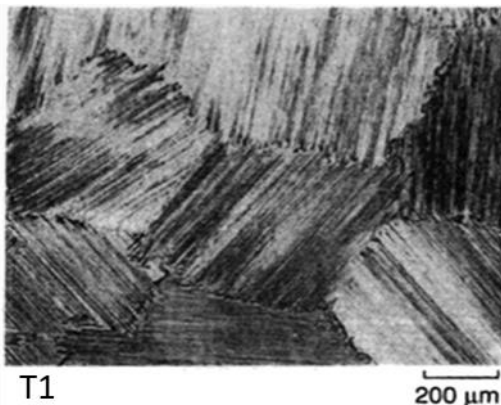


Figure 8: Fully lamellar microstructure [25]

This study by *Denquin and Naka* investigated the mechanism of lamellar formation and described how the disordered α and/or ordered $DO_{19} \alpha_2 Ti_3Al$ structure transformed into the $L1_0$ face centred tetragonal structure of γ . They found that the lamellar structure forms in two stages, first pre-nucleation. This is where dislocations upon cooling cause stacking faults of an FCC type; ABC-ABC, within the HCP α matrix, of AB-AB stacking type. This stacking fault can repeat every two basal planes,

resulting in the change of crystal structure from HCP to FCC. The crystallographic relationship between HCP and FCC, follows the Blackburn orientation relationship, $\{111\}\gamma \parallel (0001)\alpha_2$ and $\langle 110 \rangle \gamma \parallel \langle 1120 \rangle \alpha_2$,

the (0001) basal plane of the HCP structure being the habit plane interfacing the two phases, leading to the alternate adjacent phases of the lamellar structure eventually forming with further cooling.

These stacking faults lower the activation barrier for the second stage; nucleation and growth of γ from the FCC type stacking faults in the α matrix upon further cooling. Nucleation consists of atom transfer; this lowers the energy barrier for the ordering of FCC into the long range ordered $L1_0$ structure and distortion of the FCC structure to give face centred tetragonal (FCT) and so the γ phase. This sequence of events also explains why each α grain produces a single lamellar grain of identical size upon cooling due to the single set of basal planes in the HCP α structure matching that of the FCT structure of γ . The α phase present in the lamellar grain transforms at lower temperatures by an ordering reaction of α ($A3$) to α_2 (DO_{19}), meaning all α will have the same crystallographic orientation, to give the $\gamma+\alpha_2$ lamellar grain. From this mechanism the lamellar structure can form to give either the fully or nearly lamellar microstructures [29].

2.3.1.4 Duplex

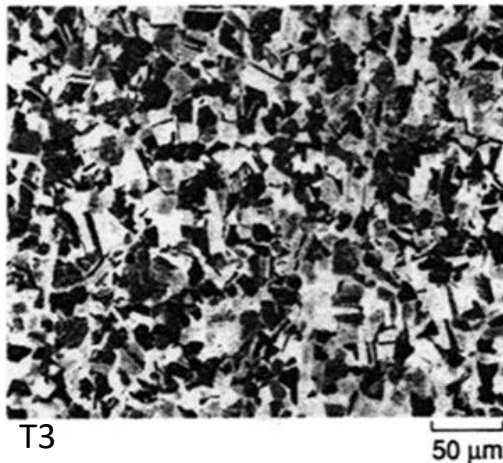


Figure 9: Duplex microstructure [25]

Duplex microstructures are composed of equal parts of $\alpha_2 + \gamma$ lamellae with equiaxed γ . This gives a compromise of good room temperature ductility and toughness, but poor high temperature creep resistance. Such structures are formed low in the $\alpha + \gamma$ phase, at a temperature that produces equal volumes of both α and γ phases, this temperature being alloy dependent. The fine-grained combination of both phases begins with the heat treatment transforming α_2 to α . To reach equilibrium, α precipitates grow into plates in

favour of the existing γ , until a 1:1 (α : γ) ratio is reached. Both phases grow in grain size at temperatures in the $\alpha + \gamma$ phase over time in a competitive process, inhibiting each other, hence the fine-grained microstructure [30].

2.3.1.5 β solidifying microstructures

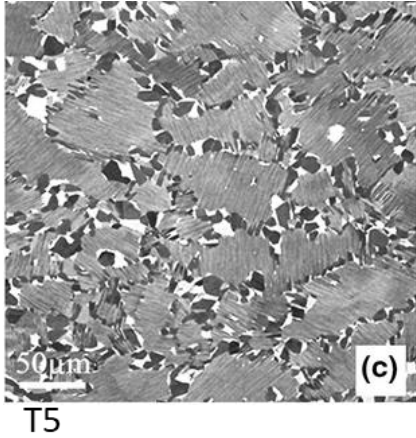
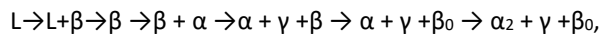


Figure 10: β solidifying microstructure [31]

through the β phase, $L+\beta \rightarrow \beta$, rather than through $L+\beta \rightarrow \alpha$ is essential to avoid segregation [32–34]. So, solidification follows as such;



The volume of α at high temperatures and retained β_0 at lower temperatures is dependent on the extent of α and β stabilisers in the alloy [35].

The microstructure itself, as given by the solidification route, consists of $\alpha_2 + \gamma$ lamellae with the equiaxed γ as seen in other microstructures of titanium aluminide, with additional grains and laths of β_0 . The retained β_0 is present if the heat treatments of the alloy allow it, removal of the β_0 from the structure at room temperature achieves a more creep resistant structure [36].

The disordered β phase, present at high temperatures, provides these alloys with several beneficial properties over other conventional titanium aluminide microstructures. Good workability/ductility, even at low volumes of β , with little segregation, leaving a homogeneous and fine microstructure even in the as-cast condition [37].

2.3.1.6 Effect of boron additions

After the first generation of boron free, dual phase alloys, additions of boron have influenced titanium aluminide metallurgy to reduce processing cost. Grain refinement of the as-cast microstructure is the aim of these additions, ideally removing much of the costly wrought processing. The boron enables refinement through the changes caused in solidification pathway [21].

Studies of the 1990s looked at the concentration and the source of boron required to achieve grain refinement. These gave the guidelines in how to apply borides successfully, but no clear-cut mechanism. These early practical studies concluded that titanium diboride (TiB_2) is preferred, with a minimum concentration of 0.5 at%, and that the borides must be homogeneously dispersed through

These microstructures are gained via the alloying of titanium aluminide with β stabilisers to the point where ordered body centred cubic (BCC) β ($B2/\beta_0$), is retained at room temperature and disordered β is present at elevated temperatures. The Al concentration, acting as α stabiliser, of the alloy dictates how suppressed the phase boundary is by the β stabilisers. In β solidifying alloys the Al concentration tends to be lean; <44 at%. [31].

Alloy refinement investigations by Zhang *et al*, Imayev *et al* and Chladil *et al* found solidification

the melt pool prior to casting [38]. From 2007, the mechanism of how boron altered the solidification pathway was beginning to reach conclusions, this was found to alter depending on the path followed, this being dictated by the aluminium concentration. With several mechanisms suggested for different aluminium concentrations and different solidification pathways, the topic was later reviewed by *Hu*. [39].

For peritectic solidifying ($L+\beta\rightarrow\alpha$) alloys, such as 45XD, the titanium boride precipitates nucleate α , α grows into the high temperature disordered β , also present as well as any liquid present. This relies on a critical boron concentration; this point is where the boride precipitate forms before the phase transformation occurs [33].

The boride gives the α its random orientation if homogeneously dispersed [40]. As cooling proceeds this gives the γ precipitated from the α and so the subsequent lamellar grain the same random orientation [41].

2.3.1.7 Effect of rapid cooling

As time at temperature and slow cooling rates influenced the cast microstructures discussed above, rapid cooling from high temperatures, particularly from the single α phase can also lead to microstructures and phase transformations of interest, in particular air cooling, which is covered here. Phase transformations are reviewed in greater detail by *Ramanujan* [29].

- Air cooling (AC) \rightarrow fine fully lamellar $\gamma+\alpha_2$, feathery γ (γ_f) and Widmanstätten-like γ transformation
- Water quench (WQ) $\rightarrow\gamma_f$ and massive γ transformation
- Ice water quench (IWQ) \rightarrow massive γ transformation

In their work on γ_f , *Dey et al.* found γ_f morphologies could be produced from AC to WQ [42]. The authors found γ_f could be obtained in two forms depending on where it had originated on the prior α grain. Internal feathery γ packets (γ_{f-int}) are randomly misorientated γ laths that nucleate within prior α grains as the lamellar structure begins to form upon cooling, without being in contact with any grain boundary. Grain boundary feathery γ packets (γ_{f-gb}) grow from the grain boundary of one lamellar grain into the adjacent lamellar grain, with no apparent orientation relationship with its host lamellar grain. The properties and compression behaviour of these γ_f dominant microstructures for TiAl alloys is not well documented.

2.4 Composition- processing-microstructure relationships of titanium aluminide

This section will describe the production of titanium aluminide stock and products, focusing on ingot metallurgy through to the wrought processing methods employed to achieve the desired microstructures, as described in Figure 11 [43]. How these techniques are applied and their impact on the microstructure and its deformation will be discussed, properties will be mentioned where appropriate, these being relevant to further processing. Special mentions of near net shape processing and powder metallurgy will be made.

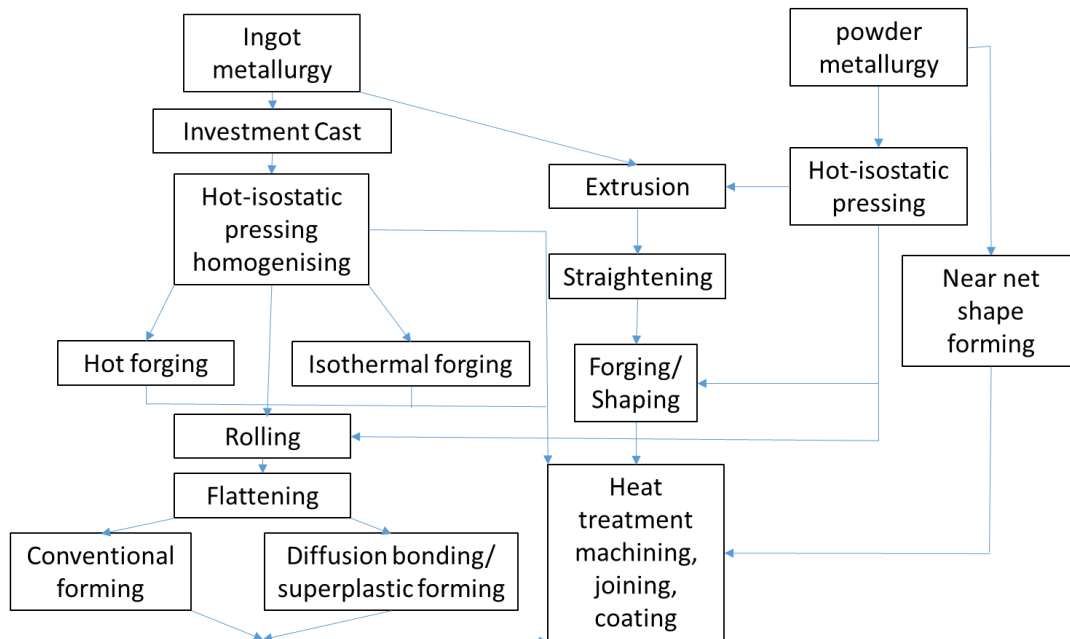


Figure 11: diagram displaying processing routes possible for titanium aluminide

2.4.1 Titanium aluminide stock production

2.4.1.1 Ingot production and casting

Titanium aluminide ingot production differs little from conventional titanium in terms of melting equipment, with vacuum arc remelting (VAR), plasma arc melting (PAM) and induction skull melting (ISM) being viable [44]. Electron beam melting (EBM) has become popular for titanium alloys but is avoided for titanium aluminide alloys due to the relatively high vapour pressure of aluminium. PAM has certain advantages over the other techniques in terms of processing cost and flexibility, as it can produce a variety of ingot sizes from different feedstock types of a reproducible homogeneity and quality, due to processing under an inert atmosphere [12].

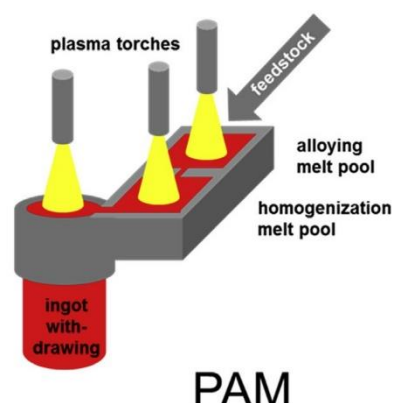


Figure 12: Diagram displaying PAM process, with homogenization step and ingot drawing[44]

A significant difference between titanium and titanium aluminide production is the feedstock required. The high proportion of aluminium and alloying elements necessarily results in three different melting temperatures to be considered: that of titanium (1668°C), any master-alloy present, containing the alloying elements, (1650°C), and the aluminium (660°C). This range of temperatures causes issues such as the formation of titanium inclusions in the melt pool, as shown in Figure 13. To

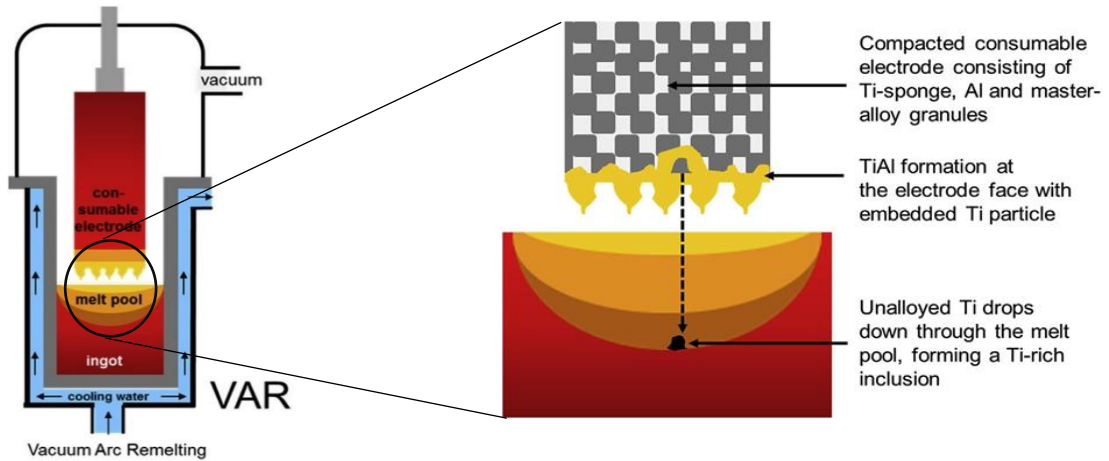


Figure 13: Diagram displaying VAR process, with method of Ti inclusion [44]

reduce inclusions, the VAR process must be run several times, though this still doesn't solve the problem completely. PAM does not have this issue with its near continual heating; however, vaporisation of alloying elements is a concern, though this can be mitigated through additions as well as maintaining an inert atmosphere under pressure [44].

When the melt pool has been homogenised, casting takes place. This can be via traditional investment casting or centrifugal casting to give an ingot ready for further processing, including machining and hot working [45].

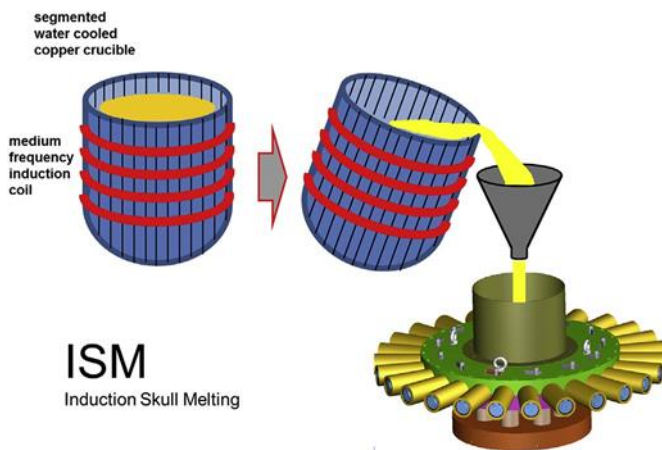


Figure 14: Diagram displaying ISM process and pouring for centrifugal casting, also used for casting melt from the VAR processes [44]

When casting-specific alloy compositions are used near-net shape products can be achieved with little further work, such as engine valves and turbocharger turbine wheels [23]. Reviewed by *Noda*, applying precision casting techniques, such as counter-gravity- low pressure casting removes the need for further consolidation or machining [22]. Usually, to achieve the desired properties, this large

grained, as-cast microstructure (in the region of 50-400 μm depending on the alloy composition) requires refining via one or more of the processes described in following sections [12].

2.4.1.2 Powder metallurgy

As shown in Figure 11, powder metallurgy can be the other starting point for producing titanium aluminide components. Powder is produced via the atomisation of a pre-alloyed electrode or from a melt pool, these are known as electrode induction melting gas atomisation (EIGA) and plasma melting induction guiding gas atomisation (PIGA) respectively. Both have their benefits and drawbacks. EIGA requires less energy and is safer as the melt pool does not have to be sustained, but relies on a pre-alloyed electrode, leading to questions over homogeneity of the powder. PIGA is in the opposite position, it requires more in terms of energy to maintain the melt pool with all the hazards that entails, however this melt pool ensures a homogeneous powder. Throughout the process, the reactive powder must be under an inert atmosphere. If exposed to air, impurities such as picking up of oxygen, nitrogen and carbon, can take place, removing the benefits of homogeneity. The argon atmosphere required for each stage of both routes must be taken into account, as it causes costs to increase [46].

If the inert atmosphere is maintained, the advantage of these techniques lies in the improved homogeneity when in comparison to ingot based metallurgy, giving more reliable components with reproducible properties [47]. The fine powder itself is also beneficial when we consider near-net shape processing; parts can be consolidated and compressed directly from powder to the finished article, with the obvious savings in machining this includes. With greater control of starting grain size, courtesy of the particle size control offered by EIGA and PIGA, deformation can also be different from the ingot-based materials. Work by *Semiatin et al.* found powder metallurgy to have lower peak flow stress when compressed compared to that of ingot-based material, this was deemed to be due to the smaller lamellar colony sizes of powder-based material, of interest if wrought processing techniques are to be used over near net shape processes [48].

2.4.1.3 Consolidation of titanium aluminide via hot isostatic pressing

When considering either powder or ingot metallurgy, consolidation via hot isostatic pressing (HIP) is a common process to bind the powder or remove porosity from the casting process [49]. This is done by applying constant pressure in three dimensions, to either the ingot or powder filled can, all via an inert gas, at high temperatures inside a high-pressure vessel [50]. With reducing porosity comes the opportunity for near-net shape processing, cast parts that require very little in the way of either final machining or further hot working.

Mechanical property changes occur from the high temperatures, pressures and long process times, not necessarily giving the microstructure desired. This can mean an already costly process can become a complex one. For example, *Bieler et al.* found the standard HIP procedure (1270 $^{\circ}\text{C}$, 175 MPa, 4 hours) for carbide doped 45XD cooled too slowly, leading to inhomogeneous carbide precipitation.

This required an additional 1300°C, 8-hour heat treatment to rectify [51]. Combined HIP and heat treatment processing provides an interesting move away from this two-step method, greater control over the post-HIP cooling rate and so grain size and microstructure type, being particularly beneficial [52].

2.4.2 Thermal mechanical processing of titanium aluminide

Thermal mechanical processing or hot working involves straining the microstructure, at a preferred temperature, with control over the total strain and the strain rate applied. Desired properties for in-service might include improvements in tensile performance and fracture toughness, which can be achieved by thermal mechanical processing [27]. These mechanical properties are also important for titanium aluminide components and depend on the elemental composition of the alloy, the resulting phase fraction, as well as the physical characteristics of the microstructure, such as grain size; these being manipulated via thermal mechanical processing techniques.

However, to get to this point the material must be able to be processed in the first place; a property referred to as workability, or forgeability when considering forging.

For titanium aluminide to achieve acceptable hot workability there are issues to consider, as reviewed by Appel *et al.*, the list as they put it is below [7];

“(i) a significant plastic anisotropy of the material, due to the lack of independent slip systems, which is reflected in the deformed state

(ii) low dislocation mobility

(iii) low diffusivity and grain boundary mobility, which retard recovery and recrystallization

(iv) the association of dynamic recrystallization and phase transformations, which might be involved in the development of textures

(v) limited ductility and susceptibility to cleavage fracture, which determine the failure modes under hot-working conditions.”

This review of hot working titanium aluminide also identifies the issues with peritectic solidifying material when considering initial ingot breakdown or primary wrought processing, these are broadly grouped as;

- ease of fracture,
- plastic anisotropy and,
- slow recrystallization.

These issues are both inherent in the material; from the lack of slip systems in the long range ordered phases present at room and working temperatures as well as a product of alloying and casting ingot material; large lamellar grain size and elemental casting segregation. These groups will repeatedly come up over the next sections as the factors that cause them are discussed.

First, the distinction between the aims of primary and secondary processing should be made clear. Successful primary processing, seen as equivalent to ingot breakdown, or forming a pre-form in this study, looks to return a crack-free, isotropic behaving microstructure ready for secondary processing. To achieve this, pre-compression processing should aim to deliver a material that responds efficiently to deformation. An efficient response to primary processing includes returning a material with high lamellar globularisation, and so high levels of dynamic recrystallisation, both terms which will be introduced in this chapter. Secondary processing covers high deformation processes such as hot rolling or isothermal closed-die forging. For a successful outcome these techniques require a refined, largely recrystallised microstructure, ideally capable of strain rate sensitivity of ≥ 0.3 [53],[54],[55],[56],[57],[58].

To discuss workability and improving forging outcomes, we need to understand the plastic deformation of relevant titanium aluminide phases and microstructures, or the permanent distortion of a material under applied stress, in metals this can occur via:

- Slip from the motion of dislocations in the crystal structure
- Twinning, where plastic deformation causes changes in crystallographic orientation
- Diffusion creep
- Grain-boundary sliding
- Grain rotation
- Deformation-induced phase transformations

2.4.2.1 Phase fraction, elemental homogeneity and dynamic recrystallisation

In phases present in titanium aluminide alloys, the deformation modes are via slip and twinning as well as elastic deformation of both phases [59]. How and when these modes play a role in deformation is dependent on the temperature and phases present. For single phase γ , Figure 4b, deformation at room temperature is by super-dislocations; a dislocation of more than one atom wide. This is via the Burgers vectors $\langle 101 \rangle$ or $\langle 011 \rangle$, but this movement is limited due to the Ti-Ti and Ti-Al bonds and their covalent nature, giving γ its brittle properties at room temperature [60]. The super-dislocations mentioned above only become active at high temperatures.

At high temperatures above the brittle to ductile transition temperature, for γ this is around 800°C, deformation proceeds by normal dislocations via $1/2 \langle 110 \rangle$, and mechanical twinning due to the $1/6$

$\langle 112 \rangle$ partial dislocation. This deformation operates in the $\{111\}$ plane of the tetragonally distorted face centred cubic (FCC) $L1_0$ structure.

Addition of the hexagonal close packed (HCP), DO_{19} α_2 phase, Figure 4a, with only two slip systems at the Burgers vectors $\langle 1126 \rangle$ on the $\{1121\}$ plane and $\langle 1120 \rangle$ on the $\{1100\}$ and $\{0001\}$ planes alters the deformation of the other, γ phase in a positive fashion, within limits [61]. Formation of the dual phase lamellar microstructures, described in 2.3.1.3, results in γ twinning of the $1/6 \langle 112 \rangle$ and normal dislocation of the $1/2 \langle 110 \rangle$ at low temperatures. This has been put down to α_2 taking up interstitial elements, known as gettering, as the solubility for these is higher in this phase than γ . This effectively purifies the γ phase by hardening the α_2 , reducing the stresses involved by interstitials interfering in Ti-Ti bonding [62]. *Holec et al.* also added to this by calculating preferential occupancy sites for different alloying elements and interstitials in α_2 , γ and β [63].

Another factor, largely ignored in previous studies on peritectic alloys, is the β_0 phase. These peritectic alloys can contain the ordered B2/ β_0 phase, without the benefit to workability of solidifying through the single, disordered β phase region [17],[18].

As previously mentioned in 2.3.1.5, both the ordered and disordered β phase has a body centred cubic (BCC) structure, Figure 15, disordered β is present at hot working temperatures and ordered β_0 at room temperature, as seen in the quasi-TNM phase diagram seen in Figure 16 [65]. Solidifying through the β phase ($L \rightarrow L + \beta \rightarrow \beta$) helps to produce a more elementally homogeneous microstructure, avoiding aluminium segregation and anisotropic casting texture seen through peritectic solidification $L \rightarrow L + \beta \rightarrow \alpha$, as reviewed by *Clemens and Mayer* [66]. This, together with its often fine grained and globular nature, allow for isotropic deformation, allowing near conventional temperatures to be used in hot working [34].

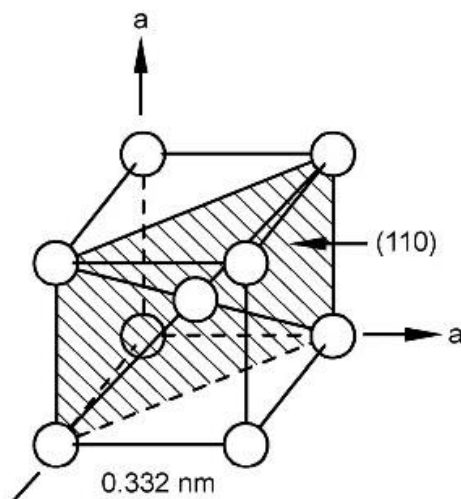


Figure 15: Ordered B2 and disordered body centred cubic unit cell structure [3]

The benefits of the β phase being present in hot deformation was investigated around the beginning of the millennium. Groups such as *Tetsui et al.* for example, applied 5 at% manganese to their alloy to gain the disordered β phase to aid hot working and production of turbine blades [67]. The team applied a variety of heat treatments and thermomechanical processing techniques; forging, rolling, bending, to produce several structural components. Mechanical properties (including tensile strength from room temperature to 1000 °C and high cycle fatigue strength) were investigated. This disordered phase

eases hot deformation when within the $\beta+\alpha$ region [32]. *Wang et al.* found the disordered β phase to be a largely positive influence regarding microstructural stability and ductility by forming laths with γ and by reducing the overall α_2 fraction, also improving oxidation resistance [68]. The disordered phase reduces flow stress and allows levels of deformation previously difficult to attain with the dual phase system. This is done via the BCC unit cell's twelve available slip systems through the $\langle 111 \rangle$ direction in the $\{110\}$ plane, as well as twinning and dynamic recrystallisation [69].

However, issues arose in terms of lower than anticipated tensile strength and poor workability at lower temperatures. This was determined to be due to a high ordered β_0 phase fraction. The ordered B2/ β_0 phase fraction is accentuated by aluminium segregation from peritectic solidification [67]. At the lower working temperatures used in this study, also examined by *Tetsui et al.* and others, the long range ordered B2/ β_0 is present [68],[70],[71]. This has limited deformability due to the loss of symmetry seen in the unit cell upon ordering and β_0 concentrates dislocation pile-ups, as identified by *Molénat et al.*, its presence contributing little to workability [72],[73].

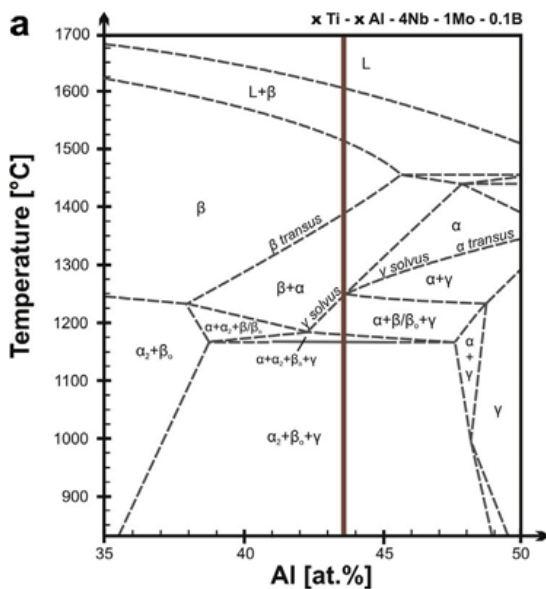


Figure 16: Phase diagram of TNM type alloying system [65]

This disordering reaction temperature is not known for all alloys so the β_0 present can have an embrittling effect in service or processing if not controlled [74], [75].

As found by *Zhang, Dehm and Clemens*, removing the β_0 phase isn't without its difficulties [32]. Investigations of the impact of HIP and homogenisation (HMG) on the content and distribution of this phase found both pressure and α phase HMG essential to removing β_0 but this came with excessive grain growth in their low boride alloy.

This was largely resolved by the design of the third generation of titanium aluminide alloys [32]. This group is referred to as TNM alloys (titanium, niobium, molybdenum), this being the first commercial β -solidifying alloy developed by GKSS of Germany in 2000 [15]. The majority of recent work regarding β deformation is based upon this alloy design. A case study of TNM in low pressure turbine blades will follow at the end of this review.

However, even in TNM alloys workable disordered β only comes with the disordering reaction of $\beta_0 \rightarrow \beta$ at high temperatures, as shown on β -solidifying TiAl alloy Ti-43.5Al-4Nb-

Attempts to retain the disordered β phase have been noted, through a high cooling rate for example, however this leads to the flow stress increasing dramatically upon deformation. This mechanism for body centred cubic materials was proposed by Seeger and Wüthrich in the 1970s, described in terms of titanium aluminide by *Appel, Clemens and Fischer* [73]. So, this technique cannot be used to increase ductility at sub $\beta_0 \rightarrow \beta$ ordering temperatures.

Deformation for β -solidifying alloys was comprehensively reviewed by *Mayer et al*, older non- β solidifying alloys by *Appel and Wagner*, with an update including modelling of deformation by *Appel, Clemens and Fischer* [31,71,76].

So, for the thermal mechanical processing of peritectic solidifying titanium aluminide alloys, of concern to this work, both dynamic and static restorative processes of γ are predominantly activated by the strain energy caused by dislocations multiplying during deformation. When the increased dislocation density reaches a critical limit, the system reacts in such a way that reduces the total energy. These are referred to as dynamic restorative processes during hot working and static restorative processes after, these using stored strain energy rather than immediate strain energy.

Dynamic processes include dynamic recovery (DRV), which is the release of strain energy through slip and dynamic recrystallisation (DRX), which is the replacement of old high strain grains with new, strain free, equiaxed material. In the γ phase, with its low stacking-fault energy, DRV is slow, giving high dislocation density, restoration is therefore reliant on DRX in dual phase alloys [77].

With compression, the DRX process activated for γ , with its low stacking fault energy, is discontinuous (dDRX, simply referred to as DRX); there are clear nucleation and growth stages involved in the formation of the new grains [77]. Once compression and so DRX has stopped, restoration of TiAl material with high dislocation density can continue via meta-dynamic recrystallisation (MDRX) [77]. MDRX refers to the growth of DRX grains into the surrounding material, causing an accumulation in dislocation density and then recrystallisation.

One theory (i), applied to austenitic steel and magnesium alloys, is that MDRX is dependent on the dynamic recrystallised fraction ($X_{\text{DRX}} > 50\%$), linked to a transition strain (ϵ^*), below this ϵ^* , static recrystallisation (SRX) takes place with the accompanying fine globular microstructure symptomatic of SRX [78],[79]. This ϵ^* can take place between peak and steady state strain, after which MDRX behaviour is independent of additional strain.

However, other authors have offered another theory, (ii), stating that MDRX will take place if DRX has been initiated at all [80]. Restoration by MDRX has been claimed to apply to titanium aluminide alloys with lamellar morphologies and identified as a possible method of reducing microstructural

heterogeneity from compression by further globularisation of lamellar colonies and equalising globular grain dimensions.

Wan et al. looked at critical conditions for dynamic recrystallisation using a PM version of an alloy to be studied, 4822, consisting of equiaxed fine grains [89]. They noted that the homogeneous microstructure of globular $\gamma+\alpha$ exhibited good hot workability due to high dislocation mobility and ease of DRX. This is one example of where a peritectic solidifying TiAl microstructure and subsequent workability does not suffer with anisotropic deformation behaviour or ease of fracture, because of the homogeneous equiaxed microstructure present. This alloy also benefited from elemental homogeneity, recrystallisation is therefore eased. As discussed in 2.4.1.2, PM alloys, are more elementally homogeneous than ingot-based metallurgy routes.

In work on peritectic solidifying ingot-based material (IM) to ensure successful and homogeneous compression *Semiatin et al.* found the material required temperatures in the α phase before wrought processing [94],[95]. They identified that if ingot material had not been held above the α transus, aluminium segregation from casting caused issues such as differing transus temperatures, flow stresses and phase distribution upon compression, as did *Fuchs* [92]. Alternative homogenisation routes have been explored. *Kong, Chen and Niu et al.* applied lengthy heat treatments to various ingot material at temperatures in the $\gamma+\alpha_2$ region in several studies, anything below this α temperature led to segregation and striations on compression [81], [99],[100],[101]. No assessment of X-DRX was made, but large lamellar microstructures can be seen in the microstructural imaging included in their work. This was seen in other work of theirs and acknowledged to be due to the poor diffusion of alloying elements and Al segregation [102].

Wang et al. found the $>\alpha$ transus homogenisation step essential preparation for grain refinement through cyclic heat treatment, avoiding hot working in the process [96]. This work has been followed by other researchers espousing the importance of the $>\alpha$ transus homogenisation step for increasing the dynamic recrystallised fraction (X-DRX) [97], [98], [81]. Heat enables atom transfer to occur and a uniform solid solution to arise. This has been addressed to some extent with the likes of centrifugal casting as discussed in 2.4.1.1 and other techniques, such as ultrasonics in the melt pool being introduced to achieve uniformity [82].

These studies on IM TiAl have a more heterogeneous microstructure to work with in initial ingot breakdown in comparison to those studying PM. To improve forging outcomes and increase the X-DRX for further steps necessitates the understanding of the lamellar structure and its behaviour through compression or heat treatment.

2.4.2.2 Lamellar microstructures and globularisation

The lamellar morphology itself and its formation is described in 2.3.1.3, here the focus will be on the breakdown or globularisation of this anisotropic behaving material. Globularisation begins to initiate when lamellar grains are under strain at the grain boundary, the kinetics of this process are dictated by several variables and processes, discussed here.

With a favourable orientation and grain size that is susceptible to the strain applied, kinking of the lamellar structure occurs. This will cause parts of the lamellae to “pinch off”, and from these new equiaxed grains will then grow, this is the basic mechanism for DRX in alloys of this type [92]. With strain and time DRX will proceed leading to further break-up of these lamellae and softening of the flow stress seen in compression. The process of lamellar grains being replaced by equiaxed material is often referred to as dynamic globularisation, as reviewed by *Seetharaman and Semiatin* [25]. Recrystallisation, and to a lesser extent phase boundary bulging, were identified as the mechanisms of globularisation by *Zhang et al*; this behaviour was further described by *Tian et al.* [37],[48]. This process removes the anisotropic character provided by this structure.

The fraction dynamically recrystallised (X-DRX) in fully lamellar TiAl material is dependent on the initial lamellar colony size, this is due to grain boundaries acting as nucleation sites for globular morphologies, with lamellar-lamellar grain boundaries being preferred for globularisation [58]. *Semiatin, Seetharaman and Weiss* reviewed earlier work looking at the relationship between starting microstructure, flow softening rate, recrystallisation and flow localisation [47]. The authors identified that the lamellar characteristics, especially lamellar grain sizes, were the most significant factor influencing the easing of the flow stress, with *Semiatin, Seetharaman and Ghosh* identifying the effect grain size and strain rate has on the fraction globularised [24].

Other microstructural details of lamellar grains also influence the deformation behaviour of the material and extent globularised. Microstructural parameters such as lamellar content, lath thickness and orientation, and in the case of duplex and nearly lamellar microstructures, the surrounding equiaxed grain size and content also contributes.

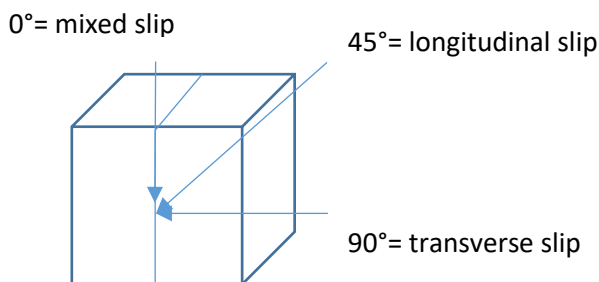


Figure 17: Angle of compression to lath of lamellar grain

Considering bulk TiAl ingot material lamellar orientation is largely random if we ignore the effect of fast cooling at the outer edges of the work. This gives hard (0 and 90°) and soft orientations (45°) in

respect to compression axis and behaviour for lamellar morphologies, this explains the anisotropic behaviour seen in processing the material. *Lebensohn et al.* used polysynthetic twinned crystal models to investigate the plastic behaviour of this structure and the effect of orientation at the single lamellar grain level, updated with high temperature modelling by *Ilyas et al.* [83], [84]. They found deformation within the lamellar structure relies on longitudinal, mixed and transverse slip modes, the mode being activated depends on the angle of compression, as shown in Figure 17. Compression applied between 15-75° (angle of compression axis to lath) gives the lowest yield stress, this activates longitudinal slip, slip between parallel laths, referred to as a soft orientation. Transverse slip, is slip perpendicular to the laths of the lamellar grain, activated at 90° compression to lath direction. This lamellar grain will show high yield stresses and initially be resistant to globularisation with this compression axis, a hard orientation. Mixed slip is activated at 0° and leads to kinking of the laths of lamellar grains. Initially this leads to high yield stresses with compression, but efficient globularisation is seen, also referred to as a hard orientation [85].

Controlling lamellar orientation can impact on the material properties, *Inui et al.* reviewed work of deformation and that of directional solidification; controlling the lamellar grain orientation and its growth is critical to the properties of the material, to negate the “*inverse relationship between tensile properties and fracture toughness*” [86], [85]. Orientation of the lamellar grains into a soft orientation is easier with higher equiaxed content present and lamellar grains of small grain sizes compared to large ones [87]. Larger grains being less mobile in high equiaxed content material or fully lamellar content material, fewer lamellar grains present means there is less chance of being in a favourable orientation for globularisation [58]. This also explains why large grained fully lamellar materials are brittle at room temperature in comparison to near fully lamellar and duplex TiAl microstructures, as investigated by *Kim* [88].

This work by *Kim* leads us back to grain size and the dimensions of the lamellar grain. They proposed that strength of lamellar and duplex titanium aluminides followed the Hall-Petch relationship, achieving higher yield stress through reducing grain size at room temperature. Noticing the anisotropic effect of soft and hard orientations of lamellae on the yield stress, this introduces an anisotropy factor for determining Hall-Petch constants for different orientations.

In the study, *Kim* also discusses the inverse relationship between grain size and ductility, showing both duplex and lamellar microstructures can tolerate higher strain to failure (fracture) values with lower grain sizes, also discussed in an earlier study of theirs, an important factor in hot working [89].

In this earlier study, they looked at the brittle-ductile transition of titanium aluminides and the effect microstructure has on this, the improvement seen in ductility was due to the higher amount of yielding accepted by the higher density of grain boundaries, preventing crack propagation. However, this was up to a point. In the later study grain size was found to be limited by scale, at single figure micron sizes,

there is simply not the plasticity to cope with crack tip strains and inhomogeneities in the microstructure.

Another observation of *Kim's* studies was the effect of lamellar spacing in terms of ductility, as the finer the spacing the higher the yield stress. *Palomares-García et al.* also found reducing lamellae thickness can increase the yield stress found when the grain is orientated in the hard orientation [90]. Both investigators being amongst others suggesting that lamellar spacing shows a Hall-Petch like relationship, these researchers show that spacing has more of an effect on increasing yield stress than lamellar grain size [91,92].

Fine lamellar microstructures are also exploited in turbine blades to improve the creep resistance of titanium aluminide alloys in service [93]. *Zhu et al.* looked extensively at the relationship between processing, microstructure and creep behaviour in XD alloys in the early 2000s, an alloy which we will become familiar with later [94–98]. *Zhu et al.* found hardness decreased with coarsening of the fully lamellar microstructure. *Kim* in their earlier study speculated that coarse lamellar dimensions would enhance ductility, with thicker γ laths behaving like a duplex microstructure, losing the anisotropic character, and improving ductility.

Heat treatments and ageing led to coarsening which included γ equiaxed and lath growth, together with break-up of α_2 . These changes reduced creep resistance, however from a processing standpoint and considering topics discussed earlier, these changes can be beneficial in terms of reducing flow stress. The focus of many studies considering lamellar dimensions has been centred around fatigue and creep resistance rather than workability for development of jet turbine applications [99–102]. However, these studies are important to understand as they help explain the complex relationship between alloying, processing, microstructure and properties of both the lamellar structure and the fine equiaxed material, vital for improving forging outcomes.

Alloying is used extensively to control lamellar dimensions. *Zhang et al.* found through simulations that lath thickness is susceptible to differences in Al content, again showing the importance of an elementally homogenous solid solution and the relationship between alloying and mechanical properties [103]. Earlier *Kastenhuber et al.* investigated carbon, silicon and molybdenum; *Lapin et al.* looked at tantalum, as did *Bresler et al.* together with zirconium and niobium [74,104,105]. All investigated improving stability of the lamellar structure and its creep resistance through alloying, with similar results. These heavy alloying elements are preferentially gettered into the α_2 from γ upon solidification or heat treatment. This means the α_2 is less prone to globularisation when under strain due to several factors: tighter lamellar spacing, slower dissolution of α_2 into γ and solid solution hardening effects. *Imayev et al.* and *Zhang et al.*, also noted the negative effect of tight interlamellar spacing and the perpendicular orientation of the starting lamellar grain with respect to deformation when globularisation of this material is the aim [105],[106].

Removing lamellar microstructures via heat treatment is also an option, as both strain energy and dislocation density control the rate of globularisation rather than temperature, this can be achieved through heat treatment. Equiaxed duplex type microstructures can be formed by heating low in the $\alpha+\gamma$ region for peritectic solidifying titanium aluminide alloys [103]. *Fuchs'* work found that duplex microstructures produce lower flow stress compared to fully lamellar microstructures, easing initial working, leading to the conclusion that the microstructure prior to processing dictates properties vital to a successful hot working outcome, i.e., flow stress, strain rate sensitivity, flow localisation. However, fully duplex microstructures are only formed over a lengthy heat treatment, in *Fuchs'* case 96 hours [103].

Other authors have looked to cyclic heat treatment to remove the lamellar microstructure completely or return a refined fully lamellar microstructure (RFL). *Wang et al.* in particular pursued grain refinement of peritectic alloys of 1 mm lamellar colony size to $\leq 50 \mu\text{m}$, with the aim of perhaps avoiding hot working altogether [106],[107],[108]. They found the importance of several parameters of the CHT process: including prior α transus homogenisation and the effect of cooling rate on microstructure formation.

The CHT process for 4822 alloy was further explored by *Kościelna and Szkliniarz*, homogeneous grain refinement being their aim [109],[110]. They found that cooling rates in the range of $10\text{-}35 \text{Ks}^{-1}$ led to consistent grain refinement. Inhomogeneous grain refinement was found to be a possibility with faster cooling, which led to a larger grain size distribution. Uniform grain refinement was improved with five controlled cycles, any more was found to have a limited benefit in terms of grain refinement or distribution, less cycles increased the grain size distribution. Having excessive hold times or temperatures was found to lead to grain growth; maximum temperature just above the α transus and a hold time to reach temperature uniformity across sample were found to be ideal.

More recent work focused on β solidifying alloys and multistage heat treatments. These relied on reaching the single β phase for homogeneity of the microstructure and its chemistry. *Schwaighofer et al.* applied heat treatments with the aim of removing hot working altogether from the process by using the β phase and the phase transformation effects of heating and cooling [65]. The study achieved parity with forged work regarding high temperature creep and strength, but moderate room temperature ductility. This was via homogenising the microstructure through heating to the β phase and annealing at "operational temperatures" (800 -900 °C). To improve ductility, cyclic heat treatments were applied after β homogenisation, these involved several cycles of heating to just under the γ solvus followed by cooling to just under the α transus and holding. This, however, had adverse effects on the high temperature tensile strength, due to an increased fraction of equiaxed γ .

Further advances into multi-stage processing aimed at grain refinement and material property improvements in peritectic alloys are well documented, but the risks of inhomogeneous grain

refinement lead back to wrought processing techniques, thus, a hybrid approach would be worth investigating [111],[112],[113].

2.4.2.3 Forging of titanium aluminide

Most titanium aluminide alloys are forged through isothermal techniques for primary ingot breakdown and secondary processing [56]. This is where the workpiece and the die are at an equal, or at least near-equal, high temperature whilst being compressed via hydraulic presses at relatively slow strain rates. High temperature die material such as TZM (titanium, zirconium, molybdenum) are used whilst forging under vacuum or inert atmosphere but are still limited to a temperature of 1150 °C to avoid excessive die wear [114]. These conditions mean reduced flow stress, little adiabatic heating or oxidation. Ideally this produces work of near-net shape, reducing machining and material costs, whilst refining and homogenising the microstructure.

2.4.2.3.1 Flow stress, processing maps and hot workability evaluation

Described here are the conditions that effect forgeability for titanium aluminide and the trials and investigations of note. Here we will focus on the process variables that impact the forging of titanium aluminide materials in relation to isothermal forging, though the approach is still relevant to other bulk forming techniques.

Significant factors and variables are:

- Flow stress
 - Strain rate
 - Temperature
 - Total Strain
- Lubrication
- Friction

As well as identifying microstructural issues, as described in the introduction to 2.4.2, a thorough evaluation of the above factors affecting workability is required to carry out wrought processing techniques successfully.

2.4.2.3.1.1 Flow stress

Flow stress can be measured through compression testing, this assesses a material by compressing it at a known strain rate in an open-die setup, at constant isothermal conditions [114]. The following equations are taken from the ASM handbook; Metalworking: Bulk forming, they describe the variables that need to be considered when assessing flow stress [115].

Once yielding stress is reached, the flow stress, σ , can be written as force, F , over cross-sectional area, A ;

$$\sigma = \frac{F}{A}$$

Change in true strain, $\bar{\epsilon}$, during deformation can be measured by monitoring the cross-sectional area before, A_o , and after, A_i , expressed as;

$$\bar{\epsilon} = \ln\left(\frac{A_i}{A_o}\right)$$

True strain can also be related to the height, h , of the piece as the volume is constant;

$$\bar{\epsilon} = \ln\left(\frac{h_o}{h_i}\right)$$

True strain rate, $\dot{\epsilon}$, for a cylindrical sample of height, h , at, v , velocity over, t , time is expressed as;

$$\dot{\epsilon} = \frac{d\epsilon}{dt} = -\frac{v}{h}$$

At constant temperature and strain, flow stress can be given by combining true strain rate, constant K together with strain rate sensitivity, m , known as the power law;

$$\sigma = K \dot{\epsilon}^m$$

2.4.2.3.1.2 Temperature and strain rate dependence

As temperature is increased, keeping constant strain and strain rate, the flow stress will usually decrease. Flow stress is similarly dependent on both strain rate, as seen in determining strain rate sensitivity. This relationship is described by temperature-compensated strain rate or the Zener-Hollomon parameter, Z , with the equation;

$$Z = \dot{\epsilon} e^{Q/RT}$$

Where R is the universal gas constant, T is the total temperature and Q is the activation energy [115].

The activation energy, Q , denotes the energy required to activate a deformation mechanism e.g., dislocation movement, so is dependent on the alloy, phase composition and its microstructural state [116].

2.4.2.3.1.3 Compression behaviour

Under compression, titanium aluminide alloys show a distinctive peak in flow stress followed by softening. The stress-strain curve can be affected by several factors, by initial microstructure, geometry, die, lubrication and compression conditions, the focus here will be on the effect the microstructure has on compression behaviour [117],[118],[119]. When compression is successful, i.e., uniform, with lamellar TiAl microstructures the stress-strain curve begins with viscoelastic to plastic behaviour followed by initial work hardening likely due to rapid dislocation pile up in the γ laths slowed by a critical strain (ϵ_c) being reached. Ideally, this is followed by high stored energy in the lamellar material initiating rapid DRX, hence the relatively sharp peak flow stress (σ_{pfs}) discussed. This prevents

further strain hardening and reduces the chances of brittle fracture, discussed later in 2.4.2.3.1.4 [120,121]. As additional strain accumulates the σ_{pts} is followed by subsequent flow softening, globularisation and DRX will proceed until a steady-state flow stress (σ_{ss}) is reached and any further DRX becomes sluggish, as reviewed by *Seetharaman and Semiatin*, discussed in greater detail in 2.4.2.2 [25], [37], [48].

With unsuccessful compression, i.e., heterogeneous deformation, flow localisation can lead to the impression of softening. As discussed in 2.4.2.2, large grained fully lamellar microstructure restrains globularisation and therefore recrystallisation [117], [118], [119].

This relationship between strain rate, temperature and peak flow stress is expressed as;

$$\dot{\epsilon} = A[\sin h(a\sigma_p)]^n \exp\left(-\frac{Q}{RT}\right)$$

Where A is a function of stress and is experimentally determined like α . n, is the strain hardening constant. We can now relate the Zener-Holloman parameter to flow stress by;

$$Z = A[\sin h(a\sigma)]^n$$

2.4.2.3.1.4 Strain rate sensitivity and processing maps

Strain rate sensitivity (m) is vital in terms of forge and die design as well as determining the conditions necessary for a successful forging operation. Strain rate sensitivity indexing (0-1, 0 being least sensitive, 1 being most) can be used to assess compression conditions [54].

The lower the m value, the less deformation is achieved; so, at low temperatures m would be near 0, as little deformation would be achieved, materials with low m microstructures during processing can suffer localised deformation, maybe cracking. The higher the temperatures and the higher the m value the better it will fill a die under strain, the better the material will flow under strain [54]. This is because the m value incorporates both microscopic and macroscopic plastic deformation behaviour, (e.g., dislocation and recrystallisation concepts as well as lamellar grain size and orientation as well as globularisation kinetics, discussed previously in 2.4.2.1 and 2.4.2.2 respectively). The m values for TiAl in compression are often evaluated as part of workability assessments, with process mapping identifying hazardous processing conditions, many of these studies were assessed and reviewed by *Bibhanshu et al.* [56], [55].

The difficulties in processing TiAl, summarised by *Appel et al.* *In the introduction to 2.4.2*, means a more thorough approach is required, which process mapping is a part of. With isothermal compression testing, an assessment of how strain rate and temperature alter the deformation mechanisms enacted in a material can be made. By altering these variables; low temperature-high strain rate and vice versa, a detailed map of conditions, deformation mechanisms and outcomes can be created. This way of displaying data was first designed by *Frost and Ashby* using temperature and shear stress in the 1980s,

now strain rate and temperature are used. For titanium aluminide alloys, *Nobuki et al.* provided much of the data on the first dual phase alloys [122]. These maps also detail the conditions where failure has occurred; their mechanisms of failure and fracture are discussed next.

From these mapping trials and other work *Gupta et al.* identify 0.2-0.3 as satisfactory for typical forming operations, *Fuchs* suggested m of ≥ 0.3 ; both found increasing temperature usually resulted in an increase of m in their compression trials mapping the alloy Ti-48Al-2Cr-2Nb (4822) [53],[57]. However, *Gupta et al.* begin by identifying that intrinsic workability still depends on the initial microstructure and its response to temperature, strain rate and strain. Forging trials on boride free Ti-45Al alloy by *Seetharaman and Semiatin*, found that m and the fraction of globularised lamellar material increased with a lower initial lamellar grain size, as did *Fuchs* with 4822 alloy, so this relationship between m in compression and microstructure is well established [58]. For this reason, temperature remains constant in the present work, as the effect of microstructure and subsequent m is investigated. This study will use m of ≥ 0.3 as a marker to track changes in forging outcomes, combined with microstructural analysis.

As described by *Ghosh*, the methods for calculating m rely on making stress-strain curves [54].

The first method uses several samples using different strain rates at constant strain and temperature,

$$m = \left(\frac{\Delta \log(\sigma)}{\Delta \log(\dot{\epsilon})} \right)_{\epsilon, T}$$

The second method applies sudden changes in strain rate to one sample, whilst under compression, monitoring the difference in stress.

$$m = \left(\frac{\Delta \sigma}{\sigma} \right) / \ln \left(\frac{\dot{\epsilon}_2}{\dot{\epsilon}_1} \right)$$

2.4.2.3.2 Compression defects; failure and fracture

In compression, failures come from non-uniform distribution of plastic strain, failure at both the micro- and macro-scale occur due to the following for TiAl alloys, described by *Semiatin* [114].

“(1) stress gradients are produced by factors inherent in the method of load application (such as friction between tool and workpiece) or in the shape of the specimen (such as stress concentration at the roots of notches or cracks),

(2) the mechanism of plastic yielding is dynamically unstable (as is the mechanism that causes the yield point in steel),

(3) the initial structure is not homogeneous but is a polycrystalline single-phase or multiphase aggregate, or

(4) the fundamental deformation process (motion of an individual dislocation) is, by its nature, a localized event.”

First *Semiatin et al.* and then *Appel et al.* reviewed failure and fracture in comprehensive review papers of hot working titanium aluminide alloys, either side of the millennium respectively [119],[6]. Both sets of researchers identify the defects possible in hot working titanium aluminide, being either fracture controlled for brittle failure or flow-localization controlled for ductile failure. Brittle failure occurs by intergranular cracks at high strain and low temperature; both internal wedge type and surface occur. Ductile failure at low strain and high temperature begins with void growth leading to wedge cracks or cavities.

Work led by *Semiatin and Seetharaman et al.* produced several papers covering isothermal compression behaviour of a variety of dual phase titanium aluminide alloys through the 1990s, however none contain the β_0 phase or borides of more recent alloys [123],[124].

They sought to define the conditions that contributed to brittle and ductile failures and the transition between the two. As mentioned earlier, a successful outcome or, alternatively, fracture is controlled by temperature, strain rate and the extent to which flow softening and so dynamic recrystallisation can take place. With increasing strain rate this transition temperature would increase and vice versa.

Another area of interest was the impact the microstructure had on this transition temperature, the larger the grain size, the higher the transition temperature. This implies similar issues would be found with as-cast material in comparison to more refined wrought work.

Semiatin and Seetharaman identified that intergranular brittle fracture proceeded via wedge cracking and is initiated at grain boundary triple points [123]. The extent to which the material cracks was covered by their criterion for intergranular failure based on grain size, d , and the material's peak flow stress, σ_p , defined as;

$$\sigma_p \sqrt{d}$$

This criterion proved useful for both single and dual phase alloys, due to the limited role α_2 plays in deformation, as discussed in 2.4.2.1.

Ductile failure at low strain but high temperature is found to proceed at triple points and grain edges by stable cavity growth, followed by eventual coalescence [114],[124]. This growth rate being countered by the rate of dynamic recrystallisation, which hinders grain boundary sliding and inhibits crack/cavity growth in both brittle and ductile fracture [124]. Cavity growth causes secondary tensile stresses in the material that can lead to bulges, known as barrelling, these can then cause surface cracks. *Seetharaman et al.* found this ductile failure to be predicted by the maximum tensile work criterion proposed by *Cockcroft and Latham* in the 1960s [125].

$$\int_0^{\bar{\epsilon}_f} \sigma_{max} d\bar{\epsilon} = constant$$

σ_{max} is the maximum local tensile stress, $\bar{\epsilon}_f$, is true strain at fracture, $\bar{\epsilon}$, being true strain. The degree that the material bulged is relative to the secondary tensile stresses in the material which is dependent on the friction involved between die and work, discussed next, as well as the work's geometry, its width and height ratio, known as the aspect ratio.

2.4.2.3.2.1 Friction and lubrication of titanium aluminide

As mentioned above, barrelling of the work is a defect caused by a discrepancy in friction between workpiece and die. This discrepancy in friction can be controlled by adequate lubrication and sample design [115].

For isothermal forging, which is required in the most part for titanium aluminide alloys, the priority is high temperature oxidation resistance. For this, as with forging of titanium alloys, a glass-based coating is used. This being preferably a water, rather than oil based colloidal suspension of graphite, boron nitride, titanium carbide amongst other proprietary constituents, which is sprayed on and cured [114]. This forms a layer of glass-ceramic lubricant that provides lubrication and oxidation protection at forging temperatures.

Depending on the material and how it deforms, two opposing models are used to quantify friction, reviewed by *Groche et al.*[126]. Friction coefficient, μ , by the contact normal forces between work and die, F_N , gives us the Coulomb friction or the friction law, relevant for low friction force, F_R ;

$$F_R = \mu F_N$$

Or for the friction stress involved, τ_R , and contact normal stresses, σ_N , it can be expressed as;

$$\tau_R = \mu \sigma_N$$

These are assuming movement at the die-work interface.

The shear friction model assumes the opposite, no movement or very high pressure.

$$\tau_R = mk$$

This takes m as the friction factor, 0 being sliding freely, 1 being no movement, and k , as the shear flow stress.

Homogeneous strain distribution is the aim, so the friction involved is somewhere between these two models. For direct measurement of homogeneous deformation, a combination of the two is used;

$$\mu = \frac{\tau_R}{\sigma_N} = \frac{F_R}{F_N} \left| \frac{d\sigma_N}{dx_i} \right| \cong 0$$

x_i is the instantaneous displacement of material.

Friction is one component of determining if work under compression will undergo successful uniform deformation. This can be understood and quantified via different tribological testing methods, these can be applied but come with their own positives and negatives, reviewed by *Groche et al.*

2.4.2.3.2.2 Alloying and phase contribution to fracture

As mentioned, the 45XD alloy to be used in this study contain borides and β_0 phase, they alter how fracture proceeds. Higher additions of β -stabilisers such as niobium retard dynamic recrystallisation, and high stacking fault energy β prefers to restore via dynamic recovery. As discussed in 2.3.1.5 and 2.4.2.1, at working temperatures the disordered β phase takes on much of the strain energy during deformation in β solidifying alloys [6]. This means the β phase acts almost as a lubricant easing deformation, preventing ductile failure via the growth of cavities as no peak stress is seen, dynamic recovery takes place, and a steady state is maintained during deformation [127].

This is not possible if only ordered β_0 is present at the working temperature, then intergranular failure as discussed above can be seen at high strain and low temperature.

Gupta et al. produced workability maps investigating the impact of 0.1 at% boride and grain size on the hot workability of titanium aluminide alloy 4822 [57]. As was described in 2.3.1.6, boron additions are used to refine the microstructure by preventing excessive grain growth, especially upon casting. Identified by *Semiatin and Seetharaman*, a refined grain size is one factor in reducing flow stress and reducing the risk of brittle fracture. *Gupta et al.* found this not to be the case, boron being present increased the flow stress at all temperatures versus 4822 without boron. They proposed that this was due to a phase containing boron, most likely titanium boride or diboride particles, these being present at working temperatures.

This was also noted by *Luo et al.*, who presented several papers on the changes in mechanical properties in 4822 with and without boron. They suggested that borides which presented at grain boundaries and triple points prevent movement or sliding, pinning grains together [128]. Hence the increased flow stress seen at all temperatures.

This is the case for other boron containing alloys of interest like 45XD, but this was only investigated at room temperature [129]. *Hu* was involved in much of the work on 45XD and its mechanical properties but first looked at the impact of boron on ductility in the early 2000s [130]. These studies found that boron particle size dictates the effect boron presence has on tensile ductility, larger particles removing the benefits of smaller grain size and promoting intergranular fracture. This study

included 4822 with and without boron as well as high niobium containing β -solidifying alloys. The mechanisms themselves of brittle and ductile fracture follow those discussed earlier in this section.

2.4.2.4. Other primary processing techniques; extrusion

Extrusion of titanium aluminides is carried out at elevated temperatures from 1050-1450°C to ease deformation as strain is applied, via a ram, in the region of 15-50mm/s [114].

Hot extrusion is also used as a consolidation technique of both powder and ingot, both being canned in mild steel, this being the first step in the two-step extruding of titanium aluminide, developed by Plansee AG.[43]. The titanium aluminide is deformed in the $\alpha+\gamma$ region leaving behind a fine-grained duplex microstructure upon cooling. This microstructure suffers from aluminium segregation during solidification, forming bands of differing aluminium content, this is resolved by a second extrusion at a similar temperature. The second extrusion leaves a refined microstructure which lends itself to applications where toughness is the priority; exhaust valves and the like have been mass produced by forming titanium aluminide rod via this method.

In the pursuit of refined fully lamellar microstructure and single step working, *Fuchs'* combined heat treatment and working at very high temperatures (1400 °C), known as super-transus working. *Fuchs* found this to be detrimental, working led to unstable refined fully lamellar microstructures, leading to recrystallization upon further heat treatments, a sign of stress in the microstructure [131].

Another factor that allows hot extrusion to take place at industrially accessible temperatures is the disordered β phase, as discussed in greater detail in 2.3.1.5 found in highly alloyed titanium aluminides such as TNM, this allows for extrusion at 1100 °C and with strain of $0.01s^{-1}$, found by *Xu et al.* [132].

2.4.2.5 Other Secondary processing techniques; hot rolling

As mentioned above, high deformation processes such as hot rolling and isothermal closed-die forging in titanium aluminide alloys is restricted to high temperatures and low strains, and particularly in the sheet and foil forming has been the reserve of fine grain structures. Teams at Plansee AG of Austria, developed an advanced sheet rolling process in the early 2000s working with predecessors of the β -solidifying alloys and successfully forming sheet of 2000x500x1 mm³ [43]. This involved the hot-rolling of both ingot and powder-based metallurgy at near isothermal conditions in the $\alpha+\gamma$ phase. Special considerations were given to the rolling speed, strain applied per pass and temperature control. This was to reduce both micro/macroscopic cracking by applying strain at low temperatures, as well as minimising risk of oxidising the material at high temperatures.

These issues were exacerbated by poor composition control, with aluminium deviations of +/-1 at% aluminium leading to significant changes in transus temperature points. This led to both powder metallurgy being adopted as the main source of metallurgy for sheet, as well as improvements in casting, as mentioned earlier for ingot-based metallurgy in 2.4.1.1 [46].

Furthering the case for sheet forming, applications such as automotive and aerospace “honeycombed” exhaust structures led to requirements of high strength and ductility to ease processing, allowing for superplastic forming and diffusion bonding to be possible [133]. *Cqm et al.* used TAB (Ti-47Al-4Nb) alloy to provide the higher strength yet ductility through deformation of fine grained equiaxed γ and α . Lamellar microstructures were avoided and removed, controlling the type of microstructure was deemed essential to enable properties necessary for these processing techniques.

Further applications such as thermal protection foils for high-speed aerospace vehicles prioritised low weight materials [134]. *Semiatin et al.* worked the $\alpha+\gamma$ phase to produce foil 200-250 μm thick. The study utilised conventional rolling mills, instead of purpose-built isothermal equipment, to deform canned titanium aluminide. This is termed hot pack rolling, referring to the encapsulated titanium aluminide foil as the pack, using the canning to insulate and protect the work from oxidation as the work goes from a furnace at 1260 °C to cold rolling equipment. To produce the foil this study aimed to deform the equiaxed α and γ grains present and globularisation of any remnant lamellar left from prior sheet rolling. The lamellar colonies present even after foil rolling, give the reason for the +/-15 % difference in thickness found. These change orientations rather than breaking up in both sheet and foil forming, highlighted the importance of breaking up these colonies prior to secondary processing for the workability required. Heat treatments were used to finally remove the remnant lamellar colonies from the microstructure ready for the components use.

2.4.2.6 Post-hot working heat treatments

For titanium aluminide that has been worked by any wrought process post-hot working heat treatments are applied to relieve internal stress; via static recovery or recrystallisation, or for further control of the microstructure-properties relationship seen, such as improving ductility [65],[81].

Improving ductility via heat treatments works via controlling the brittle equiaxed α_2 and lamellar content. This applies to dual phase alloys as shown by *Tang et al.* and for β -solidifying alloys, shown by *Bolz et al.*, both applying two-step heat treatments [37,135]. Both also recognise the importance of the refined microstructures for ductility and further workability.

However, simple heat treatments above α transus are still a common process. As will be discussed in the next section, the demand for creep resistance by the low-pressure turbine blade requires the fully lamellar microstructure, easily achieved through heat treating above the α transus.

2.5 The low-pressure turbine blade

Throughout this review reference to titanium aluminide and its association with aero engine turbines has been made. In this section we will go into the component itself and the titanium aluminide alloys currently being used.

The temperature and weight sensitivity of titanium and nickel based super alloys in jet engines led to the rise in interest in the intermetallic, titanium aluminide in the 1980s. Above 600°C properties of conventional titanium alloys rapidly worsen, allowing oxidation and creep to occur. This keeps nickel-based superalloys as the material of choice for high temperature areas, despite a near doubling of density [136].

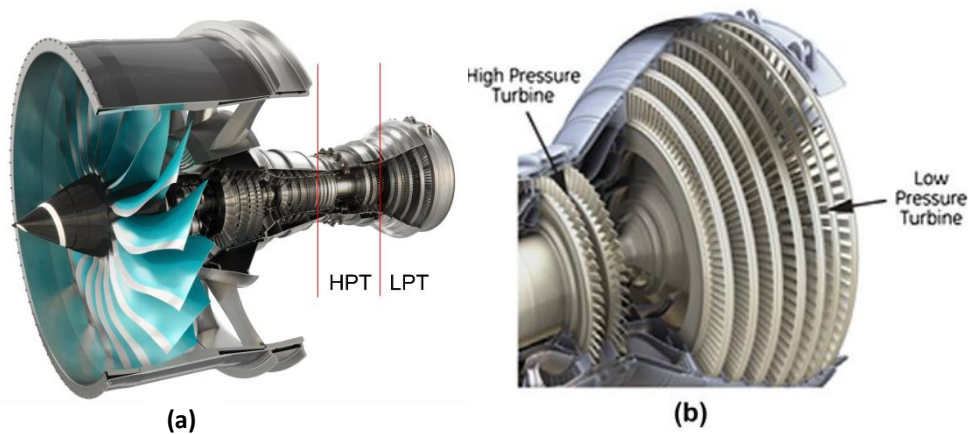


Figure 18: a) Rolls Royce UltraFan, (b) Turbine section[14]

From the 1980s, 20 years of research led to the point of applying these materials to jet turbine engines. Now at the stage of application by the major aero-engine manufactures as the material of choice for low pressure turbine (LPT) blades, the major light weighting benefits of titanium aluminide are being realised in terms of fuel efficiency and reduced emissions. They noted the critical importance of oxidation and creep resistance for the turbine blade's longevity at higher temperature >600°C, whilst maintaining the material's strength and ductility. *Dimiduk* comprehensively reviewed early titanium aluminide alloys, their properties and their position as a future structural material in aero-engines in comparison to other structural materials [4].



Figure 19: (a) Low pressure turbine blade (LPT), (b) Turbine assembly [14]

Bewley *et al.*, Kim *et al.* and Gunther *et al.* provided updated information on the application of three different titanium aluminide alloys by the three major gas turbine manufacturers. Case studies of the alloys and low-pressure turbine production follow this section with information these groups provided, with additional references to work on singular alloy processing where required [7,14,44].

Alloy name	4822	45XD	TNM
Composition	Ti-47.2-48Al-2Nb-2Cr	Ti-45Al-2Nb-2Mn-1B	Ti-43Al-4Nb-1Mo-0.1B
Alloy type	peritectic solidified	peritectic solidified, exothermic dispersion (XD) lamellar	β solidified
Processing	Cast-heat treatment 1, (~1093°C, 4hrs)-HIP, (1185°C, 175MPa, 4hrs)- heat treatment 2, (1260°C, 2hrs with controlled cooling)	Cast-HIP, (1260°C, 175MPa, 4hrs)-heat treatment, (~1350°C, 2hrs, oil cooling)	Cast- HIP, (1200°C, 175MPa, 4hrs)- forge (1000-1200°C, <10 ⁻³ s ⁻¹) - Heat treatment, (~1250-1400°C, 4hrs, with controlled cooling)
Application	GE _{EnX} (2012) & LEAP engine by CFM (50:50 GE& Safran)	Rolls Royce (~2018)	Pratt & Whitney, GTF engines (2016)
Microstructure used	Casting duplex/ nearly lamellar	XD fully lamellar	Wrought nearly lamellar
Max temp (°C)	<700°C	<700°C	<750°C

Table 2: Alloys in use as low pressure turbine blade material

2.5.1 4822

General Electric (GE) first started to develop titanium aluminide low pressure turbine blades in the early 1990s, to produce 4822, eventually being the first to introduce titanium aluminide low pressure turbine blades to commercial engines in the GE_{EnX} aero engine, flying in early 2012.

These were machined, cast parts without wrought processing. Achieving the properties described in Table 2 through heat treatment and hot isostatic pressing alone, to give a duplex/nearly lamellar microstructure.

2.5.2 45XD

Developed by Martin Marietta laboratories in the USA along with 47XD. Traditionally an investment cast only alloy. The first commercial alloy to introduce borides for grain refinement [137,138].

XD or exothermic dispersion essentially is a casting melt treatment, which involves titanium diboride particles to nucleate fine lamellar grains. The process also gives anisotropic properties, through

random lamellar grain orientation [45]. Blades from this alloy may be incorporated into Rolls-Royce's new UltraFan at its intermediate-pressure turbine and at the low-pressure turbine in Advance model.

2.5.3 TNM

Titanium, niobium and molybdenum offer their initials to this 3rd generation of titanium aluminide alloy. Developed by MTU aero engines and Pratt & Whitney, manufactured by Leistriz. Much of the research and development work was led by *Clemens*, with many papers and reviews on titanium aluminide processing from the early 2000s to the present day, some of which is discussed throughout this literature review [34].

TNM alloys are currently in service in Pratt & Whitney GTF (Geared Turbofan) type turbine engines. However, the Federal Aviation Authority (FAA) in early 2020 released an airworthiness directive, detailing the high failure rate of blades in the third stage low pressure turbine. No mention of the alloy was made but failure was suspected to be from foreign object damage causing excessive wear, cost of replacement predicted by the FAA; ~ \$750,000 per engine [139]. Post-mortem studies into the relative brittleness of TNM in service found that the β_0 hardened under tensile testing resulting in premature fracture between lamellar-lamellar grain boundaries compared to alloys where the β_0 is absent [72].

2.5.4 Other alloys of interest and their uses

While developing wrought processing routes for low-pressure turbine and high-pressure compressor blades, MTU and Leistriz used a couple of other β -solidifying alloys for engine trials with Rolls-Royce Germany [140]. These included alloys TAB (Ti-47Al-4Nb) and TNB-V4 (Ti-45Al-5Nb-0.2B-0.2C). This cast material was consolidated via hot extrusion to form bar, which was then forged in three steps at high temperature and low strain rate. Producing crack free work when forged at temperatures of $>1000^\circ\text{C}$, with strain rate of 0.001 s^{-1} . With additional heat treatment and machining, hundreds of these blades were evaluated in Rolls-Royce's E3E experimental engine [140].

The first commercial application for titanium aluminide was in automotive turbochargers, developed by Mitsubishi Motors to replace heavy nickel-based superalloys. Due to the reduction in turbine wheel weight, the longevity of the part, which suffers high centrifugal stress as well as temperatures up to

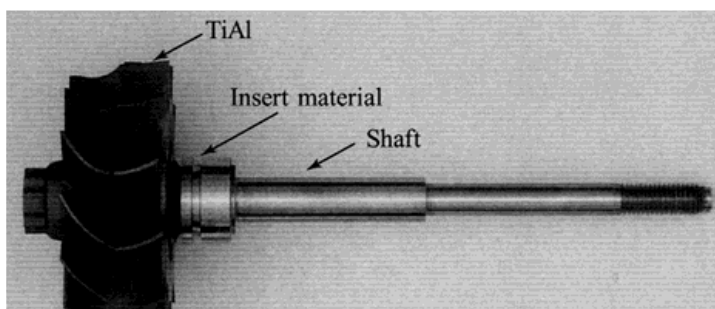


Figure 20: Turbocharger turbine wheel [22]

RNT 650

Composition: Ti-(33-48) Al-(2-4.8)Nb-(0.7-1)Cr-(0.2-0.3)Si

Microstructure used: Duplex

Processing: Cast-HIP-HT

Application: Turbo chargers/ engine valves

900°C, was extended. It had the additional benefits of improved fuel efficiency by allowing the turbo to run hotter, and reduced turbocharger response time [141].

Turbocharger wheels, and later exhaust valves were cast, from a material such as RNT 650. These would then be hot isostatic pressed to consolidate the material and produce a duplex microstructure. This microstructural ductility allowed the heavy machining necessary to give the complex design of the turbine wheel seen in Figure 20 [22].

Those research alloys that have not reached a commercial stage are far too many and varied to include all in this section, however throughout the review a variety of alloys will have been used in the studies referenced. Alloys of interest are also mentioned as “advanced conventional gamma-alloys” in the research pathways identified by *Kim, S.L., and Kim, Y. W.*, in their review of titanium aluminide research [7].

2.6 Summary of the knowledge gap

Together with our industrial partners, desired processes have been identified, such as isothermal closed die forging and hot rolling, which require specific levels of workability from the microstructure. Hot isostatic pressing (HIP) is an essential step applied to remove the solidification porosity and will be the starting point for this study on both alloys. However, there appears room for improvement on the HIP microstructure for optimising forging outcomes. As has been discussed in several reviews, homogenising as the next step has been explored but its positive and negative aspects have made conclusions on the need for this step, and its details for each alloy, difficult to come by [7],[8],[9],[10],[11],[12]. This study will look to clarify this situation for these two alloys and develop additional stages if required to improve the removal of the anisotropy-causing lamellar grains and casting segregation upon primary compression (i.e., forming a pre-form or ingot upsetting), both of which are known to hinder secondary processing stages, such as isothermal closed die forging and hot rolling.

2.7 Aims and Objectives

The aim of this PhD thesis is to investigate and develop thermomechanical processing techniques for the cast TiAl alloys 45XD and 4822, in the HIP condition, that can then improve the forging and microstructural outcome of these difficult to work titanium aluminide alloys.

The experimental part of this PhD thesis will describe the investigations into the processing techniques discussed in the preceding literature review that may improve the efficiency of the initial ingot breakdown stage, referred to as primary compression. The literature for 45XD is not as thorough as for 4822 alloy so there is more ground to cover before developing a process to improve forging outcomes, the aims of these experiments for 45XD are to:

- Establish the impact of HIP and heat treatment on initial 45XD microstructures as well as their compression behaviour and resulting microstructure.
- Identify a homogenisation temperature for 45XD to improve the microstructural outcome from primary compression.
- Investigate multi-stage uniaxial compression for 45XD, including the effect that intermediate heat treatment and dwell time at compression temperature has on microstructural outcomes.
- Investigate whether HIP and homogenisation can be integrated into one process and establish its effect on the microstructural outcome of primary compression.
- Bring together the learning from the previous aims to quantify their effects on secondary processing in terms of compression behaviour, through strain rate sensitivity indexing and microstructural analysis.

For 4822 alloy, the literature considering its processing is more extensive, but practical methods of improving the microstructural outcome of initial ingot breakdown are lacking. Thus, the objectives are:

- Establish the impact of HIP and homogenisation, as well as integrating the two processes on initial 4822 microstructures as well as their compression behaviour and resulting microstructure.
- Combining elemental homogeneity and refinement of the large-grained microstructure is anticipated to improve primary forging outcomes, this will be aimed for and investigated by applying cyclic heat treatment. This technique, described in 2.4.2.2, has shown promise at a smaller scale using electrical resistance heating equipment to refine the lamellar microstructure of 4822 alloy. This study will apply induction heating equipment as a step up in scale and industrial relevance, with a view to this producing a refined microstructure leading to improvements in forging outcomes, with the anticipated higher globularisation of lamellar content.
- Quantify their effects on secondary processing in terms of compression behaviour, through strain rate sensitivity indexing and microstructural analysis.

3 Experimental Methods

This chapter covers the steps from the raw material received from TIMET, through initial material preparation, experimental processes, and characterisation. Calculated phase diagrams (CALPHAD), metallurgical analysis, combined with compression testing and analysis of flow behaviour looks to provide the base with which to measure the effect of alternative processing techniques on the forging outcomes of cast 45XD and 4822.

3.1 Materials and their pre-compression processing

Here the different pre-compression processing sequences are described to provide several distinct starting conditions for each alloy. Each process imparts a different microstructural condition on the subsequent compression sample, which looks to replicate primary ingot breakdown, this will then be assessed for its effect on overall workability.

3.1.1 As received material (ASR)

Two cast, plasma arc melted ingot known as 45XD (~Ti-45Al- 2Nb-2Mn at% 0.8 TiB₂ vol%) and 4822(~Ti-48Al- 2Nb-2Cr at%), courtesy of TIMET were received at the Advanced Forming Research Centre (AFRC), this condition is referred to as ASR.

Ti	Al	Nb	Mn	B	Fe	Cu	C	Si
49.80	44.31	1.93	2.93	0.84	0.02	0.03	0.02	0.02

Table 3: Average chemical composition of supplied 45XD ingot, analysed via ICP at three points by TIMET

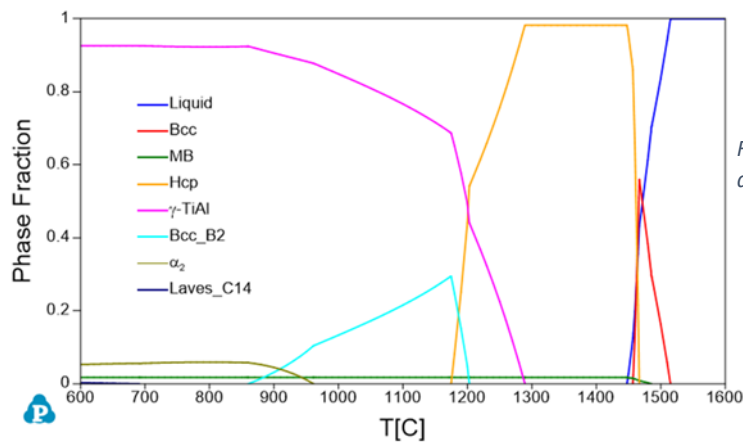


Figure 21: Phase fraction diagram determined from CALPHAD for 45XD

Ti	Al	Nb	Cr	Fe	Si
49.1	47.2	1.83	1.83	0.03	0.03

Table 4: Average chemical composition of supplied 4822 ingot, analysed via ICP at four points by TIMET

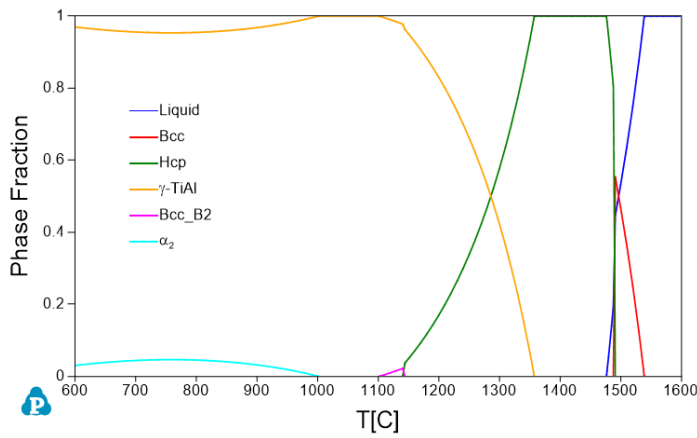


Figure 22: Phase fraction diagram determined from CALPHAD for 4822

The composition data used for calculating the phase diagram (CALPHAD, Figure 21 and Figure 22) was determined via inductively coupled plasma (ICP) by the manufacturer, the results are shown in Table 3 and Table 4 respectively. The CALPHAD used was the commercially available PANDAT software from CompuTherm, using their TiAl database. These CALPHAD plots are estimates but together with the literature and preliminary experiments was used to select processing temperatures.

a



b



Figure 23: (a) Ingot of 45XD alloy of $\varnothing 146 \times 245$ mm and 18kg. (b) Ingot of 4822 alloy of $\varnothing 140 \times 233$ mm and 15kg. Courtesy of TIMET.

3.1.2 Hot isostatic pressing (HIP)

For each HIP run, a full-length cylindrical core sample of $\varnothing 60$ mm, the maximum diameter for the HIP equipment used, for both ASR 45XD and 4822 was cut via electrical discharge machining (EDM).

These samples were individually hot isostatically pressed (HIP) to remove any residual casting porosity and consolidate the material. All investigations started in the HIP condition for both alloys, a AIP8-

45H press based at the Royce Translational Centre, University of Sheffield, was used with a cooling and heating rate of 10 °C/min. All other conditions were constant and common practice for HIP of TiAl ingot alloys; 4 hours at 1270 °C, 175 MPa under argon. This material condition is referred to as the “HIP” material throughout this work and is the starting point for these studies.

3.1.3 Determining the impact of heat treatment on the HIP microstructure of 45XD pre-compression

Enough literature was available to confidently pursue and justify the use of a super α transus heat treatment to homogenise the 4822 alloy prior to compression [53],[142],[143]. This was not the case for 45XD. An investigation of heat treatments in the different phases present to see their impact on the HIP microstructure and subsequent compression behaviour was necessary.

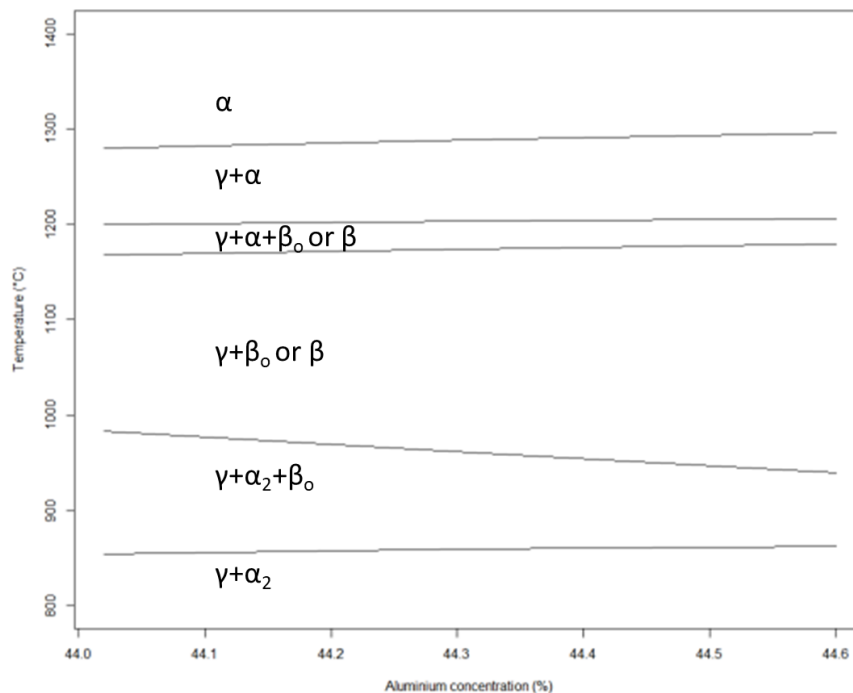


Figure 24: 45XD Ti-Al phase diagram calculated from data received from CompuTherm.

Using cylindrical HIP compression samples, cut via EDM of $\varnothing 13 \times 20$ mm, a Carbolite lab furnace was used for each heat treatment, described in Table 5. Two cooling methods were applied after a 2-hour dwell time: furnace cool (FC, 13.5°C/min) and air cool (AC, 200°C/min), to investigate the microstructural effect of industrially viable cooling rates and their subsequent impact on compression behaviour. AC and FC, as well as time at temperature, were monitored by K-type thermocouples. These thermocouples are capable of monitoring at these high temperatures and were placed within the alumina crucible (10 x 30 mm) holding the sample, as seen in Figure 26, but not in contact with the sample in the furnace for each heat treatment. Heat treatment was under normal lab conditions, without a protective atmosphere. All cylindrical samples were coated with glass lubricant (87.2.207) to reduce oxidation, courtesy of Prince Minerals before heat treatment and compression.

Sample ID	1130-AC	1130-FC	1200-AC	1200-FC	1270-AC	1270-FC	1350-AC	1350-FC
Phase	$\gamma+\beta$		$\gamma+\alpha+\beta$		$\gamma+\alpha$		α	

Table 5: Heat treatment sample identification, temperature (°C)- cooling rate together with the phase the heat treatment is working within

3.1.4 Traditional HIP and homogenisation (THH)

Using information from the literature described in 2.4.2.1 and the experimental evidence from 4.1, homogenisation temperatures and conditions were identified for both alloys. Material in the HIP condition was homogenised (HMG) in bulk via a vacuum carbon furnace (FCT GmbH) at the Royce Institute facility based at the University of Manchester. The heating rate used was 3 °C/min, under 0.5 mBar of vacuum for 2 hours at 1300 °C and 1380 °C for 45XD and 4822, respectively followed by furnace cooling of 3 °C/min. This material condition is referred to as traditional HIP & homogenised (THH); traditional due to the state of the current literature around processing of peritectic solidifying TiAl alloys.

3.1.5 Integrated HIP and homogenisation (IHH)

Integrating HIP and homogenisation (IHH) aims to combine the two costly processes, in terms of time and energy, into one stage using HIP equipment based at the University of Sheffield. A cylinder of each alloy was consolidated using the same HIP conditions for each alloy, but, following the HIP cycle and before cooling, the temperature was ramped up to reach the homogenisation temperature of 1300 °C for 45XD and 1380 °C for 4822 for two hours, maintaining pressure in the vessel throughout, with a cooling rate of 10 °C/min. This material is referred to as the integrated HIP and homogenised (IHH).

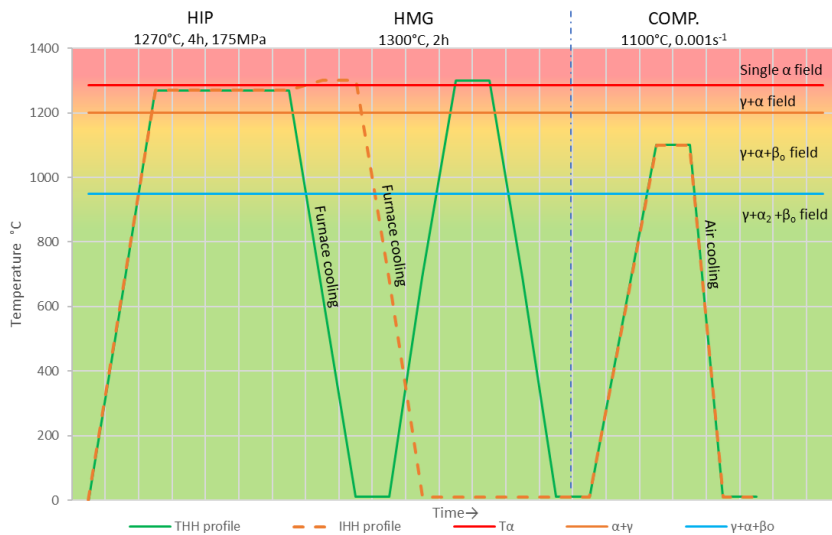


Figure 25: Idealised temperature-time profile of the traditional and integrated HIP and homogenisation heat treatment, including consolidation (HIP), homogenisation (HMG), and integrating the two for 45XD before primary compression (COMP.)

3.1.6 Intermediate heat treatment for 45XD

To investigate the effect of an intermediate heat treatment post primary compression (1'), a Carbolite lab furnace was used to reach 1200 °C for two hours, followed by air cooling (AC, 200 °C/min), as identified as potentially beneficial in sections 4.1 and 4.3. The heat treatment and AC was monitored by K-type thermocouples placed next to the sample in the furnace. Heat treatment was under normal lab conditions, without a protective atmosphere however all cylindrical samples were coated with glass lubricant (Prince 87.2.207) to reduce oxidation, before heat-treatment and compression. This was investigated using primary compressed THH material, (1'THH) giving the traditional HIP and homogenisation plus heat treatment (1'THH+HT) material condition referred to in this work.

3.1.7 Cyclic induction heat treatment for 4822

From cast plasma arc melted 4822 ingot material of Ø140 x 233 mm (Ti-47.2Al-1.83Nb-1.83Cr at. %), a cylindrical sample of Ø 60 x 233 mm was machined via electrical discharge machining (EDM) from the centre of the ingot. This material was in a homogeneous, fully lamellar condition with a large lamellar grain size, ~1mm. This sample was consolidated via hot isostatic pressing (HIP) for four hours at 1270 °C, 175 MPa under argon followed by homogenisation (HMG) within the single α phase at 1380 °C for two hours under vacuum, followed by natural cooling for each process. This material, referred to as HIP and HMG (HH), was then cut into cylindrical compression samples of Ø13 x 20 mm via EDM. The composition data used for calculating the phase diagram (CALPHAD), Figure 22, was determined via inductively coupled plasma (ICP) by the supplier, shown in Table 4. From CALPHAD and

the literature describing cyclic heat treatment in 2.4.2.2, the target temperatures and cooling rates for cyclic heat treatment were identified. However, these were established at a smaller scale than desired for the present study, using electric-thermal resistance mechanical testing (ETMT) equipment. This study applied industrially relevant induction based cyclic heat treatment (CHT) equipment to investigate its effect on the microstructure pre-compression compared to HH alone. Using induction equipment allows greater control over the CHT process i.e., temperatures and cooling rates, than is possible with other traditional heat treatment techniques such as gas or vacuum furnaces. This enables the lamellar grain refinement or complete globularisation, shown by others using ETMT to be essential for lamellar grain refinement, which could improve the rate of globularisation upon compression by reducing lamellar grain size and maintaining elemental homogeneity [58],[122].

The cyclic heat treatments on the alloy 4822 samples were carried out using the 15 kW Ambrell EKOheat induction heating system in conjunction with the large inductor. The inductor and system electronics were water cooled during the heat treatment using a recirculating chiller. The inductor consisted of a 6-turn copper coil with an internal diameter of 97 mm, working length of 95 mm and wall thickness of 0.81 mm. The inductor was mounted within a refractory concrete enclosure with an empty tubular region of \varnothing 87 mm in its centre to position sample(s). The settings for the induction heating control system were as follows:

- Resonant frequency: \sim 93 kHz. Tap setting: 16.
- Capacitance: series/parallel arrangement $(-2 \mu\text{F} \times 1 \mu\text{F}) - (2 \mu\text{F} \times 1 \mu\text{F}) \rightarrow$ equivalent to $1 \mu\text{F}$.
- Starting voltage: approximately 550 V (decreased to \sim 350 V to prevent overshooting target temperature at 1340 °C). The voltage settings for each sample varied due to differences in their thermal, electrical, and magnetic properties.
- Temperature control was achieved manually by adjustment of the induction voltage.

The temperature was monitored and recorded with a dual wavelength SPOT pyrometer (Land Instruments) using ratio mode to minimise the impact of changing surface emissivity. The pyrometer beam (\sim few mm²) was focused on the surface as a precaution to minimise temperature overshoot.

The target temperature-time profile is shown in Figure 27. Compression samples were coated with glass lubricant 87.2.207 from Prince Minerals to reduce oxidation. To start, samples were rapidly heated to 1370 °C from room temperature and held for 30 seconds before cooling to 800 °C, where the cycle would start again for five cycles. Furnace and air cooling (FC, AC) were applied to achieve different pre-compression microstructures. FC was applied by reducing the power, to induce cooling at a constant cooling rate to 1200 °C followed by switching the power off. AC was applied by simply turning the power to induction equipment off. These conditions are referred to as furnace-cooled cyclic heat treatment (FCCHT) and air-cooled cyclic heat treatment (ACCHT). Samples were held in an alumina jig within the induction coil for repeatability of positioning, this would also provide enough insulation for the part to reach the target temperature.

Following metallurgical preparation, the microstructural analysis of all cross sectioned pre-compression samples was focussed on the centre and at the faces of CHT material as per Figure 26.

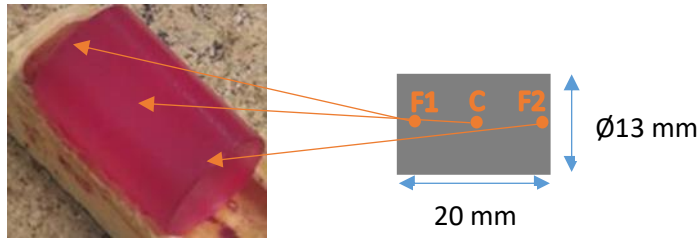


Figure 26: Compression sample ready for ACHT or FCCHT with glass-based coating, -C= centre, -F1= one face, -F2= the opposite face to F1 for post heat treatment analysis.

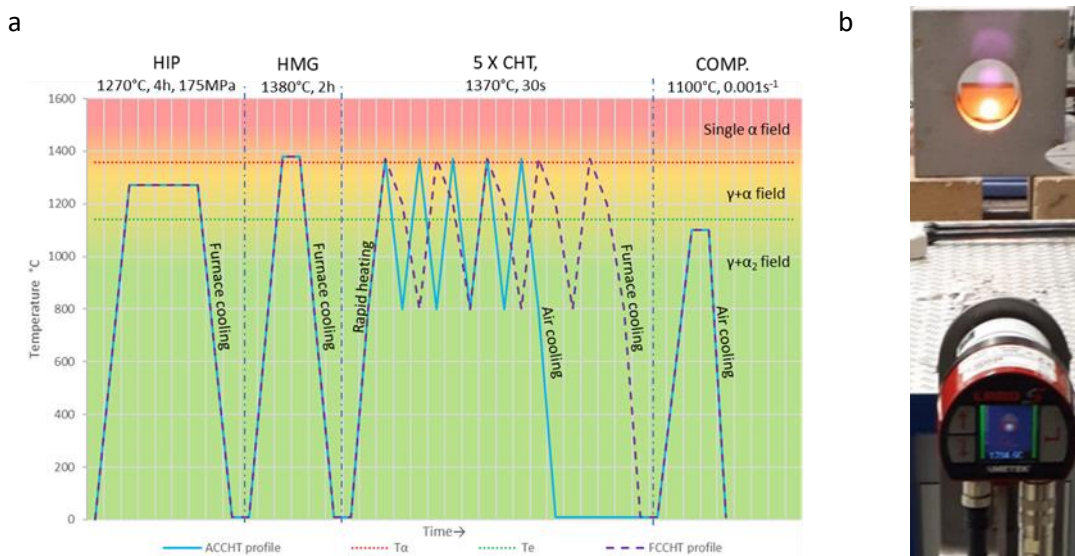


Figure 27: (a) Idealised temperature-time profile of air-cooling cyclic and furnace cooling cyclic heat treatment, including consolidation (HIP), homogenisation (HMG), and five cycles of induction cyclic heat treatment (CHT) of 4822 before primary compression (COMP.) (b) Induction cyclic heat treatment set-up with pyrometer temperature monitoring.

3.2 Compression testing

3.2.1 Primary compression

As discussed, all samples for compression were cut into cylindrical compression samples of $\varnothing 13 \times 20$ mm, via EDM for primary (1') compression, with the aim of resembling ingot breakdown or forming a pre-form. For compression, all cylindrical samples were coated with glass lubricant (87.2.207) from Prince Minerals to reduce oxidation. The test machine platens were lubricated with boron nitride before compression to 50 % at 1100 °C after a 5-minute soak, to establish a uniform temperature throughout the sample, with a strain rate ($\dot{\epsilon}$) of 0.001 s^{-1} for 4822 and $0.001, 0.005$ and 0.01 s^{-1} for 45XD to determine strain rate sensitivity (m), using a Zwick Roell Z250 machine, followed by air cooling.

3.2.2 Secondary compression

For secondary (2'') compression, only samples that were 1' compressed at 0.001 s^{-1} were used to produce 2'' compression samples via EDM of $\varnothing 6 \times 9$ mm cylinders. The 2'' compression conditions followed the same procedure as the 1' compression stage, at 1100 °C, but at $\dot{\epsilon}$ of $0.001, 0.01$ and 0.1 s^{-1} to establish the m value of the sample material for both alloys.

a



b

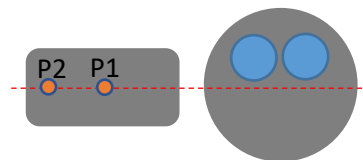


Figure 28: (a) Image of electrical discharge machined primary compression sample, (b) diagram indicating EDM pattern of primary compression samples (0.001 s^{-1} only, faster strain rates only have the red dashed cut) giving two cylindrical samples ready for secondary compression and central cut for microstructural analysis.

3.2.3 Compression behaviour analysis

From compression data, this includes force, F (Newtons), time, t (seconds) and platen travel (mm) recorded by the automated data logger system attached to the Zwick Roell Z150 machine combined with the starting dimensions of the sample; height, h (mm), cross sectional area, A (mm^2) and volume, V (mm^3) true stress-strain (σ - ϵ) curves were produced.

True strain, ϵ , is monitored through compression through the height, h , of the work piece as the volume, V , is constant;

$$\varepsilon = \ln\left(\frac{h_o}{h_i}\right)$$

This compression in height then alters the instantaneous cross-sectional area, A_i , assuming no barrelling due to friction between work and platen, calculated by

$$A_i = \frac{V}{h_i}$$

From this we can follow σ throughout compression once yielding stress is reached, the flow stress, σ , can be written as force, F , over cross-sectional area, A ;

$$\sigma = \frac{F}{A}$$

From these values the true stress-strain (σ - ε) curve is produced for that compression test. From this curve it can show characteristics of different restoration mechanisms active through compression and values can be determined such as the peak flow stress; σ_{pfs} .

From this, plots of change in $\log \sigma$ versus change in $\log \dot{\varepsilon}$, with the compression temperature (T , °C) and the strain of 0.04 ($\varepsilon \approx \sigma_{pfs}$ constant), the slope of this plot is strain rate sensitivity (m).

$$m = \left(\frac{\Delta \log(\sigma)}{\Delta \log(\dot{\varepsilon})}\right)_{\varepsilon, T}$$

3.3 Microstructural Characterisation

3.3.1 Specimen preparation and microscopy

All samples were cross sectioned via EDM for microstructural analysis and imaged, as per Figure 26 for pre-compression material and Figure 28 for post-compression samples, with compression direction from top to bottom of images. The analysis included scanning electron microscopy (SEM) using an FEI Quanta-250 with field-emission gun, with back-scattered electron (BSE) detector fitted, using an accelerating voltage of 20 kV and a working height of 10 mm for imaging. Working alongside this setup, a NordlysNano electron back-scattered diffraction (EBSD) system acquired crystallographic data. For both alloys the EBSD was setup with an acquisition time of 120 mS and 0.5 μm step size, as this achieved the best compromise between allowable run time and achieving the 90 % indexing aimed for.

For these analytical techniques samples were mounted in conductive copper resin, followed by six grinding stages using increasingly fine silicon carbide paper, starting at 240 down to 4000 grit for 2 minutes. This was finished with two stages of chemical-mechanical polishing in 0.02 μm colloidal silica using a microcloth polishing plate followed by vibro-polish overnight in 20 vol% 0.02 μm silica. This was followed by washing with water and methanol plus forced air drying.

For optical microscopy (OM) a Leica model was used, samples were ground and polished as described above with additional chemical etching in Kroll's solution for 5 s.

3.3.2 Data processing

To determine microstructural parameters including average lamellar grain size (μm), and phase fraction ($\% \gamma$, α_2 or β_0) together with their morphology i.e., lamellar, equiaxed or feathered microstructure content ($\%_{\text{lam}}$, $\%_{\text{eq}}$, $\%_{\text{f}}$), different analytical and processing techniques were applied. Here, each parameter was quantified at P1, unless specified otherwise in the results.

3.3.2.1 Morphology grain size and content

Firstly, morphology volume fraction was estimated for lamellar, equiaxed or feathery γ content (%) via the systematic manual point count method detailed in ASTM E562-19e1 using OM and BSE imaging, processed using ImageJ software. To clarify, this study defines lamellar grains as colonies consisting of alternate parallel $\alpha_2 + \gamma(+\beta_0)$ plates, referred to as laths; equiaxed grains are described as globular in shape with axes of approximately the same length. Feathery γ microstructures are described as short, randomly misorientated γ laths, exclusively of γ , in comparison to lamellar laths. These morphologies, their formation as well as appearance are described in greater detail in 2.3.1. The lamellar content results of the systematic manual point count method are then applied to calculate lamellar grain size (μm) via the linear intercept method ASTM E112-13 at 0° and 90° to compression axis. This is to assess, in two axes, the complicated microstructure of kinked/bent laths in compression samples or laths of different thickness in heat treated material for example, these complicated microstructures also made

automated image analysis difficult. Examples of microstructural images analysed are given in each section where discussed.

3.3.2.2 Phase fraction

Phase contributions and their resulting morphologies are estimated from a combination of the above %_{lam} and EBSD phase analysis, discussed below.

From EBSD phase analysis, total γ (% γ_{tot}), β_0 (% β_{tot}) and α_2 (% α_{2tot}) phase contributions are determined but it is not possible to distinguish the equiaxed or lamellar forms for the γ , β_0 or α_2 . Here the %_{lam} is used to estimate lamellar content for each phase γ (% γ_{lam}), β_0 (% β_{lam}) and α_2 (% α_{2lam}).

$$\% \gamma_{lam} = \left(\frac{\% \gamma_{tot}}{100} \right) \times \%_{lam}$$

$$\% \beta_{lam} = \left(\frac{\% \beta_{tot}}{100} \right) \times \%_{lam}$$

$$\% \alpha_{2lam} = \left(\frac{\% \alpha_{2tot}}{100} \right) \times \%_{lam}$$

And from this the equiaxed content (X_{eq}) for each phase can be estimated by subtracting the lamellar content from the rest of the total phase given by EBSD.

$$\% \gamma_{eq} = \% \gamma_{tot} - \% \gamma_{lam}$$

$$\% \beta_{eq} = \% \beta_{tot} - \% \beta_{lam}$$

$$\% \alpha_{2eq} = \% \alpha_{2tot} - \% \alpha_{2lam}$$

As feathery γ (γ_f) can also be calculated by removing γ_{eq} from the above equation and replacing with γ_f . A similar methodology for estimating microstructural constituents and phase fraction was applied using image processing tools on BSE micrographs by *Schwaighofer et al.*[65].

3.3.2.3 Grain area $\leq 50 \mu m^2$ fraction

Electron back-scatter diffraction (EBSD) was used to identify grain boundaries,, to define a grain, 10° of mis-orientation was used. However, EBSD itself cannot distinguish between morphologies; lamellar and equiaxed or feathery γ , itself, so is not used for determination of the morphology content fraction. As the fraction and size of the remnant morphology is an important factor in further workability, as identified by *Zhang et al.*, the fraction of grains under $50 \mu m^2$ look to quantify this and set a marker for the comparison of compression samples in this study [144].

3.3.2.4 Dynamic recrystallised fraction

With a grain defined the dynamic recrystallised fraction (X-DRX) of compressed material and the deformed content can be estimated, this was done through the grain orientation spread (GOS) approach. GOS uses the average misorientation degree within grains, the misorientation spread in DRX grains is lower than that of deformed grains, an approach identified by *Hadadzadeh et al.* [145]. This GOS approach has been applied to work on TiAl alloys as a reliable and convenient method to quantify X-DRX and has been used to validate DRX predictive modelling and form processing maps, using $\leq 2^\circ$ as the benchmark for DRX grains, as has been used here [146],[147]. However, it has its limitations, the GOS approach will not be able to distinguish between “recrystallised and deformed” grains and those that are just “deformed”, consequently only recently recrystallised grains are included in X-DRX. For the GOS of grain i ,

$$GOS(i) = \frac{1}{J(i)} \sum_j \omega_{ij}$$

The number of pixels per grain is given by $J(i)$, ω_{ij} is the angle of misorientation between pixel orientation of grain J and the mean orientation of grain i . This was done using script and commands written in MTEX, an add-on to MATLAB, to construct maps of microstructure observed, including band contrast, grain boundary/phase and DRX.

4 Thermomechanical processing trials of 45XD

4.1 The impact of HIP and heat treatment on the microstructure and subsequent compression behaviour of 45XD

4.1.1 Introduction

To summarise the findings of the literature review in respect to 45XD, simple HIP and uniaxial compression could be optimised to improve the removal of the anisotropy causing lamellar grains and casting segregation which will hinder secondary processing [86]. An emphasis on controlling and optimising this starting microstructure to globularise the lamellar content and return a favourable microstructure that improves forging outcomes is missing.

The work reported, here evaluates the effect of pre-compression consolidation and heat treatment on the as-received cast microstructure. By maintaining constant compression conditions these pre-compression microstructures were assessed for their influence on the compression behaviour. The resulting post-compression microstructures were assessed in terms of lamellar grain dimensions and content as well as phase fraction, with a view to facilitating secondary processing of 45XD (Ti-44.31Al-1.93Nb-2.93Mn-0.87B). This study is necessary as a starting point for subsequent work to provide isotropic-behaving material ready for secondary processing i.e., isothermal closed die forging or rolling.

Ti	Al	Nb	Mn	B	O	Fe	Cu	C	N	Si
49.80	44.31	1.93	2.93	0.84	0.10	0.02	0.03	0.02	0.01	0.02

Table 6: Average chemical composition of supplied 45XD ingot, analysed via ICP at three points by TIMET.

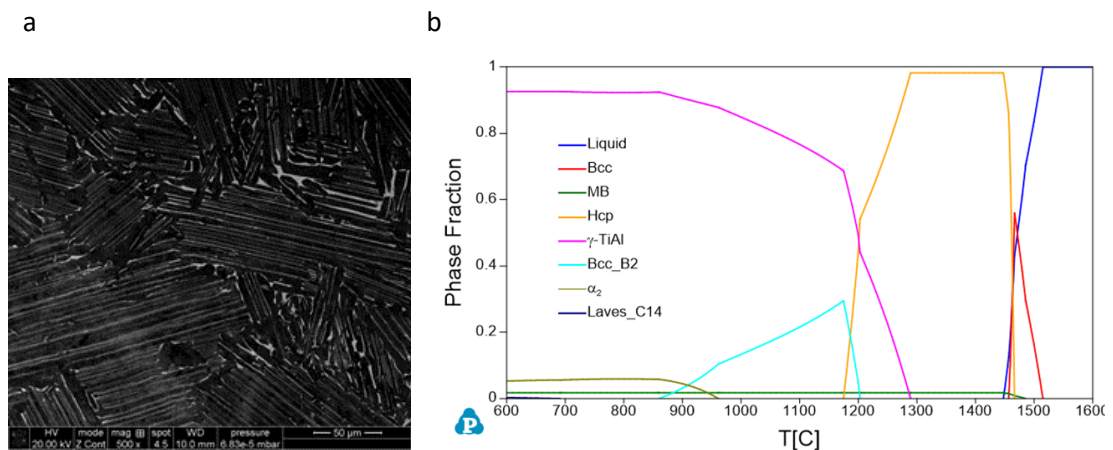


Figure 29: (a) BSE image of as-received (ASR) cast microstructure of 45XD from the centre of the received ingot, equivalent of position C in Figure 26, at 500x magnification, where black areas correspond to γ phase, white β_0 and grey α_2 . (b) Calculation of phase diagram (CALPHAD) of 45XD alloy from ICP analysis in Table 6.

4.1.2 Results and discussion

The influence of the starting microstructure on the deformation behaviour of the material relies on several parameters, these are discussed here. This is followed by an explanation of the compression behaviour for each processing condition, as well as the associated extent of globularisation of lamellar grains, together with the resulting X-DRX and the fraction of grains $\leq 50 \mu\text{m}^2$. The potential for future use in processing will be assessed by exploring the relationship between the initial microstructures formed by the different HT applied; the lamellar content, lamellar grain size and phase fraction produced, and the microstructure returned after primary compression; remnant lamellar content, remnant lamellar grain size, X-DRX and the fraction of grains $\leq 50 \mu\text{m}^2$ as well as phase fraction. Regression analysis will help identify characteristics which are most important in returning the preferred microstructure discussed. To start, the ASR and HIP microstructure and analysis is discussed.

4.1.2.1 Pre-compression microstructures

In Figure 29a and Figure 30, BSE imaging shows the 45XD alloy in the as-received cast and consolidated condition (HIP) respectively, both with nearly fully lamellar microstructures, consisting of coarse lathed lamellar colonies of $\gamma+\alpha_2$ as well as equiaxed γ and α_2 at lamellar grain boundaries. A third phase, β_0/β , referred to as simply β when discussing microstructures at room temperature, is also present as both equiaxed β at lamellar grain boundaries and β deposits within lamellae grains themselves.

Hot isostatic pressing (HIP) was used to consolidate the material, reducing porosity. The HIP temperature for this alloy is high in the $\alpha+\gamma$ region, within 20°C of the α transus according to Figure 29b. The influence of this process on the microstructure of titanium aluminides has been explored by several investigators for both finishing of cast parts and as preparation for further processing [129],[49],[51]. The HIP microstructure is casting porosity free and consists of lower lamellar content and grain sizes when compared just to ASR. An increase in the overall γ_{eq} suggests HIP causes some form of static globularisation [148]. This is perhaps due to the time spent high in the $\gamma+\alpha$ region during the HIP process causing γ morphologies to coarsen. Table 7 shows microstructural characteristics from BSE image processing. The microstructure of ASR and the HIP material is largely dictated by the solidification pathway of the ingot.

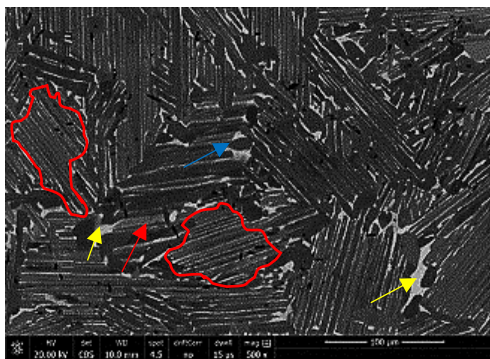


Figure 30: BSE images of 45XD alloy in the HIP condition respectively, at 500x, where black areas correspond to γ phase, white β_0 and grey α_2 . Lamellar grain and boundary examples outlined in red blue arrow identifies γ_{eq} , yellow arrows identify β_{eq} examples and red arrow identifies an α_2 lath.

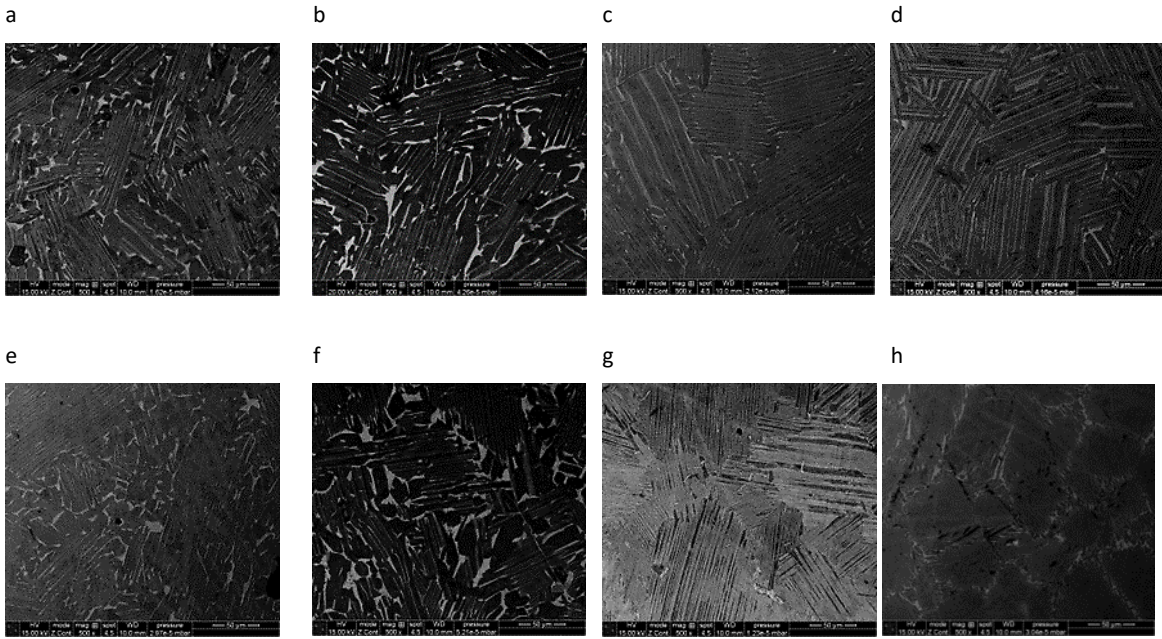


Figure 31: SEM micrographs (BSE) at 500x magnification of 45XD alloy before compression, heat treated for 2 hours at different temperatures with either FC or AC cooling rates; 1130 °C FC(a) and AC(e), 1200 °C FC(b) and AC(f), 1270 °C FC(c) and AC(g), 1350 °C FC(d) and AC(h). Where black areas correspond to γ phase, white β_0 and grey α_2 , respectively.

Peritectic solidifying ($L+\beta\rightarrow\alpha$) alloys, such as 45XD, use the titanium boride precipitates to nucleate α , as shown in the CALPHAD phase fraction diagram in Figure 29b, here α is growing into the disordered β , as well as any liquid present. Grain refinement, compared to the non-boride doped alloys, of the as-cast microstructure is the aim of these additions, ideally removing much of the costly wrought processing [137]. The boron enables refinement through the changes caused in solidification pathway, as reviewed by *Hu*. [39]. The boride also gives the growing α laths their orientation, as described by *Hu et al.*, so giving the random lamellae grain orientation seen here in ASR material upon cooling and in the subsequent HIP microstructure, giving engineering properties sufficient for cast low pressure turbine blades [45],[40].

Starting from the HIP material condition, shown in the annotated Figure 30, the effect on the microstructure of different heat treatment temperatures, heating in different phase regions, followed by either air (AC) or furnace cooling (FC), is shown in the resulting BSE images in Figure 31a-h. Table 7 shows microstructural characteristics from BSE image processing.

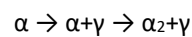
Heat treatment temperatures <1270 °C produce nearly fully lamellar microstructures, with lamellar colonies of $\gamma+\alpha_2$ and the presence of equiaxed γ and β_0 grains at lamellar grain boundaries. At room temperature this type of microstructure typically gives more ductility and toughness, compared to the fully lamellar microstructure [27]. However, when in comparison at higher temperatures they are inferior for practical applications.

In general, the lamellar grain content is largely constant from the HIP microstructure to the HIP plus 1130 °C and 1200 °C HT material, there is however an overall increase in the lamellar grain size. At 1200 °C, in the $\alpha+\gamma+\beta_0$ region, lamellar laths visibly saw growth and swelling, perhaps explaining the increase in lamellar grain size. The high temperature and furnace cooling provided the energy and time for this growth, the air cooling prevented any obvious lath growth.

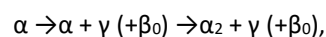
In samples HT at 1130 °C, a rise in both lamellar and equiaxed $\alpha_2+\beta_0$ content compared to HIP material is noted. This HT sees an increase of around double the HIP values for equiaxed $\alpha_2+\beta_0$ material. This is expected to increase the flow stress seen during compression with the increase of these slip restricted phases [70]. Casting segregation of the aluminium content of 45XD alloy also accentuates the β_0 phase present from ingot formation of peritectic solidifying titanium aluminides. This segregation and resulting β_0 phase causes processing issues such as narrow processing windows, heterogeneous deformation and poor recrystallisation kinetics, as identified by *Imayev et al.* and *Chladil et al.* [33],[34]. There is very little difference between microstructures of the FC and AC material HT at 1130 °C.

The high temperatures of HT at 1270 °C and 1350 °C led to fully lamellar microstructures, as well as an increase in both lamellar grain size and overall content with both air and furnace cooling. The lamellar content increased at these temperatures and cooling rates, via type 1 lamellar formation, as described by *Denquin and Naka* [28]. The lamellar structure can form from three phases in the Ti-Al phase diagram, to give either the fully or nearly lamellar microstructures, as reviewed by *Ramanujan* [29]. Type 1 lamellar structure, fully lamellar, is formed above the alpha transus (~1300 °C for 45XD)

In Type 1, lamellar grains are formed via the pathway;



For 45XD alloy this pathway is adjusted to follow the pathway below, the extent of β_0 phase being dependent on the time spent in this temperature region;



In this reaction, plate-like γ begins to precipitate out of the α matrix when temperatures reach below the α transus (~1300 °C), mechanism described in greater detail in section 2.3.1.3. This structure transforms at lower temperatures to a $\gamma+\alpha_2$ lamellar structure by the α to α_2 ordering reaction, this occurs below the $\alpha_2+\gamma$ transus line (~1125 °C). This is shown with HT at 1350 °C, AC giving fine laths with α/β_0 at the grain boundaries frozen in place; AC not giving the time to form lamellar microstructures. The FC material has the time to form lamellar grains, with consequently more coarse laths, with no equiaxed γ material at the grain boundaries, as seen in Figure 31d.

45XD material condition	% _{Lam}	Average lamellar grain size (μm)	Standard deviation of average lamellar grain size (μm)	% α ₂ + β _{0 lam}	% γ _{lam}	% α ₂ + β _{0 eq}	% γ _{eq}
ASR	64	62	15	9	46	7	38
HIP	53	47	13	7	46	6	41
1130FC	53	57	21	14	39	12	35
1130AC	49	56	13	14	35	14	37
1200FC	52	59	13	6	46	5	43
1200AC	61	54	12	8	53	5	34
1270FC	70	60	41	11	59	5	25
1270AC	90	83	23	49	41	5	5
1350FC	85	72	17	14	71	2	13
1350AC	88	69	11	24	65	3	9

Table 7: breakdown of lamellar grain content and size, as well as lamellar and equiaxed morphology and respective phase composition for 45XD in different conditions before compression from BSE image processing.

Material homogenised at 1270 °C has larger lamellar grain sizes than 1350 °C, with AC higher than FC. The 1270 °C AC sample sees a high fraction of α_{2lam} which could be due to the time spent high in the γ+α phase, with α growth being dominant over γ, the fast-cooling rates then freezing the growing and dominant α phase in place. This suggests that 1270 °C could be below the α transus, as indicated by Figure 29b.

To summarise, in samples with a rise in α₂+β₀ content, particularly 1130FC and AC, there is expected to be an increase in the flow stress seen during compression and a reduction in the resulting globularised fraction compared to HIP material with the increase of these slip restricted phases [58],[70]. Using a heat treatment near or within the α phase, 1270 °C and 1350 °C, for elemental and microstructural homogeneity does not appear to cause excessive grain growth in this alloy, as found by other researchers with non-boride containing TiAl alloys [53],[149]. These fully lamellar microstructures, favoured for creep and fatigue resistance in LPT blade production, are anticipated to produce the highest flow stress results during compression but when combining fully lamellar microstructures with low average lamellar grain size, the high lamellar to lamellar grain boundary density promises higher globularised fractions [58].

4.1.2.2 Compression behaviour

This section describes mechanisms at play during compression and the effect the pre-compression microstructure has on the flow behaviour. This behaviour is largely affected by the characteristics of

the lamellar grains present, this includes grain dimensions, lath thickness and the orientation of the lamellar grain to the load applied as well as the phase fraction [86]. These tests aim to simulate ingot breakdown or upsetting, these processes are referred to as primary compression.

This will be discussed in terms of microstructural details mentioned in 4.1.2.1 and their impact on flow behaviour.

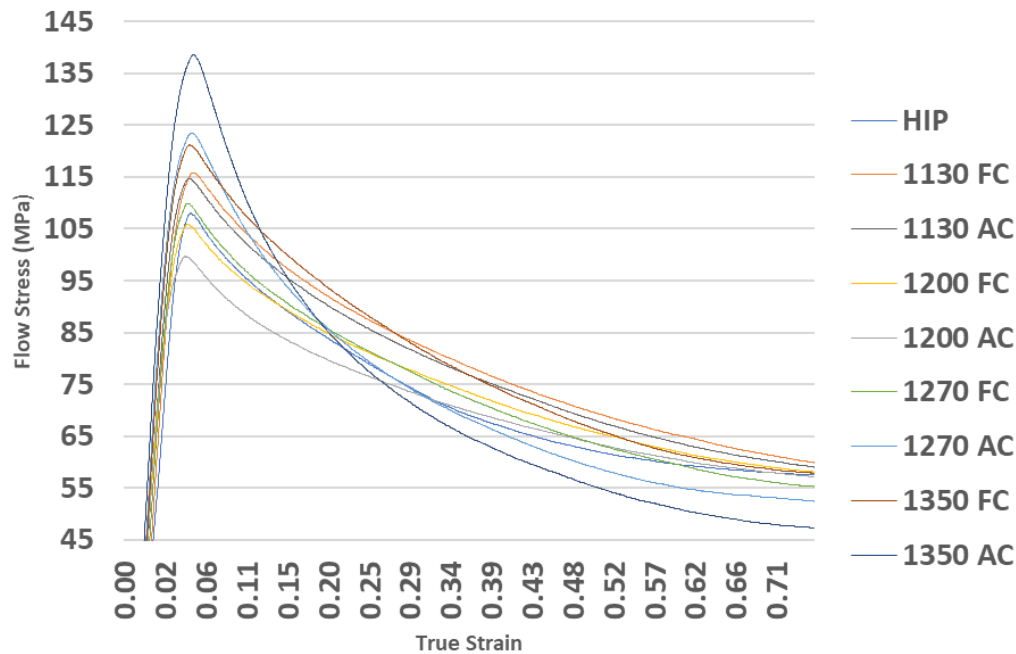


Figure 32: Flow stress-true strain curves for each 45XD material condition through 50% compression at 1100°C, 0.001s⁻¹, over 760 seconds.

Flow stress and true strain were calculated for each of these microstructural conditions with uniaxial compression testing to 50% at 1100 °C, with a strain rate of 0.001 s⁻¹. Each curve follows a similar pattern, peak flow stress (σ_{pfs}) reached at a true strain of 0.04, in Figure 32 for each 45XD condition, followed by flow softening. This flow behaviour is a characteristic of dynamic recrystallisation in this material [114],[150]. In titanium aluminide alloys at hot working temperatures, γ phase is deformed with a low stacking-fault energy, this means dynamic recovery (DRY) is slow, giving a high dislocation density, restoration is therefore reliant on dynamic recrystallisation (DRX), as discussed in 2.4.2.1 [77]. The formation of this stress-free recrystallised material is key to producing workable material for secondary processing [53].

When considering the compression and breakdown of lamellar material, dynamic recrystallisation is often referred to as dynamic globularisation, this is similar in nature to discontinuous dynamic recrystallisation, discussed in detail in sections 2.4.2.1 and 2.4.2.2, with reviews and mechanisms by *Seetharaman and Semiatin*, and *Zhang et al* and *Tian et al*. Respectively [58], [144], [151]. With constant compression conditions, these studies found the extent of globularisation, and therefore DRX, is dependent on the lamellar content, size, and orientation as well as phases present.

Heat treatments at 1270 °C or 1350 °C, high in the $\gamma+\alpha$ phase region or above the α transus, respectively, returned the highest lamellar grain sizes and content seen, particularly with AC. The fully lamellar microstructures and large lamellar grain sizes, seen in both FC and AC pre-compression samples, limits the opportunity for lamellar grains to orientate perpendicular to compression when compared to samples with a higher fraction of equiaxed material, and explains the higher flow stresses seen [87]. This is due to larger lamellar grains being less mobile in either equiaxed or fully lamellar material, relatively few and large lamellar grains being present also means there is less chance of the lamellar grain being in a favourable orientation for globularisation [58].

. However, globularisation favours higher lamellar to lamellar grain boundary density, seen extensively in material heat treated at 1270 °C and 1350 °C pre-compression, shown by the higher lamellar content in Table 7 as compared to HIP, also identified by *Seetharaman and Semiatin*, explaining the greater extent of flow softening [58]. This relationship between large starting lamellar microstructures, flow softening rate, recrystallisation and flow localisation was reviewed by *Semiatin, Seetharaman and Weiss* [119].

Another aspect of these AC samples that resisted recrystallisation and dynamic globularisation, is the fine lath spacing, however this has not been quantitatively assessed here[91,92]. No obvious signs of flow localisation i.e., sheared samples, were identified in these trials but the high σ_{pfs} and extent of flow softening seen in the AC samples from HT at 1270 °C and 1350 °C is a concern.

The coarser lathed lamellar structures in the 1350 °C and 1270 °C FC samples show lower σ_{pfs} , due to the relative ease of recrystallisation initiation in comparison to AC, even with similar starting phase fraction, lamellar content, and sizing in the case of 1350 °C FC [144]. The σ_{pfs} of 1270 °C FC is the lowest of the fully lamellar microstructures, perhaps due to the combination of low lamellar grain sizing and relatively high lamellar content compared to HIP, seen in Table 7. Potentially this leads to a higher lamellar-lamellar grain boundary density in comparison to other fully lamellar microstructures and so initiating DRX at lower flow stresses, this is promising for improving globularisation kinetics [119].

Material	HIP	1130FC	1130AC	1200FC	1200AC	1270FC	1270AC	1350FC	1350AC
1' σ_{pfs} (MPa)	108.0	115.8	114.7	105.8	99.7	117.8	123.5	121.1	138.5

Table 8: maximum flow stress seen for each 45XD material condition with 50% compression at 1100 °C, 0.001 s⁻¹.

Samples HT at 1200 °C give the lowest σ_{pfs} , followed by HIP and 1270FC respectively. This is likely to be due to a combination of low lamellar content and lamellar grain size, as well as a favourable fraction of $\alpha_2+\beta_0$ [58]. This looks to have reduced peak flow stress and increased the extent of flow softening, especially when compared to samples held at 1130 °C, where considerably higher flow stresses were seen without the extent of flow softening.

Both HT samples at 1130 °C give higher σ_{pfs} despite lower lamellar content compared to 1270 °C AC. The higher fraction of the equiaxed and lamellar $\alpha_2+\beta_0$ perhaps contributing to this higher than anticipated result.

Cooling having fairly little effect at this temperature. This temperature region, dominated by $\gamma+\beta_0$, seen in Figure 29, the β_0 fraction is high and appears detrimental in terms of compression behaviour [69].

4.1.2.3 Post-compression microstructures

a

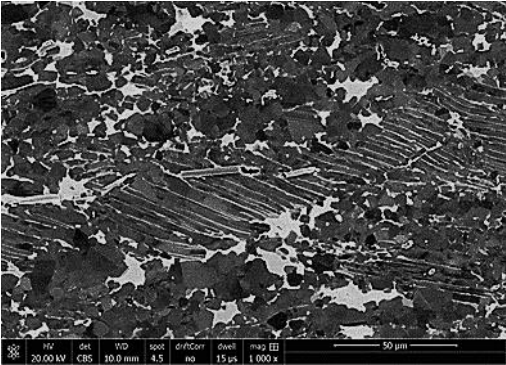
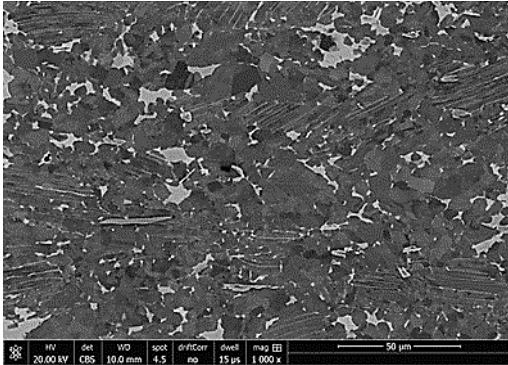
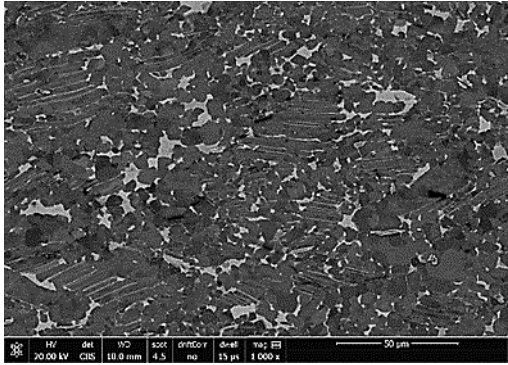


Figure 33: SEM micrographs (BSE) at 1000x magnification of 45XD alloy after compression, in the HIP condition (a) and heat treated for 2 hours at different temperatures with either FC or AC cooling rates; 1130 °C FC(b) and AC(c), 1200 °C FC(d) and AC(e), 1270 °C FC(f) and AC(g), 1350 °C FC(h) and AC(i). Where black areas correspond to γ phase, white β_0 and grey α_2 , respectively.

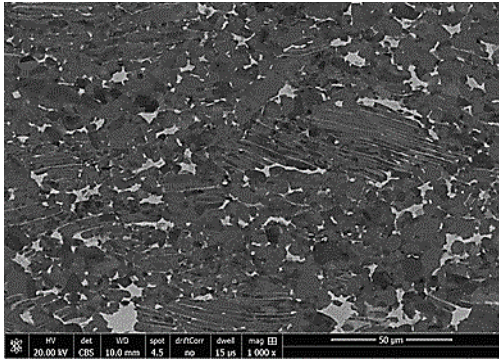
b



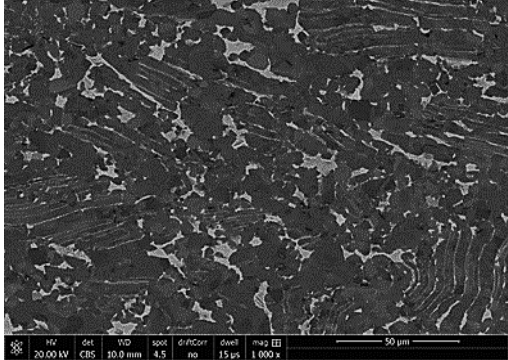
c



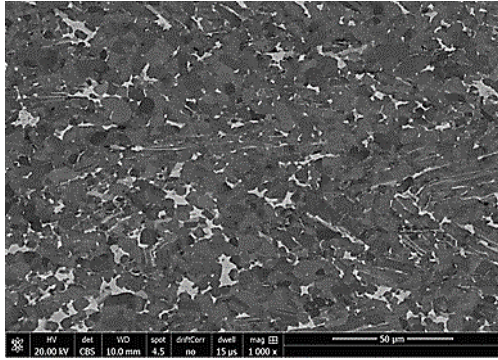
d



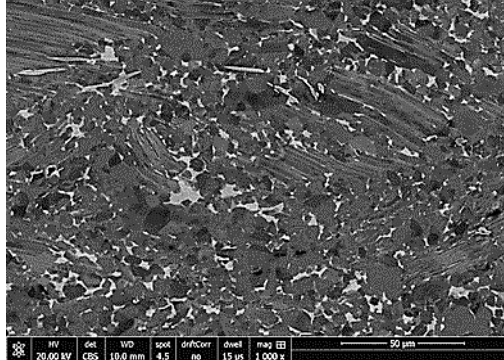
e



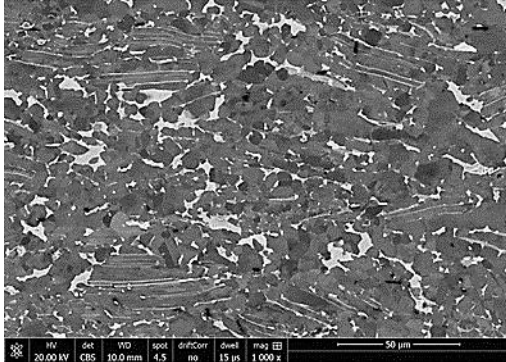
f



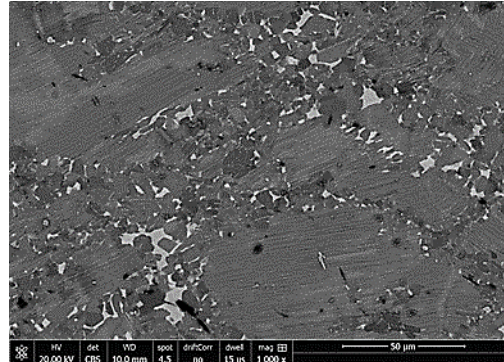
g



h

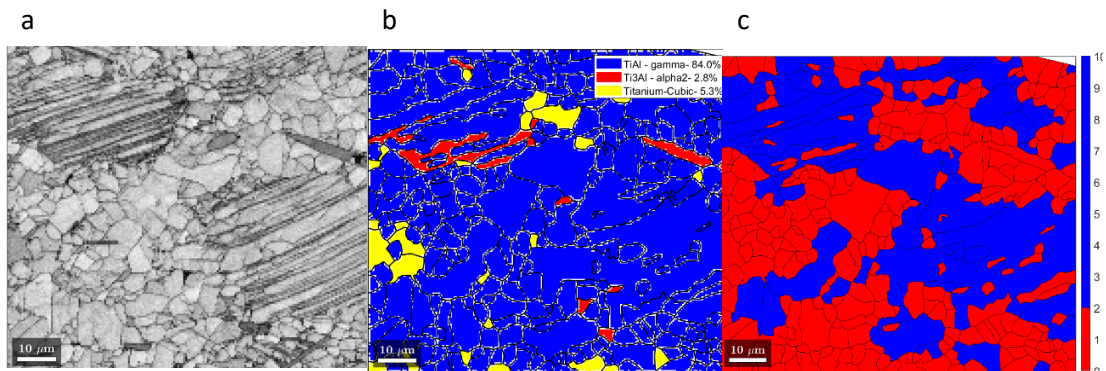


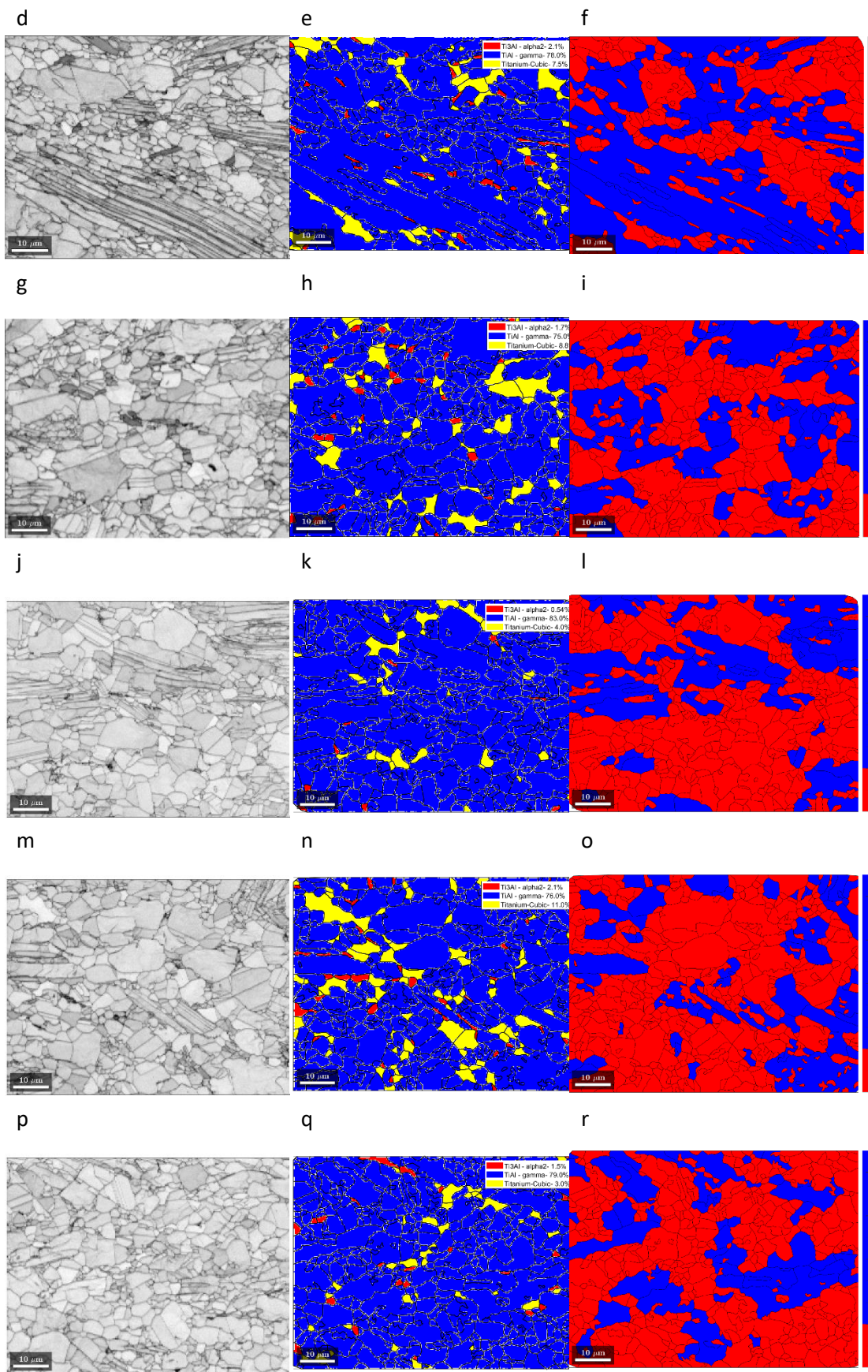
i



Microstructural analysis was conducted on 50 % compressed samples of 45XD material to analyse the influence of initial microstructure on the evolution of the microstructure after compression. With particular focus on the phase fraction, remnant lamellar grain size content, as well as the resulting DRX fraction (X-DRX). These factors contribute to material behaviour and response in the following processing steps.

All samples show γ material is dominant, as seen in phase maps in Figure 33 and Table 9, as well as α_2 and β_0 morphology contributions. These α_2 and β_0 morphology contributions appear to have become more consistent across all compressed samples, in comparison to the pre-compressed material. However, in general, β_0 material does appear in larger fractions in material HT ≤ 1200 °C than the material in a fully lamellar state before compression. The 1200AC material shows the highest fraction at 11 %, the 1350AC sample showing the lowest β_0 at 4 %.





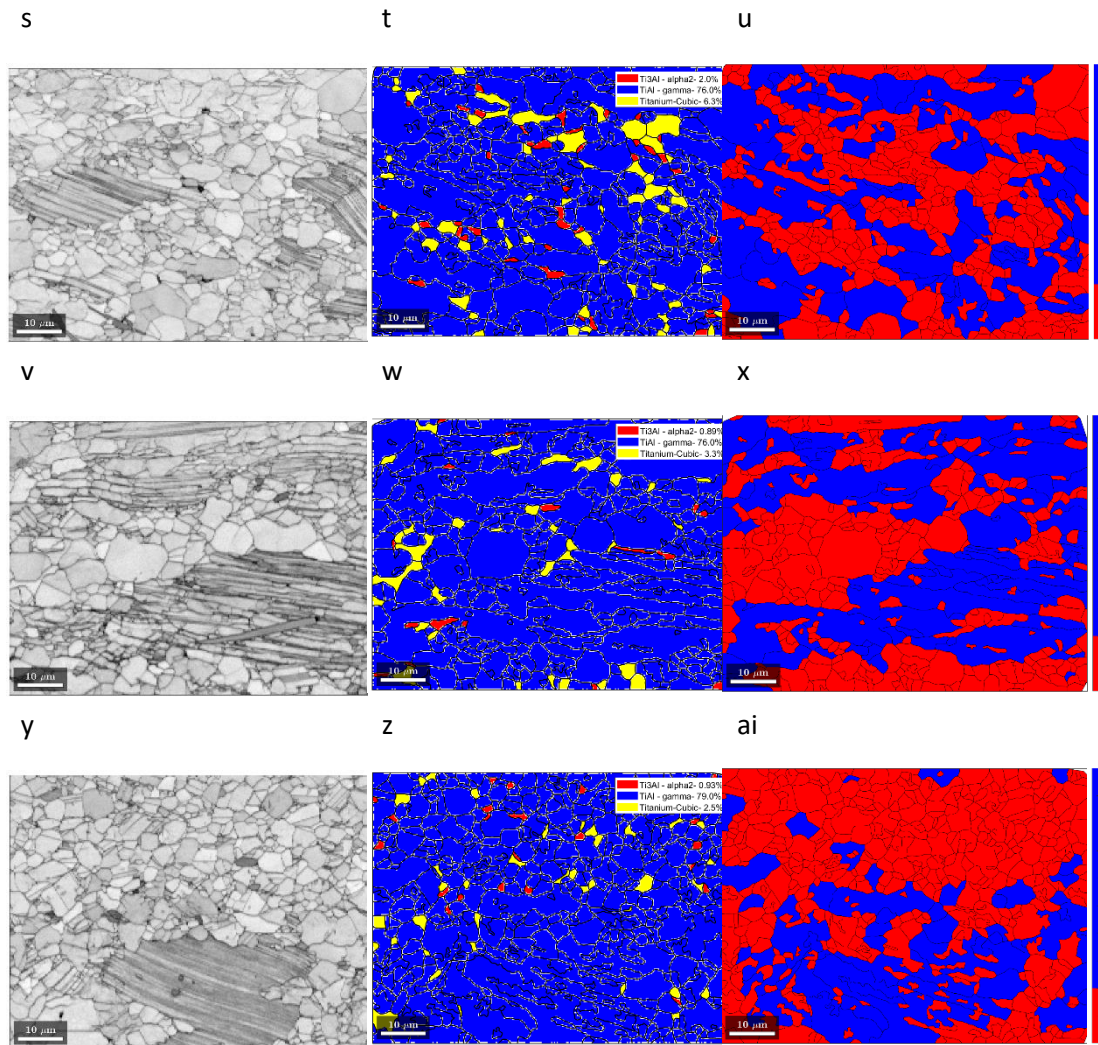


Figure 34: EBSD used to give maps of, (left) band contrast, (middle) phase map; blue is γ , red is α_2 , yellow is β_0 , (Right) X-DRX; red is the recrystallised fraction, blue is deformed, of 45XD alloy in the HIP condition (a-c), and heat treated for 2 hours at different temperatures with either FC or AC cooling rates; 1130 °C FC (d-f) and AC(g-i), 1200 °C FC(j-l) and AC(m-o), 1270 °C FC (p-r), and AC (s-u), 1350 °C FC (v-x) and AC(y-ai), at 1600x magnification,

Considering the lamellar content of compression samples, those HT at 1270AC show the greatest reduction in lamellar content at 76 % with the smallest average lamellar grain size at 19 μm , but not the highest X-DRX, at 69 %. The HT sample 1200AC shows the highest X-DRX at 71 %, 1270FC the highest X-DRX value of the fully lamellar material. Compression of material HT at 1350 °C AC and 1270 °C FC gives the highest content of grains under 50 μm^2 , 78 % and 77 %, respectively. Figure 35 shows how the X-DRX is calculated through the GOS approach, together with the grain area frequency density plots from EBSD analysis.

45XD material condition +50% compression	% α_2	% β_0	% γ	DRX fraction (%)	Grain area fraction $\leq 50 \mu\text{m}^2$ (%)
HIP	3	5	84	53	57
1130FC	3	8	89	43	57
1130AC	3	9	88	61	76
1200FC	2	5	94	65	72
1200AC	3	11	86	71	75
1270FC	2	4	94	69	77
1270AC	3	7	90	51	69
1350FC	2	5	93	48	58
1350AC	3	4	94	65	78

Table 9: breakdown of phase composition for 45XD in all material conditions at P1 after compression from BSE image processing and EBSD mapping.

The X-DRX was calculated in this work through the GOS approach, seen in Figure 35, from EBSD data. GOS uses the average misorientation degree within grains, the misorientation spread in DRX grains is lower than that of deformed grains, an approach identified by *Hadadzadeh et al.* [145]. This has been applied to work on TiAl alloys to validate DRX predictive modelling and form processing maps, using $\leq 2^\circ$ as the benchmark for DRX grains, as has been used here [146],[147]. Table 10 displays the range of remnant lamellar dimensions still present at P1 and P2 of compression samples, the purpose of both P1 and P2 here is to look at the homogeneity of compression outcome across the work piece.

Including outliers, 1270 °C HT material shows the lowest average of lamellar grain sizes for all compressed material, the AC sample showing the lowest value at 19 μm . After compression, lamellar grains were still present in all samples, however, *Zhang et al.* suggested lamellar grains below 80 μm should not be considered detrimental [144]. Using this value, only 1270FC, 1200FC and AC comply. The orientation of these remnant lamellar grains appears to largely align perpendicular to compression, as the maximum lamellar grain size 0° to compression shows in Table 10.

Uniform globularisation of lamellar grains, with similar remnant lamellar grain sizes, across the workpiece is also an important factor. This appears to be the case with only 1270FC, 1200FC and AC. In fully lamellar material, for example 1270FC, re-orientating the lamellar grains is difficult with lamellar-to-lamellar grain boundaries, if these are relatively small grains with favourable lath thickness, globularisation proceeds. Larger lamellar grains are less mobile, with a higher chance of being in an unfavourable orientation for globularisation, as is likely the case with 1350FC [58].

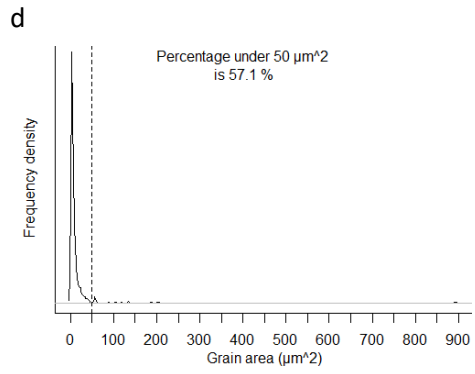
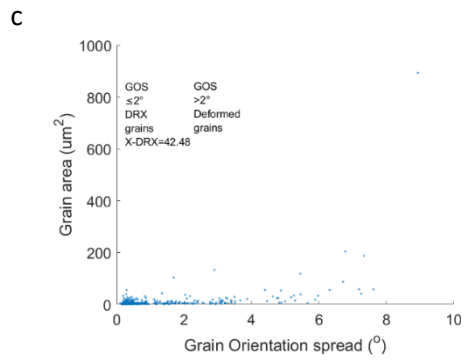
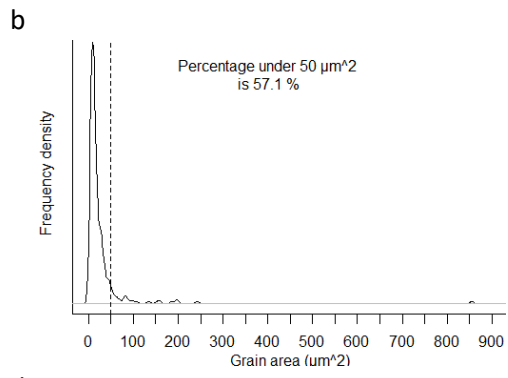
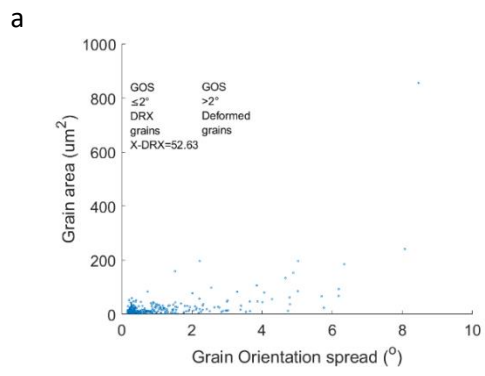
The opposite position to this is where we have smaller lamellar grains with equiaxed material present at grain boundaries as in nearly fully lamellar microstructures pre-compression. Rotation of lamellar grains rather than globularisation is a possible reason for the lack of globularisation seen in samples

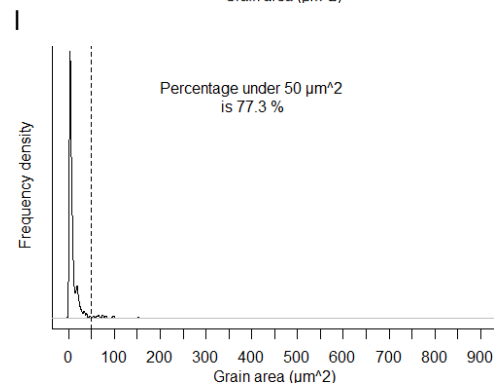
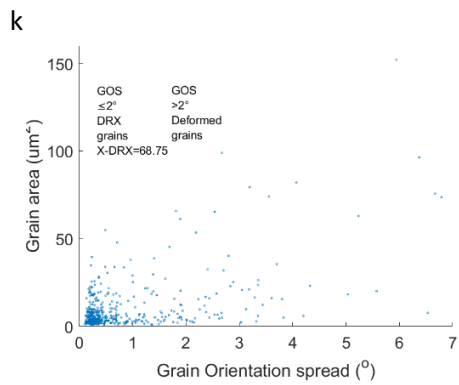
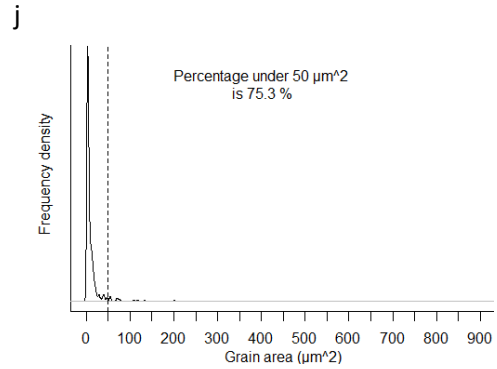
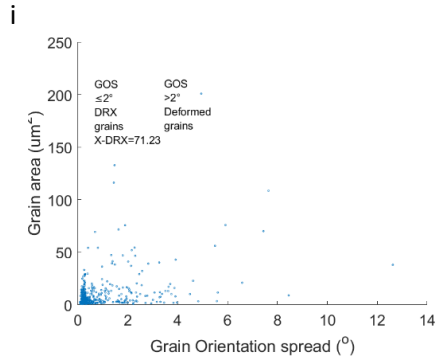
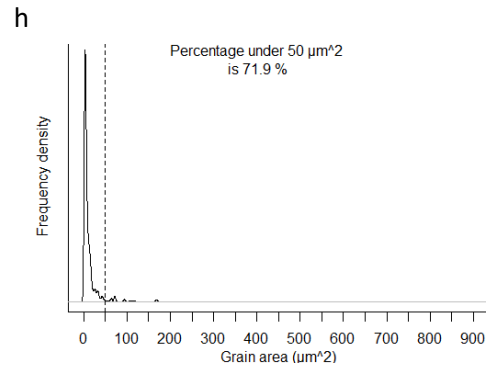
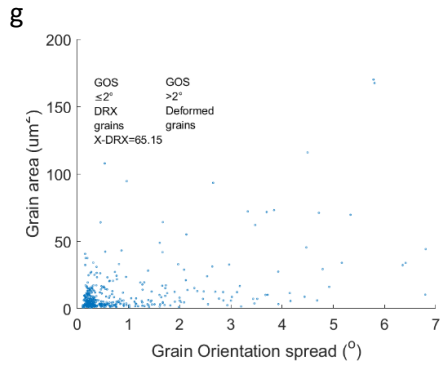
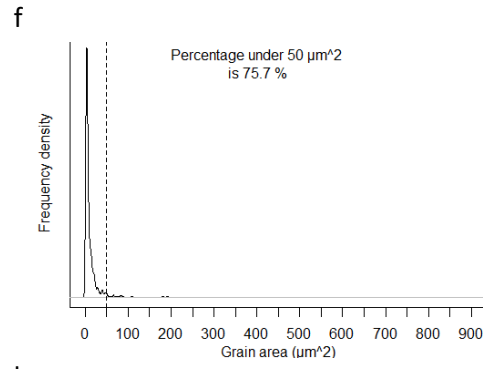
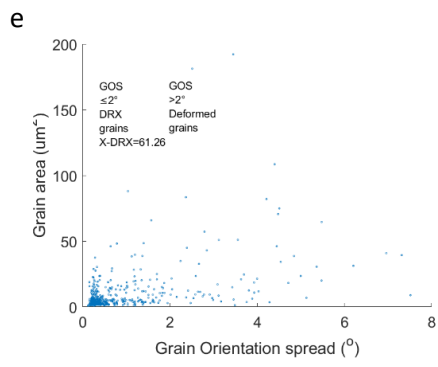
with low starting lamellar content, such as those HT at 1130 °C, 1200FC and HIP [87]. Exhibited by the low values for reduction in lamellar content in Table 10.

45XD material condition +50% compression	%Lam		Reduction in %Lam		Average lamellar grain size (μm , from 0° and 90°)		Standard deviation of average lamellar grain size (μm , from 0° and 90°)	
	P1	P2	P1	P2	P1	P2	P1	P2
HIP	23	39	30	14	34	57	18	20
1130FC	33	36	20	17	50	38	31	13
1130AC	26	37	23	12	37	45	25	24
1200FC	21	39	30	13	26	46	13	15
1200AC	17	31	44	29	22	37	10	16
1270FC	24	30	46	49	31	33	22	12
1270AC	14	29	76	61	19	47	7	31
1350FC	24	83	61	2	55	71	54	26
1350AC	21	29	67	60	49	29	29	18

Table 10: Remnant lamellar morphologies of all 45XD material conditions at P1 and P2 after 50% compression, 1100 °C, 0.001 s⁻¹.

The relatively high flow stress results and low globularisation extent from the 1130 °C heat treatment could be due to the same mechanism seen in creep and fatigue trials. Where heavy alloying elements and interstitials are preferentially gettered into the α_2 from γ during HT. This means the α_2 is less prone to globularisation when under strain in compression due to several factors; possibly tighter lamellar spacing compared to other samples, slower dissolution of α_2 into γ and solid solution hardening effects [74],[104],[152].





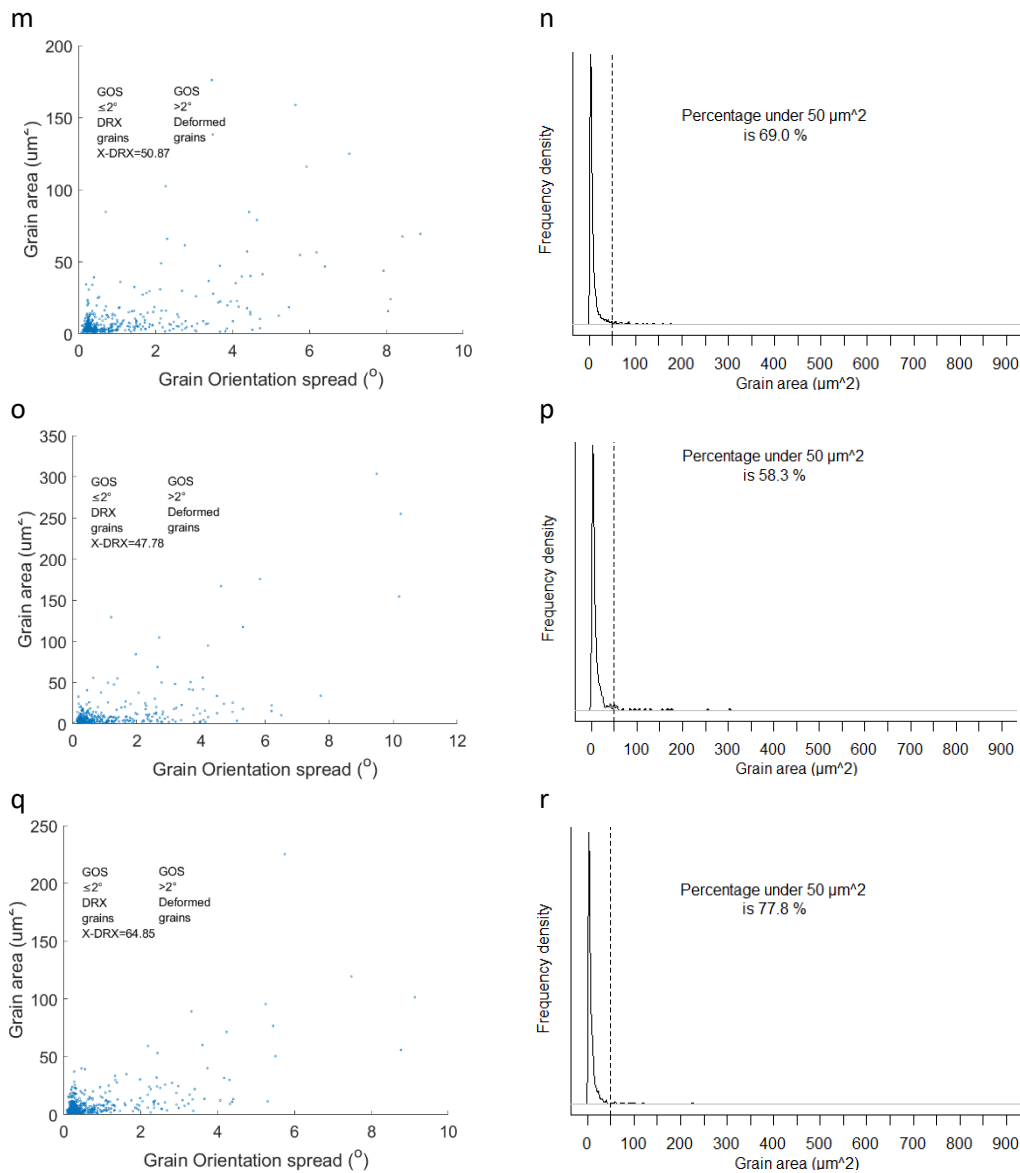


Figure 35: Plots calculating the DRX fraction from the GOS approach on the left, grain area frequency density on the right, for each material condition after 50% primary compression at $1100 \text{ }^\circ\text{C}$ and 0.001 s^{-1} , HIP (a, b), and heat treated for 2 hours at different temperatures with either FC or AC cooling rates; $1130 \text{ }^\circ\text{C}$ FC (c, d) and AC (e, f), $1200 \text{ }^\circ\text{C}$ FC (g, h) and AC (i, j), $1270 \text{ }^\circ\text{C}$ FC (k, l), and AC (m, n), $1350 \text{ }^\circ\text{C}$ FC (o-p) and AC (q, r).

With respect to future processing of the material discussed here, studies by *Kim* discuss the inverse relationship between grain size and ductility, their study showing microstructures with low grain sizes can tolerate higher strain to failure (fracture), also discussed in an earlier study of theirs [89],[88].

In their study on strength and ductility of TiAl alloys, they looked at the brittle-ductile transition of titanium aluminides and the effect microstructure has on this, higher ductility came about due to the higher amount of yielding accepted by the higher density of grain boundaries, preventing crack propagation. This is relevant to the present work as it is apparent that maintaining elemental homogeneity is vital, but to do this heating above the α transus is required. This leads to a larger

grained fully lamellar microstructure, which can be difficult to process with a possibility of flow localisation and resistance to dynamic globularisation if lamellar grain sizes are too large.

So, achieving a refined fully lamellar microstructure, largely absent of β_0 , may improve forging outcomes through the refined grain size and elemental homogeneity required for the material to respond to thermo-mechanical processing promptly and efficiently.

4.1.3 Summary

The aim of this study was to understand how consolidation, heat treatment and cooling rate influence the pre-compression microstructure and subsequent compression behaviour of 45XD, with a focus on the extent of homogeneous globularisation across the work piece. This is required to improve the chances of successful outcomes in subsequent processes i.e., hot rolling or closed die isothermal forging. The extent of globularisation during compression was found to rely on characteristics of the pre-compression microstructure, and the following conclusions regarding the primary processing stage of the alloy were drawn.

- Hot isostatic pressing to remove porosity and consolidate the ingot does not return a microstructure best placed to remove the lamellar content upon compression or phase fraction for further processing.
- The literature states that for other alloys the ideal pre-compression microstructure for efficient globularisation is a homogeneously sized microstructure, fully lamellar, with elemental homogeneity, making a heat treatment near or above the α transus necessary. This study partially agrees with the literature when we consider the 1270FC material, this temperature is close to the α transus for this alloy. The homogenisation heat treatment temperature is further explored in the next section; 4.2.
- The growth of the β_0 phase by heat treatment or time spent in the $\gamma+\beta_0$ region and the presence of large, fine lamellar grains induced by air cooling from single phase α temperatures, have been identified in these studies as detrimental to globularisation.
- Heat treatment just below the α transus followed by furnace cooling (1270FC) and within the $\gamma+\alpha+\beta_0$ phase followed by air cooling (1200AC) appear to be useful heat treatments for promoting the microstructural and elemental conditions that increase the extent of globularisation. Intermediate heat treatments, between primary and secondary compression, should be explored to improve microstructural outcomes.

4.2 Identifying the homogenisation temperature for 45XD in respect to compression behaviour and microstructural outcome

4.2.1 Introduction

The summary of 4.1 describes the ideal pre-compression microstructure for efficient globularisation as a homogeneous microstructure, fully lamellar, with elemental homogeneity. Defining the heat treatment temperature, anticipated to be close to the α transus, that fulfils these criteria is therefore necessary. This is explored here with a closer examination of the microstructure pre-compression of HIP and 1270FC, as well as another HT temperature above the α transus, 1300FC, using EBSD to investigate the effect phase composition has on forging outcomes, with forging conditions constant. Furnace cooling from these high temperature heat treatments has been deemed most significant from a practical industry perspective as well as the results of 4.1, with compression behaviour and post-compression microstructure being most promising in terms of flow softening and globularisation, therefore X-DRX, without flow localisation.

4.2.2 Results and discussion

4.2.2.1 Pre-compression microstructures

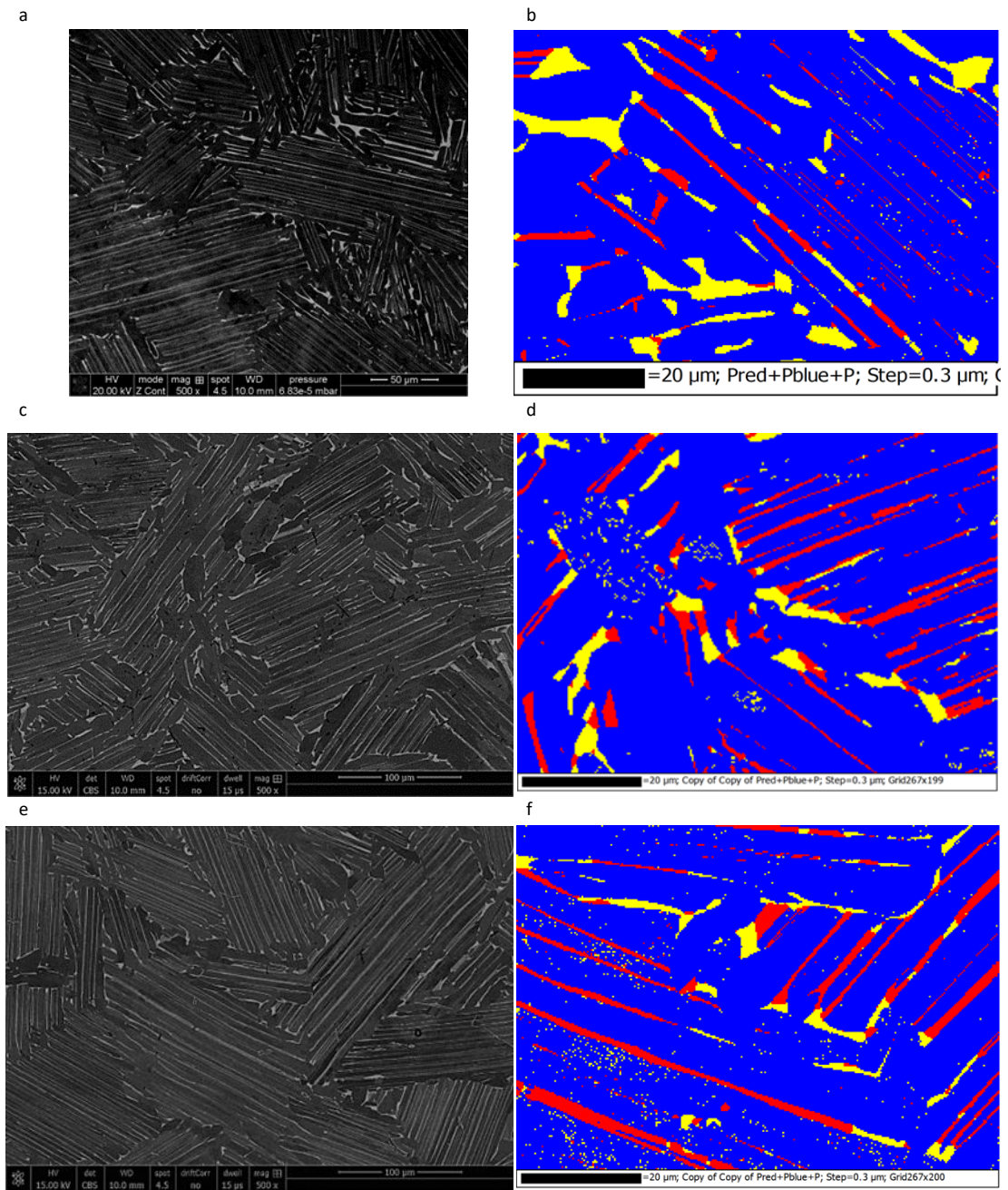


Figure 36: (a) SEM used to give BSE images at 500x magnification (left) where black areas correspond to γ phase, white β_0 and grey α_2 , and EBSD phase maps at 1600x magnification, (right); where blue is γ , red is α_2 , yellow is β_0 , of 45XD alloy in the HIP condition (a-b), and heat treated for 2 hours at ; 1270 °C FC (c-d), and 1300 °C FC (e-f).

45XD material condition	%Lam	Average lamellar grain size (μm)	Standard deviation of average lamellar grain size (μm)	% α_2 lam	% β_0 lam	% γ lam	% α_2 eq	% β_0 eq	% γ eq
HIP	53	47	13	3	5	45	8	4	40
1270FC	70	60	18	6	4	60	3	2	26
1300FC	81	71	23	8	4	70	2	1	16

Table 11: breakdown of lamellar grain content and size, as well as lamellar and equiaxed morphology and respective phase composition for 45XD in different conditions before compression from BSE image processing and EBSD mapping.

The heat treatment above the α transus, 1300FC, leads to an increase in lamellar content and average lamellar grain size as versus the HIP and 1270FC material, seen in 4.1.2.1. It also leads to a small decrease in the overall β_0 content, perhaps due to elemental homogeneity. The energy dispersive spectrometry (EDS) mapping, available in the appendix also exhibits the elemental homogenising effect of α phase heat treatment, β_0 regions containing greater concentrations of Mn in particular without homogenising, as discussed by others on similar alloys [153], [154].

With HT material at 1270FC and 1300FC, although both HT is near or just above the α transus, differences do exist in the microstructure, particularly in the decrease seen in the overall equiaxed material content from 1270FC to 1300FC. This is an important factor identified in 4.1.3; lamellar to lamellar grain boundaries promote globularisation [58].

4.2.2.2 Compression behaviour

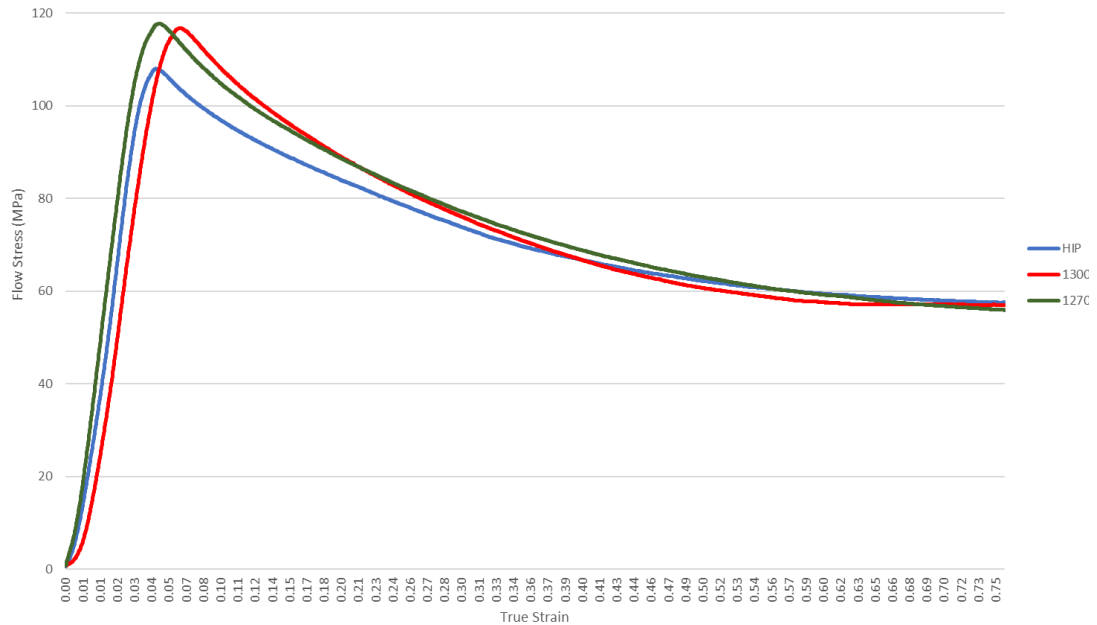


Figure 37: Flow stress-true strain curves for each 45XD material condition through 50% compression at 1100°C, 0.001s⁻¹, over 760 seconds.

Flow stress and true strain were calculated for each of these microstructural conditions with uniaxial compression testing to 50 % at 1100 °C, with a strain rate of 0.001 s⁻¹. Each curve follows a similar pattern, peak flow stress (σ_{pfs}) reached at a true strain of about 0.04, followed by flow softening, as in 4.1.2.2, seen in Figure 37. However, the steep, relative to non-TiAl alloys, initial work hardening seen before σ_{pfs} is of interest. The differences seen in work hardening rate, with 1270FC being the steepest followed by HIP and then 1300FC is perhaps at first counter intuitive given the fully lamellar microstructure of the 1300FC material.

Material	HIP	1270FC	1350FC
1' σ_{pfs} (MPa)	108.0	117.8	116.8

Table 12: maximum flow stress seen for each 45XD material condition with 50% compression at 1100 °C, 0.001 s⁻¹.

The steep initial stress-strain curve shows several processes taking place, both elastic and plastic, including work hardening, this is due to rapid dislocation pile-up in the γ laths, only slowed by a critical strain (ϵ_c) being reached, high stored energy in the fragmented lamellar material initiating rapid DRX, hence the relatively sharp peaks seen here and in working other TiAl alloys [155]. This dislocation pile-up perhaps being slowed by the elemental homogeneity of the γ laths, the effect of heat treatment in the single α phase, seen in 1300FC. The lower σ_{pfs} of the HIP material may be explained by its lower lamellar content, lamellar grain mobility being higher with higher γ_{eq} content, allowing rotation of lamellar grains rather than globularisation/DRX [156].

4.2.2.3 Post compression microstructures

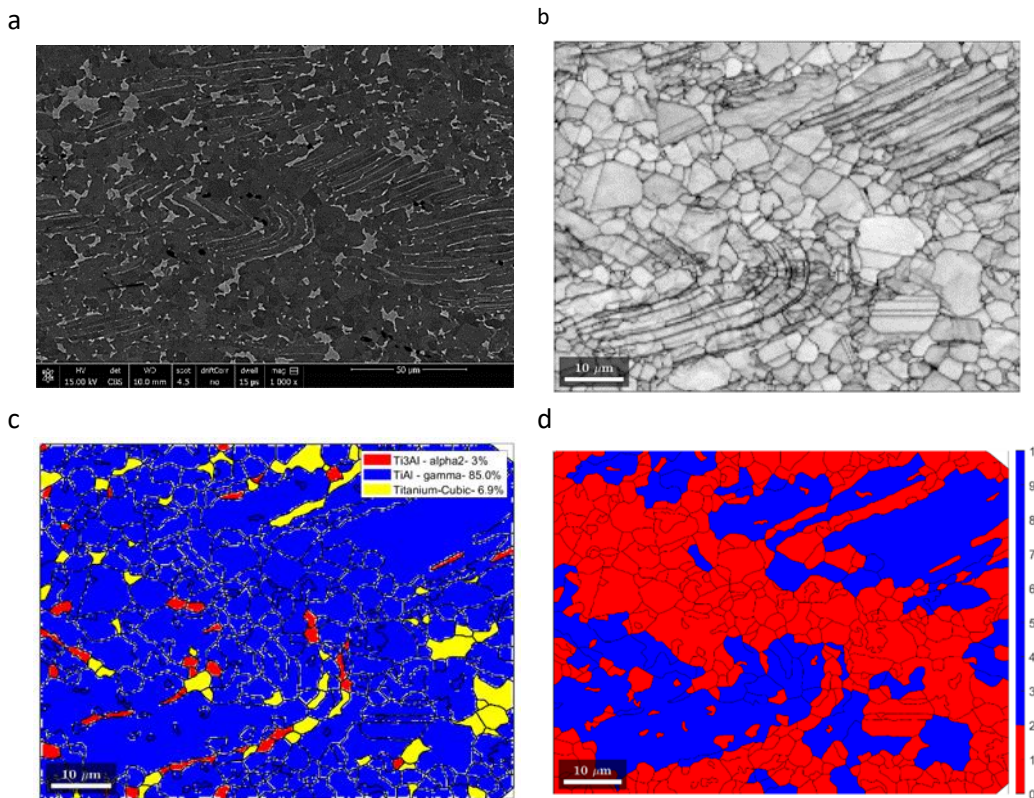


Figure 38: (a), SEM micrograph in BSE mode at 1000x magnification of 45XD alloy in the 1300 FC condition after compression, where black areas correspond to γ phase, white β_0 and grey α_2 , respectively. EBSD used to give maps of, (b) band contrast, (c) phase map; blue is γ , red is α_2 , yellow is β_0 , (d) X-DRX; red is the recrystallised fraction, blue is deformed, at 1600x magnification.

45XD material condition +50% compression	% Lam	Reduction in lamellar content (%)	Average lamellar grain size (μm , from 0° and 90°)	SD of average lamellar grain size (μm)	% α_2	% β_0	% γ	DRX fraction (%)	Grain area fraction $\leq 50\mu\text{m}^2$ (%)
HIP	23	30	34	18	3	5	84	53	57
1270FC	24	46	31	20	2	4	94	69	77
1300FC	13	69	22	13	3	7	85	59	70

Table 13: breakdown of lamellar grain content and size, as well as lamellar and equiaxed morphology and respective phase composition for 45XD in different conditions after 50% compression at 1100°C , $0,001\text{ s}^{-1}$ from BSE image processing and EBSD mapping.

The compression of the 1300FC sample, heat treated in the single α phase, returns the lowest lamellar content at 13 % this consists of the smallest average grain size of $22\ \mu\text{m}$ and maximum grain size of $55\ \mu\text{m}$. The HIP and 1270FC results are presented in greater detail in 4.1.2.3, these are presented here in

Table 13 for comparison. The increased lamellar-lamellar grain boundary density seen with 1300FC appears to be the catalyst for the high extent of globularisation seen, with a 69 % reduction in lamellar content.

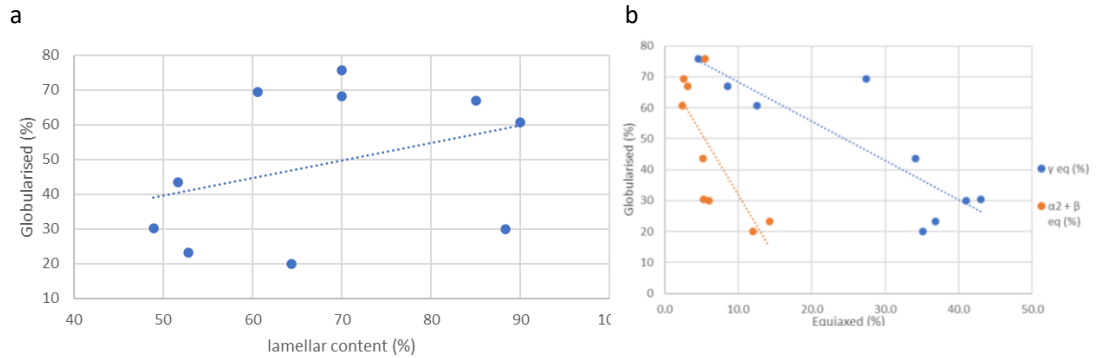


Figure 39: Trend line between pre-compression (a) lamellar content and (b) equiaxed content and globularised fraction returned from primary compression at $0.001 s^{-1}$. This scatter plot includes material described in chapter 4.1 and 4.2

This is due to grain boundaries acting as nucleation sites for globular morphologies, lamellar-lamellar grain boundaries being preferred for globularisation [24], [58]. This relationship is shown in Figure 39a-b. However, the fraction dynamically recrystallised (X-DRX) is a little more nuanced, smaller average lamellar grain sizes does result in higher X-DRX, but the trend is not so strong, Figure 40 [47].

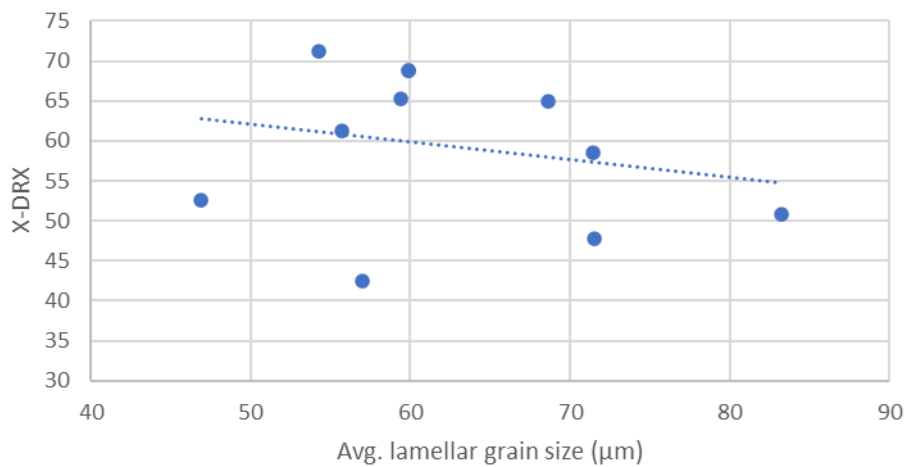


Figure 40: relationship between pre-compression average lamellar grain size and DRX fraction returned from primary compression at $0.001 s^{-1}$. This scatter plot includes material described in chapter 4.1 and 4.2.

This seems to have impacted the X-DRX of 1300FC compressed material, with lower X-DRX at 59 % compared to 1270FC at 69 %, a similar effect is seen in the grain area fraction $\leq 50 \mu m^2$ values. The phase fraction appears constant, the highest β_0 value is noted for 1300FC and will be considered in any further processing steps.

4.2.3 Summary

The aim of this study was to identify a temperature for 45XD that produces a homogeneous fully lamellar microstructure, with elemental homogeneity, to optimise the microstructure from compression. The temperature range 1270-1350 °C, as well as furnace cooling, looked promising for forming this microstructure based on the findings of 4.1. This study took a closer look at the pre-compression microstructure through EBSD mapping and subsequent compression behaviour and microstructure, with a focus on the extent of globularisation and X-DRX. The aim of this is to provide a microstructure capable of improving the forging outcome of the material for subsequent processing i.e., hot rolling or closed die isothermal forging. This target microstructure is identified from the literature as being refined, elementally homogeneous and free of lamellar morphologies. The following are conclusions regarding the primary processing stage of the alloy.

- Hot isostatic pressing to remove porosity and consolidate the ingot does not return a material microstructure best placed to remove the lamellar content upon compression or phase fraction for further processing. A homogenisation heat treatment within the α transus improves globularisation extent and X-DRX.
- The literature, as well as the analysis and regression plots in this study show that the ideal pre-compression microstructure for efficient globularisation is fully lamellar. To increase X-DRX refining the initial lamellar grain size looks beneficial, also improving elemental homogeneity. This makes a heat treatment low within the single α transus, 1300 °C, most promising, followed by furnace cooling.

4.3 The effect of multi-stage forge processing on the forging outcome of consolidated 45XD

4.3.1 Introduction

As has been discussed already, simple HIP and uniaxial compression is not the most efficient process for removing the anisotropy causing lamellar grains and casting segregation which hinders secondary processing [86]. Combined with the other sections of this work on controlling and optimising the starting microstructure, an investigation into the effect of multiple stages in the forging sequence is of interest.

The study started with HIP only material, as described in Table 14. From the results of sections 4.1 and 4.2 it could be anticipated that forging outcomes of all sequences described here would be improved by homogenising this material first, however there were restrictions on the availability of processing equipment and supply of material.

By maintaining constant compression conditions (1100 °C, 0.001 s⁻¹) the resulting compression behaviour and post-compression microstructures are assessed in terms of lamellar grain sizes and content as well as phase, X-DRX and grains ≤ 50 μm² fraction, with a view to easing secondary processing of 45XD.

The reasoning behind these alternative sequences is based on promoting material with low lamellar and high recrystallised content, this is key to producing workable material for secondary processing, as discussed already in previous sections [53].

Sample ID	HIP 50%	25% + RT + 25%	25% + Dwell + 25%	50% + 1200AC	25% +1200AC + 25%
Anticipated active restoration mechanisms	DRX	DRX	DRX + MDRX or SRX	DRX + SRX	DRX + SRX
Expected effect on X-DRX and %_{Lam}	For comparison	-ve	+ve	+ve	+ve

Table 14: Sample identification and expectations for each test, all material is in the HIP (hot isostatic pressed) condition first, then described sequentially for simplicity. Any compression is described per blow (%), any heat treatment is described by temperature (°C)- cooling rate. Any dwell is for 30 minutes at compression temperature. RT is where the sample is returned to room temperature.

Samples 25% + RT + 25% and 25% + Dwell + 25%, Table 14, are of interest as dynamic recrystallisation (DRX) is not the only restoration process active in the forging of titanium aluminide alloys and

contributing to the recrystallised fraction [80],[77],[157]. With a dwell at compression temperature, also referred to as inter-pass annealing, other restoration processes can be active. Firstly, with compression, the dynamic recrystallisation process active here can be described as discontinuous DRX, for γ with its low stacking fault energy DRX is discontinuous (dDRX, simply referred to as DRX), that is, there are clear nucleation and growth stages involved in the formation of the new grains [77]. Once compression and so DRX has stopped, refinement of TiAl material could continue via meta-dynamic recrystallisation (MDRX) [77]. MDRX refers to the growth of DRX grains into the surrounding material, causing an accumulation in dislocation density and then recrystallisation.

One theory, referred to here as (i), applied to austenitic steel and magnesium alloys, is that MDRX is dependent on $X\text{-DRX} > 50\%$, linked to a transition strain (ϵ^*), such that below this ϵ^* , static recrystallisation (SRX) takes place with the accompanying fine globular microstructure symptomatic of SRX [78],[79]. This ϵ^* can take place between peak and steady state strain, after which MDRX behaviour is independent of additional strain.

However, other authors have stated that MDRX will take place if DRX has been initiated at all [80]. This will be subsequently referred to as theory (ii).

Restoration by MDRX has been claimed to apply to titanium aluminide alloys with lamellar morphologies and identified as a possible method of reducing microstructural heterogeneity from compression by further globularisation of lamellar colonies and equalising globular grain dimensions. If MDRX takes place with 25% compression it should be identified by the 25% + dwell + 25% sample compared to the compression behaviour and microstructure of 25% + RT + 25%. The analysis of lamellar dimensions, X-DRX and recrystallised grain size distribution plots, which reveal the grain area fraction $\leq 50 \mu\text{m}^2$ values should identify any noticeable microstructural effects of MDRX [80], [157]. From the X-DRX values of previous sections 4.1 and 4.2, X-DRX has not reached 50%. So according to theory (i) the ϵ^* has not been reached, MDRX will not take place with either 25% + Dwell + 25% or 25% + RT + 25%, as rapid air cooling to room temperature will prevent MDRX [158],[159]. If this is the case, according to (i), with 25% + Dwell + 25% it could be expected that SRX will take place during the dwell, so a softening effect on the recompression behaviour compared to 25% + RT + 25% could be identified [77]. This is also industrially relevant as forging processes can have interruptions at temperature, with multi-axial forging for example [80]. If theory (ii) is followed then no softening will be seen with the second blow of 25% + Dwell + 25% compared to 25% + RT + 25%, as MDRX will lead to a hardening effect caused by subtle grain growth of the globular microstructures, showing an increase in flow behaviour [157].

As discussed above, compression increases the dislocation density up to a critical strain where DRX is initiated, flow softening commences. If compression does not reach a steady state, such as at 25% compression, the deformed material, with its high dislocation density, stimulates SRX upon heat treatment (HT), this has been found to largely eliminate remnant lamellar microstructures, yielding

more homogeneous compression microstructures upon recompression or secondary processing [53],[149].

The HT applied in 4.1, within the $\gamma+\alpha+\beta$ phase for 2 hours followed by air cooling (1200AC) appeared to be useful for promoting the microstructural and elemental conditions that increase globularisation. Here it is applied as both an intermediate and post compression heat treatment as 25%+1200AC+25% and 50%+1200AC.

If the HT removes lamellar microstructures this would appear as lower lamellar content in post compression analysis as compared to HIP. It could also be expected that σ_{pfs} be lower in the sample 25%+1200AC+25% compared to 25%+RT+25%.

These investigations are necessary as another pathway to providing isotropic-behaving material ready for secondary processing i.e., isothermal closed die forging or hot rolling.

4.3.2 Results and discussion

4.3.2.1 Pre-compression microstructure

Microstructural analysis was conducted on 45XD on the consolidated condition to analyse the influence of initial microstructure on compression behaviour and resulting microstructural evolution.

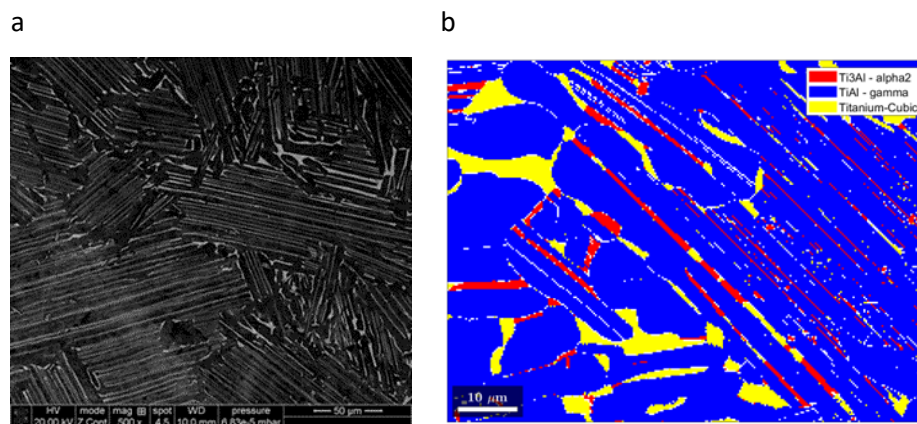


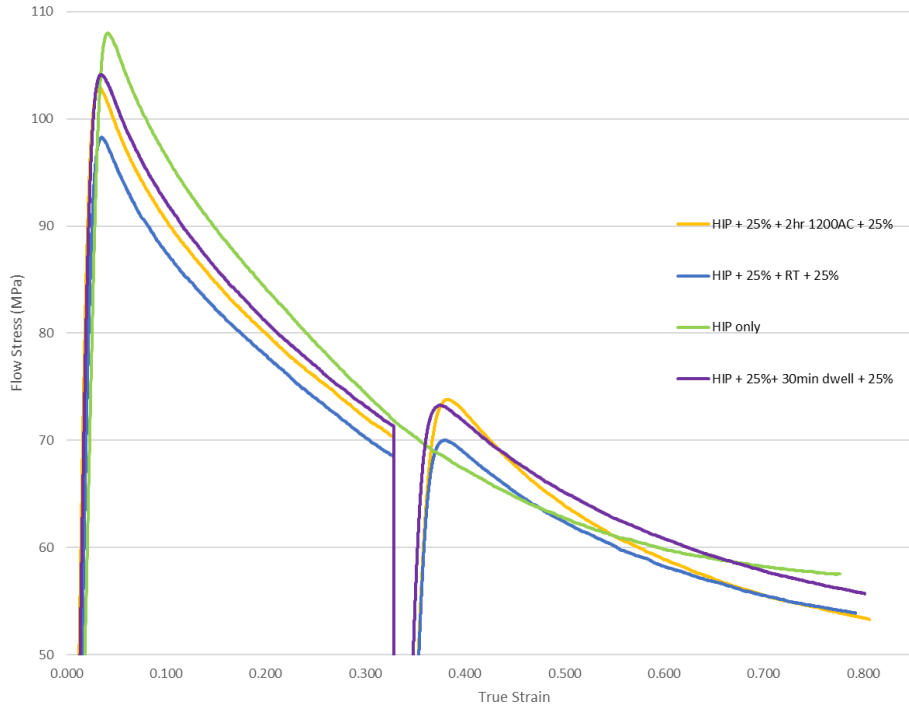
Figure 41: BSE images of 45XD alloy in the (a), HIP condition, at 1000x magnification, where black areas correspond to γ phase, white β_0 and grey α_2 . (b) Phase map from EBSD at 1600x, blue areas correspond to γ phase, yellow to β_0 and red to α_2

Figure 41a BSE imaging shows 45XD alloy in the HIP condition, with a nearly fully lamellar microstructure consisting of all three phases contributing to the 53 % lamellar content, with average lamellar grain size of 47 μm and equiaxed grains present at lamellae grain boundaries. A more detailed description of the HIP microstructure and its formation is part of 4.1.2.1, Table 11.

4.3.2.2 Compression behaviour

Table 14 details the conditions of the multi-forge sequences, with uniaxial compression flow stress and true strain calculated for each of these sequences, to 25 % and 50 % compression respectively. No machining of compression samples takes place in between blows, so the changes in aspect ratio of

a



b

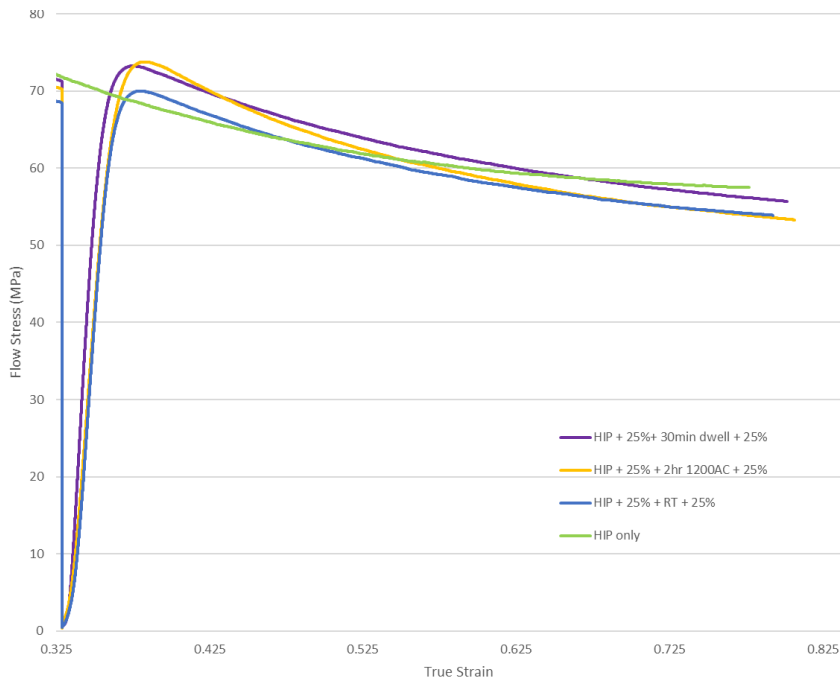


Figure 42: Flow stress-true strain chart of 45XD following different intermediate steps showing the both blows (a), first blow is of material in a similar HIP condition, and (b) a zoomed in view of the second blow of hot compression at 1100°C, 0.001s⁻¹, 25 - 50%.

height to width of 1.5 (20 mm: Ø13 mm), important for comparing compression behaviour, makes the two compression stages difficult to compare against each other. However, comparisons can be made between the rec-compression stages.

Each curve follows a similar pattern, for both compression stages, with max flow stress reached, visualised in Figure 42 for each 45XD condition, followed by flow softening.

All the first blows are of the same HIP material and there is a spread of 10.5 MPa or 8.5 %, present in the σ_{pfs} seen with compression, suggesting there could be microstructural differences in the starting material or that more and/or larger lamellar grains have a “hard” orientation to the compression axis, as in lamellar laths parallel to compression [84]. The orientation of the lamellar grains present in 45XD is random so with more compression samples the variation in σ_{pfs} is likely to follow a normal distribution [40]. This random element should be considered in these studies but is not likely to cause large differences in σ_{pfs} . However, directional solidification and controlling the orientation of lamellar grains has been of interest to other authors for final material properties and processing [86], [160], [161].

With the second blow, after intermediate dwell or heat treatment, we begin to see differences in the work hardening and σ_{pfs} . The sample 25% + Dwell + 25% having the steepest work hardening rate followed by the almost identical curves of 25% + RT + 25% and 25% + 1200-AC + 25%. This hardening effect could be due to MDRX taking place within the dwell time at compression temperature [80]. Described as theory (ii) in 4.3.1, no softening of 25% + Dwell + 25% with recompression is seen compared to 25% + RT + 25%, as MDRX can lead to globular grain growth, this creating a hardening effect leading to an increase in flow stress [157]. It should also be noted that the compression temperature at 1100 °C is within the “spike” in β_0 according to Figure 29b. This temperature region, dominated by $\gamma+\beta_0$, sees a rise in β_0 fraction, this has appeared detrimental in terms of workability in our earlier studies on material heat treated at 1130 °C in 4.1.2.2. [69],[70]. So, it could also be proposed that a rise in β_0 is the cause for this hardening effect and the higher σ_{pfs} seen with 25% + Dwell + 25%, compared to 25% + RT + 25%, similar to that seen in 4.1.2.2.

The lower σ_{pfs} anticipated with the sample 25%+1200AC+25% compared to 25%+RT+25% did not materialise, there is no sign in the compression behaviour of the intermediate HT initiating SRX and eliminating remnant lamellar microstructures at this stage [53],[149]. This could be due to changes in morphology dimensions, as seen in 1200AC from 4.1.2.1, this saw swelling of any lath or globular structures present, including $\alpha_2+\beta_0$, this would make any initiation of DRX sluggish, giving a higher σ_{pfs} .

The increase in σ_{pfs} of both 25% + Dwell + 25% and 25% + 1200AC + 25% in comparison to 25%+RT+25% could also be attributed to the random orientation of lamellar grains discussed above. As the first blow sees 25%+RT+25% noticeably lower than the flow curves of 25% + Dwell + 25% and 25% + 1200AC + 25%, Figure 42a, it could be proposed that 25 % compression is not enough to reorientate or globularise large lamellar grains present with laths parallel to compression. This then influences the σ_{pfs} second compression in a similar fashion to the first blow.

4.3.2.3 Post compression microstructures

Microstructural analysis was conducted only on 50 % compressed samples to analyse the influence of different forging sequences on the evolution of the microstructure after compression. With compression microstructure imaging at Figure 43a-f.

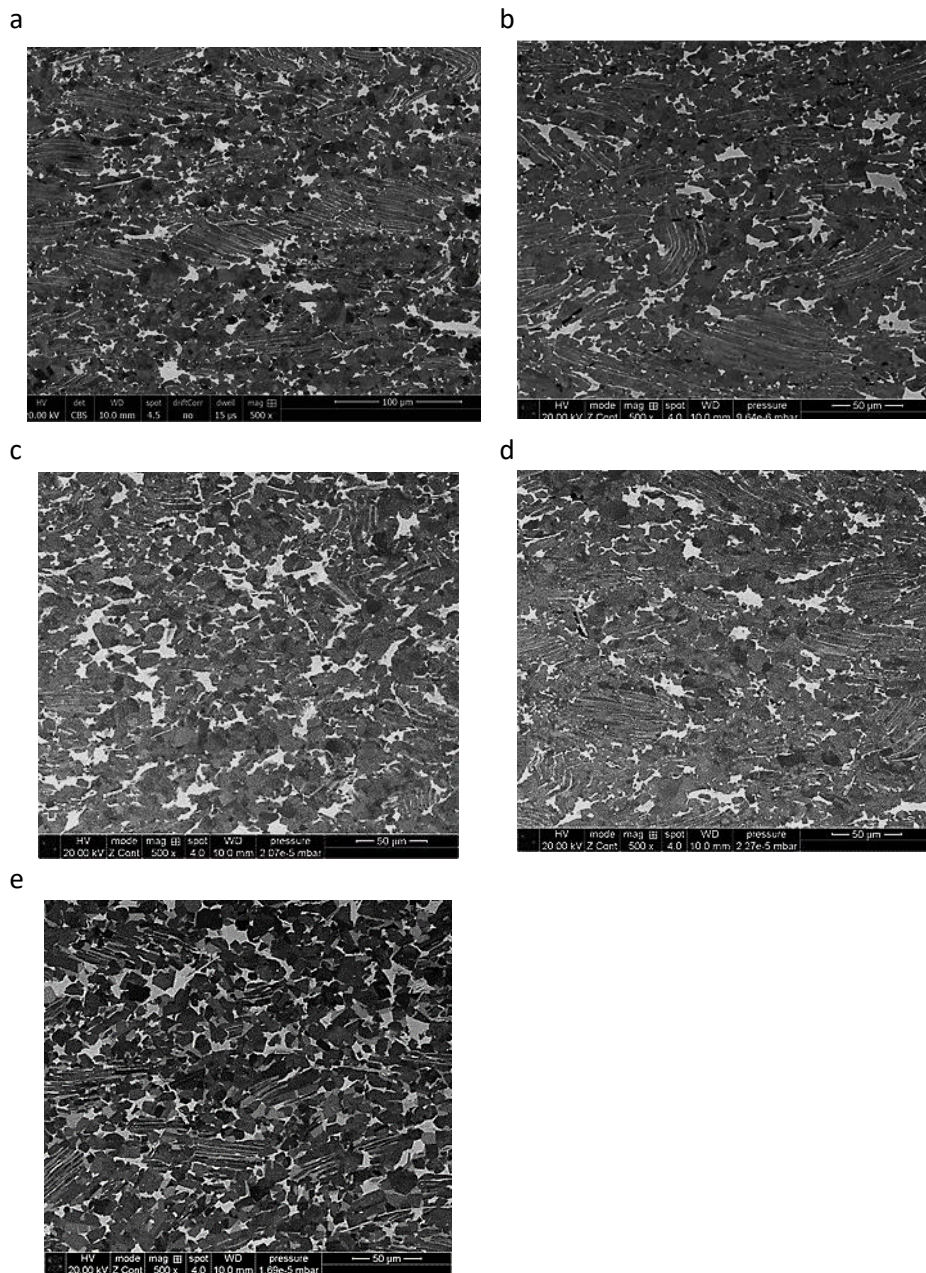


Figure 43: SEM micrograph (BSE) of 45XD alloy after 50% compression in (a), the HIP+50% condition, (b), 25% + RT + 25%, (c), 25% + 1200-AC+25%, (d), 25% + Dwell + 25%, (e), 50% + 1200-AC., all at 500X magnification, where black areas correspond to γ phase, white β_0 and grey α_2 , respectively.

Compression leaves HIP material in a refined condition, in terms of lamellar grain size and content, as discussed in greater detail in 4.1.2.3 and 4.2.2.3. Table 15 shows microstructural details of the

compressed material. Comparing compressed HIP material with deformed 25% + RT + 25% and 25% + Dwell + 25%, differences in the compressed microstructure are minimal and not beneficial.

An interrupted compression, 25% + RT + 25%, sees a higher remnant lamellar content compared to HIP, with higher average lamellar grain sizes. X-DRX, Grain area fraction $\leq 50 \mu\text{m}^2$ and β_0 are all negatively affected by interrupting compression compared to the full 50 % compression of HIP. This is likely to be due to 25 % compression not imparting the strain necessary to initiate globularisation, as well as cooling back to room temperature and re-heating to compression temperature (1100 °C) possibly reducing any accumulated strain in the microstructure, slowing any globularisation possible in secondary compression.

The 25% + Dwell + 25% sees a minor increase in the lamellar content globularised, of 2 % compared to HIP, but all other details analysed are negatively affected. As discussed in 4.3.2.2, 25% + Dwell + 25% had the steepest work hardening rate. This hardening effect could be due to MDRX taking place. The lowest grain area fraction $\leq 50 \mu\text{m}^2$ could also be a symptom of MDRX, with globular grain growth within the dwell time at the compression temperature, perhaps explaining the distribution of grains in Figure 45h [69],[70],[157]. The 25% + Dwell + 25% sample suggests MDRX could be taking place in this alloy at these conditions but does not bring with it noticeable globularisation of lamellar morphologies or improved homogeneity across the workpiece, these being aspects of MDRX claimed by *Tang et al.* [157].

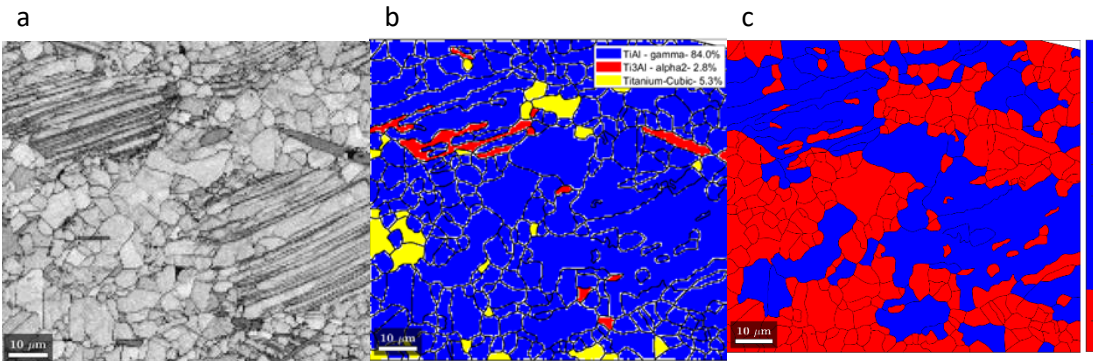
The intermediate HT of 25%+1200AC+25% showed very little difference from 25% + RT + 25% in terms of compression behaviour, but with the second blow of compression the microstructure shows the lowest lamellar content and average lamellar grain sizes in this study. The extent of globularisation is high, however the X-DRX is the lowest seen in the study with a small fraction of grains $\leq 50 \mu\text{m}^2$ in area. This suggests that the globularisation of the lamellar content was largely completed by the end of the intermediate heat treatment, with SRX likely to have taken place [53],[149],[144]. However, the time spent at temperature during the HT would also grow globular material as shown in 1200AC material in 4.1.2.1., perhaps explaining the low fraction of grains under $\leq 50 \mu\text{m}^2$. The further 25 % compression possibly deforming the recrystallised content already present rather than further recrystallising material.

With 50% compression, before additional heat treatment, the material is anticipated to be in a similar condition to HIP 50% in Figure 43a. Heat treatment within the $\gamma+\alpha+\beta_0$ region (1200 °C followed by air cooling) for two hours leads to a further reduction in lamellar content but not grain size, the sample also exhibits the highest X-DRX and relatively low fraction of grains $\leq 50 \mu\text{m}^2$ in area, as seen in Figure 43e and Table 15. The further reduction in lamellar content caused by the heat treatment could be due to a combination of factors. With heat treatment, SRX is promoted by the high dislocation density in deformed material imparted by compression [144]. Uniformity of the macro and microstructures was also identified by *Seetharaman, Semiatin and Jain* with post compression heat treatment at this

temperature with a similar alloy, removing dead metal zones and reducing lamellar content compared to their equivalent of HIP 50 % [149]. This temperature, within a triple phase region, is also promoting competitive growth between all three phases, as seen in the formation of the duplex-like microstructure in Figure 43e [53]. The competitive phase growth is not equal as the α_2 phase has been promoted, with globular α_2 present, as shown in Figure 44n. The impact of this on further workability is likely to be similar to the second blow of the 25%+1200AC+25% sample, where no softening behaviour is seen with the removal of lamellar microstructures for higher α_2 content. However, from secondary compression of 25%+1200AC+25% material it is seen that the phase fraction returns to what can be considered normal for this alloy. This could be considered for improving future forging outcomes.

45XD material condition	%Lam	Reduction in lamellar content (%)	Average lamellar grain size (μm , from 0° and 90°)	SD of average lamellar grain size (μm)	% α_2	% β_0	% γ	DRX fraction (%)	Grain area fraction $\leq 50\mu\text{m}^2$ (%)
HIP+50%	23	30	34	18	3	5	84	53	57
25%+RT+25%	25	28	36	19	4	8	73	51	51
25%+dwell+25%	21	32	42	28	3	13	69	46	35
25%+1200AC+25%	8	45	31	23	3	8	47	40	49
50% + 1200AC	17	36	38	28	27	5	56	74	52

Table 15: Breakdown of microstructural analysis; lamellar grain size and content, phase and DRX fraction including grain area fraction $\leq 50\mu\text{m}^2$, for 45XD following different processing sequences through hot compression at 1100°C, 0.001s⁻¹, to 50%.



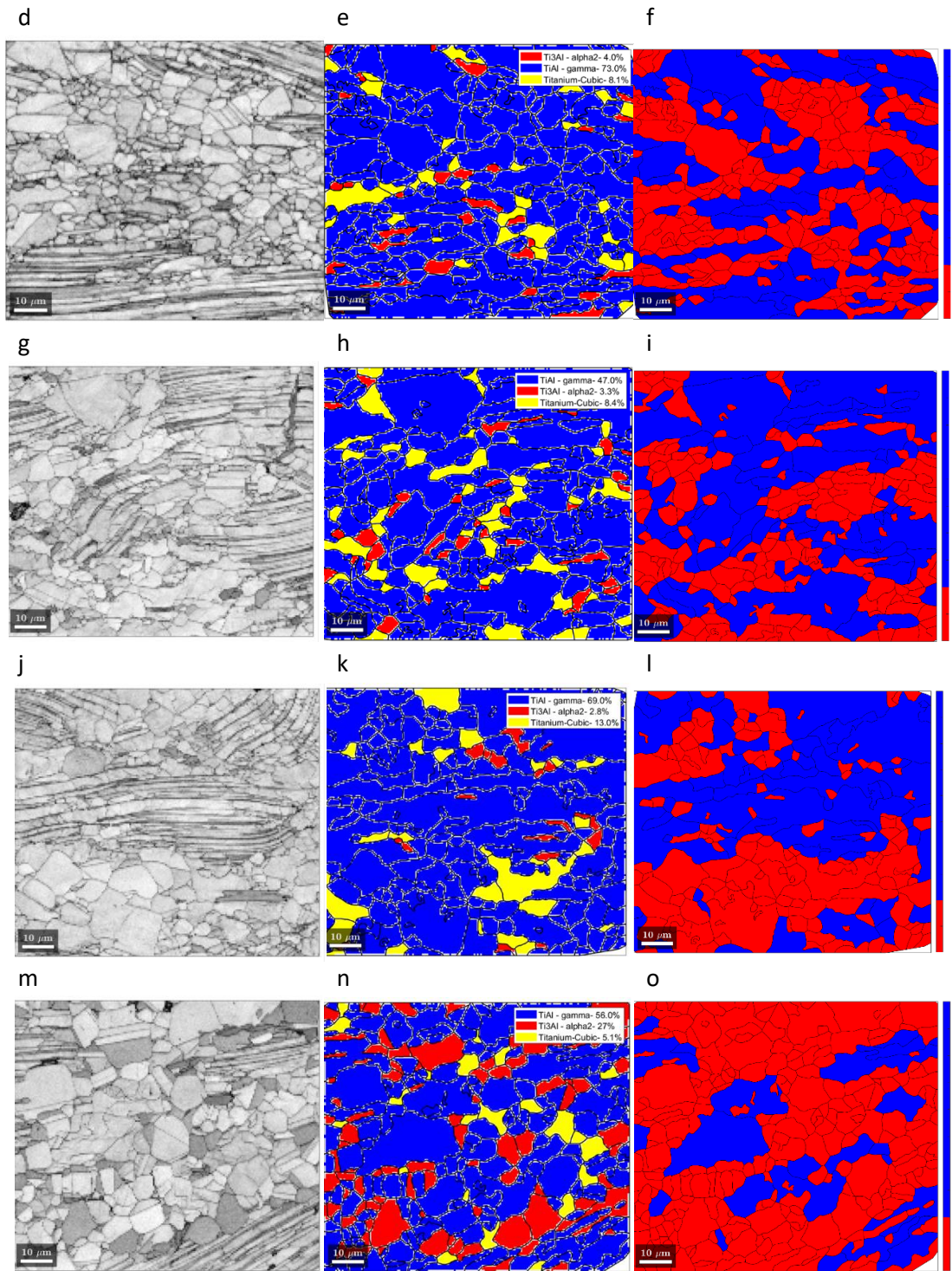
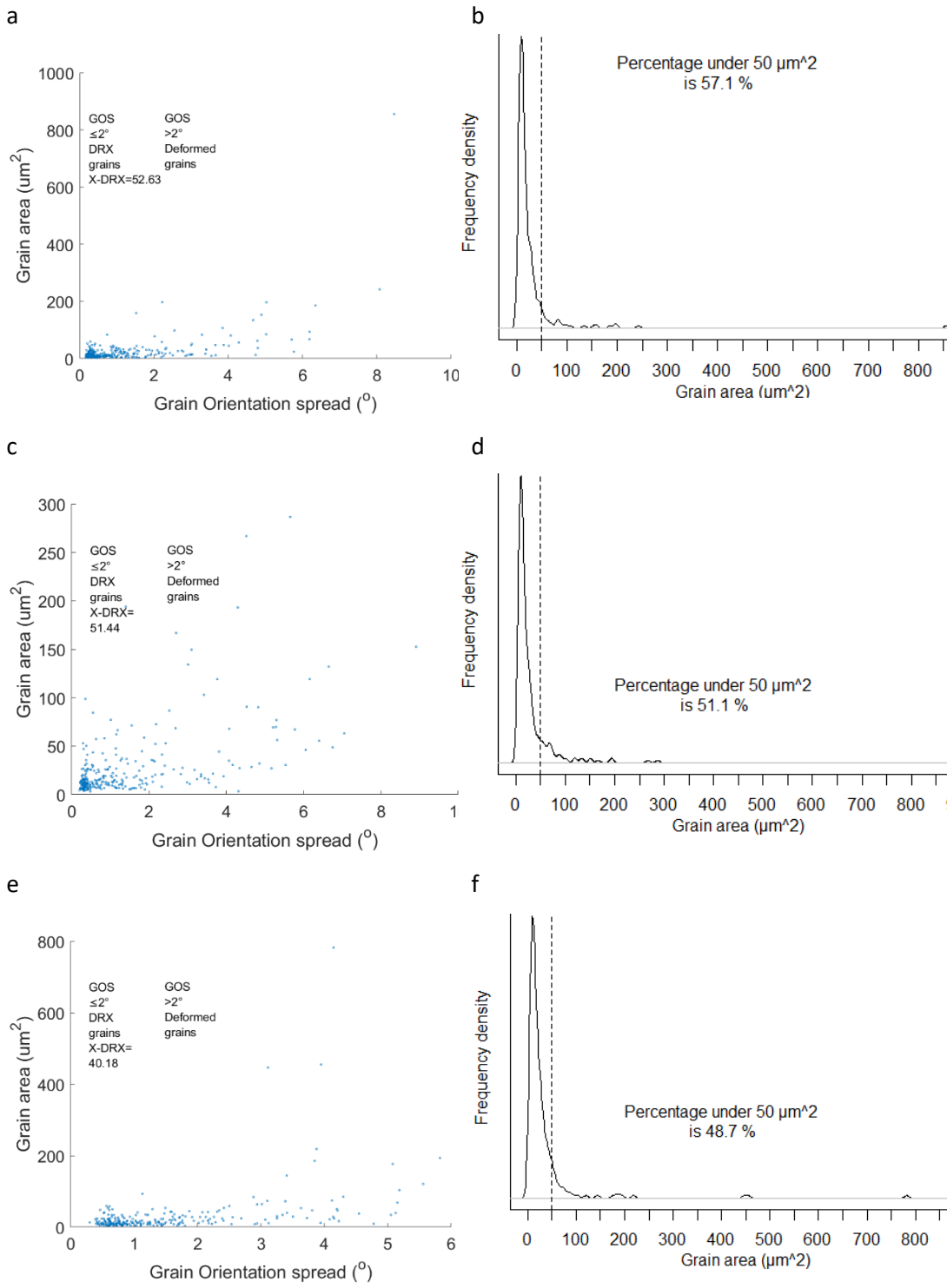


Figure 44: EBSD used to give maps of, (left) band contrast, (middle) phase map; blue is γ , red is α_2 , yellow is β_0 , (Right) X-DRX; red is the recrystallised fraction, blue is deformed, of 45XD alloy after 50% compression in (a-c), the HIP condition plus intermediate stages (d-f), 25% + RT + 25%, (g-i), 25% + 1200-AC+25%, (j-l), 25% + Dwell + 25%, post compression stages are (m-o), 50% + 1200-AC, all at 1600X magnification.



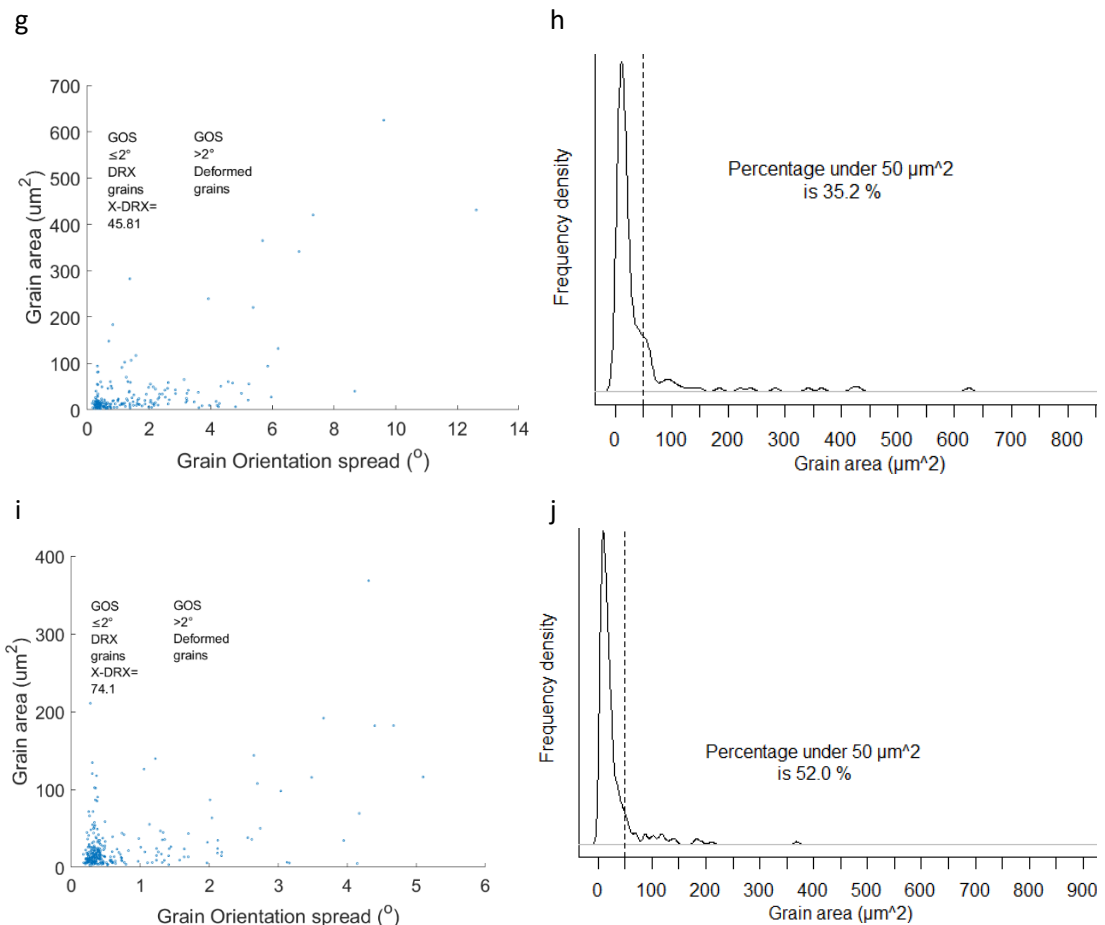


Figure 45: Plots calculating the DRX fraction from the GOS approach on the left, grain area frequency density on the right, for each material condition after 50% primary compression at 1100 °C and 0.001 s⁻¹ (a-b), the HIP condition plus intermediate stages (c-d), 25% + RT + 25%, (e-f), 25% + 1200-AC+25%, (g-h), 25% + Dwell + 25%, post compression stages are (i-j), 50% + 1200-AC,

4.3.3 Summary

The aim of this study was to assess the effect of alternative forging sequences on the microstructural outcome after 50 % compression. These strategies were identified as beneficial for workability by other researchers for different TiAl alloys and their mechanisms have been considered here for how they influence subsequent compression behaviour and microstructure, with a focus on the extent of globularisation and formation of recrystallised material. Here, with pre-compression microstructure being constant (the HIP microstructure), the following conclusions were obtained regarding the effectiveness of alternative forging sequences.

- Interrupting compression at 25 %, with a return to room temperature or dwell at compression temperature, sees no benefit in terms of microstructural outcome, compared to the compression of HIP microstructure.
- Dwell at this compression temperature, 1100 °C, within the $\gamma+\beta_0$, exhibited by the 25%+ Dwell + 25% sample, leads to growth of the β_0 fraction post compression, with a

suspected negative impact on the second blow and future forging outcomes. This hardening effect could be due to MDRX taking place, the lowest grain area fraction $\leq 50 \mu\text{m}^2$ (35 %) could also be a symptom of MDRX with globular grain growth within the dwell time at compression temperature.

- The heat treatment of 1200AC, whether as an intermediate or post compression heat treatment leads to high extents of globularisation. Restoration via SRX is likely to have taken place as part of the further globularisation of lamellar content compared to compression of HIP microstructures, however, it does promote a high fraction of globular α_2 phase. This could be considered for improving forging outcomes in future studies.
- This heat treatment, 1200AC, will be applied as part of following work as an intermediate heat treatment after 50 % primary compression, to replicate initial ingot breakdown. As also identified by other researchers, it can homogenise the microstructure, not elementally, but in terms of lamellar content.

4.4 Integrating HIP and homogenisation heat treatment and its effect on the primary processing of 45XD

4.4.1 Introduction

To ensure successful and homogeneous compression *Semiatin et al.* found that heating is required at temperatures in the α phase before wrought processing [149],[162]. This homogenisation process has been identified and described in this work on 45XD, with homogenisation at 1300 °C for two hours followed by furnace cooling, as described in 4.2. *Semiatin et al.* identified that if ingot material had not been held above the α transus, aluminium segregation from casting caused issues such as variable transus temperatures, flow stresses and phase distribution upon compression. This improvement in forging outcomes was also noted in this work, in sections 4.1 and 4.2, anticipated to improve outcomes in secondary processing.

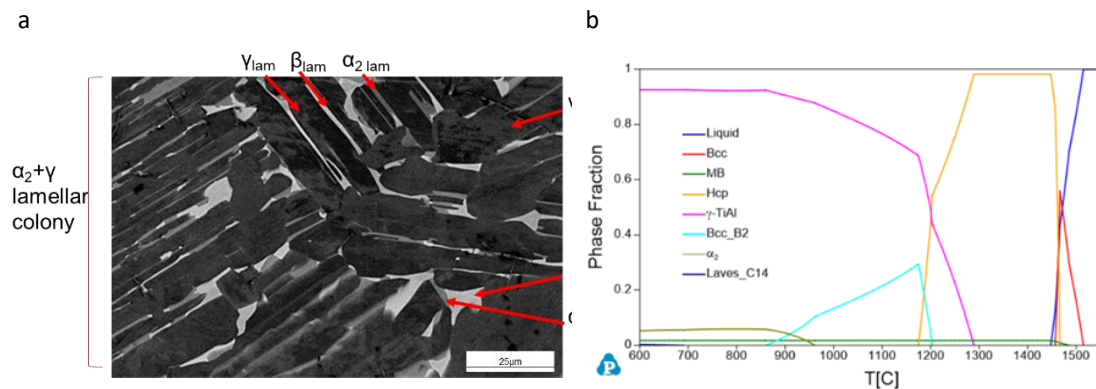


Figure 46: (a) SEM image of HIP microstructure to identify phases and lamellar (lam) and equiaxed (eq) microstructures, as indicated dark grey/black areas correspond to γ phase, white β_0 and light grey α_2 , (b) phase fraction diagram determined from CALPHAD, with main crystal structures (including metallic boride (MB))

However, as well as lamellar microstructures of γ and α_2 phases, 45XD also contains the ordered β_0 phase, without the benefit to workability of solidifying through the single, disordered β phase region, as discussed in 2.4.2.1 [17],[18],[68],[70],[71]. The β_0 phase fraction is accentuated by segregation and grows with time spent within the $\gamma + \beta_0$ phase region as seen in this work, in 4.1 and 4.3 [67]. This has limited deformability due to the loss of symmetry seen in the unit cell upon ordering and β_0 concentrates dislocation pile-ups, as identified by *Molénat et al.*, its presence contributing little to workability [72]. Workable β only comes with the disordering reaction of $\beta_0 \rightarrow \beta$ at high temperatures, as was shown on TiAl alloy Ti-43.5Al-4Nb-1Mo-0.1B in TNM by *Schwaighofer et al.* [15]. The disordering reaction temperature for 45XD is not known.

As found by *Zhang, Dehm and Clemens*, removing the β_0 phase isn't without its difficulties [32]. Investigations on the impact of HIP and homogenisation (HMG) on the content and distribution of this

phase found both pressure and α phase HMG essential to removing β_0 but this came with excessive grain growth in their low boride alloy.

As found in section 4.2, the traditional HIP and α transus homogenisation (THH) stages are deemed necessary to improve microstructural outcomes from primary compression. However, HMG is often avoided due to the costs linked with vacuum heat treatment and/or excessive grain growth. Integrating HIP and HMG (subsequently referred to as IHH), using HIP equipment for both stages, will be investigated in this study. The process has been investigated as an alternative approach before on 4822 alloy but looked at final material properties [52]. *Chen et al.* concluded that the isostatic pressure had no bearing on morphology evolution, but suppressed microcrack formation, which proved beneficial in their study on mechanical performance.

To assess the effect on forging outcomes of HIP, THH and IHH processes for 45XD, microstructural analysis as in 4.1, 4.2 and 4.3 will be conducted together with strain rate sensitivity (m) indexing (0-1, 0 being least sensitive, 1 being most). This is used in both primary compression in this section (4.4) and secondary compression in section 4.5 [54]. The m value incorporates both macroscopic and microscopic plastic deformation behaviour, (e.g., lamellar grain globularisation, or orientation and dislocation concepts, respectively) for that microstructure. The m values for TiAl in compression were assessed and studies compiled by *Bibhanshu et al.* [55]. Materials with low m value microstructures during processing can suffer localised deformation. This inhomogeneous deformation behaviour can lead to failure, so processing conditions where m is high are preferred, this being supported by process mapping [56]. *Gupta et al.* identify 0.2-0.3 as satisfactory for typical forming operations, *Fuchs* suggested m of ≥ 0.3 ; both found increasing temperature usually resulted in an increase of m in their compression trials mapping the alloy Ti-48Al-2Cr-2Nb (4822) [53],[57]. However, *Gupta et al.* begin by identifying that intrinsic workability still depends on the initial microstructure and its response to temperature, strain rate and strain. Forging trials on boride free Ti-45Al alloy by *Seetharaman and Semiatin*, found that m and the fraction of globularised lamellar material increased with a lower initial lamellar grain size, as did *Fuchs* with 4822 alloy, so this relationship between m in compression and microstructure is well established [58]. For this reason, temperature remains constant in the present work, as the effect of IHH on microstructure and subsequent m is investigated. This study will use m of ≥ 0.3 as a marker to track changes in forging outcomes, combined with microstructural analysis.

To summarise, simple HIP has been shown not to produce microstructures best placed for optimising the microstructural outcome of uniaxial compression, with globularisation resistant lamellar grains, and casting segregation hindering secondary processing [86]. The work reported here evaluates the effect of pre-compression consolidation and homogenisation on 45XD as well as the option of integrating the process, and its effect on forging outcomes.

4.4.2 Results and discussion

First, the distinction between the aims of primary and secondary processing should be made. Successful primary compression, seen as equivalent to ingot breakdown, or forming a pre-form in this study, looks to return a crack-free, isotropic behaving microstructure ready for secondary compression, investigated in 4.5. To achieve this, pre-compression processing should aim to deliver a material that responds efficiently to deformation. An efficient response to primary compression includes returning a material with high lamellar globularisation, and so high X-DRX. Secondary compression in this study is seen as equivalent to high deformation processes such as hot rolling or isothermal closed-die forging, ideally these techniques require a microstructure capable of strain rate sensitivity of ≥ 0.3 [53],[54],[55],[56],[57],[58].

4.4.2.1 Pre-compression microstructure

Microstructural analysis was conducted on 45XD in the three starting material conditions already discussed; HIP, THH and IHH, to assess the influence of initial microstructure on compression behaviour and the resulting microstructural evolution post primary (1') compression.

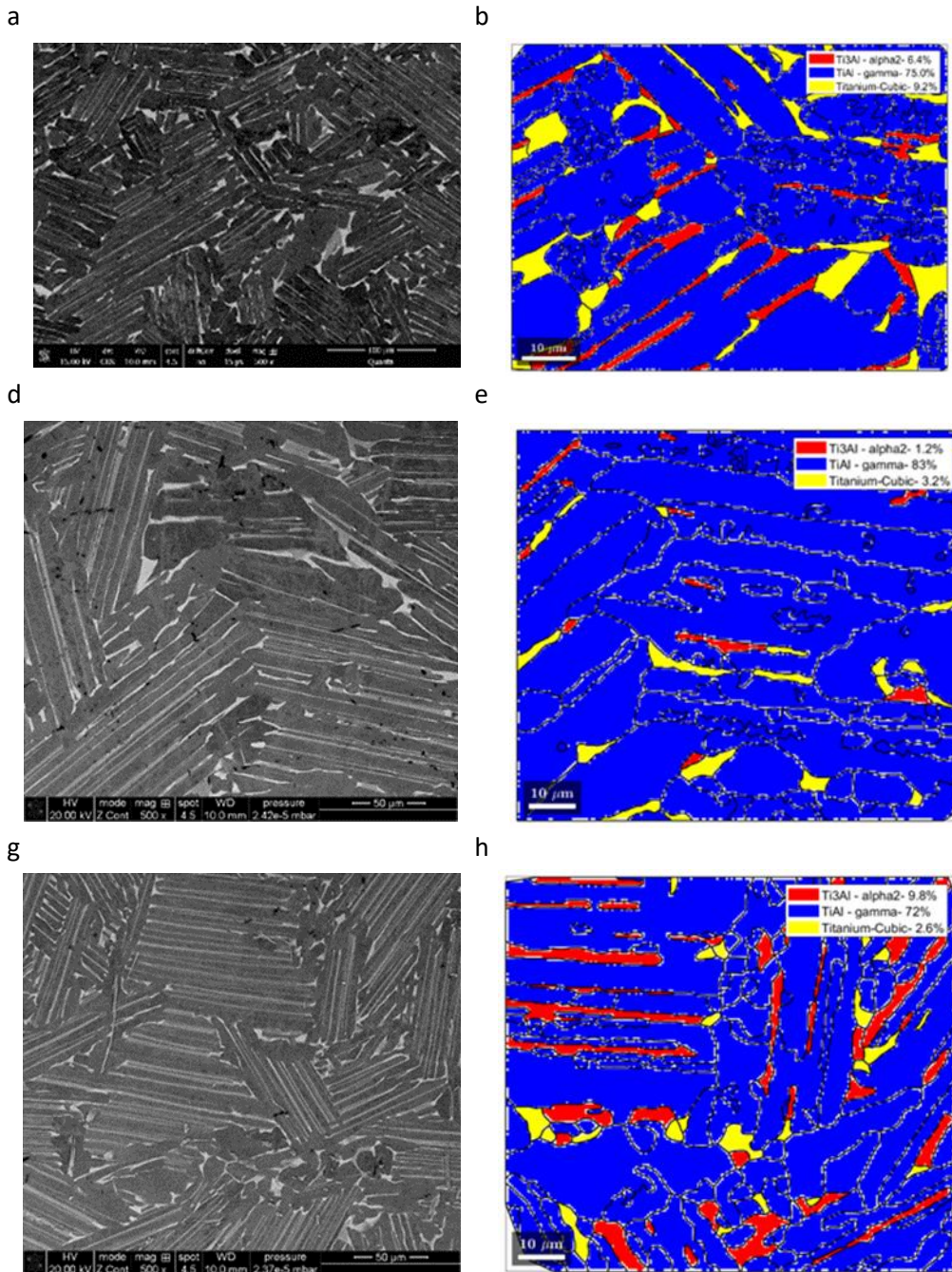


Figure 47: BSE images of 45XD alloy in the HIP (a), THH (d), IHH (g) condition at 500x magnification. Black areas correspond to γ phase, white β_0 and grey α_2 . EBSD phase fraction maps HIP (b), THH (d), IHH (h) condition at 1600x magnification

Figure 47 BSE imaging compares the three pre-compression microstructures. Pre-compression, each of HIP, THH and IHH returns a nearly fully lamellar microstructure, with β_0 phase present as grains at lamellae grain boundaries as well as within the lamellar laths, most prominently in the HIP material at 3 % β_{eq} and 6 % β_{lam} respectively. The HIP material shows a nearly fully lamellar microstructure. The β_0 content is higher than both THH and IHH, as shown in Table 16, which quantifies these microstructural characteristics from BSE and EBSD image processing. A decrease in the brittle β_0 lamellar and equiaxed

morphologies is seen from the THH and IHH processes, with β stabilising elements being distributed homogeneously [32].

45XD material condition	%Lam	Average lamellar grain size (μm)	SD of average lamellar grain size (μm)	% α_2 lam	% β_0 lam	% γ lam	% α_2 eq	% β_0 eq	% γ eq
HIP	69	111	23	4	6	52	2	3	23
THH	75	113	22	1	2	62	0	1	21
IHH	90	98	16	9	2	65	1.	0	7.0

Table 16: Phase morphology fraction and lamellar content in the three material conditions before compression

Lamellar content for HIP and THH is similar at 69 and 75 % respectively, IHH resulting in higher lamellar content of 90 %. The lamellar grain size details for each condition show large grains present, $>100 \mu\text{m}$, the largest on average being for THH, Table 16. The traditional HIP and homogenisation (THH) route included a separate homogenisation heat treatment in the single α phase and is well established to return a fully lamellar and elementally homogeneous microstructure, as found in section 4.2 [149],[162].

The associated $\gamma_{\text{lam}}\%$ rises with lamellar content in IHH, this being 65 % versus 52 % in HIP and $\gamma_{\text{eq}}\%$ decreases from 23 % compared to 7 %.

This larger fraction in γ_{eq} morphologies seen in THH compared to IHH is likely to be due to the slow furnace cooling and time spent within γ dominant phase regions, Figure 46b, from both HIP and HMG processes. This has led to lamellar grain growth, coarsening of γ laths and separate globular γ grain growth i.e., it has reduced structural homogeneity, as quantified in Table 16. This lamellar grain growth is not thought to be due to the high temperature HMG, due to the boride content of this alloy restricting grain growth [39],[129].

The integrated HIP and homogenisation (IHH) route see both HIP and HMG times and temperatures being comparable with THH, the differences being that each stage is under pressure within the HIP vessel and the THH treatment has an intervening cooling stage. Zhang, Dehm and Clemens' investigations into the HIP and HMG of peritectic alloys found both pressure and α phase HMG essential to removing β_0 , but it came with excessive grain growth [32]. As mentioned, the boride content of the alloy used in this study is higher, at 0.84 at%, than the alloy used in their study, 0.27 at%, and so restrains the grain growth associated with α phase heat treatment more effectively. The combination of temperature and pressure also generates a reduction in the overall β_0 morphology content versus both HIP and THH routes. Zhang, Dehm and Clemens commented that pressure probably reduces the activation barrier to decompose β_0 .

In addition to this, the single cooling stage, as opposed to two cooling stages of THH, would explain the lack of γ morphology coarsening seen in IHH. The IHH process returned a more fully lamellar

microstructure in comparison to HIP and THH routes, with a higher overall lamellar content and a tighter spread of standard deviation of lamellar grain size values, giving a more homogeneous lamellar microstructure in comparison, Figure 47 and Table 16.

4.4.2.2 Primary compression behaviour

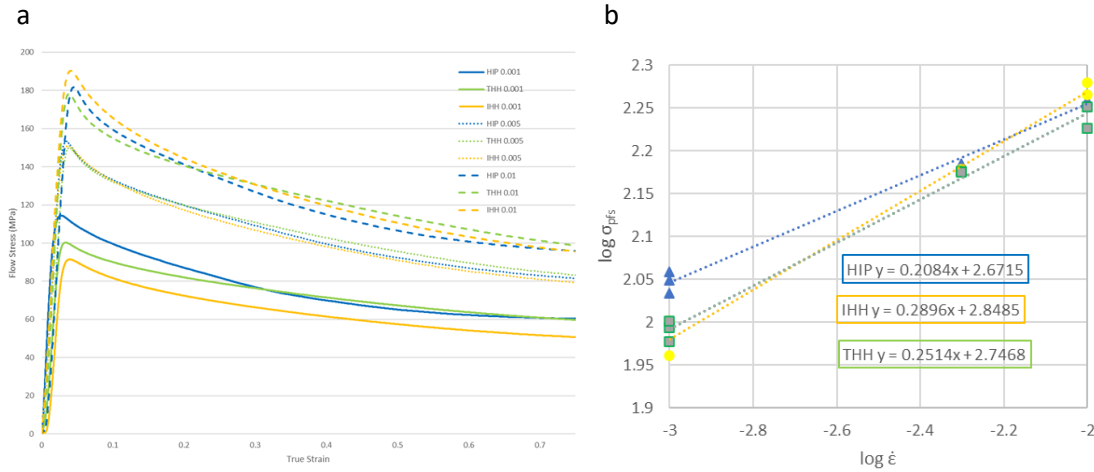


Figure 48: Primary stress-strain curves (a), compression at 1100 °C to 50 % at 0.001, 0.005 and 0.01 s⁻¹ over 760, 152, and 76 seconds respectively. Calculation of strain rate sensitivity (*m*) for each material for primary compression (b).

Each stress-strain curve follows a similar pattern, work hardening contributing to the initial steep rise in flow stress as strain builds, followed by peak flow stress (σ_{pfs}), σ_{pfs} rising with increasing strain rate ($\dot{\epsilon}$), due to a build-up of dislocation density, this being followed by flow softening; shown in Figure 48a. Flow softening at all $\dot{\epsilon}$ suggests that there was time for microstructural breakdown to occur as strain increased. This behaviour is a characteristic of lamellar grain fragmentation in this material, this can be followed by DRX of this material with an increase in strain [114],[150]. From Figure 48, the unitless strain rate sensitivity (*m*) can be estimated; seen in Table 17.

45XD Material condition	HIP			THH			IHH		
	0.001	0.005	0.01	0.001	0.005	0.01	0.001	0.005	0.01
1' σ_{pfs} (MPa)	111.5	153.3	181.7	97.9	149.9	173.3	95.9	150.3	187.4
1' <i>m</i> (σ_{pfs})	0.21			0.25			0.29		

Table 17: Peak flow stress and strain rate sensitivity, measured at peak flow stress, strain of 0.04, for each material condition over primary compression

IHH shows the highest *m* value at 0.29, HIP showing the lowest from σ_{pfs} in 1' compression at 0.21. From the compression stress-strain curves for 1' compression, once a strain (ϵ) of 0.7 is reached IHH consistently shows the lowest value of σ , for each strain rate and material. This being the case even with the highest flow stress at 0.01 s⁻¹ with the largest degree of flow softening seen. All material

conditions show stable material flow under these 1' compression conditions. *Semiatin, Seetharaman and Weiss* reviewed earlier work looking at the relationship between starting microstructure, flow softening rate, recrystallisation and flow localisation [119]. The authors identified that the lamellar characteristics, especially differences in lamellar grain size, were the most significant factor influencing the compression behaviour. *Fuchs* also identifying strain rate sensitivities dependence on initial lamellar grain size as well as temperature [53]. This has also been noted in this work, with IHH material, presenting the lowest lamellar grain size values and m at this temperature. The microstructure of IHH generating lower peak flow stresses from the slower strain rates; 0.001 and 0.005 s⁻¹. However, at the faster strain rate of 0.01 s⁻¹ the flow stress for IHH is the highest out of the three material conditions: smaller grain structures giving higher flow stresses. This is probably due to resistance to globularisation at these speeds, globularisation kinetics being enhanced by slower strain rates. This aligns with the observations of *Semiatin, Seetharaman and Ghosh* [118].

The relatively high flow stress from the HIP material at slow strain rates could be due to the same mechanism seen in creep and fatigue trials. Segregation leads to heavy alloying elements and interstitials being preferentially gettered into the α_2 , from γ , leaving the α_2 less prone to globularisation when under strain, due to slower dissolution of α_2 into γ and solid solution hardening effects [74],[104],[152].

For each strain rate, IHH leads to the lowest flow stress after a strain of 0.7. Once this stress-strain profile levels out further globularisation is sluggish due to lamellar grains orientating perpendicular to compression axis. The level of this flow stress is related to the extent of recrystallised material and its size [58].

Incorporating the contributing factors discussed above, Figure 48b shows the 1' strain rate sensitivity (m) of IHH to be greatest, HIP to be lowest at σ_{pfs} , this trend does not change with strain [118].

4.4.2.3 Primary compression microstructure

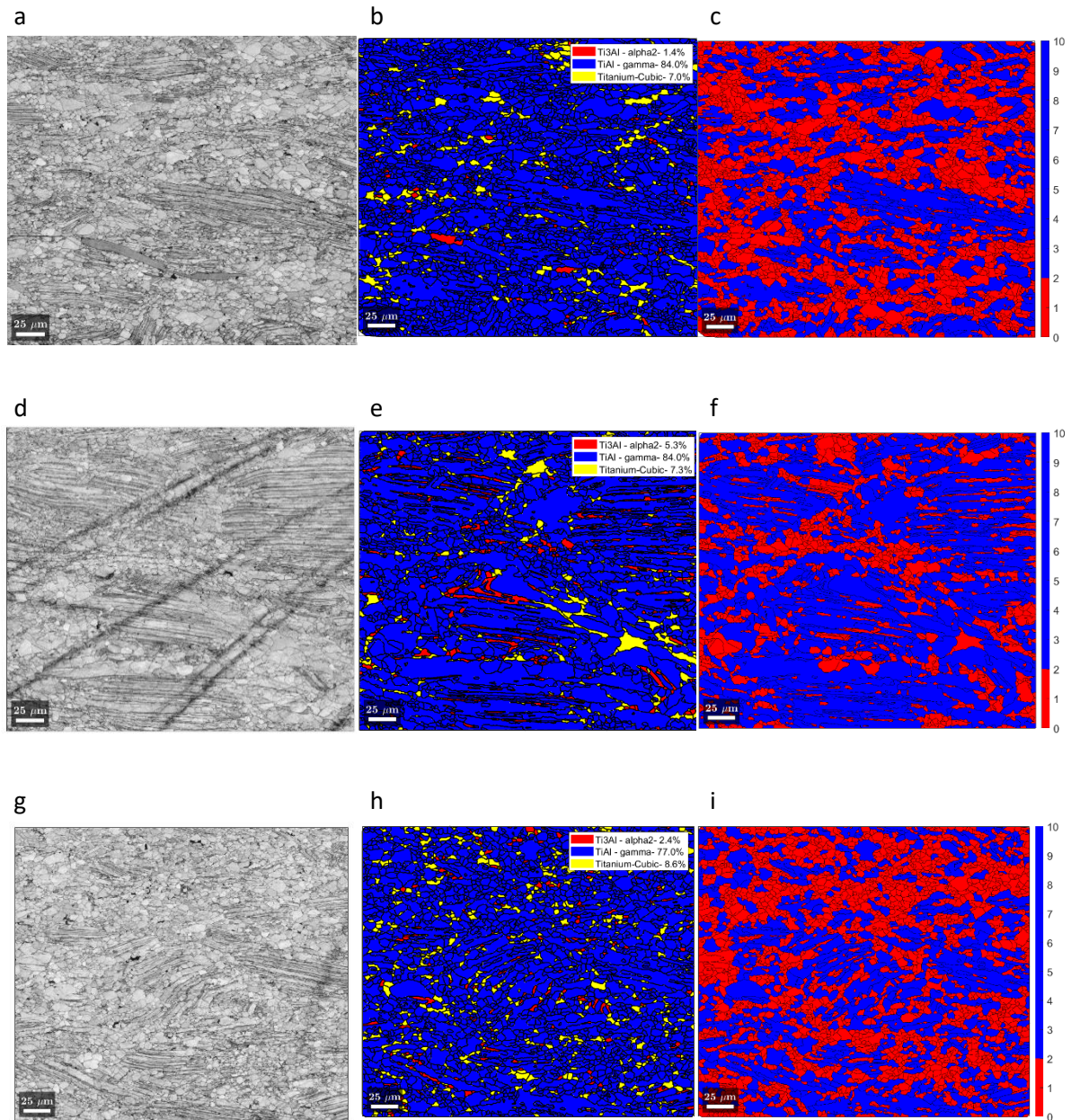


Figure 49: EBSD used to give maps of, (left) band contrast, (middle) phase map; blue is γ , red is α_2 , yellow is β_0 , (right) X-DRX; red is the recrystallised fraction, blue is deformed, of 45XD alloy after 50% compression in the HIP (a, b, c), THH (d, e, f), IHH (g, h, i) condition at 500x magnification.

As the mapping in Figure 49 illustrates, all processing conditions returned successfully compressed material, though each starting state returned material still containing some lamellar morphologies after 1' compression. The orientation of any remnant lamellar grains again appeared to align

perpendicular to compression, as found by other researchers and earlier in this study [163],[144],[164].

The content and details of these morphologies are shown in Table 18. A reduction in lamellar content and the respective morphologies from pre-compression for all material conditions is seen. With strain rate of 0.001 s^{-1} THH material shows the highest lamellar content at 46 %, as well as the lowest X-DRX and “grains $\leq 50 \mu\text{m}^2$ ” fraction at 29.6 % and 42 % respectively, versus 53 % and 57 % for HIP.

With IHH and its initial refined lamellar grain structure exhibited the lowest lamellar content values due to an increase in grain boundary density, these grain boundaries being the nucleation sites for globularisation to occur. The fraction and size of the remnant lamellar is an important factor in further workability as identified by *Zhang et al.* [144]. The fraction of grains under $50 \mu\text{m}^2$, identified by grain distribution plots in Figure 50b, d, f, look to quantify non-lamellar material. The relationship between this and X-DRX on m for secondary compression of this material will be discussed in 4.5.

From a phase fraction point of view, an increase in overall β_0 content for IHH and THH conditions with compression was seen. The β_{eq} content increased from below 1 %, to 4 % and 7 % for THH and IHH respectively. The HIP phase fraction stayed relatively constant with a small increase from 2.9 % to 5.2 % for 0.001 s^{-1} . The increase in β_0 content post 1' compression is of concern for further processing of IHH and THH material. As seen in 1' compression of the HIP material and in section 4.1, a high β_0 content appears to contribute to high flow stress. This increase in β_0 post compression, could be due

45XD material condition (s^{-1})	%Lam	Reduction in lamellar content (%)	Average lamellar grain size (μm , from 0° and 90°)	SD of average lamellar grain size (μm)	% α_2	% β_0	% γ	X-DRX (%)	Grain area fraction $\leq 50 \mu\text{m}^2$ (%)
HIP 0.001	26	43	60	63	1	7	84	53	57
HIP 0.005	43	26	59	41	3	4	84	35	66
HIP 0.01	47	22	70	40	1	4	85	39	60
THH 0.001	46	29	80	56	5	7	84	30	42
THH 0.005	51	24	68	32	7	6	83	36	47
THH 0.01	51	24	80	41	3	11	66	33	48
IHH 0.001	19	71	36	29	2	9	77	67	68
IHH 0.005	39	51	52	33	2	9	79	38	56
IHH 0.01	56	34.	61	34	3	4	82	32	62

Table 18: Phase, morphology, DRX and grain area $<50 \mu\text{m}^2$ fraction for each material after 50% primary compression at $1100 \text{ }^\circ\text{C}$ and 0.001 , 0.005 and 0.01 s^{-1} calculated from a combination of BSE and EBSD analysis.

to the compression temperature lying within a spike in β_0 fraction, as shown in CALPHAD, Figure 46b. This increase in β_0 being more noticeable due to the homogenised microstructure of the initial THH and IHH material; segregation promoting β_0 formation in HIP material. An intermediate heat treatment

could prove useful to alter this phase fraction to a more beneficial ratio, as identified by other researchers and in 4.3 [144],[53],[149].

Concerning the material deformed with strain rate of 0.001 s^{-1} , the most effective strain rate for dynamic globularisation, IHH returned the highest X-DRX and grains $\leq 50 \mu\text{m}^2$ fraction at 67 % and 68 %, with the lowest overall lamellar content at 19 %, these lamellar structures being of the smallest grain area.

For IHH at faster strain rates of 0.005 and 0.01 s^{-1} , the trend is for X-DRX to reduce to 38 % and 32 %, respectively and the remnant lamellar fraction to increase to 39 % and 56 %. The efficiency of globularisation/ recrystallisation is reduced with an increase in strain rate for IHH, in common with Ti based lamellar materials, as discussed above [118]. The case for the HIP and THH material is not as clear.

In the case of HIP material, the lack of a clear trend in lamellar grain size with increasing strain rate could be due to a combination of factors. To start, the elemental segregation present from the lack of homogenisation means recrystallisation is sluggish as discussed in 4.2. There is also a high γ_{eq} and low lamellar content in the starting HIP microstructure. This favours micro-buckling/rotation rather than globularisation, explaining the higher lamellar grain size values and the higher lamellar fraction, and so in turn lower extent of X-DRX material seen from 50 % compression of HIP when compared to IHH, in Table 18 [58],[87]. Globularisation favours lamellar to lamellar grain boundaries, as seen in the IHH microstructure pre-compression, this was also noted by *Seetharaman and Semiatin* [58].

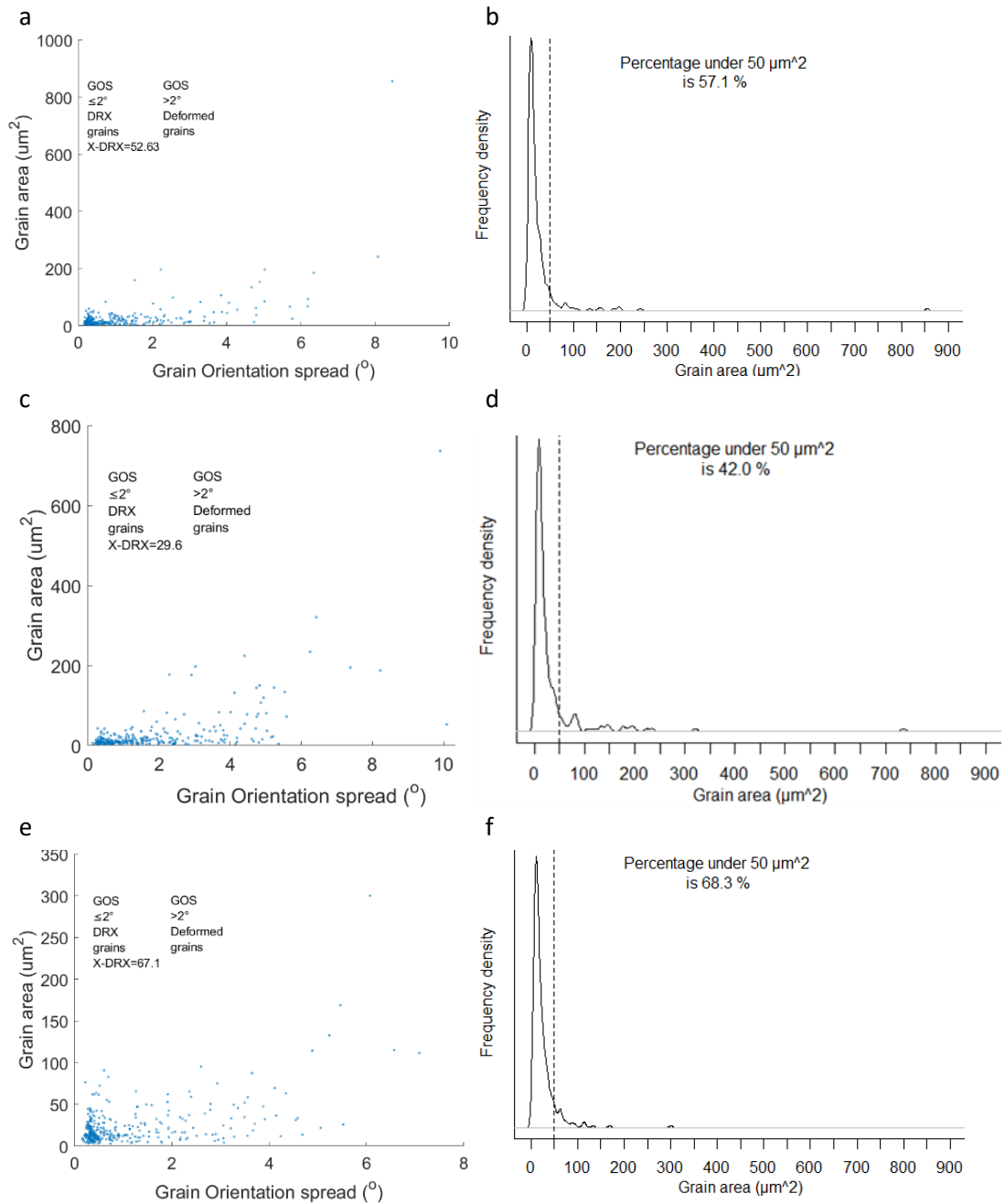


Figure 50: Plots calculating the DRX fraction from the GOS approach on the left, grain area frequency density on the right, for each material condition after 50 % primary compression at 1100 °C and 0.001 s⁻¹, (a, b) HIP, (c, d) THH, (e, f) IHH

However, even with a HMG stage, the THH material returned a lower X-DRX value than either HIP or IHH at 0.001 s⁻¹, and similar values for lamellar fraction and X-DRX for 0.005 and 0.01 s⁻¹. This perhaps is a consequence of having the highest starting lamellar grain size, due to the slow cooling of both HIP and HMG stages. The relationship between average lamellar grain size values and X-DRX is

shown in Figure 40, of section 4.2, and is in agreement with the work of others identifying the effect of large lamellar colonies on globularisation kinetics [118].

4.4.2.4 Overview of the IHH process in respect to potential forging outcomes

This work examines the suitability of the IHH process to facilitate thermo-mechanical processing under the conditions described for this boride containing alloy. Reducing the time spent at temperatures high in the $\gamma+\alpha$ lamellar phase field, due to the single cooling stage of the IHH process, reduces the window for lamellar grain and lath coarsening, both of which are detrimental to globularisation in primary compression. Studies by *Seo et al.* on 45XD have shown the coarsening effect of slow furnace cooling rates on both grain size and lath thickness of fully lamellar microstructures [165]. However, fine lamellar morphologies also should be avoided as these are also detrimental to globularisation kinetics [144],[163]. A compromise is required.

With regard to the pressure used in IHH, *Chen et al.* concluded that the isostatic pressure had no bearing on morphology evolution but suppressed microcrack formation [52]. *Zhang, Dehm and Clemens*, suggested that pressure reduced the activation barrier required for decomposition of the β_0 in subsequent HMG [32]. *Zhang, Dehm and Clemens* used a similar triple phase containing alloy to that used in the present study. The work presented here shows no identifiable effect of pressure on the morphology present but there is evidence for the overall reduction of the β_0 phase fraction with HIP and HMG compared to HIP alone, as displayed in Table 16. Based on the results from the research reported here, it can also be proposed that cooling between HIP and HMG is unnecessary and can be detrimental in terms of further workability. IHH could thus be an alternative approach for pre-compression processing for boride containing, fully lamellar, peritectic TiAl alloys like 45XD.

4.4.3 Summary

The aim of this study was to investigate if the consolidation and homogenisation stages could be integrated into one process, how it influences the pre-compression 45XD microstructure and its subsequent compression behaviour and microstructure. This research differs from existing work with its emphasis on understanding the effect of integrating consolidation and homogenisation on forging outcomes, as well as how these processes influence the pre-and post-compression microstructure individually.

The following conclusions for this alloy can be drawn:

- Pressure and temperature during the integrated HIP and homogenisation (IHH) process reduced β_0 content compared to that seen in the traditional HIP and homogenisation (THH) process and HIP alone.
- Integrating the two processes also removed slow cooling from homogenisation, returning a more fully lamellar microstructure, so improving the microstructure for globularisation. This resulted in a higher dynamic recrystallised fraction and strain rate sensitivity (m) from primary processing. However, none of the starting materials reached m of ≥ 0.3 , secondary compression would be necessary.
- All three starting material conditions that were primary compressed at 0.001 s^{-1} , the most effective strain rate in terms of globularisation and formation of high X-DRX, will go through machining and further secondary compression. This will simulate high deformation secondary processing techniques, so investigating if secondary compression will reach the strain rate sensitivity required by these secondary processing techniques at these compression conditions, as well as investigate the effect of an intermediate heat treatment identified in 4.3.

4.5 Effect of prior processing on secondary compression behaviour of 45XD

4.5.1 Introduction

The aim of this section is to bring together the learning from the other sections on 45XD and assess the secondary compression behaviour and corresponding strain rate sensitivity of this industry accepted, peritectic solidifying titanium aluminide ingot alloy; 45XD.

Secondary processing covers high deformation processes such as hot rolling or isothermal closed-die forging, it is well established that these techniques require an isotropic behaving microstructure, ideally capable of strain rate sensitivity of ≥ 0.3 . It has been identified from the literature that this is achieved by a material containing low lamellar content of small grain size and high dynamic recrystallised content (X-DRX), it can be anticipated from the literature and analysis of the microstructures of 4.4 that this is a reasonable goal [53],[54],[55],[56],[57],[58].

Sample ID	HIP	THH	IHH	THH+HT
Prior processing	HIP, (1270 °C, 175 MPa, 4 hours) + 50% compression at 1100 °C, 0.001 s ⁻¹	Traditional HIP + HMG (1300 °C, 2 hours) + 50% compression at 1100 °C, 0.001 s ⁻¹	Integrated HIP + HMG (1270 °C, 175 MPa, 4 hours, temperature increased to 1300 °C, 2 hours) + 50% compression at 1100 °C, 0.001 s ⁻¹	Traditional HIP + HMG + 50% compression at 1100 °C, 0.001 s ⁻¹ + HT (1200 °C, 2hours, air cooling)

Table 19: Sample identification, all material is in the HIP (hot isostatic pressed) condition first, then further processing is described sequentially for simplicity. All material is primary compressed to 50%, any heat treatment is described by temperature (°C), time, cooling rate.

4.5.2 Results and discussion

4.5.2.1 Intermediate microstructure prior to secondary compression

The images and analysis of the primary compressed microstructure is part of 4.4.2.3. Results of primary compressed material at 0.001 s^{-1} , together with the impact of heat treatment for 2 hours, $1200 \text{ }^\circ\text{C}$, followed by air cooling shown in Figure 51 and combined in Table 20.

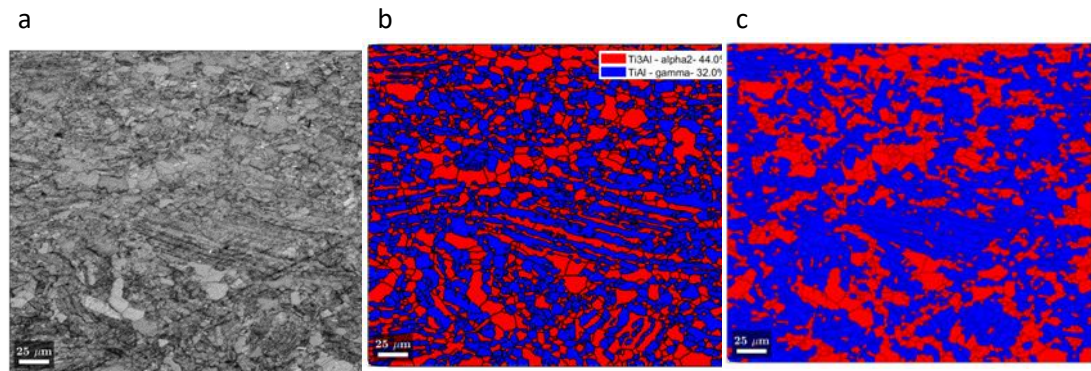


Figure 51: Band contrast (BC) (a), phase fraction (b) and X-DRX map (c) of 45XD alloy in the THH+HT condition. This is THH material, primary compressed at $1100 \text{ }^\circ\text{C}$, 0.001 s^{-1} followed by intermediate heat treatment of $1200 \text{ }^\circ\text{C}$, 2 hours followed by air-cooling.

45XD material condition	%Lam	Reduction in lamellar content (%)	Average lamellar grain size (μm , from 0° and 90°)	SD of average lamellar grain size (μm)	% α_2	% β_0	% γ	X-DRX (%)	Grain area fraction $\leq 50 \mu\text{m}^2$ (%)
HIP	26	43	60	63	1	7	84	53	57
THH	46	29	80	56	5	7	84	30	42
IHH	19	71	36	36	2	9	77	67	68
THH +HT	22	53	77	71	44	0	32	39	44

Table 20: Phase, morphology, DRX and grain area $< 50 \mu\text{m}^2$ fraction for each material after 50% primary compression at $1100 \text{ }^\circ\text{C}$ and 0.001 s^{-1} calculated from a combination of BSE and EBSD analysis.

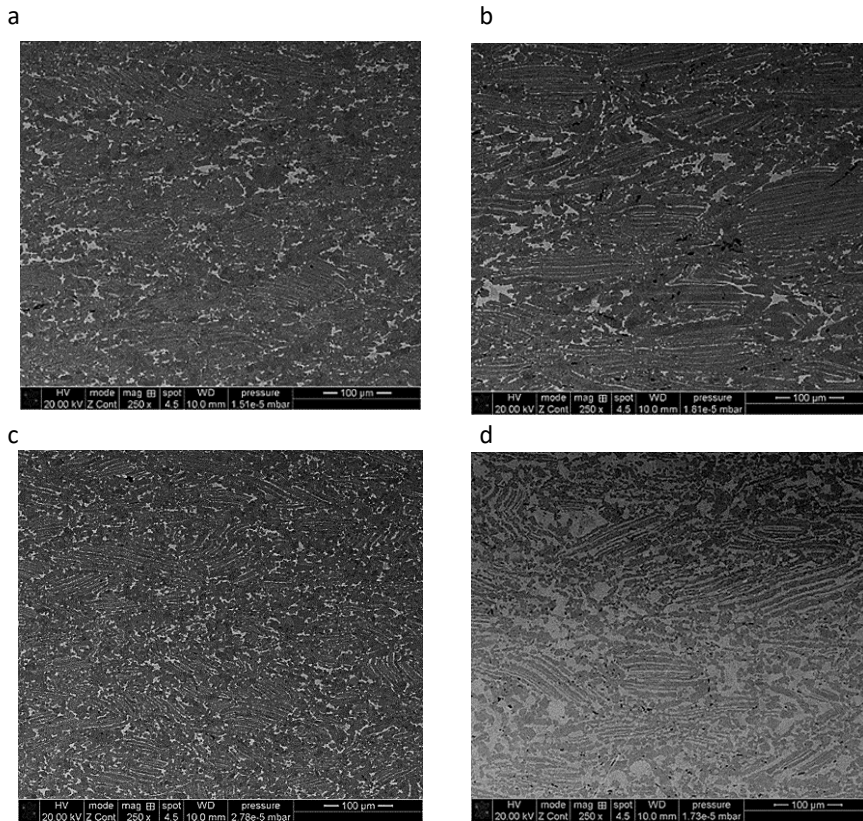


Figure 52: SEM micrograph (BSE) of 45XD alloy after 50% compression, in the following conditions (a), HIP, (b), THH, (c), IHH, (d), THH+HT, all at 250X magnification, where black areas correspond to γ phase, white β_0 and grey α_2 , respectively.

To identify the impact of the intermediate heat treatment, comparisons should be drawn between THH and THH+HT. With heat treatment, the extent of globularisation is high and X-DRX increases by 10 %, THH showing the lowest values seen in the study at 30 %. However, the time spent at temperature during the HT also grows globular material of both γ and α_2 , removing β_0 in the process, explaining the relatively low fraction of grains under $\leq 50 \mu\text{m}^2$ compared to IHH and HIP, seen in Table 10. The excessive time at temperature leading to grain growth, as discussed in 4.3.2.3 for this alloy, also described by other researchers in work on heat treatments for other peritectic alloys [53],[149],[144].

4.5.2.2 Secondary compression behaviour

The secondary (2nd) compression stress-strain curves at Figure 53a, show that a similar profile to 1st compression was followed i.e., strain hardening to a peak flow stress (σ_{pfs}) followed by flow softening. Notably, compression at 0.001 s^{-1} returns a poorly defined σ_{pfs} and steady state stress gained at a strain of 0.5, with little flow softening for all material conditions at 1100 °C. IHH material showed the lowest steady state stress at which a quasi-constant structure is assumed to have been reached, stabilising between 40-45 MPa [54]. This is not achieved with faster strain rates. This indicates that each material

is still resistant to both dynamic globularisation of any remnant lamellar content from 1' compression and dynamic recrystallisation at these speeds, as described by *Semiatin, Seetharaman and Ghosh*[118].

The peak flow stresses and extent of flow softening increased with strain rate as in 1' compression for each material. With a strain rate of 0.001 s^{-1} all material reaches a steady-state flow stress with 2'' compression strain of 0.7, With strain rates of 0.001 and 0.01 s^{-1} HIP, IHH and THH show very similar steep work hardening rates. The work hardening could be due to rapid dislocation pile-up, the relatively sharp peaks seen in 1' compression are gone, replaced by broader peaks at slower strain rates due to the relative absence of lamellar morphologies [155]. The rate of dislocation pile-up may have been slowed by the lack of γ content in THH+HT material; the rate quickly catches up with additional strain, but there is a definite lag present in each stress strain profile. The effect of the heat treatment is also seen in the higher σ_{pfs} than for THH without HT, at each strain rate. The relatively high flow stress from the THH+HT material at slow strain rates could be due to a similar reason as seen with HIP material in 1' compression. Segregation, from HT, leads to heavy alloying elements and interstitials being preferentially gettered into the α_2 from γ . This means the α_2 is less prone to recrystallisation when under strain, due to slower dissolution of α_2 into γ , and solid solution hardening effects [74],[104],[152]. Another reason could also be that the dominant α phase, with HCP crystal structure, has limited slip systems available during deformation, this in itself could lead to higher flow stress' observed [166].

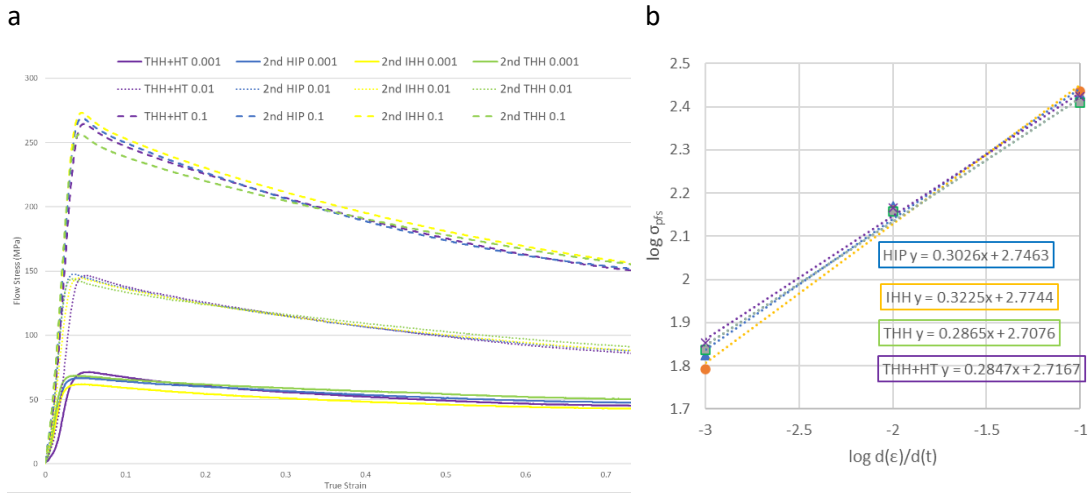


Figure 53: Secondary stress-strain curves (a), secondary compression at 1100 °C to 50 % at 0.001, 0.01 and 0.1 s^{-1} over 870, 87 and 8.7 seconds respectively. Calculation of strain rate sensitivity (m) for each material for secondary compression (b).

From Figure 53b and Table 21, HIP and IHH reach m of ≥ 0.3 , IHH shows the highest m value at 0.32, THH+HT showing the lowest from σ_{pfs} in 2" compression at 0.29, no great difference in compression behaviour being identified. The lack of difference seen between stress-strain curves of the different samples could be due to several factors from the methodology and microstructure. The single compression test for each sample cannot confidently identify any differences when the curves are similar. As the second compression is in the same axis as the first compression, the majority of remnant lamellar grains will be perpendicular to compression and as seen when comparing Table 16 and 20, of a smaller size and overall content, so will not contribute to the flow stresses seen in the same manner as seen in primary compression [40],[84].

In the secondary compressed microstructures, shown in the appendix, all microstructures with lamellar content below 10% and X-DRX greater than 60%.

The relationship between the primary upset microstructure and secondary compression strain rate sensitivity could be dictated by the X-DRX and the size of any remnant lamellar colonies; Figure 54a-b. The lamellar content shown in Figure 54c appears to play a role, but to a lesser extent compared to the lamellar grain sizes. The picture with phase fraction appears simpler with 2" compression compared to 1", Figure 54d.

There were concerns raised regarding future processing for IHH material, discussed in 4.4.2.3, with an overall β_0 content increase from pre-compression and 1' compressed material. However, it appears that it is the absence of β_0 laths with 2" compression that is the important factor, as the overall β_0 fraction does not seem to impact on the 2" compression behaviour of IHH.

Both the HIP and IHH material fulfil the criteria outlined by other researchers, which these findings agree with, that higher strain rate sensitivity is achieved with a microstructure containing a low

lamellar content of small grain size and high dynamic recrystallised content (X-DRX), however this is not achieved with only one compression. [53],[54],[55],[56],[57],[58].

The THH material does not achieve m of ≥ 0.3 ; THH has the largest remnant lamellar grain sizes as well as lowest X-DRX and grain area fraction under $\leq 50 \mu\text{m}^2$ from 1' compression. The reasoning for this was discussed in section 4.4.2.3. This is not to say that the THH process cannot be adapted to produce relatively refined lamellar grains, i.e., by cooling rate control [94]. The THH+HT material also does not achieve m of ≥ 0.3 , this could be due to the significant volume of α phase upon compression restricting DRX together with the large remnant lamellar grains. All material conditions show stable material flow under the 2'' compression conditions. It is likely that higher temperatures would increase m , due to nucleation and growth of dynamic recrystallised grains being temperature driven, easing dislocation destruction [146].

Material	HIP			IHH			THH			THH+HT		
Strain rate (s^{-1})	0.001	0.01	0.1	0.001	0.01	0.1	0.001	0.01	0.1	0.001	0.01	0.1
2'' σ_{pfs} (MPa)	66.8	147.6	269.0	61.9	144.7	273.1	68.6	144.0	256.6	71.3	146.6	264.6
2'' $m(\sigma_{\text{pfs}})$	0.30			0.32			0.29			0.29		

Table 21: peak flow stress and strain rate sensitivity for each material condition over secondary compression

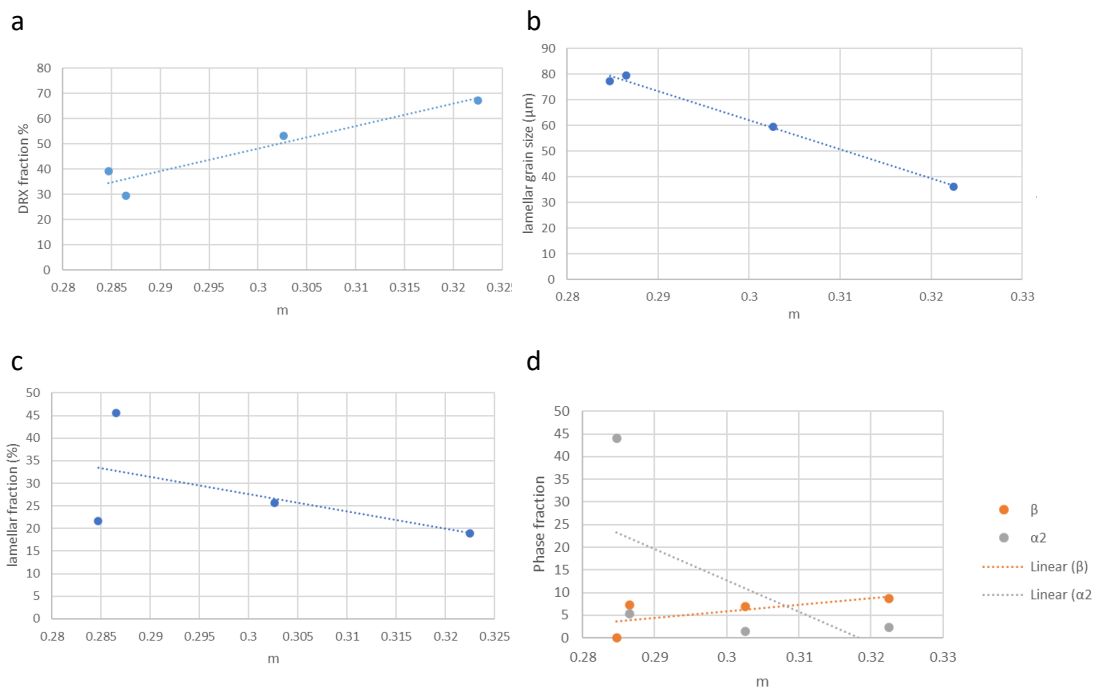


Figure 54: relationship between strain rate sensitivity of secondary compression and, (a) primary compression DRX fraction, (b) primary compression lamellar grain size, (c) primary compression lamellar content, (d) secondary compression relationship between β_0 and α_2 phase fraction and strain rate sensitivity.

4.5.3 Summary

The aim of this study is to bring together the learning from the other sections on 45XD and assess the secondary compression behaviour and strain rate sensitivity of this industry accepted, peritectic solidifying titanium aluminide ingot alloy; 45XD. Secondary processing covers high deformation processes such as hot rolling or isothermal closed-die forging, it is well established that these techniques require an isotropic behaving microstructure ideally capable of strain rate sensitivity ≥ 0.3 . The following conclusions for secondary processing of this alloy are as follows:

- To achieve strain rate sensitivity of ≥ 0.3 in secondary compression this study found 45XD should consist of dynamic recrystallised fraction of $> 50\%$, with any remnant lamellar material of an average size of $< 50 \mu\text{m}$, combined with phase fraction of α_2 restrained below 5%. A β_0 fraction present as globular morphologies and below 10% does not appear to have a negative impact on secondary strain rate sensitivity.
- Homogenisation does not appear necessary to achieve the strain rate sensitivity ≥ 0.3 targeted, as identified by the HIP material. However, findings from 4.2 and 4.4 should not be ignored, the integrated HIP and homogenisation (IHH) approach should be of industrial interest to achieve both elemental and microstructural homogeneity before compression, which subsequently promotes dynamic recrystallisation and globularisation with compression.
- The heat treatment of 1200AC leads to high extents of globularisation, SRX likely to have taken place as part of the further globularisation of lamellar content compared to only compression of THH microstructures, however, it does promote a high fraction of globular α_2 phase, available as disordered α phase at compression temperatures. This is unlikely to be considered for improving forging outcomes when looking at the strain rate sensitivity of the material and the practicality of adding another step to the process.

4.6 Conclusions and industrial relevance for 45XD

To summarise, the work reported here has an emphasis on controlling and optimising the microstructure of 45XD (Ti-44.31Al-1.93Nb-2.93Mn-0.87B at%) to improve the forging outcome of primary compression and provide the high integrity isotropic behaving material required for secondary processing. The following conclusions for primary processing of this alloy were drawn:

- For initial ingot breakdown, referred to as primary compression, the initial microstructure should be elementally and microstructurally homogeneous i.e., fully lamellar. A homogenisation (HMG) heat treatment just within the α phase (2 hours, 1300 °C) is best placed to achieve this.
- Cooling from this heat treatment is key to controlling the lamellar grain dimensions returned; too slow and grain growth is an issue, Figure 55a and c, too fast and fine lath dimensions are apparent, both resist globularisation and subsequent formation of strain free dynamic recrystallised material. A compromise is required to achieve refined fully lamellar microstructures, furnace cooling in the region of 10 °C/min appears sufficient and industrially viable.
- Therefore, the HIP and HMG stages can be integrated into one process using HIP equipment without any negative effects on the HIP equipment or compression behaviour of this alloy in primary or secondary compression. As well as removing a separate processing step, HMG; using costly vacuum furnace equipment, there is evidence that pressure and heat treatment above the α transus reduces the activation barrier required to reduce the brittle β_0 phase. The absence of an additional cooling stage also restricts the opportunity for grain growth. This in turn improves the forging outcome by returning a homogeneously refined microstructure, free of large lamellar grains with a favourable dynamic recrystallised fraction for secondary processing.

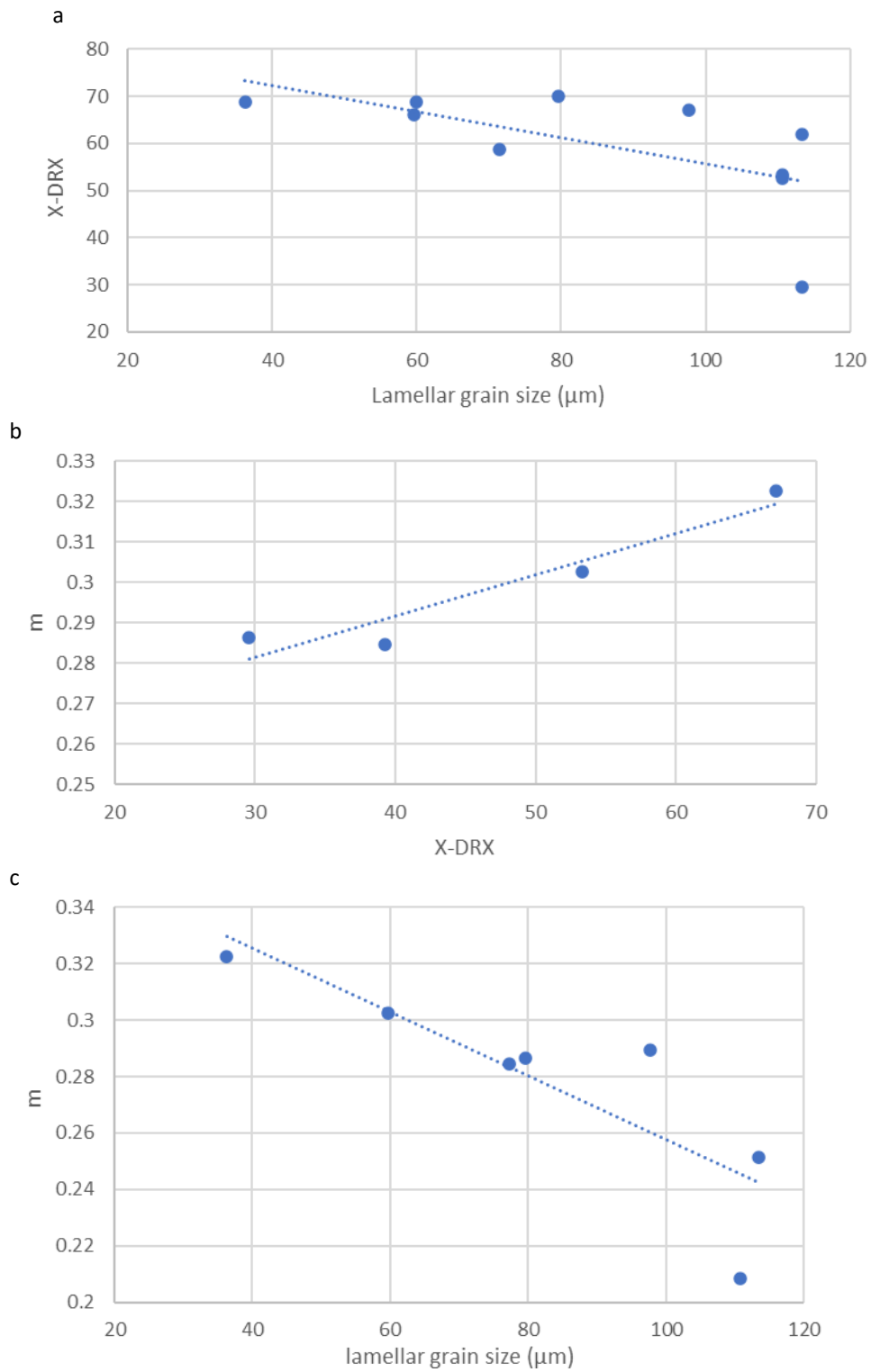


Figure 55: (a) relationship between pre-compression lamellar grain size (μm) and dynamic recrystallised fraction (X-DRX) returned (b) relationship between X-DRX returned from primary compression and its relationship with secondary strain rate sensitivity (m) (c) primary and secondary compression relationship between lamellar grain size (μm) and strain rate sensitivity (m), from work without intermediate and post working heat treatment in 4.1, 4.2, 4.4 and 4.5

Investigations into intermediate stages, between compression stages, show that:

- Dwell between compression stages at this compression temperature, 1100 °C, within the $\gamma+\beta_0$, leads to growth of the β_0 fraction, with a negative impact on the extent of globularisation and hardening compression behaviour. This hardening effect could be due to higher β_0 and/or MDRX taking place.
- The heat treatment of 1200AC (2 hours, 1200 °C, air cooling), whether as an intermediate or post compression heat treatment leads to high extents of globularisation, SRX likely to have taken place as part of the further globularisation of lamellar content. However, it does promote a high fraction of globular α_2 phase available as disordered α phase at compression temperatures. This cannot be considered an improvement for further processing as it adds another step to the process with limited benefit.

The following conclusions from secondary processing of this alloy are as follows:

- To achieve strain rate sensitivity of ≥ 0.3 in secondary compression this study found 45XD should consist of > 50 % volume fraction of strain free, equiaxed dynamic recrystallised material, with any remnant lamellar grains of an average size of < 50 μm , combined with α_2 phase fraction restrained below 5%. A β_0 fraction present as globular morphologies and below 10% does not appear to have a negative impact on secondary strain rate sensitivity.

4.7 Future work recommendations for 45XD

- Cooling rates from homogenisation, either as integrated with HIP or in the traditional sense, can be controlled with both vacuum furnace and HIP equipment. The cooling rate from HMG has been identified, in this work and by others, as the variable that influences lamellar grain size and controls lath thicknesses. The optimum lath thickness for improving globularisation kinetics should be identified.
- Primary compression at 1100 °C, within the $\gamma+\beta_0$ phase, leads to growth of the β_0 fraction. This may have a larger impact on the initial ingot breakdown (primary compression) of fully lamellar microstructures if β_0 presents itself as laths within lamellar colonies. At industrial scale, with slower heating and cooling rates, longer soak times before compression and unavoidable dwell times at temperature the growth of β_0 could slow globularisation kinetics, as seen in this work. Higher compression temperatures would result in an even higher possible β_0 fraction, Figure 29, lower temperatures would increase flow stresses and reduce recrystallised fraction produced, so compression temperature should remain the same. Water quench trials would build greater understanding of the microstructure, at a similar scale, at compression temperature.
- Multi-axial compression or cogging trials were considered in this work, but as seen in section 4.3 interrupting compression at 25%, with a return to room temperature or dwell at compression temperature, sees no benefit in terms of the forging outcome compared to the compression of HIP microstructure. It is anticipated that compression to $\leq 25\%$ is not enough to globularise lamellar material, as shown by the lack of steady-state flow stress in compression, but it will orientate laths perpendicular to the compression axis and kink the lamellar morphologies present. Secondary compression of all material discussed in section 4.5 (HIP, THH, IHH, THH+HT) at strain rates of 0.001 s^{-1} , in the same axis as primary compression, returns material with a promising combination of low lamellar content, $\leq 10\%$, of small average size, $<40 \mu\text{m}$, and high X-DRX, $>60\%$. Multi-axial working may be of interest at this stage, where lamellar morphologies have been largely removed, to further refine the microstructure.
- With the strain rate sensitivity of the integrated HIP and HMG (IHH) material with secondary compression reaching ≥ 0.3 , and 0.29 in primary compression, hot rolling and isothermal closed-die forging trials should be viable.

5 Thermomechanical processing trials of 4822

5.1 The impact of HIP, homogenisation and integrating the two processes on 4822 cast ingot material and its subsequent response to primary compression

5.1.1 Introduction

The work reported here evaluates the effect of pre-compression consolidation and heat treatment of TiAl alloy 4822 (Ti-47.2Al-1.3Nb-1.83Cr at%) and whether they can be integrated, as introduced in work described in section 4.4 for 45XD alloy. Hot isostatic pressing and homogenisation have been found to improve the forging outcome of as-cast material, the former to remove casting porosity, the latter reduces casting segregation seen in peritectic solidifying titanium aluminides, as identified by *Imayev et al.*, *Zhang et al.* and *Chladil et al.* so both processes are deemed necessary for this alloy [33],[32],[34]. However, neither process refines the large grained lamellar microstructure present from casting 4822 alloy [53],[149].

An emphasis on controlling and optimising this starting microstructure to improve the forging outcome of primary compression, globularise the lamellar content and return a favourable dynamic recrystallised fraction (X-DRX) that eases secondary processing is missing. By maintaining constant compression conditions these pre-compression microstructures were assessed for their influence on the compression behaviour. The resulting post-compression microstructures were assessed in terms of lamellar grain dimensions and content as well as X-DRX and phase fraction.

Ti	Al	Nb	Cr	Fe	Si
49.1	47.2	1.83	1.83	0.03	0.03

Table 22: Average chemical composition of supplied 4822 ingot, analysed via ICP at three points by TIMET.

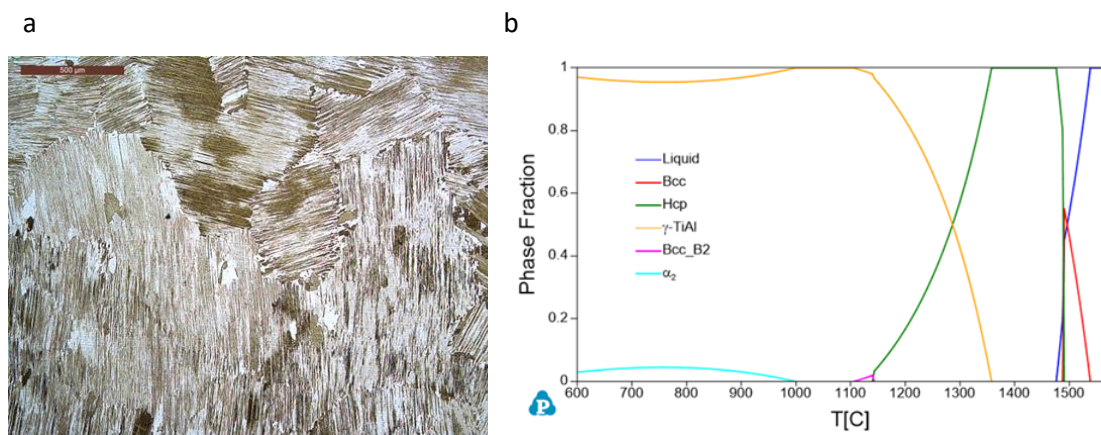


Figure 56: (a) OM image of as-received (ASR) cast microstructure of 4822 at 5x magnification, (b) Calculation of phase diagram (CALPHAD) of 4822 alloy from ICP analysis in Table 22.

5.1.2 Results and discussion

The influence of the starting microstructure on the deformation behaviour of the material relies on several parameters, these are discussed here. This is followed by an explanation of the compression behaviour for each processing condition, as well as the associated extent of globularisation of lamellar grains, together with the resulting X-DRX and the fraction of grains $\leq 50 \mu\text{m}^2$ from compression, with the subsequent effect on secondary processing strain rate sensitivity. To start, pre-compression microstructures from solidification and consolidation via hot isostatic pressing (HIP) are discussed, as is the influence of homogenisation (HMG) in the traditional HIP and HMG fashion, THH and whether it can be integrated (IHH) into one process using HIP equipment.

5.1.2.1 Pre-compression microstructures

Peritectic solidifying TiAl alloys, such as cast 4822, use the disordered BCC β precipitates, present only at high temperatures ($>1450 \text{ }^\circ\text{C}$), to nucleate α , as shown in the CALPHAD phase fraction diagram in Figure 56b. Here α is growing into the β , as well as any liquid present, until the single α phase remains during solidification ($L+\beta \rightarrow \alpha$). Grain growth is then unrestricted and rapid, this problem is exaggerated by scaling up to ingot production [137].

With further cooling, the crystallographic relationship between the long range ordered α_2 and γ follows a Blackburn orientation relationship to form a single lamellar colony from each α grain, due to the single set of basal planes in α matching that of γ , discussed in greater detail in 2.3.1.3 [28],[29]. This dictates the size of the lamellar grain presented to primary ingot upsetting. The effect of time in, or near the single α phase is shown with microstructural analysis conducted on 4822 in the three starting material conditions discussed: HIP, THH, and IHH. This is to assess the influence of initial microstructure on compression behaviour and the resulting microstructural evolution post 1' compression. From optical microscopy (OM), average lamellar grain sizes as well as lamellar and equiaxed γ (γ_{eq}) fraction, were determined and shown in Table 23.

The increase in lamellar grain size prior to upsetting should be noted, time within or near the α phase increasing from THH to IHH explaining the lamellar grain growth seen, as discussed above. The α grain growth is rapid and uninhibited by grain refining alloy additions in this alloy [39]. However, including both HIP and HMG in the process has been found to improve the forging outcome of as-cast TiAl material. The former to remove casting porosity, the latter reduces casting segregation seen in peritectic solidifying titanium aluminides, improving material response to compression [33],[32],[34]. As already identified, neither process refines the initial large grained lamellar microstructure, as shown in Table 23, this large grain structure still leaves some alloys difficult to forge at industrially viable temperatures i.e., up to $1150 \text{ }^\circ\text{C}$ with TZM dies [53],[149].

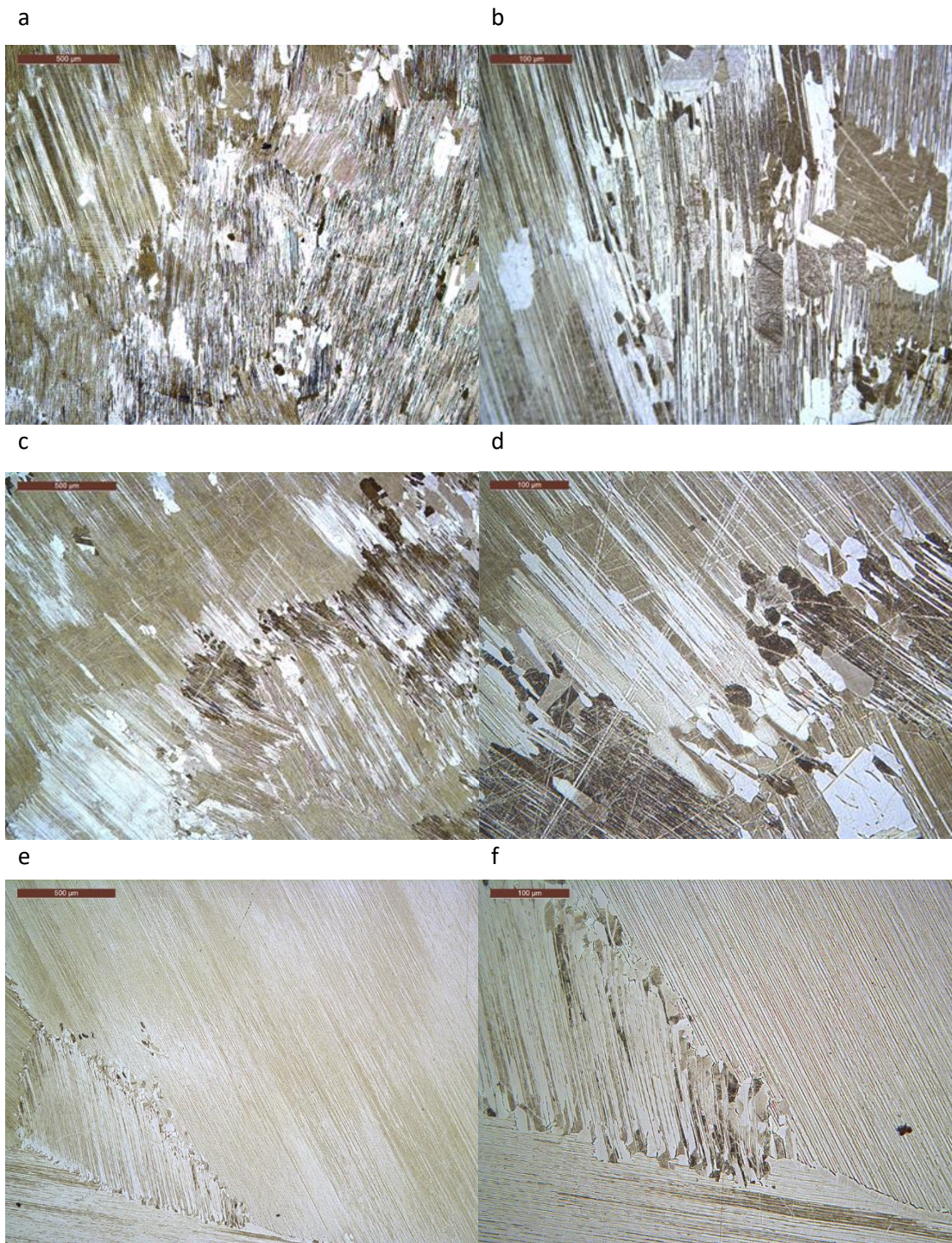


Figure 57: OM images of 4822 alloy in the HIP (a, b), THH (c, d), IHH (e, f), condition at 5x magnification (a, c, e,) and 20x magnification (b, d, f,) before compression.

The traditional HIP and homogenisation (THH) route included a separate homogenisation heat treatment in the single α phase and is well established to return a fully lamellar and elementally homogeneous microstructure [149],[162]. However, the larger fraction in γ_{eq} morphologies seen in THH compared to IHH is likely to be due to the slow furnace cooling from vacuum furnace HMG, so

more time spent within γ dominant phase regions. This has led to coarsening of γ laths and separate globular γ grain growth i.e., has reduced microstructural homogeneity, as quantified in Table 23.

Position analysed	Centre			
	% lam	% γ_{eq}	Avg. lamellar grain size (μm)	SD of Avg. lamellar grain size (μm)
HIP	91	9	665	324
THH	88	12	1059	622
IHH	95	5	2039	1313

Table 23: Microstructural details of 4822 material conditions investigated pre-compression from optical microscopy analysis.

5.1.2.2 Primary compression behaviour

First, the distinction between the aims of primary (1') and secondary (2'') processing should be made. Successful primary compression, seen as equivalent to ingot breakdown, or forming a pre-form in this study, looks to return a crack-free, isotropic behaving microstructure ready for secondary processing. To achieve this, pre-compression processing should aim to deliver a material that responds efficiently to deformation. An efficient response to primary compression includes returning a material with high lamellar globularisation, and so high X-DRX. Secondary processing covers high deformation processes such as hot rolling or isothermal closed-die forging, these techniques require a microstructure ideally capable of strain rate sensitivity of ≥ 0.3 [53],[54],[55],[56],[57],[58].

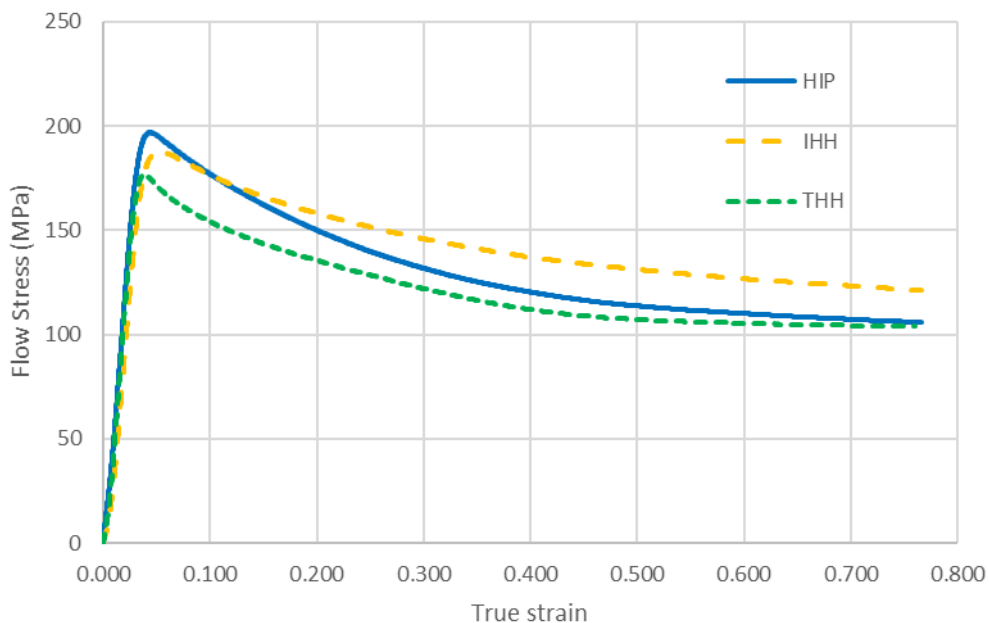


Figure 58: Primary stress-stain curves, compression at 1100 °C to 50% at 0.001 s⁻¹ over 760 seconds.

From 1' compression stress-strain curves THH shows the lowest σ_{pfs} value at 176.6 MPa, HIP showing the highest σ_{pfs} at 196.8 MPa, Table 24. With primary compression, each curve follows a similar pattern for each condition, with work hardening followed by peak flow stress (σ_{pfs}), followed by flow softening. This is visualised in Figure 58, this curve shape is common for alloys undergoing dynamic recrystallisation (DRX), as described in 4.1.2.2 for 45XD [114],[150]. The steep initial work hardening seen in all three samples is due to rapid dislocation pile-up in the γ laths, only slowed by a critical strain (ϵ_c) being reached, high stored energy in the fragmented lamellar material initiating rapid DRX, one reason for the relatively sharp peaks seen here and in working other TiAl alloys [155]. The rate of strain hardening appears similar between the three materials, HIP showing the highest σ_{pfs} , perhaps the lack of homogenisation heat treatment and elemental homogenisation that this brings could be to blame, as suggested by *Fuchs*, this in turn slowing dislocation pile-up in the γ laths, restraining the initiation of DRX [53] [77]. Or this could be simply down to chance and the random orientation of lamellar grains in the material being in a hard orientation [84].

THH shows the earliest ϵ_c , sharpest peak and steepest degree of flow softening, characterising its flow behaviour. The lower σ_{pfs} of THH is perhaps explained by its lower lamellar content; lamellar grain mobility being higher with higher γ_{eq} content, allowing flow localisation and slip of lamellar grains rather than globularisation and DRX [156].

Continued flow softening shows that DRX has initiated and there is the time for this strain free material to contribute to reducing flow stress as strain increases. The formation of this strain-free recrystallised material is key to producing workable material for secondary processing [53].

Material condition	HIP	IHH	THH
σ_{pfs} - peak flow stress (MPa)	196.8	180.2	176.6

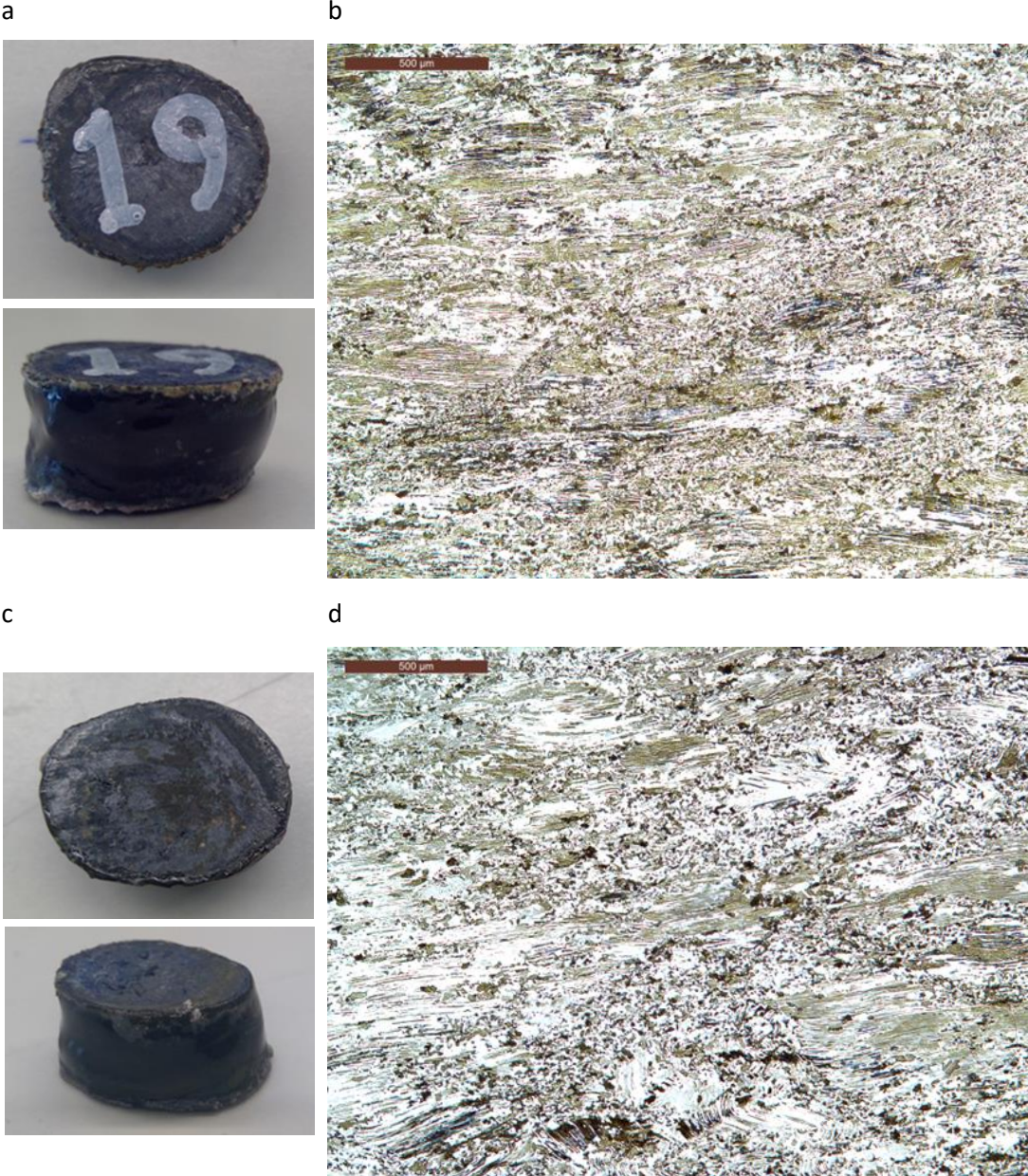
Table 24: Peak flow stress for each material condition over primary compression.

However, all samples show unstable material flow under these 1' compression conditions, Figure 59. Compression failure; as geometry, die, lubrication and compression conditions were the same across the three tests, is a sign of flow localisation caused by the large grained, fully lamellar microstructures present [117],[118],[119]. All pre-compression material has a high lamellar grain size, $\geq 500 \mu\text{m}$, so flow localisation is not a surprise and similar observations were noted in the work of *Semiatin, Seetharaman and Weiss*. Their review of earlier work discussed the relationship between large starting lamellar microstructures, flow softening rate, recrystallisation and flow localisation [119]. Flow localisation was identified in their review as a symptom of high levels of flow softening, due to large lamellar

microstructures being present during hot working and failing to globularise, resulting in non-uniform deformation, this can be attributed to each material seen here.

5.1.2.3 Primary compression microstructure

As shown by Figure 59, all starting conditions returned poorly compressed material, with clear shearing of the samples and each material still containing large lamellar morphologies orientated perpendicular to the compression axis after 1' compression. Zhang et al. suggested remnant lamellar grains above 80 μm should be considered detrimental, here average lamellar grain sizes are 300-750 μm [163],[144],[164].



e



f



Figure 59: Unstable material flow shown by images of compression samples (a, c, f). Of material in the 4822 alloy in the HIP (a, b), THH (c, d), IHH (e, f) condition at 5x OM magnification, after 50% primary compression at 1100°C, 0.001 s⁻¹

The DRX fraction (X-DRX), calculated via the grain orientation spread (GOS) approach shown in Figure 60 and Figure 61a, c, e is considered low for 50% compression. Work on a similar alloy by *Seetharaman and Semiatin*, noted the importance of controlling lamellar content and grain size in the starting microstructure, when pursuing high rates of globularisation and so high X-DRX [58].

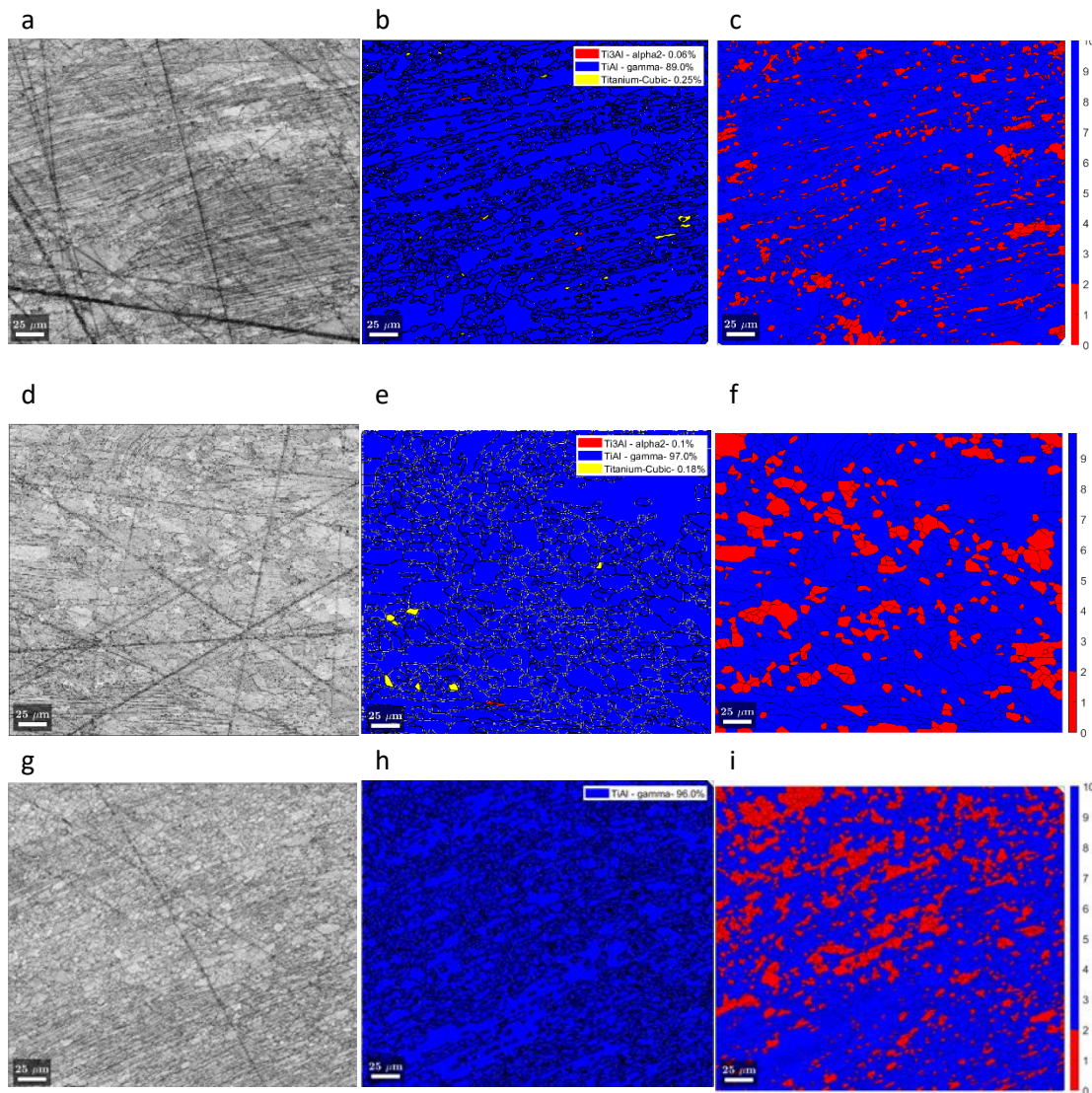


Figure 60: EBSD used to give maps of, (left) band contrast, (middle) phase map; blue is γ , red is α_2 , yellow is β_0 , (right) X-DRX; red is the recrystallised fraction, blue is deformed, of 4822 alloy in the HIP (a, b, c), THH (d, e, f), IHH (g, h, i) condition at 500x magnification, after 50% primary compression at 0.001 s^{-1} .

Compression of the 4822 HIP material sees the highest reduction in lamellar content, Table 25, the lower initial lamellar grain size increasing the lamellar-lamellar grain boundary density necessary to promote globularisation upon compression compared to IHH and THH, as identified by *Seetharaman and Semiatin* [58]. However, the low X-DRX and grains under $50 \mu\text{m}^2$ fraction for HIP suggest recrystallisation is not progressing as would be anticipated. The elemental segregation present from the lack of homogenisation means recrystallisation is sluggish, as noted in section 4.4.2.3 for 45XD and the description of HIP compression behaviour in 5.1.2.2, explaining the high σ_{pfs} . The relatively high flow stress and low X-DRX from compression of HIP material could be due to the same mechanism seen in creep and fatigue trials. Segregation leads to heavy alloying elements and interstitials being preferentially gettered into the α_2 from γ . This means the α_2 is less prone to globularisation and

therefore recrystallisation when under strain, due to slower dissolution of α_2 into γ and solid solution hardening effects [74],[104],[152]. The opposite position to this is the IHH material which shows the highest values for X-DRX and grains under $50 \mu\text{m}^2$ fraction, but lowest globularised fraction. The large initial lamellar grain size, in the region of $2000 \mu\text{m}$, and low lamellar-lamellar grain boundary density restraining complete globularisation with lamellar content beginning to kink, as seen in Figure 59f. The higher X-DRX in this latter case possibly being down to the elemental homogenisation of the IHH process.

4822 material condition (s^{-1})	% Lam	Reduction in lamellar content (%)	Average lamellar grain size (μm , from 0° and 90°)	SD of Average lamellar grain size (μm)	% α_2	% β_0	% γ	X-DRX (%)	Grain area fraction $\leq 50 \mu\text{m}^2$ (%)
HIP 0.001	34	57	300	222	0	0	89	12	25
THH 0.001	44	44	350	173	0	1	94	23	30
IHH 0.001	59	36	765	680	0	0	96	24	36

Table 25: Phase, morphology, DRX and grain area $< 50 \mu\text{m}^2$ fraction for each material after 50% primary compression at 1100°C and 0.001 , 0.005 and 0.01 s^{-1} calculated from a combination of OM and EBSD analysis.

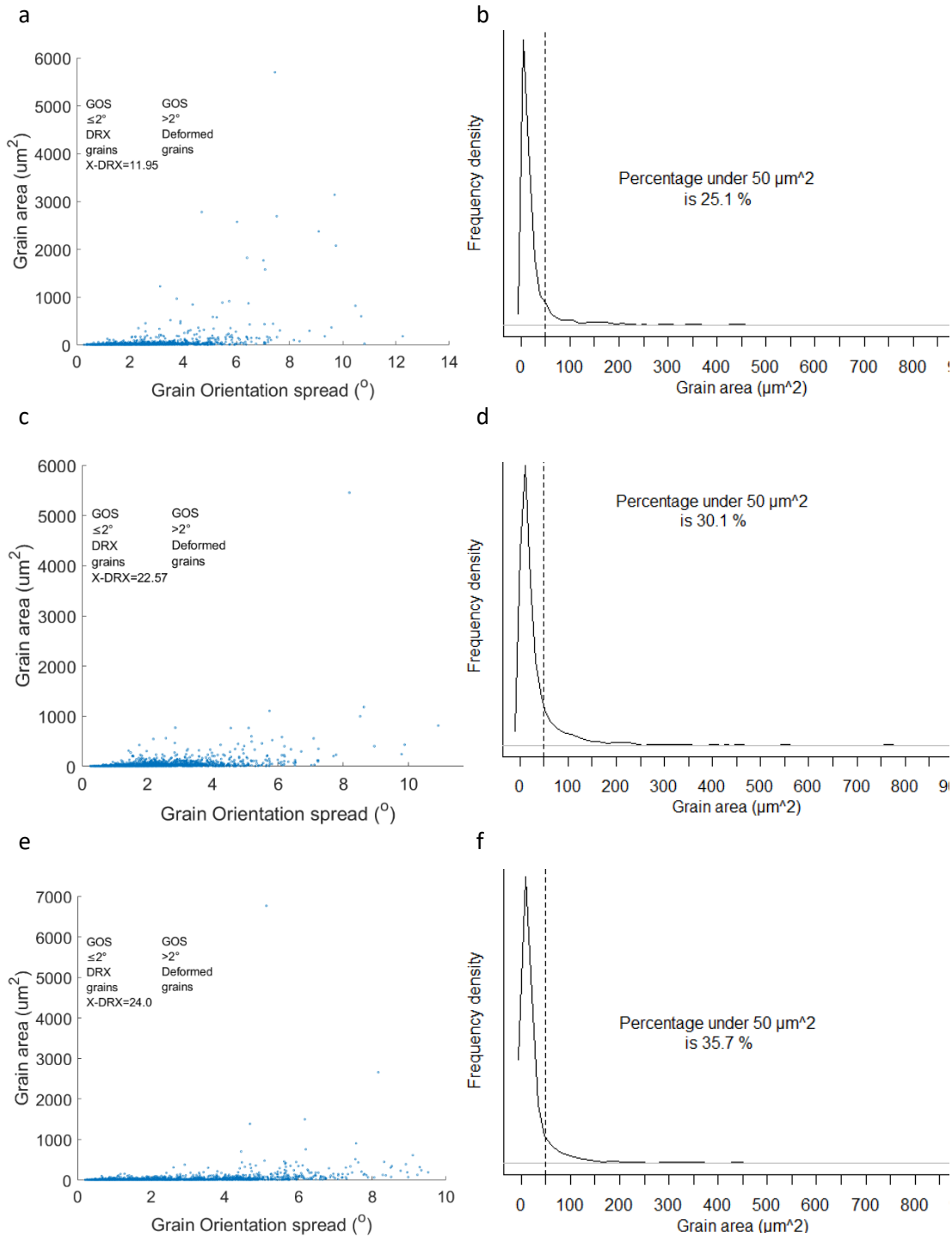


Figure 61: Plots calculating the DRX fraction from the GOS approach on the left, grain area frequency density on the right, for each material condition after 50% primary compression at 1100 °C and 0.001 s^{-1} , (a, b) HIP, (c, d) THH, (e, f) IHH

5.1.2.4 Secondary compression behaviour

Secondary compression stress-strain curves, Figure 62a, follow the same pattern as that seen in primary compression, described in 5.1.2.2. Notably, compression at 0.001 s^{-1} returns a poorly defined σ_{pfs} and steady state stress gained at a strain of 0.5, with little flow softening for all material conditions. The IHH material shows the highest σ_{pfs} at each strain rate and steady state stress, THH shows the lowest σ_{pfs} and steady state stress at 0.001 s^{-1} , where a quasi-constant structure is assumed to have been reached [54]. This steady state stress is not achieved with faster strain rates. This indicates that each material is still sensitive to strain rate in terms of dynamic recrystallisation kinetics and extent. The strain rate sensitivity (m) index from the σ_{pfs} of each material at each strain rate also looks to quantify this behaviour, but m results do not differ greatly between the three conditions. The IHH material has the lowest m at 0.23, possibly due to the large remnant lamellar grains from primary compression. The HIP and THH m values are identical at 0.25.

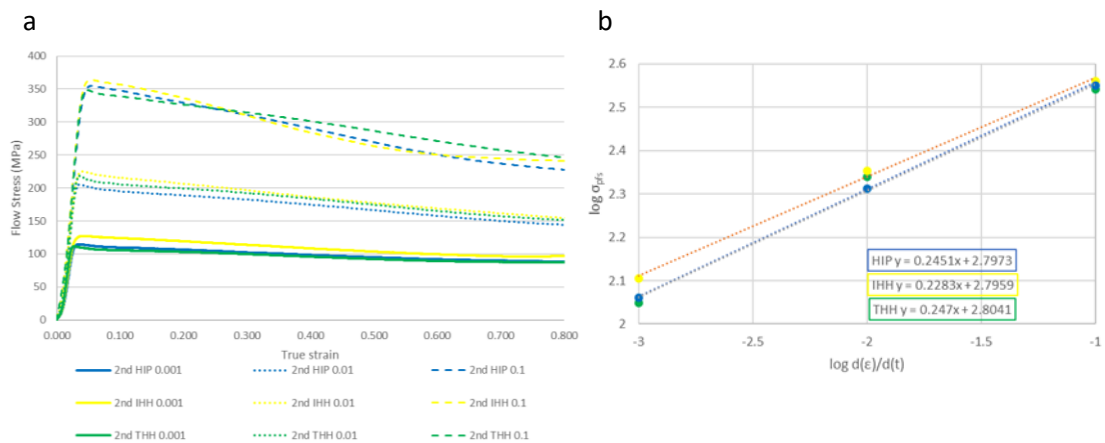


Figure 62: Secondary stress-strain curves (a), secondary compression at $1100 \text{ }^{\circ}\text{C}$ to 50 % at 0.001, 0.01 and 0.1 s^{-1} over 870, 87 and 8.7 seconds respectively. Calculation of strain rate sensitivity (m) for each material for secondary compression (b).

The relationship between the primary upset microstructure and secondary compression behaviour is dictated by factors including X-DRX, the remnant lamellar grain size and its content, as well as phase fraction. As found by other authors with this alloy, *Fuchs* did not find m to exceed 0.3 at industrially viable temperatures for large 4822 samples in the forged, extruded or powder metallurgy state [53],[150]. This is not to say that these levels of strain rate sensitivity for this alloy have not been recorded for similar processing conditions. *Gupta et al.* found, admittedly on smaller samples, m values exceeding 0.3 with HIP and homogenised 4822 [57]. It is likely that higher temperatures would increase m , due to nucleation and growth of dynamic recrystallised grains being temperature driven, easing dislocation destruction. However, the m value during secondary compression does not give a clear picture of the outcome of compression on its own for this ingot of 4822, assessing this alloy solely on m being ≥ 0.3 is not sufficient [146]. The secondary compression microstructure returned as well as

the physical appearance of specimens should also be considered; only THH and HIP at 0.001 s^{-1} showed uniform compression.


Material	HIP			IHH			THH		
Strain rate (s^{-1})	0.001	0.01	0.1	0.001	0.01	0.1	0.001	0.01	0.1
$2'' \sigma_{\text{pfs}}$ (MPa)	114.8	204.9	354.8	127.2	225.3	363.8	111.7	218.9	348.4
$2'' m(\sigma_{\text{pfs}})$	0.25			0.23			0.25		
Secondary compression samples									

Table 26: Compression behaviour values, peak flow stress and strain rate sensitivity for each material condition over secondary compression at $1100\text{ }^\circ\text{C}$ to 50% at 0.001 s^{-1} over 800 seconds, 0.01 s^{-1} over 80 seconds, 0.1 s^{-1} over 8 seconds.

5.1.2.5 Secondary compression microstructure

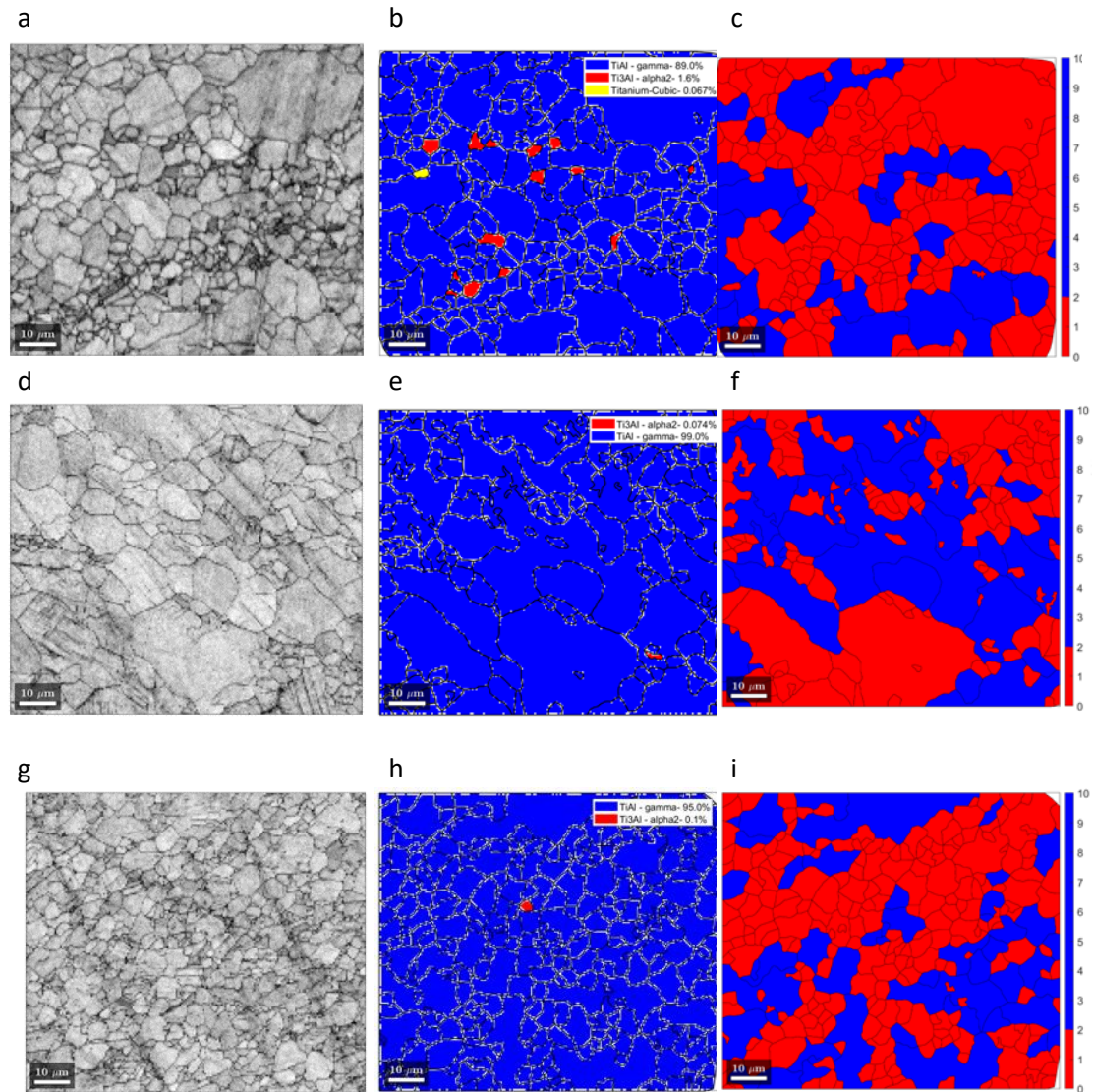


Figure 63: EBSD used to give maps of, (left) band contrast, (middle) phase map; blue is γ , red is α_2 , yellow is θ_0 , (right) X-DRX; red is the recrystallised fraction, blue is deformed, of 4822 alloy in the HIP (a, b, c), THH (d, e, f), IHH (g, h, i) condition at 1600x magnification, after 50% secondary compression at 1100 °C, 0.001 s⁻¹.

Remnant lamellar content and grain sizes from primary compressed microstructures have been reduced as would be expected with secondary compression, as shown by Table 27. Each starting condition returns material still containing lamellar morphologies orientated perpendicular to the compression axis after 2" compression, however these are below the 80 μm suggested by *Zhang et al.* for all strain rates, so they should not be considered detrimental for further processing [163],[144],[164]. However, with THH at 0.1 s⁻¹ there is adiabatic shear occurring, visible in EBSD mapping in Figure 64d, suggesting this strain rate is too fast for this compression temperature and microstructure, the microstructure produced cannot be considered homogeneous [167].

4822 material condition (s ⁻¹)	%Lam	Average lamellar grain size (μm, from 0° and 90°))	SD of average lamellar grain size (μm)	% α ₂	% β ₀	% γ	X-DRX (%)	Grain area fraction ≤50μm ² (%)
HIP 0.001	7	28	25	2	0	89	67	43
HIP 0.01	18	55	47	0	0	95	57	77
HIP 0.1	19	52	50	0	0	94	42	54
THH 0.001	7	22	25	0	0	99	47	27
THH 0.01	28	66	74	0	0	90	50	54
THH 0.1	19	40	26	1	0	95	32	38
IHH 0.001	5	19	16	0	0	95	58	56
IHH 0.01	4	14	13	0	0	91	64	82
IHH 0.1	21	22	20	0	0	92	36	51

Table 27: Phase, morphology, DRX and grain area <50 μm² fraction for each material after 50% secondary compression at 1100 °C and 0.001, 0.01 and 0.1 s⁻¹ calculated from a combination of BSE and EBSD analysis.

Adiabatic shear has not been identified in the IHH or HIP material but considering the non-uniform deformation obvious in the compression samples in Table 26, it would suggest that adiabatic shear or flow localisation has occurred in all material except that processed at strain rates of 0.001 s⁻¹ in material tested.

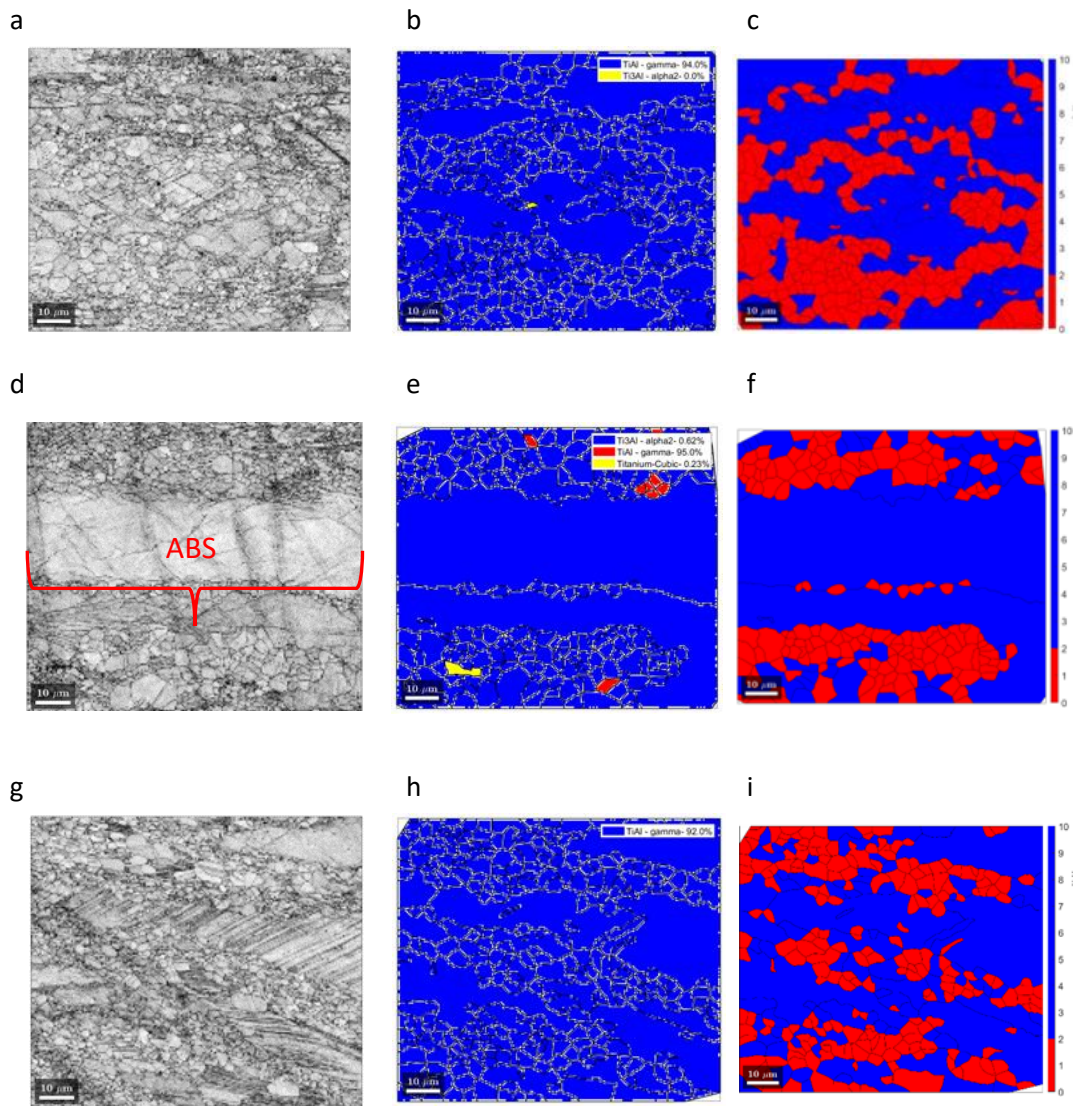


Figure 64: EBSD used to give maps of, (left) band contrast, (middle) phase map; blue is γ , red is α_2 , yellow is β_0 , (right) X-DRX; red is the recrystallised fraction, blue is deformed, of 4822 alloy in the HIP (a, b, c), THH (d, e, f), IHH (g, h, i) condition at 1600x magnification, after 50% secondary compression at 1100 °C, 0.1 s⁻¹. Adiabatic shear (ABS) example outlined in red.

5.1.3 Summary

The work reported here evaluated the effect of pre-compression consolidation and heat treatment on TiAl alloy 4822 (Ti-47.2Al-1.3Nb-1.83Cr at%) and whether they can be integrated into one stage using HIP equipment. By maintaining constant compression conditions these pre-compression microstructures were assessed for their influence on the compression behaviour. The following conclusions for this alloy and process sequences are below and next steps outlined:

- All samples, HIP, THH and IHH show unstable material flow under these primary compression conditions. Compression failure; as geometry, die, lubrication and compression conditions were the same across the three tests, is a sign of flow localisation

caused by the large grained, fully lamellar microstructures present. Integrating the two process exaggerates this lamellar grain growth, making the problem worse.

- The increase in lamellar grain size from HMG is due to time within or near the α phase, this time increasing from THH to IHH, explaining the lamellar grain growth seen, as discussed above. The α grain growth is rapid and uninhibited by grain refining additions absent in this alloy.
- The addition of HMG to pre-compression processing has been found to improve the forging outcome by other researchers by reducing casting segregation, this study can partly agree with this as the return of X-DRX material is improved. This could be due to homogenisation removing this elemental segregation, allowing dislocation mobility and recrystallisation to proceed.
- Compression of the 4822 HIP material sees the highest extent of globularisation, the lower initial lamellar grain size of HIP increasing the lamellar-lamellar grain boundary density necessary to promote globularisation upon compression compared to IHH and THH
- However, the low X-DRX and grains under 50 μm^2 fraction for HIP suggest recrystallisation is not progressing as would be anticipated. The elemental segregation present from the lack of homogenisation means recrystallisation is sluggish.
- Neither HIP alone or HMG in addition, produces the refined initial fully lamellar microstructure required to produce uniformly deformed forgings with high globularisation and X-DRX required for further processing at these industrially viable compression conditions.
- Combining elemental homogeneity and refinement of the large-grained microstructure is anticipated to improve primary forging outcomes, this will be aimed for and investigated in section 5.2.

5.2 Effect of induction cyclic heat treatment on the microstructure of HIP and homogenised 4822 and its forging outcomes

5.2.1 Introduction

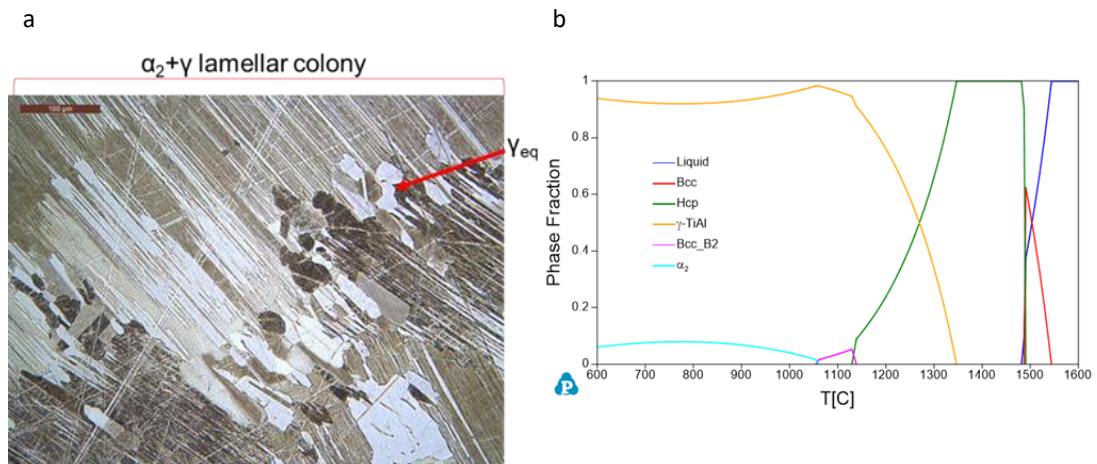


Figure 65: (a)HIP and Homogenised microstructure of 4822 under 5X magnification OM (b) Phase fraction diagram for 4822 cast alloy determined from CALPHAD.

Grain refinement of the hot isostatic pressed (HIP) and homogenised (HMG), together referred to as (HH) microstructure, is the aim of cyclic heat treatments (CHT). Other authors have looked to CHT to achieve refined fully lamellar microstructures (RFL). *Wang et al.* in particular pursued the use of CHT for grain refinement of peritectic alloys of 1 mm lamellar colony size to $\leq 50\mu\text{m}$, with the aim of perhaps avoiding hot working altogether [106],[107],[108]. They found the importance of several parameters of the CHT process: including prior α phase homogenisation and of cooling rate on microstructure formation. Phase transformations are reviewed in greater detail by *Ramanujan* and summarised in section 2.3.1.7 [29].

The CHT process for 4822 alloy was further explored by *Kościełna and Szkliniarz*, homogeneous grain refinement being their aim [109],[110]. They found that cooling rates in the range of $10\text{-}35\text{ Ks}^{-1}$ led to consistent grain refinement. Inhomogeneous grain refinement was found to occur with faster cooling, which led to a larger grain size distribution. Uniform grain refinement was improved with five controlled cycles, any more were found to have a limited benefit in terms of grain refinement or distribution, less cycles increased the grain size distribution. Having excessive hold times or temperatures was found to lead to grain growth; the maximum temperature being just within the α phase and a hold time to reach temperature uniformity across sample were found to be ideal. The refinement mechanism relies on this short-term exposure to temperatures above the α transus as the γ lamellar does not have the time to completely dissolve, these γ precipitates prevent unrestricted α grain growth during the heat treatment and are then nucleation sites for the new lamellar grains to form upon cooling [113],[109].

In this work the CHT process does not return to room temperature (RT) but to 800 °C, still in the same $\alpha_2+\gamma$ phase as RT, to cut down processing time and improve energy efficiency. Furnace and air cooling (FC, AC) were applied to achieve different pre-compression microstructures. These conditions are referred to as furnace-cooled cyclic heat treatment (FCCHT) and air-cooled cyclic heat treatment (ACCHT), described in greater detail in 3.1.7.

In the present study, CHT is investigated as a pre-compression heat treatment compared to HH alone. The CHT process has been shown by others to produce both γ_f dominant microstructures from air cooling, compression of γ_f is not well documented and will be examined in section 5.1.2.3., and the more familiar refined fully lamellar microstructure (RFL) on a smaller scale. Both could improve the rate of globularisation by reducing lamellar content, its size and maintaining elemental homogeneity, which could subsequently return a material with a better forging outcome from secondary processing. [58],[122].

5.2.2 Results and discussion

5.2.2.1 Pre-compression processing and microstructures

Microstructural analysis was conducted on 4822 alloy in the three starting material conditions already discussed; HH, ACCHT and FCCHT, to assess the influence of CHT on the microstructure. From optical microscopy, lamellar grain dimensions as well as lamellar, feathery γ (γ_f) and equiaxed γ (γ_{eq}) fraction, were determined.

The starting condition, HH, seen in Figure 65a, leaves a largely fully lamellar (FL) microstructure, at 89 % lamellar content with 12 % γ_{eq} at lamellar grain boundaries, with a large average lamellar grain size of 1059 μm . Figure 68a shows these lamellar grain sizes obtained from OM image processing in comparison to CHT material, details in Table 29.

The CHT process, shown by the temperature-time profile in Figure 66 obtained from pyrometer monitoring, shows the different temperature pathways for both air cooled (AC) and furnace cooled (FC) cyclic heat treatment (CHT). Operation of this equipment was a manual process, hence timings at 1370 °C do differ between cycles, as do maximum temperatures between cycles. An automated system would be desirable for reproducibility but may prove difficult with the rapid heating and cooling rates seen in the process. Details of each cycle are shown in Table 28, with further details in the appendix.

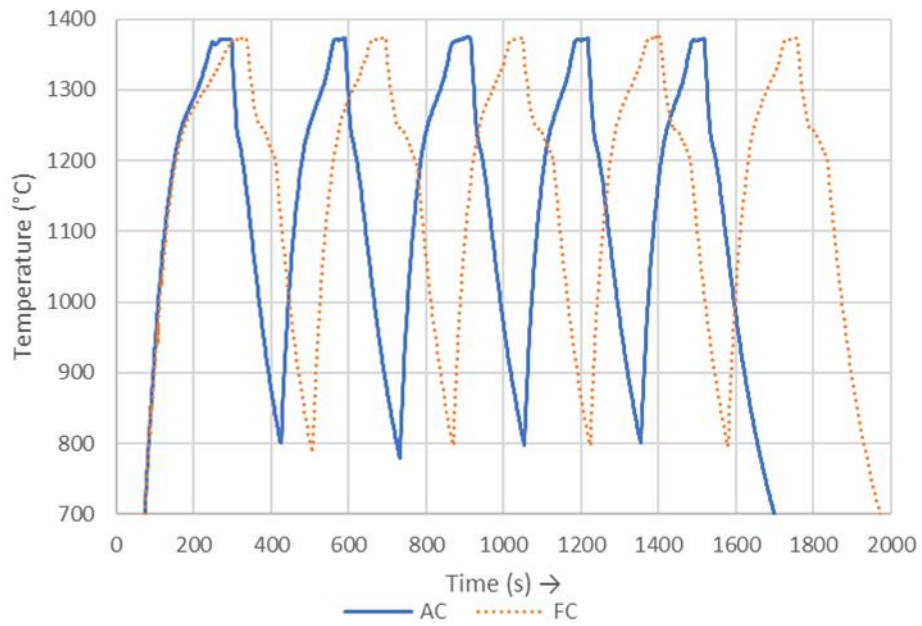
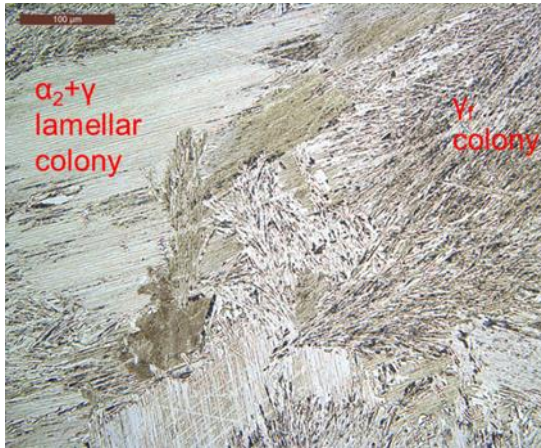


Figure 66: Recorded temperature-time profile of (AC) air cooled cyclic heat treatment and (FC) furnace cooled cyclic heat treatment from LAND instruments pyrometer.

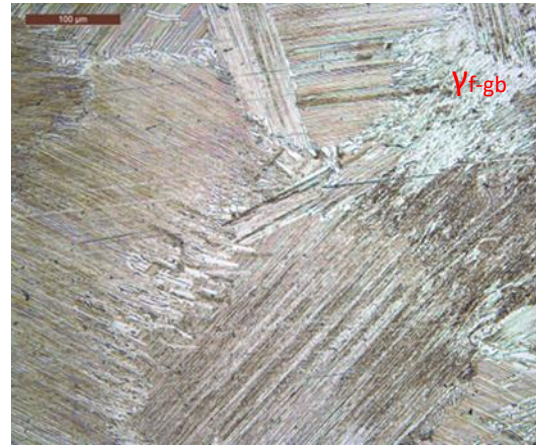
Material	Avg. heating rate (°C ⁻¹) over five cycles		Max temperature (°C) recorded on each cycle					Avg. hold time above 1370 °C over five cycles (sec)	Avg. cooling rate (°C ⁻¹) over five cycles		
	800-1200 °C	1250-1370 °C	1371.6	1372.8	1374.1	1372.2	1372.5		1370-1250 °C	1250-1200 °C	1200-800 °C
ACCHT	7.3	1.7	1371.6	1372.8	1374.1	1372.2	1372.5	30.4	8.8	3.2	3.8
FCCHT	7.3	1.4	1373.0	1374.9	1374.0	1374.7	1373.7	31.0	3.8	1.2	4.2

Table 28: CHT details for both FC and AC from pyrometer temperature monitoring

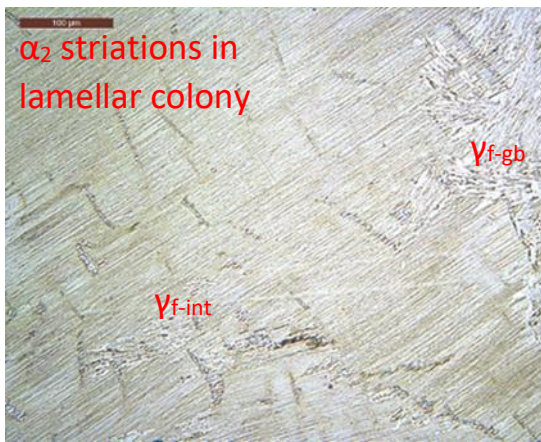
a



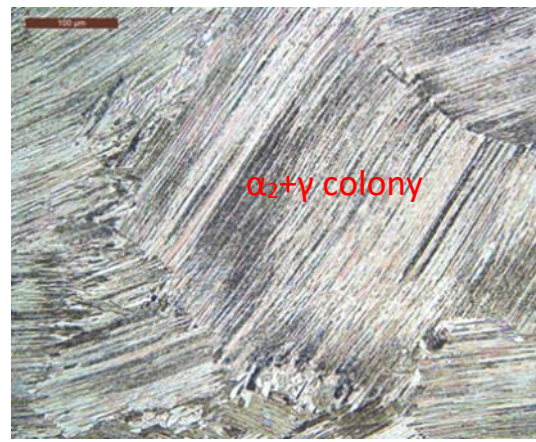
b



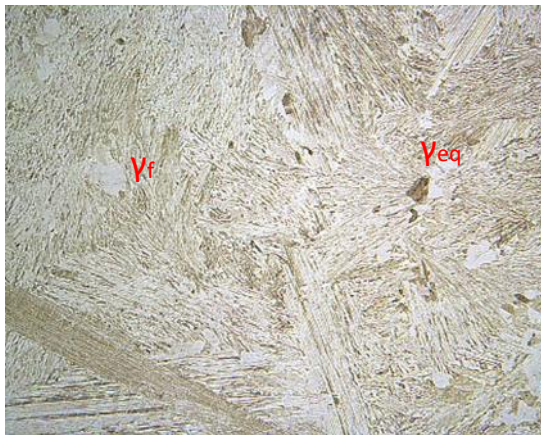
c



d



e



f



Figure 67: OM images of 4822 alloy in the ACCHT (a, c, e), FCCHT (b, d, f), condition at 20x magnification. (a, b) at Face 1, (c, d) at the centre, (e, f) at Face 2.

Of interest is the change in both heating and cooling rate seen from ~1250 °C upon heating, then cooling from 1250- 1200 °C, in all cycles, with no change in voltage at this point. This would suggest there is a change in the thermophysical properties of the alloy within this range, perhaps a change in

Position analysed	Face 1				Centre					Face 2			
	% α_{lam}	% γ_{eq}	% γ_f	Avg. lam. Size (μm)	% α_{lam}	% γ_{eq}	% γ_f	Avg. lam size (μm)	SD avg. lam size (μm)	% α_{lam}	% γ_{eq}	% γ_f	Avg. lam. Size (μm)
HH	-	-	-	-	88	12	0	1059	622	-	-	-	-
ACCHT	40	0	60	229	69	0	31	761	353	33	0	67	191
FCCHT	84	0	16	243	86	0	14	369	131	91	0	9	455

Table 29: Microstructural details of 4822 material conditions investigated pre-compression from optical microscopy analysis.

phase composition would explain this. This was likely the change from an α dominant material to γ dominant for cooling, and vice versa for heating, as shown by the phase diagram in Figure 65b.

With CHT the homogeneity of microstructural change also needs considering because of the nature of induction heating. Only the surface region will heat with induction, the interior heating through conduction from the skin [168]. This is known as the skin effect.

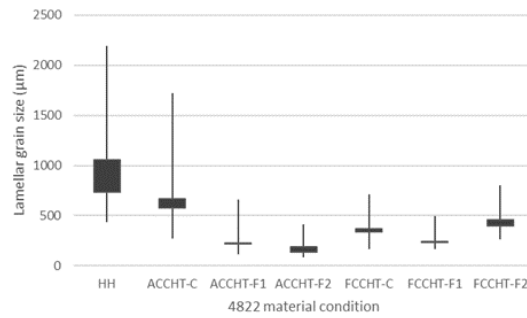
The degree of skin effect depends on the working frequency, electrical and magnetic properties of the sample, and the geometry/shape of the workpiece.

The skin or penetration depth (δ , using coefficient 503 for value in m) can be calculated using the following formula:

$$\delta = 503 \sqrt{(\rho / (\mu_r * f))}$$

where f is the induction heating frequency in Hz, ρ the electrical resistivity of the alloy 4822 (ohm metre, $\Omega * m$) at that temperature [169]. The μ_r is the unitless relative magnetic permeability. For paramagnetic alloys, such as 4822, μ_r is slightly >1 at room temperature, μ_r falls to unity with temperature, as such unity is used [168]. Based on this the δ for 4822 alloy with the CHT conditions discussed is anticipated to be in the region of 1.9 - 2.5 mm.

a



b

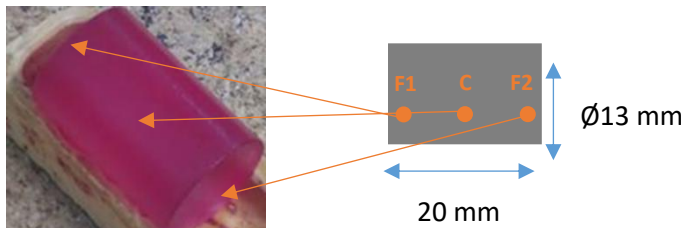


Figure 68: (a) Lamellar grain size, (b) Compression sample ready for ACCHT or FCCHT with glass-based coating, - C= centre, -F1= one face, -F2= the opposite face to F1 for post heat treatment analysis

The insulating effect of the alumina jig holding the sample as well as the need for faces to be exposed for the pyrometer to monitor the temperature should also be considered when the temperature across the workpiece is considered. ACCHT and FCCHT are both analysed at three sites, the centre of the sample (-C), and at both flat faces (-F1 and -F2), as detailed in Table 29.

Both CHT sequences result in a microstructure absent of equiaxed material, consisting of refined lamellar grains and γ_f . Figure 67. With ACCHT, γ_f has formed at both grain boundaries (γ_{f-gb}) and within lamellar grains (γ_{f-int}). The fraction of γ_f throughout the ACCHT sample being similar at the faces but the fraction flipping to largely lamellar dominant at the centre of the sample, suggesting formation of γ_f is dependent on cooling rate. FCCHT shows a more homogeneous microstructure, with lamellar fraction dominant and γ_f relatively constant in comparison and only present at grain boundaries.

The extent of grain refinement identified by *Wang et al.*, described in 5.2.1, is not seen in this study. This could be for several reasons; including that the CHT process does not return to RT, but to 800°C, though still in the same $\alpha_2+\gamma$ phase field as at RT. This is practically beneficial in terms of cutting down processing time and improving energy efficiency.

However, average lamellar grain size is still reduced with both CHT sequences across the work piece compared to HH material, Figure 30a-b. Lamellar dimensions and morphology contributions are homogenised across the work piece with FCCHT, suggesting temperature uniformity in the FCCHT cycle. This is not the case with ACCHT. The microstructures produced appear heavily influenced by the cooling rate, as identified by *Wang et al.*, with the FCCHT treatment, leading to less γ_f forming, any

present being in a γ_{f-gb} form, Table 29. Lamellar colonies are the dominant morphology across the FCCHT material. The FCCHT material could be described as a refined fully lamellar (RFL) microstructure, much sought after for final material properties of toughness and ductility, where a small lamellar grain size of the fully lamellar microstructures resists crack initiation and growth [7],[170],[27].

With ACCHT, the microstructure is more heterogeneous in comparison to HH or FCCHT, with differences in morphology fraction across the workpiece, consisting of $\gamma+\alpha_2$ lamellar colonies and γ_f . The γ_f present in ACCHT is in both forms, γ_{f-gb} and γ_{f-int} , the γ_{f-int} apparent at F1 and F2, this appearing to nucleate at the centre of lamellar grains in ACCHT material. This agrees with the findings of *Dey et al.*, regarding the γ_f form being dependent on cooling rate, this supports the idea that the temperature across the piece was not uniform. This was an issue anticipated with the fast-cooling rates of induction heating and the skin effect, but one which could be mitigated with further refinement and modelling of the thermal cycle. As the δ is anticipated to be in the region of 1.9-2.5 mm depth for this alloy, which will lead to a more uniform temperature across the workpiece compared to CHT of steels, the skin effect is unlikely to be the cause of temperature heterogeneity in this material and at this scale [168],[42]. Little lamellar grain refinement at the centre of ACCHT material is apparent in comparison to FCCHT at the centre, Table 29. This is anticipated to be due to the fast heating and cooling rates seen with induction heating at the monitored surface of the workpiece, not being reflected at the centre. In comparison the temperature oscillations with each cycle will be dampened at the centre, with the temperature not reaching the α phase [109],[110]. Two other observations support this theory. The striations of α seen in the OM image Figure 67c, all in the same direction, would suggest the α phase has begun to grow into the γ laths of the $\gamma+\alpha$ lamellar grain but the dominant γ laths cannot be described as a precipitate so do not nucleate new grains upon cooling [109]. Additionally, uniform lamellar grain refinement is only enabled by the combination of sufficient time within the α phase to dissolve γ to form a precipitate and slower/less sudden cooling of FCCHT, to allow the lamellar morphology to form [113].

5.2.2.2 Primary compression of CHT material compared to HH

The CHT process has been shown to produce a refined fully lamellar microstructure (RFL) together with elemental homogeneity on a smaller scale. Both are proven to promote globularisation of lamellar content, this could ease the replacement of the anisotropic lamellar morphology with recrystallised material, which could improve forging efficiency for primary upsetting and subsequently return a material in a better condition for improving outcomes for secondary wrought processing [58],[122]. The overall extent of globularisation, is assessed by monitoring the lamellar content as well as size and the dynamic recrystallised fraction (X-DRX), both are of interest as indicators for improving forging outcomes. Both static and dynamic globularisation or recrystallisation (SRX and DRX, respectively) can occur as strain energy and dislocation density can be imparted during CHT, these

control the rate of globularisation [148]. The forging outcome is assessed in section 5.2.2.3 by taking the secondary processing strain rate sensitivity, due to the difficulty in processing this alloy at faster strain rates before refining further and assessing the resulting microstructure of each material condition after primary and secondary compression.

The impact of the presence of γ_f will be discussed in the next section 5.2.2.2.1

5.2.2.2.1 Primary compression behaviour

Each curve follows a similar pattern for each 4822 condition, with steep initial work hardening due to rapid dislocation pile up in the γ laths only slowed by a critical strain (ϵ_c) being reached, high stored energy in the fragmented lamellar material initiating rapid DRX, hence the relatively sharp peaks seen here and in working other TiAl alloys, such as 45XD. This is quickly followed by peak flow stress (σ_{pfs}), within 0.02 ϵ of the critical strain; flow stress softening with increasing ϵ , seen in Figure 69 This can be explained by several processes. Compression of fully lamellar material leads to fragmentation and kinking of these morphologies, as seen in OM images in 5.2.2.2.2. With strain and time DRX will proceed leading to further softening, as reviewed by *Seetharaman and Semiatin* [25].

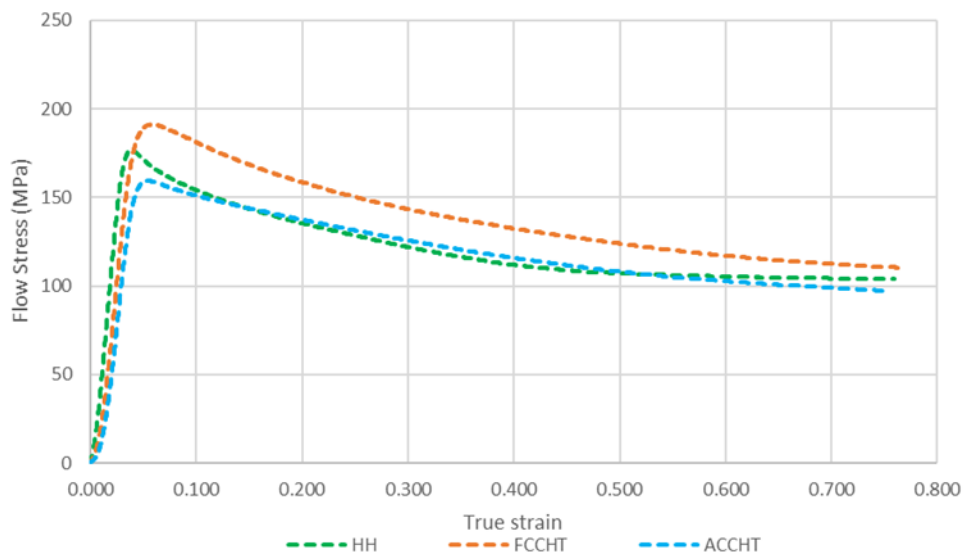


Figure 69: Primary stress-stain curves of the three material conditions under compression at 1100 °C to 50% at $0.001s^{-1}$ over 760 seconds.

There are differences in the flow curves of the three material conditions, values of σ_{pfs} , ϵ_c and the abruptness of softening are of interest when considering stable material flow. FCCHT shows the highest value of σ_{pfs} and extent of flow softening upon compression, ACCHT showing the lowest σ_{pfs} . All CHT material shows stable material flow under these compression conditions. HH material has non-uniform deformation under these compression conditions, with the highest rate of strain hardening, earliest ϵ_c and the highest level of flow softening, characterising its flow behaviour. Table 30 exhibits these compression samples, with HH material showing compression instability.


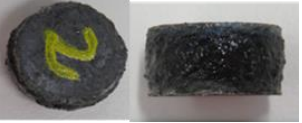
Material condition	HH	ACCHT	FCCHT
σ_{pfs} - peak flow stress (MPa)	176.6	159.3	191.1
Primary compression samples			

Table 30: Compression behaviour values for each material condition over 760s compression at 1100 °C and 0.001 s^{-1}

With heating to the compression temperature and soaking for 5 minutes (1100 °C, high $\gamma+\alpha_2$), the packets of γ_f present in the ACCHT material, present as both $\gamma_{f\text{-int}}$ and $\gamma_{f\text{-gb}}$ forms, largely transform to fine γ_{eq} grains, as in Figure 70 and Figure 31.

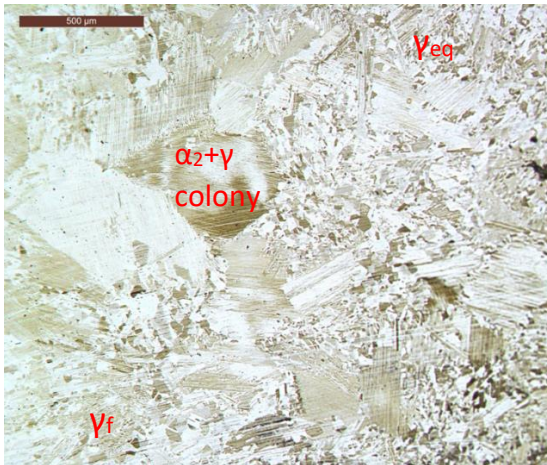


Figure 70: OM image at the Face 1 of 4822 alloy in the ACCHT condition at 5x magnification after water quench from the compression thermal cycle at 1100 °C, with a 5-minute soak.



Figure 71: OM image at the Face 1 of 4822 alloy in the ACCHT condition at 5x magnification

Phase morphology	%Lam	% γ_{eq}	% γ_f	Avg. lam. Size (μm)	SD avg. lam. Size (μm)
ACCHT Face 1	40	0	60	229	120
ACCHT Face 2	33	0	67	191	100
ACCHT + compression thermal cycle Face 1	37	57	7	184	122

Table 31: Microstructural details of 4822 material conditions investigated after cyclic heat treatment and water quench from the compression thermal cycle at 1100 °C, with a 5-minute soak.

The $\gamma_f \rightarrow \gamma_{\text{eq}}$ transformation is exploited in non-wrought grain refinement processing, by Yim *et al.* and Hu and Yang *et al.* applying annealing heat treatment at the high end of the $\gamma+\alpha$ phase region

[171],[112]. The $\gamma_f \rightarrow \gamma_{eq}$ transformation is due to the inherent instabilities of the γ_f microstructure from its initial formation. *Dey et al.* identify the initial packets of γ_f as being chemically unstable, with higher localised strain compared to prior lamellar morphologies, which subsequently drives the transformation into globular morphologies, almost to completion, as seen in this study [42]. The high γ_{eq} content and lack of lamellar morphologies to globularise at the outer edges of work would explain the low σ_{pfs} seen with compression.

5.2.2.2.2 Primary compression microstructure

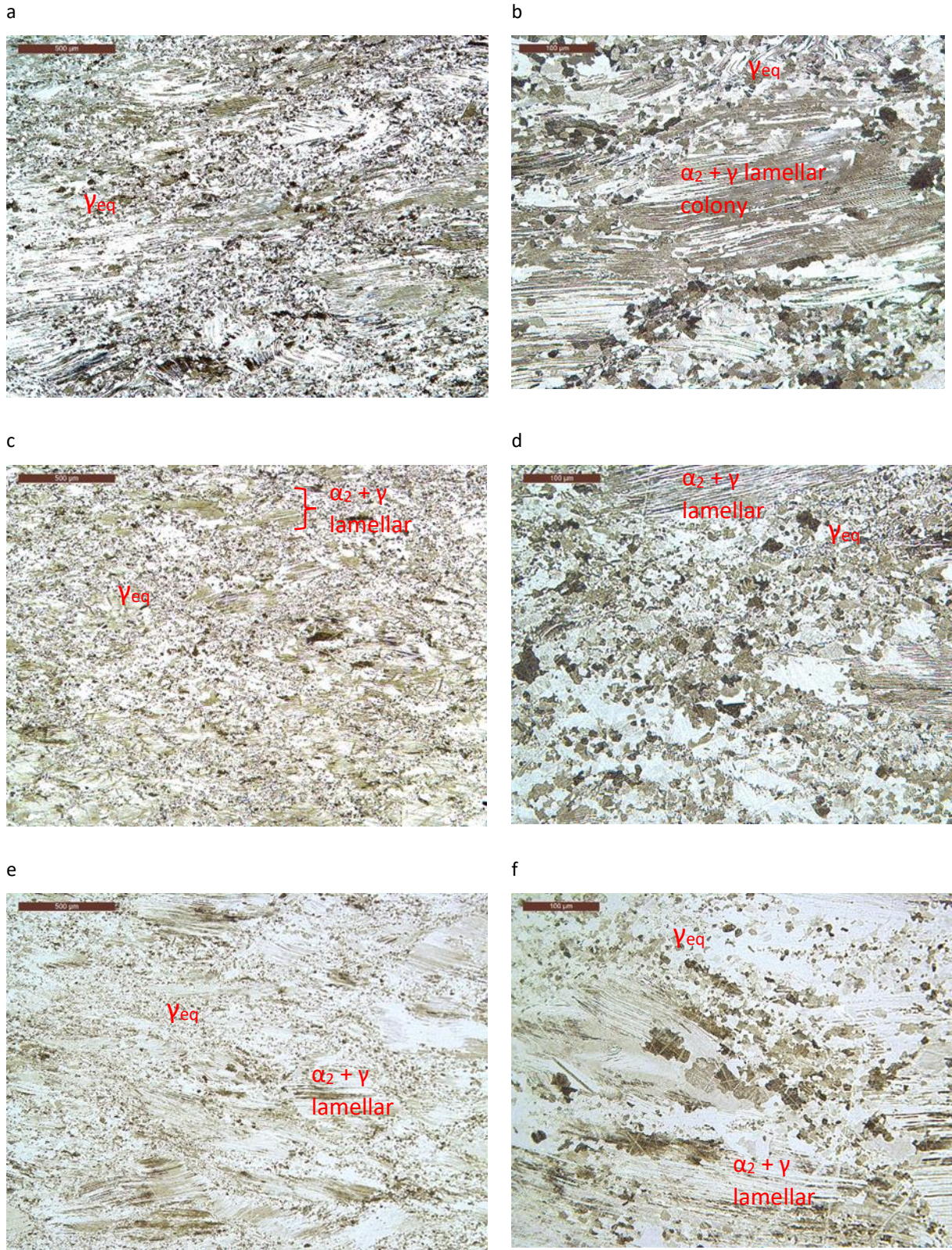


Figure 72: OM images at P1 (centre) of 4822 alloy in the HH (a, b), ACCHT (c, d), FCCHT (e, f) condition at 5x magnification (a, c, e) and 20x magnification (b, d, f) after 50% primary compression at 1100 °C, 0.001 s⁻¹.

As Figure 72 shows, each material returns a microstructure still containing lamellar morphologies after primary compression. Recrystallised and deformed material can be seen to necklace the large remnant lamellar grains, with different X-DRX for each compression material. The content and details of the remnant morphologies are shown in Table 32.

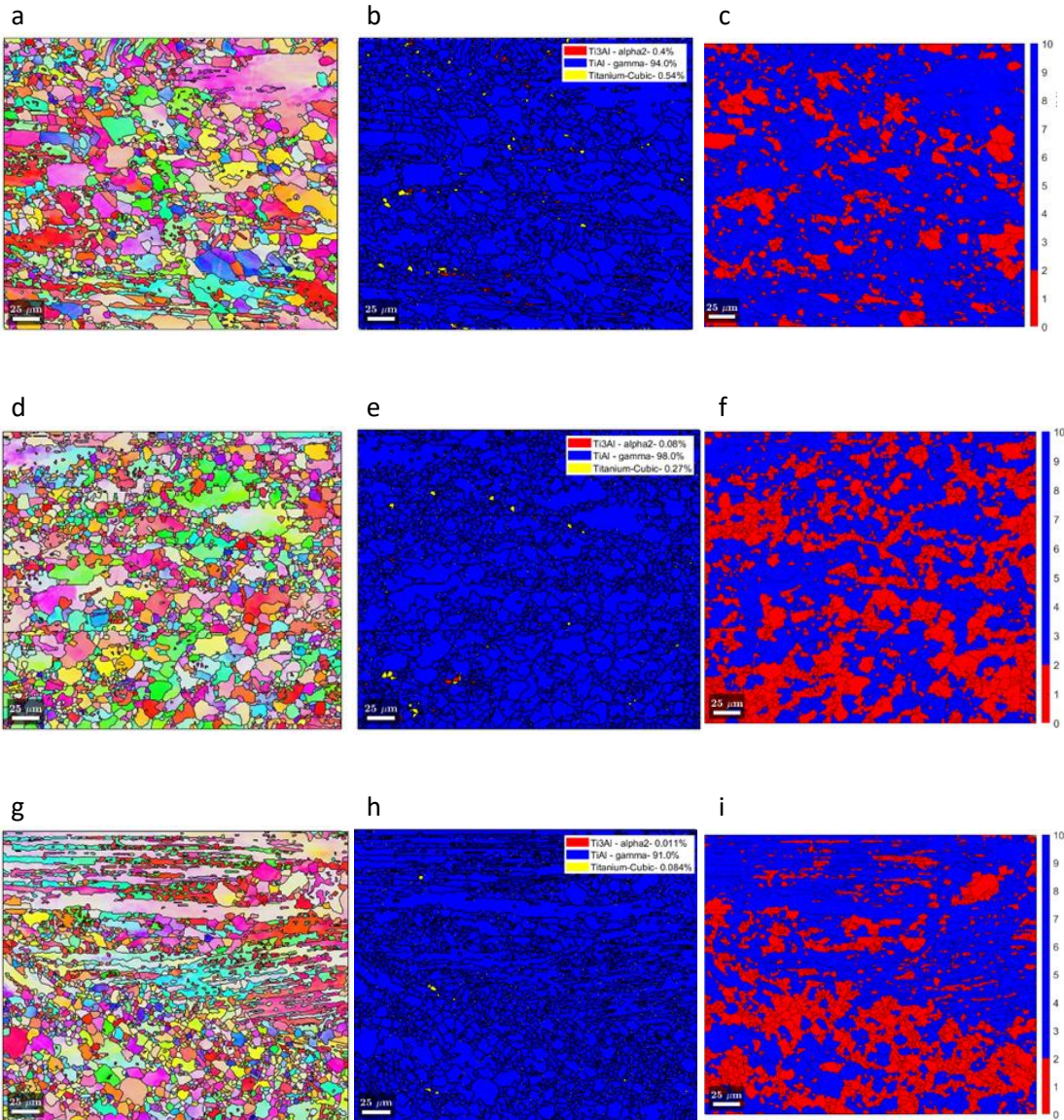


Figure 73: EBSD used to give maps to identify grains of similar orientation (a, d, g) , phase fraction (b, e, h) and X-DRX maps (c, f, i) of 4822 alloy in the HH (a, b, c), ACCHT (d, e, f), FCCHT (g, h, i) condition at P1 (centre) 500x magnification, after 50% primary compression at 1100 °C, 0.001 s⁻¹.

4822 material condition(s^{-1})	$\%v_{eq}$	$\%l_{lam}$	Average lamellar grain size (μm)	SD average lamellar grain size (μm)	X-DRX (%)	Grain area fraction $\leq 50\mu m^2$ (%)
HH 0.001 P1	56	44	350	173	23	30
HH 0.001 P2	51	50	296	164	29	14
ACCHT 0.001 P1	71	29	222	146	45	36
ACCHT 0.001 P2	84	16	171	131	55	52
FCCHT 0.001 P1	56	44	266	132	35	38
FCCHT 0.001 P2	55	45	271	159	22	23

Table 32: Morphology fraction for each material after 50% primary compression at 1100 °C and 0.001 s^{-1} calculated from OM and EBSD analysis.

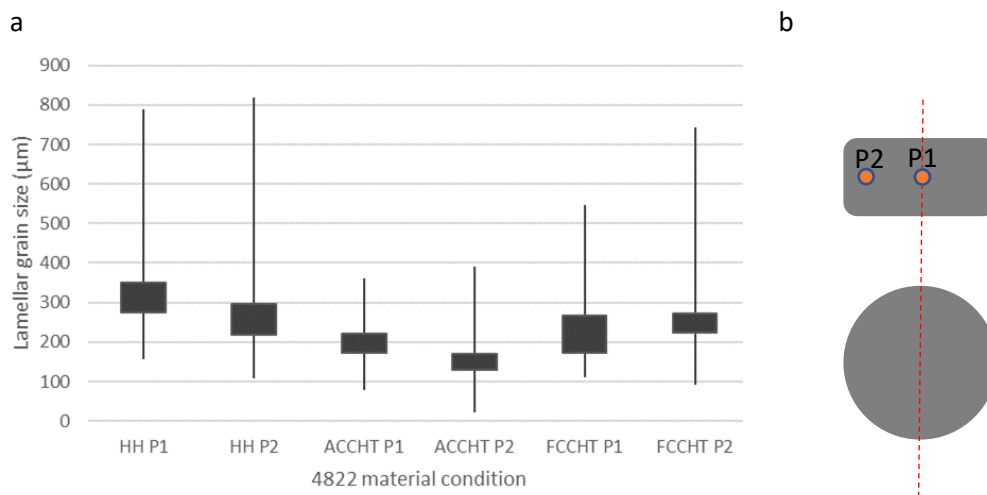


Figure 74: (a) Remnant lamellar grain area analysis of maximum, minimum and inter-quartile range of each material condition at P1 and P2 after 50% primary compression at 1100 °C and 0.001 s^{-1} . (b) positioning of analysis

The X-DRX, calculated via the grain orientation spread (GOS) approach is shown in Figure 75a, c, e. Following this method, those grains with less than or equal to 2° spread within the grain are deemed to have been recrystallised, above this they are considered deformed. In addition to this the grain area frequency, is shown in Figure 75b, d, f, for HH, ACCHT and FCCHT respectively.

ACCHT returns the highest X-DRX fraction at both P1 and P2, of 45 % and 55 % respectively, together with the lowest overall lamellar content at 29 % for P1 and 16 % at P2, these lamellar structures being of the smallest grain size as shown by Figure 74a. HH material shows the highest lamellar content at P1 with 44 %, with the largest spread of lamellar grain size and the lowest X-DRX fraction, at 23 %.

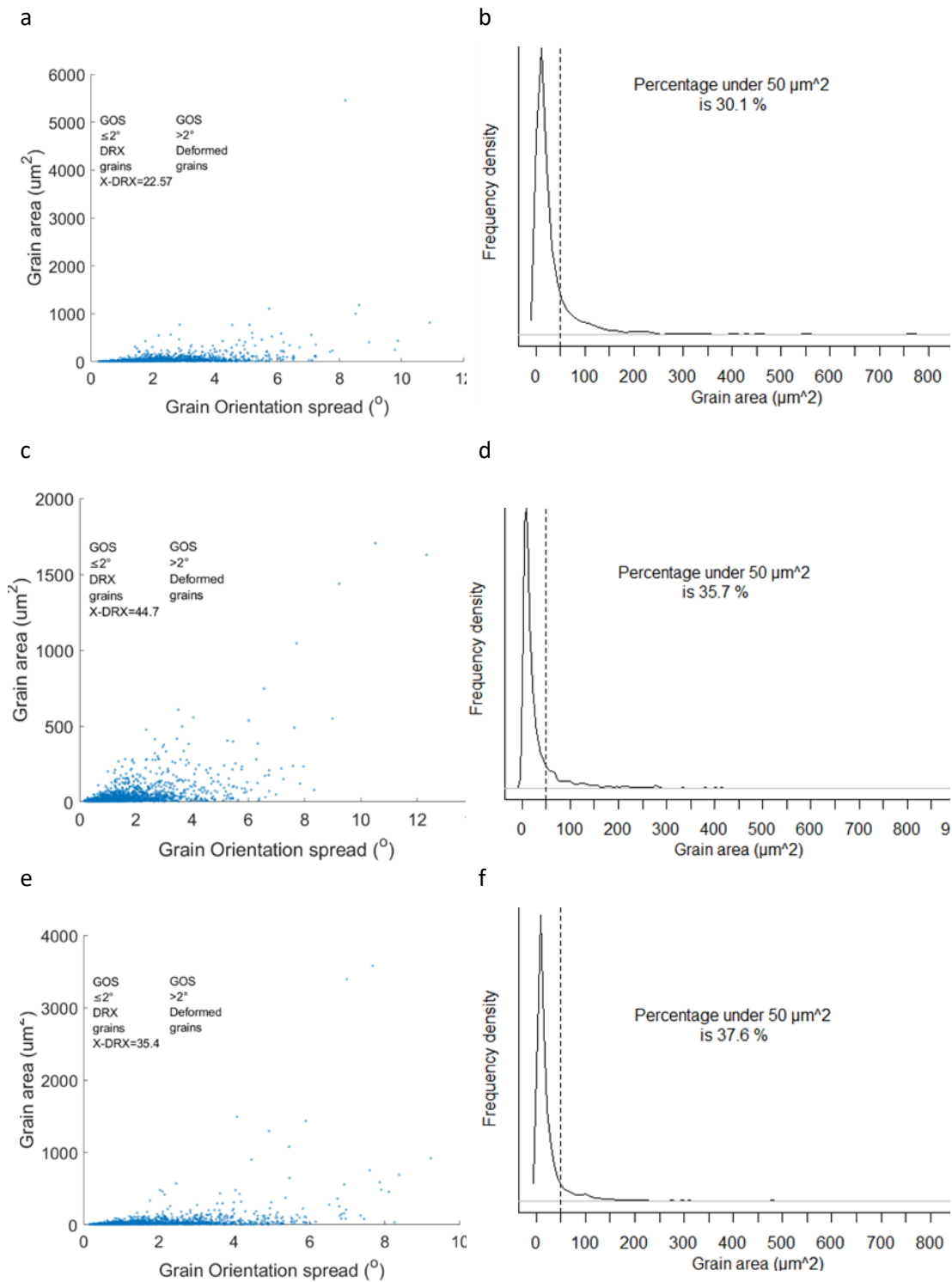


Figure 75: Plots calculating the DRX fraction from the GOS approach on the left, grain area frequency density on the right, for each material condition at P1 after 50% primary compression at 1100 °C and 0.001 s⁻¹, (a, b) HH, (c, d) ACCHT, (e, f) FCCHT

The X-DRX tends to be dependent on the initial lamellar colony size, this is due to grain boundaries acting as nucleation sites for globular morphologies, high lamellar-lamellar grain boundary density

being preferred for globularisation [58]. *Semiatin, Seetharaman and Weiss* reviewed earlier work looking at the relationship between starting microstructure, flow softening rate, recrystallisation and flow localisation [47]. The authors identified that the lamellar characteristics, especially lamellar grain sizes, were the most significant factor influencing the reduction of the flow stress, with *Semiatin, Seetharaman and Ghosh* identifying the effect grain size and strain rate has on the fraction globularised [24]. Another factor in the X-DRX and fraction globularised is the heterogeneous strain distribution across the work piece [80]. This is shown by the microstructural analysis of lamellar content at P1 and P2; Table 32.

The HH material shows the highest lamellar grain sizes in this study, this returns non-uniform deformation under these compression conditions, with the highest rate of strain hardening, earliest ϵ_c and steepest degree of flow softening, characterising its flow behaviour. As geometry, die, lubrication and compression conditions were the same across the three tests this is a sign of flow localisation caused by the large grained fully lamellar microstructure [117],[118],[119]. The flow localisation then leads to poor conditions for globularisation, the post-compression HH material returning the highest lamellar content and size values at both P1 and P2.

The homogenous refined fully lamellar microstructure of FCCHT material returns higher X-DRX than HH at P1, as well as the highest fraction of grain area $\leq 50 \mu\text{m}^2$ and smaller remnant lamellar colonies at P1 and P2. The higher X-DRX and grain area $\leq 50 \mu\text{m}^2$ values are due to the initial higher grain boundary density than HH, as discussed above. However, there are similar post compression lamellar content values for FCCHT and HH, Table 32. These remnant lamellar grains, perpendicular to compression, could be difficult to globularise with further processing [163],[144],[164].

As already discussed in 5.2.2.2.1 the γ_f present in ACCHT material transforms to γ_{eq} upon heating to compression temperature, however it is still relatively heterogeneous, with lamellar morphologies present to differing degrees depending on the cooling seen across the sample, Table 29. Given that lamellar-lamellar grain boundaries support globularisation, the heterogeneous microstructure at the faces does not appear to be detrimental to the microstructural outcome, resulting in a microstructure across P1 and P2 with the lowest remnant lamellar size and content, together with highest X-DRX, highest at P2.

With ACCHT material at P1, the higher extent of globularisation and X-DRX, compared to HH, is likely to be due to the initial grain refinement offered by CHT compared to HH alone, higher lamellar-lamellar grain boundary density leading to improved conditions for globularisation. Compared to FCCHT, looking at results in 5.2.2.1 a higher X-DRX would be predicted for FCCHT at P1, when considering the influence of low lamellar grain size and high lamellar-lamellar grain boundary density has on globularisation. However, this is not the case, conversion of any γ_{f-gb} material at P1 in ACCHT material to γ_{eq} upon compression may contribute to the higher X-DRX value for ACCHT compared to FCCHT.

5.2.2.3 Secondary compression of CHT material compared to HH

5.2.2.3.1 Secondary compression behaviour

The secondary compression stress-strain curves at Figure 76a, show a similar profile to that of primary compression was followed i.e., strain hardening to a peak flow stress followed by flow softening. The peak flow stresses increased with strain rate for each material. With a strain rate of 0.001 s^{-1} all material moved towards a near steady-state flow stress of between 90-100 MPa with increasing strain during secondary compression. The ACCHT material showed the lowest steady state stress; it is assumed that the steady state condition would correspond to a quasi-stable microstructure being achieved [54].

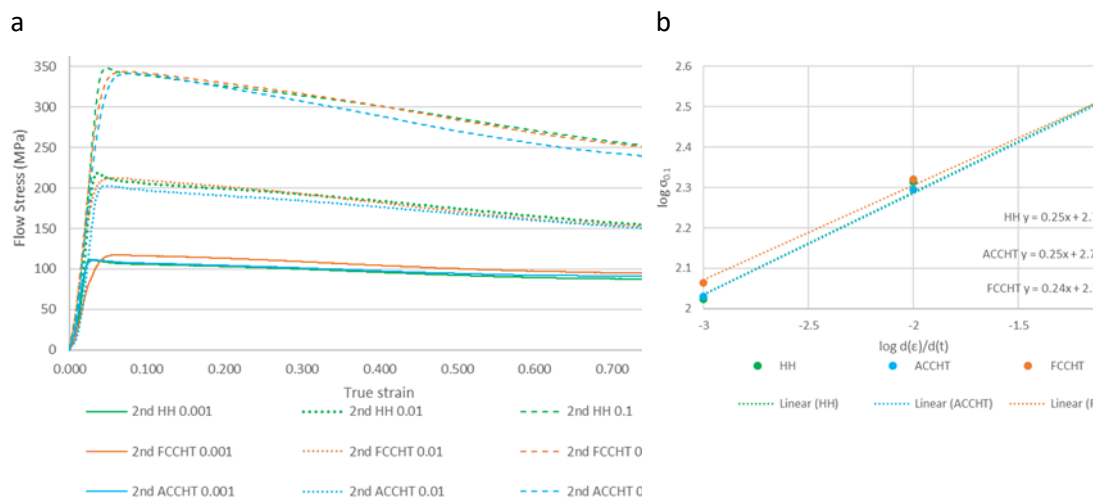


Figure 76: Secondary stress-strain curves (a) of the three material conditions under compression at 1100 °C to 50% at 0.001s^{-1} over 800 seconds, 0.01s^{-1} over 80 seconds, 0.1s^{-1} over 8 seconds. Calculation of strain rate sensitivity (m) for each material for secondary compression (b).


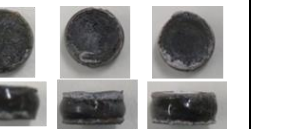
Material condition	HH			ACCHT			FCCHT		
Strain rate (s^{-1})	0.001	0.01	0.1	0.001	0.01	0.1	0.001	0.01	0.1
σ_{pfs} - peak flow stress (MPa)	111.7	218.9	348.5	111.2	202.8	341.5	117.3	212.4	343.6
m at $\epsilon_{0.1}$	0.25			0.25			0.24		
Secondary compression samples									

Table 33: Compression behaviour values, peak flow stress and strain rate sensitivity for each material condition over secondary compression at 1100 °C to 50% at $0.001s^{-1}$ over 800 seconds, $0.01s^{-1}$ over 80 seconds, $0.1s^{-1}$ over 8 seconds.

Secondary compression strain rate sensitivity, m , as in 5.1.2.4, does not give a clear picture on its own in this study. None of the 4822 material conditions, HH, ACCHT or FCCHT achieves the targeted m of ≥ 0.3 at $\epsilon_{0.1}$ using these compression conditions. It is likely that only compression of this alloy at higher temperatures would increase m ; this was generally found in *Fuchs'* work, due to nucleation and growth of dynamic recrystallised grains being temperature driven, easing dislocation destruction [146].

From Figure 76b and Table 33, HH and ACCHT shows the same m value at 0.25, with FCCHT showing the lowest m value from $\sigma_{0.1}$ in secondary compression at 0.24. The HH material shows the steepest degree of strain hardening with each strain rate, with a definite sharp peak at σ_{pfs} . However, there appears to be unstable material flow with all samples at 0.01 and $0.1 s^{-1}$. Flow localisation and shear of the HH sample is visible in microstructural analysis, with abnormal barrelling seen with the samples of ACCHT and FCCHT, as illustrated in Table 33. This is likely to be due to the HH primary compressed material containing the largest remnant lamellar grains as well as lowest X-DRX and grain area fraction under $\leq 50 \mu m^2$. For these reasons the m value of 0.25 for HH should not be taken as a true representation of its strain rate sensitivity.

The FCCHT material shows the highest secondary σ_{pfs} at slow strain rates and lowest m , this may be due to the primary compressed FCCHT material containing larger remnant lamellar grains than ACCHT at both P1 and P2. The lamellar grains appeared to be resistant to globularisation in a similar fashion to the larger lamellar grains seen in HH material, perhaps due to the lath dimensions [144],[163].

Secondary compression of the ACCHT material has the lowest σ_{pfs} at all strain rates and an m equivalent to HH at 0.25. It is anticipated that m is being restrained here by the compression temperature rather than any remnant morphology.

5.2.2.3.2 Secondary compression microstructure

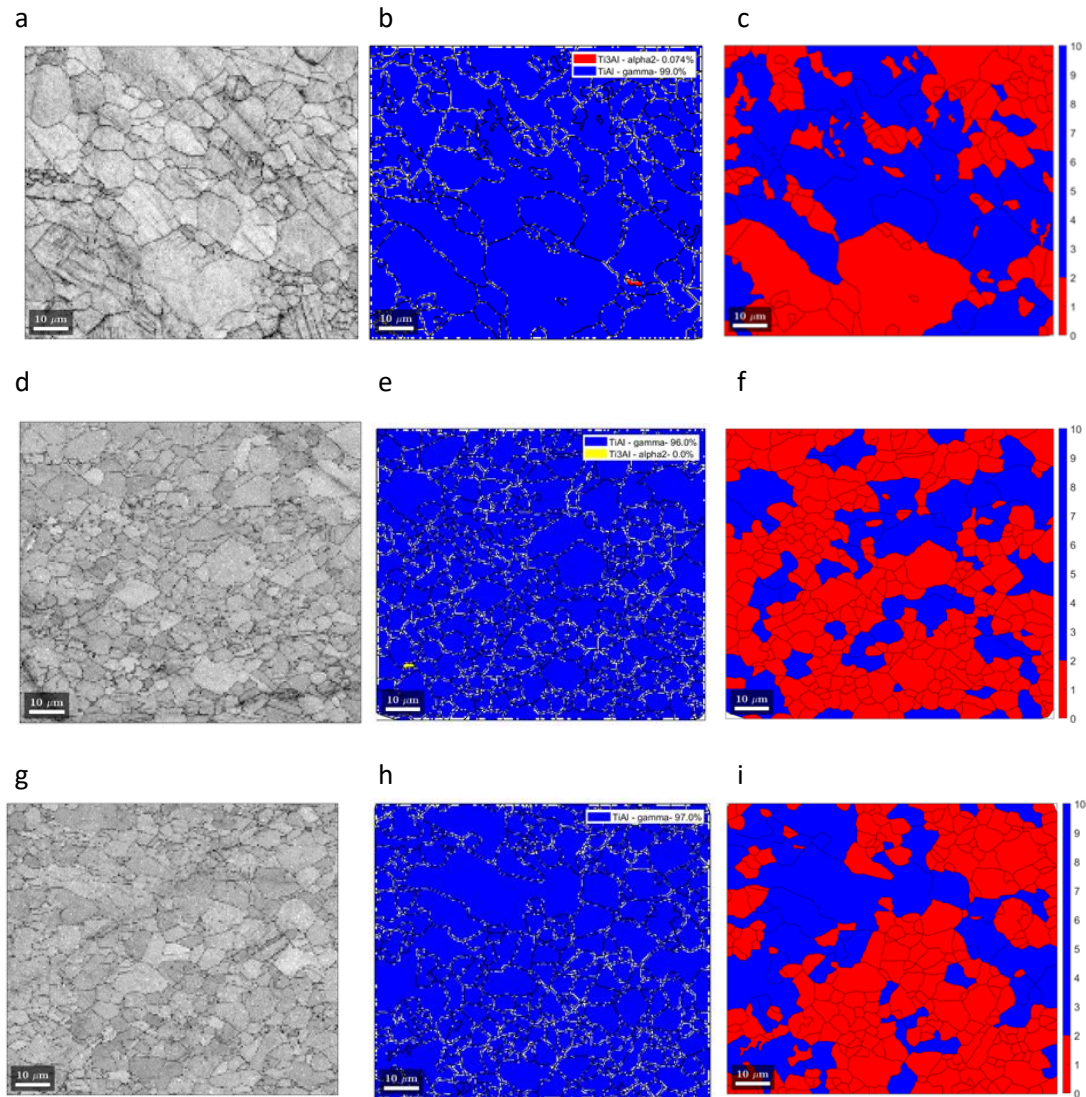


Figure 77: EBSD used to give maps of, (left) band contrast, (middle) phase map; blue is γ , red is α_2 , yellow is β_0 , (right) X-DRX; red is the recrystallised fraction, blue is deformed, of 4822 alloy in the HH (a, b, c), ACCHT (d, e, f), FCCHT (g, h, i) condition at 1600x magnification, after 50% secondary compression at 1100 °C, 0.001 s⁻¹.

The X-DRX maps, calculated via the grain orientation spread (GOS) approach, shown in Figure 77c, f, i, show ACCHT returning the highest X-DRX fraction at 66 %, with a strain rate of 0.001 s⁻¹ together with zero lamellar content. At the same strain rate, the FCCHT material was also lamellar free with 58 % X-DRX. The HH material gave the highest lamellar content at 7 % and the lowest X-DRX fraction, at 47 % for the same strain rate of 0.001 s⁻¹.

45XD material condition (s^{-1})	% _{Lam}	Average lamellar grain size (μm , from 0° and 90°))	SD of average grain size (μm)	% α_2	% β_0	% γ	X-DRX (%)	Grain area fraction $\leq 50\mu m^2$ (%)
HH 0.001	7	22	25	0	0	99	47	27
HH 0.01	28	66	74	0	0	90	50	54
HH 0.1	19	40	26	1	0	95	32	38
ACCHT 0.001	0	0	0	0	0	96	66	69
ACCHT 0.01	2	2	4	0	0	90	47	67
ACCHT 0.1	9	15	17	0	0	91	57	72
FCCHT 0.001	0	0	0	0	0	97	58	55
FCCHT 0.01	0	0	0	0	0	91	60	81
FCCHT 0.1	0	0	0	0	0	94	42	54

Table 34: Morphology fraction for each material after 50% secondary compression at 1100 °C, 0.001, 0.01 and 0.1 s^{-1} calculated from OM and EBSD analysis.

All material tested has returned average lamellar grain sizes below the 80 μm value suggested by Zhang *et al.* for facilitating further processing [147]. However, without CHT, remnant lamellar content is still present for each strain rate, X-DRX returned is lower at the slowest strain rate and the presence of adiabatic shear is also clear at the fastest strain rate.

To produce a microstructure of high X-DRX and low lamellar content, homogeneous compression is first required. From the present results it would appear that faster strain rates may be deleterious. Adiabatic shearing is present with HH at 0.1 s^{-1} , shown in appendix, this appears absent with secondary compression of CHT material, but can't be dismissed as a possibility with the large remnant lamellar grain structures from primary compression [167]. Considering the bulging obvious in compression samples in Table 33, it would suggest that adiabatic shear or flow localisation has occurred in all material other than at a strain rate of 0.001 s^{-1} . Adiabatic shear and flow localisation may explain the lack of any trend between strain rate and the remnant lamellar content and X-DRX returned.

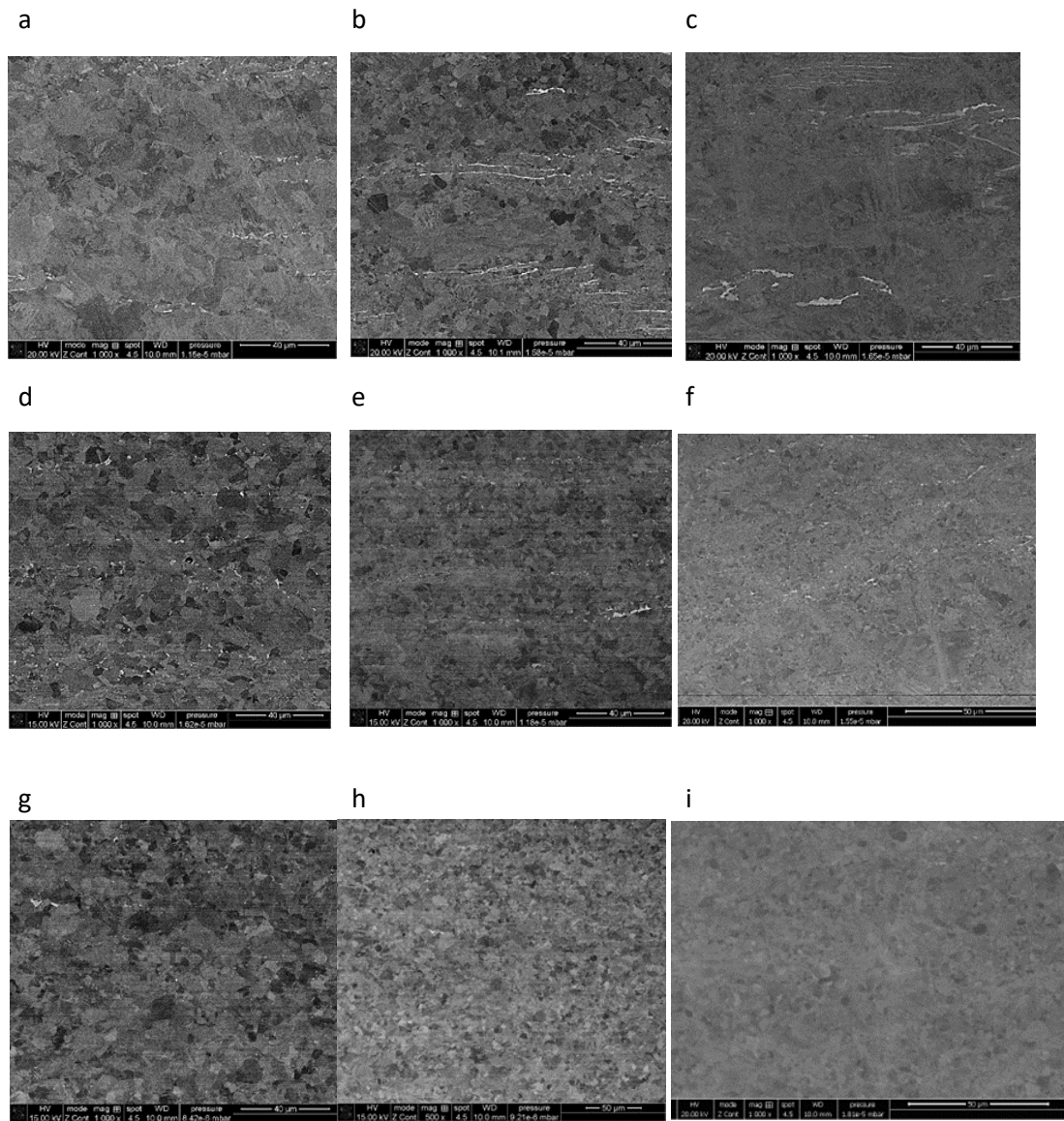


Figure 78: SEM-BSE used to give details of microstructural morphologies, (left) 0.001 s^{-1} , (middle) 0.01 s^{-1} , (right) 0.1 s^{-1} ; of 4822 alloy in the HH (a, b, c), ACCHT (d, e, f), FCCHT (g, h, i) condition at 1000x magnification, after 50% secondary compression at $1100\text{ }^{\circ}\text{C}$.

5.2.3 Summary

The prospect of using the CHT process as a replacement for wrought processing seems improbable based on the results of the present research, but it is likely that CHT could be applied as a complementary technology to improve forging outcomes. There is a considerable impact from cooling rate on the microstructure formed from CHT, with significant differences in microstructure with only a 2-5 °C⁻¹ difference between cooling rates of FCCHT and ACCHT, both being under 10 °C⁻¹. These cooling rates are only going to be practical at the outer surface of billet of any realistic scale. Induction heating processes tend to impact at the skin, as seen through the modelling on the induction heat treatment of Ti64 [172].

The CHT process investigated here has taken as-cast 4822 material in an unforgeable condition and made it forgeable at these compression conditions through initial grain refinement. Therefore, this type of pre-processing could be considered to improve forging outcomes and reduce forging steps for cast titanium aluminide with large lamellar microstructures by initial grain refinement as seen in FCCHT or removing lamellar material completely as with ACCHT. The CHT process could therefore be considered as a complementary technology to standard uniaxial and multi-axial forging to improve forging efficiency [80], [173].

This section set out to examine the possibility of improving the forging outcome of large grained fully lamellar cast 4822 by applying cyclic induction heat treatment. The following conclusions regarding the primary and secondary processing of 4822 alloy in the HH and CHT conditions are drawn:

- Hot isostatic pressing to remove porosity and consolidate the ingot does not return a microstructure best placed for optimising initial forging outcomes of primary initial ingot breakdown.
- Cyclic induction heat treatment (CHT) can provide both lamellar grain refinement through a controlled cooling rate (FCCHT) or largely γ_f via air cooling (ACCHT). The γ_f then transforms to γ_{eq} upon re-heating within the high $\gamma+\alpha_2$ phase region, i.e., 1100 °C. Both lead to successful compression under the primary compression conditions examined.
- The controlled cooling rates applied in this study (FCCHT), allow the time for a homogeneous refined fully lamellar material to form. This should generate good final material properties, but also leads to uniform i.e., stable, compression compared to the HH condition.
- The heterogeneous microstructure from air cooling, consisting of differing quantities of $\gamma+\alpha_2$ lamellar grains and γ_f across the work piece, does not appear to hinder primary or secondary processing at these conditions, resulting in high dynamic recrystallised fraction and low lamellar content.

5.3 Conclusions and industrial relevance for 4822

The work reported here has an emphasis on controlling and optimising the microstructure of 4822 (Ti-47.2Al-1.3Nb-1.83Cr at%) to improve the forging efficiency of primary ingot breakdown and provide high integrity, forged titanium aluminide stock ready for secondary processing. The following conclusions for this alloy were drawn:

- HIP and homogenisation (HMG) cannot be integrated for this alloy. The lack of grain refining alloy additions makes grain growth rapid and unrestricted at the temperatures used for HIP and HMG. With the dual stage traditional approach, the time at temperature and cooling rate from HMG can be investigated. These have been identified, in this work and by others, as the variables that influences lamellar grain size and controls lath thicknesses.
- Primary compression at 1100 °C, within the $\gamma+\alpha$ phase, leads to unsuccessful compression of the HIP and HMG 4822 alloy used in this study. The large initial cast grain structure, which is grown further by HIP and HMG, must be first refined before ingot breakdown (primary compression). This ingot was of industrial scale, with slow heating and cooling rates and unavoidable dwell times at temperature, the large lamellar grains present slow globularisation kinetics, as seen in this work, causing flow localisation and adiabatic shear at fast strain rates. Preventing the grain growth from casting may prove difficult or expensive at industrial scales i.e., cooling control from casting or using centrifugal casting techniques, so practical methods of rectifying the ingot before breakdown are of interest.
- Cyclic induction heat treatment (CHT) can be considered as a means of improving efficiency of ingot breakdown through five controlled cycles to a temperature just within the α phase (1370 °C) for 30 seconds. The cooling rate dictates whether the lamellar material is removed and replaced with γ_f or refined. Cooling rates from 1370- 1250 °C of 3.8 °C s^{-1} were found to remove lamellar material, 8.8 °C s^{-1} for refinement. Both lead to successful primary and secondary compression at industrially viable temperatures within $\gamma+\alpha_2$ phase region, i.e., 1100 °C, with a strain rate of 0.001 s^{-1} .

5.4 Future work recommendations for 4822

- The optimum combination of lath thickness and lamellar grain sizing for improving globularisation kinetics for 4822 alloy should be further explored. Refining the lamellar grain improves forging efficiency, as described in this work, however, control of lath thickness could aid globularisation, particularly at the primary compression stage, further still.
- Cyclic heat treatment using induction equipment could be one option for investigating combinations of lamellar grain sizing and lath thickness at an industrially relevant scale. As the equipment can be controlled in terms of times at temperature and cooling rate relatively easily. An automated system would improve reproducibility.
- With the strain rate sensitivity of the secondary compressed cyclic heat-treated material reaching 0.25 and being lamellar free, hot rolling and isothermal closed-die forging trials of this two-stage processed material should still be considered viable.

6 Contributions to knowledge

The contributions to knowledge of this work are summarised for each TiAl alloy worked on, the two alloys, 45XD and 4822, have been considered separately throughout this work and so are here.

- For 45XD alloy, it has been found that the HIP and HMG stages can be integrated into one process using HIP equipment without any negative effects on equipment or compression behaviour of this alloy. As well as removing a separate processing step, HMG, which uses costly vacuum furnace equipment, there is evidence that pressure and heat treatment above the α transus reduces the activation barrier required to reduce the brittle β_0 phase and the absence of an additional cooling stage restricts the opportunity for grain growth. This in turn improves the extent of globularisation of lamellar microstructures and returns a favourable dynamic recrystallised fraction for secondary processing. Integration has a negative impact on initial ingot breakdown for 4822 alloy.
- For 4822 alloy, these studies show that cyclic induction heat treatment, an equipment setup not previously used for pre-compression processing, can be considered as a means of improving ingot breakdown using five controlled heating cycles to just within the α phase (1370 °C) for 30 seconds. It was found that the cooling rate dictates whether the lamellar material is removed and replaced with γ_f or refined in lamellar grain size. Cooling rates from 1370- 1250 °C of 3.8 °Cs⁻¹ were found to remove lamellar material, 8.8 °Cs⁻¹ provided a refined fully lamellar microstructure. Both lead to successful primary and secondary compression at industrially viable temperatures within $\gamma+\alpha_2$ phase region, i.e., 1100 °C, with a strain rate of 0.001 s⁻¹.

Other contributions that are industrially relevant for each TiAl alloy include:

- Clarification of the importance of the homogenisation stage; much work is reported on both 45XD and 4822 alloys and other TiAl alloys without homogenising. It has its negative impacts, particularly on those alloys without doping with grain refining particles, but this work has highlighted the importance of this stage for workability and the materials efficient and homogeneous response to deformation.
- Integrating HIP and HMG stages is possible and could prove beneficial for other TiAl alloys but the alloy must be doped with grain refining particles such as borides to prevent excessive grain growth.
- From the literature review and this work, compression at 1100 °C appears ideal for 45XD alloy and the minimum temperature for 4822 alloy, with ingot material in similar condition. Anything but a strain rate of 0.001 s⁻¹ has a negative impact on compression behaviour and outcome i.e., globularisation kinetics and dynamic recrystallised material returned.

7 References

- [1] Schulze G.E.R., *Metallphysik*. 1967, Berlin: Akademie - Verlag, (1967).
- [2] R. Nesper, *Bonding Patterns in Intermetallic Compounds*, *Angew. Chemie Int. Ed. English*. 30 (1991) 789–817. <https://doi.org/10.1002/anie.199107891>.
- [3] J. Williams, G. Lutjering, *Titanium*, (2003) 1–18.
- [4] D.M. Dimiduk, *Gamma titanium aluminide alloys - An assessment within the competition of aerospace structural materials*, *Mater. Sci. Eng. A*. 263 (1999) 281–288. [https://doi.org/10.1016/S0921-5093\(98\)01158-7](https://doi.org/10.1016/S0921-5093(98)01158-7).
- [5] F.J. Appel, J.D. Paul, M. Oehring, *Gamma titanium aluminides*, 1981.
- [6] F. Appel, M. Oehring, J.D.H. Paul, C. Klinkenberg, T. Carneiro, *Physical aspects of hot-working gamma-based titanium aluminides*, *Intermetallics*. 12 (2004) 791–802. <https://doi.org/10.1016/j.intermet.2004.02.042>.
- [7] Y.-W. Kim, K. Sang Lan, *Advances in Gammalloy Materials–Processes–Application Technology: Successes, Dilemmas, and Future*, *Jom*. 70 (2018) 553–560. <https://doi.org/10.1007/s11837-018-2747-x>.
- [8] M.P. ed. Christoph Leyens, *Titanium and Titanium Alloys: fundamentals and applications*, 2013. <https://doi.org/10.1002/9783527649846.ch4>.
- [9] D.M. Dimiduk, P.L. Martin, Y.W. Kim, *Microstructure development in gamma alloy mill products by thermomechanical processing*, *Mater. Sci. Eng. A*. 243 (1998) 66–76. [https://doi.org/10.1016/S0921-5093\(97\)00780-6](https://doi.org/10.1016/S0921-5093(97)00780-6).
- [10] McCullough C., Valencia J.J., Levi C.G., Mehrabian R., *Phase equilibria and solidification in Ti-Al alloys*, *Acta-Metallurgica*. 37 (1989) 1321–1336. [https://doi.org/https://doi.org/10.1016/0001-6160\(89\)90162-4](https://doi.org/https://doi.org/10.1016/0001-6160(89)90162-4).
- [11] M. Werwer, R. Kabir, A. Cornec, K.H. Schwalbe, *Fracture in lamellar TiAl simulated with the cohesive model*, *Eng. Fract. Mech*. 74 (2007) 2615–2638. <https://doi.org/10.1016/j.engfracmech.2006.09.022>.
- [12] D.M. Dimiduk, P.A. Mcquay, Y. Kimt, *GAMMA ALLOY TECHNOLOGY 1999*, *Titan. '99 Sci. Technol.* (1999) 259–268.
- [13] Y.W. Kim, D.M. Dimiduk, *Progress in the understanding of gamma titanium aluminides*, *Jom*. 43 (1991) 40–47. <https://doi.org/10.1007/BF03221103>.
- [14] B.P. Bewlay, S. Nag, A. Suzuki, M.J. Weimer, *TiAl alloys in commercial aircraft engines*, *Mater. High Temp*. 33 (2016) 549–559. <https://doi.org/10.1080/09603409.2016.1183068>.
- [15] F. Appel, M. Oehring, R. Wagner, *Novel design concepts for gamma-base titanium aluminide alloys*, *Intermetallics*. 8 (2000) 1283–1312. [https://doi.org/10.1016/S0966-9795\(00\)00036-4](https://doi.org/10.1016/S0966-9795(00)00036-4).
- [16] F. Appel, U. Brossmann, U. Christoph, S. Eggert, P. Janschek, U. Lorenz, J. Müllauer, M. Oehring, J.D.H. Paul, *Recent progress in the development of gamma titanium aluminide alloys*, *Adv. Eng. Mater*. 2 (2000) 699–720. [https://doi.org/10.1002/1527-2648\(200011\)2:11<699::AID-ADEM699>3.0.CO;2-J](https://doi.org/10.1002/1527-2648(200011)2:11<699::AID-ADEM699>3.0.CO;2-J).
- [17] D.J. Jarvis, D. Voss, N.P. Lavery, *Advanced intermetallic materials and processes: Overview of the impress integrated project*, *TMS Annu. Meet.* (2007) 69–76.
- [18] J. Lapin, *TiAl-BASED ALLOYS : PRESENT STATUS AND FUTURE PERSPECTIVES*, *Metal*. 19 (2009) 1–12.
- [19] Y. Song, D.S. Xu, R. Yang, D. Li, Z.Q. Hu, *Theoretical investigation of ductilizing effects of alloying elements on TiAl*, *Intermetallics*. 6 (1998) 157–165. [https://doi.org/10.1016/S0966-9795\(97\)00060-5](https://doi.org/10.1016/S0966-9795(97)00060-5).

- [20] Y. Shida, H. Anada, The effect of various ternary additives on the oxidation behavior of TiAl in high-temperature air, *Oxid. Met.* 45 (1996) 197–219. <https://doi.org/10.1007/BF01046826>.
- [21] Q. Wang, R. Chen, Y. Yang, J. Guo, Y. Su, H. Ding, H. Fu, Effects of V and B, Y additions on the microstructure and creep behaviour of high-Nb TiAl alloys, *J. Alloys Compd.* 747 (2018) 640–647. <https://doi.org/10.1016/j.jallcom.2018.03.055>.
- [22] T. Noda, Application of cast gamma TiAl for automobiles, *Intermetallics.* 6 (1998) 709–713.
- [23] S.W. Kim, J.K. Hong, Y.S. Na, J.T. Yeom, S.E. Kim, Development of TiAl alloys with excellent mechanical properties and oxidation resistance, *Mater. Des.* 54 (2014) 814–819. <https://doi.org/10.1016/j.matdes.2013.08.083>.
- [24] J. Qiu, C. Zhou, B. Liu, Y. Liu, H. Li, X. Liang, X. Zan, Precipitation behavior of Ti-45Al-3Fe-2Mo-0.5C intermetallics after creep tests at 750 °C, *Mater. Charact.* 155 (2019) 109825. <https://doi.org/10.1016/j.matchar.2019.109825>.
- [25] K. Kothari, R. Radhakrishnan, N.M. Wereley, Advances in gamma titanium aluminides and their manufacturing techniques, *Prog. Aerosp. Sci.* (2012). <https://doi.org/10.1016/j.paerosci.2012.04.001>.
- [26] J. Chrapoński, W. Szkliniarz, A. Kościelna, B. Serek, Microstructure and chemical composition of phases in Ti-48Al-2Cr-2Nb intermetallic alloy, *Mater. Chem. Phys.* 81 (2003) 438–442. [https://doi.org/10.1016/S0254-0584\(03\)00042-7](https://doi.org/10.1016/S0254-0584(03)00042-7).
- [27] C.T. Liu, J.H. Schneibel, P.J. Maziasz, J.L. Wright, D.S. Easton, Tensile properties and fracture toughness of TiAl alloys with controlled microstructures, *Intermetallics.* 4 (1996) 429–440. [https://doi.org/10.1016/0966-9795\(96\)00047-7](https://doi.org/10.1016/0966-9795(96)00047-7).
- [28] A. Denquin, S. Naka, Phase transformation mechanisms involved in two-phase TiAl-based alloys - I. Lamellar structure formation, *Acta Mater.* 44 (1996) 343–352. [https://doi.org/10.1016/1359-6454\(95\)00167-4](https://doi.org/10.1016/1359-6454(95)00167-4).
- [29] R. V. Ramanujan, Phase transformations in γ based titanium aluminides, *Int. Mater. Rev.* 45 (2000) 217–240. <https://doi.org/10.1179/095066000101528377>.
- [30] H.Z. Niu, F.T. Kong, Y.Y. Chen, F. Yang, Microstructure characterization and tensile properties of β phase containing TiAl pancake, *J. Alloys Compd.* 509 (2011) 10179–10184. <https://doi.org/10.1016/j.jallcom.2011.08.078>.
- [31] S. Mayer, P. Erdely, F.D. Fischer, D. Holec, M. Kastnerhuber, T. Klein, H. Clemens, Intermetallic β -Solidifying γ -TiAl Based Alloys – From Fundamental Research to Application, *Adv. Eng. Mater.* 19 (2017) 1–27. <https://doi.org/10.1002/adem.201600735>.
- [32] D. Zhang, G. Dehm, H. Clemens, Effect of heat-treatments and hot-isostatic pressing on phase transformation and microstructure in a β /B2 containing γ -TiAl based alloy, *Scr. Mater.* 42 (2000) 1065–1070. [https://doi.org/10.1016/S1359-6462\(00\)00341-9](https://doi.org/10.1016/S1359-6462(00)00341-9).
- [33] R.M. Imayev, V.M. Imayev, M. Oehring, F. Appel, Alloy design concepts for refined gamma titanium aluminide based alloys, *Intermetallics.* 15 (2007) 451–460. <https://doi.org/10.1016/j.intermet.2006.05.003>.
- [34] S. Kremmer, H. Chladil, H. Clemens, A. Otto, V. Güther, Near conventional forging of titanium aluminides, *Ti-2007 Sci. Technol.* (2008) 989–992.
- [35] N. Cui, Q. Wu, K. Bi, T. Xu, F. Kong, Effect of Heat Treatment on Microstructures and Mechanical Properties of a Novel β -Solidifying TiAl Alloy, *Materials (Basel).* 12 (2019) 1672. <https://doi.org/10.3390/ma12101672>.
- [36] M. Kastnerhuber, T. Klein, H. Clemens, S. Mayer, Tailoring microstructure and chemical composition of advanced γ -TiAl based alloys for improved creep resistance, *Intermetallics.* 97 (2018) 27–33. <https://doi.org/10.1016/j.intermet.2018.03.011>.
- [37] S. Bolz, M. Oehring, J. Lindemann, F. Pyczak, J. Paul, A. Stark, T. Lippmann, S.

- Schrüfer, D. Roth-Fagaraseanu, A. Schreyer, S. Weiß, Microstructure and mechanical properties of a forged β -solidifying γ TiAl alloy in different heat treatment conditions, *Intermetallics*. 58 (2015) 71–83.
<https://doi.org/10.1016/j.intermet.2014.11.008>.
- [38] A.B. Godfrey, M.H. Loretto, The nature of complex precipitates associated with the addition of boron to a γ -based titanium aluminide, *Intermetallics*. 4 (1996) 47–53.
[https://doi.org/10.1016/0966-9795\(95\)00017-5](https://doi.org/10.1016/0966-9795(95)00017-5).
- [39] D. Hu, Role of boron in TiAl alloy development: a review, *Rare Met.* 35 (2016) 1–14.
<https://doi.org/10.1007/s12598-015-0615-1>.
- [40] D. Hu, C. Yang, A. Huang, M. Dixon, U. Hecht, Solidification and grain refinement in Ti₄₅Al₂Mn₂Nb₁B, *Intermetallics*. 22 (2012) 68–76.
<https://doi.org/10.1016/j.intermet.2011.11.003>.
- [41] U. Hecht, V. Witusiewicz, A. Drevermann, J. Zollinger, Grain refinement by low boron additions in niobium-rich TiAl-based alloys, *Intermetallics*. 16 (2008) 969–978.
<https://doi.org/10.1016/j.intermet.2008.04.019>.
- [42] S.R. Dey, E. Bouzy, A. Hazotte, Features of feathery γ structure in a near- γ TiAl alloy, *Acta Mater.* 56 (2008) 2051–2062. <https://doi.org/10.1016/j.actamat.2007.12.056>.
- [43] H. Clemens, H. Kestler, Processing and applications of intermetallic γ -TiAl-based alloys, *Adv. Eng. Mater.* 2 (2000) 551–570. [https://doi.org/10.1002/1527-2648\(200009\)2:9<551::AID-ADEM551>3.0.CO;2-U](https://doi.org/10.1002/1527-2648(200009)2:9<551::AID-ADEM551>3.0.CO;2-U).
- [44] V. Güther, M. Allen, J. Klose, H. Clemens, Metallurgical processing of titanium aluminides on industrial scale, *Intermetallics*. 103 (2018) 12–22.
<https://doi.org/10.1016/j.intermet.2018.09.006>.
- [45] J. Aguilar, A. Schievenbusch, O. Kättlitz, Investment casting technology for production of TiAl low pressure turbine blades - Process engineering and parameter analysis, *Intermetallics*. 19 (2011) 757–761.
<https://doi.org/10.1016/j.intermet.2010.11.014>.
- [46] R. Gerling, H. Clemens, F.P. Schimansky, Powder Metallurgical Processing of Intermetallic Gamma Titanium Aluminides, *Adv. Eng. Mater.* 6 (2004) 23–38.
<https://doi.org/10.1002/adem.200310559>.
- [47] B. Liu, Y. Liu, Powder metallurgy titanium aluminide alloys, Elsevier Inc., 2015.
<https://doi.org/10.1016/B978-0-12-800054-0.00027-7>.
- [48] S.L. Semiatin, G.R. Cornish, D. Eylon, Hot-compression behavior and microstructure evolution of pre-alloyed powder compacts of a near- γ titanium aluminide alloy, *Mater. Sci. Eng. A*. 185 (1994) 45–53. [https://doi.org/10.1016/0921-5093\(94\)90926-1](https://doi.org/10.1016/0921-5093(94)90926-1).
- [49] G. Wegmann, R. Gerling, F.P. Schimansky, H. Clemens, A. Bartels, High-temperature mechanical properties of hot isostatically pressed and forged gamma titanium aluminide alloy powder, *Intermetallics*. 10 (2002) 511–517.
[https://doi.org/10.1016/S0966-9795\(02\)00026-2](https://doi.org/10.1016/S0966-9795(02)00026-2).
- [50] M.J. Donachie, S.J. Donachie, *Superalloys: A Technical Guide*. ASM International, 2008., 2002.
- [51] R.J. Simpkins, M.P. Rourke, T.R. Bieler, P.A. McQuay, The effects of HIP pore closure and age hardening on primary creep and tensile property variations in a TiAl XDTM alloy with 0.1 wt.% carbon, *Mater. Sci. Eng. A*. 463 (2007) 208–215.
<https://doi.org/10.1016/j.msea.2006.09.114>.
- [52] L. Chen, L. Zhu, Y. Guan, B. Zhang, J. Li, Tougher TiAl alloy via integration of hot isostatic pressing and heat treatment, *Mater. Sci. Eng. A*. 688 (2017) 371–377.
<https://doi.org/10.1016/j.msea.2017.02.028>.
- [53] G.E. Fuchs, The effect of processing on the hot workability of Ti-48Al-2Nb-2Cr alloys,

- Metall. Mater. Trans. A Phys. Metall. Mater. Sci. 28 (1997) 2543–2553.
<https://doi.org/10.1007/s11661-997-0012-y>.
- [54] A.K. Ghosh, On the measurement of strain-rate sensitivity for deformation mechanism in conventional and ultra-fine grain alloys, *Mater. Sci. Eng. A.* 463 (2007) 36–40. <https://doi.org/10.1016/j.msea.2006.08.122>.
- [55] N. Bibhanshu, A. Bhattacharjee, S. Suwas, Hot deformation response of titanium aluminides Ti–45Al-(5, 10)Nb-0.2B-0.2C with pre-conditioned microstructures, *J. Alloys Compd.* 832 (2020) 154584. <https://doi.org/10.1016/j.jallcom.2020.154584>.
- [56] S.L. Semiatin, A. Force, M. Directorate, *ASM Handbook: Metalworking: Bulk Forming*, 2005. <https://doi.org/10.1361/asmhba0003971>.
- [57] R.K. Gupta, S.V.S. Narayana Murty, B. Pant, V. Agarwala, P.P. Sinha, Hot workability of $\gamma+\alpha$ 2 titanium aluminide: Development of processing map and constitutive equations, *Mater. Sci. Eng. A.* 551 (2012) 169–186.
<https://doi.org/10.1016/j.msea.2012.05.005>.
- [58] V. Seetharaman, S.L. Semiatin, Effect of the lamellar grain size on plastic flow behavior and microstructure evolution during hot working of a gamma titanium aluminide alloy, *Metall. Mater. Trans. A Phys. Metall. Mater. Sci.* 33 (2002) 3817–3830. <https://doi.org/10.1007/s11661-002-0254-7>.
- [59] R. Porizek, S. Znam, D. Nguyen-Manh, V. Vitek, D.G. Pettifor, Atomistic studies of dislocation glide in γ -TiAl, *Mater. Res. Soc. Symp. - Proc.* 753 (2003) 181–186.
<https://doi.org/10.1557/proc-753-bb4.3>.
- [60] E. Cerreta, S. Mahajan, *Formation of Deformation Twins in Metallic Crystals*, 49 (2001) 2005.
- [61] *Philosophical Magazine A Plastic deformation of single crystals of Ti 3 Al with D0 19 structure* Yasuhide Minonishi, (n.d.). <https://doi.org/10.1080/01418619108213939>.
- [62] V.K. Vasudevan, M.A. Stucke, S.A. Court, H.L. Fraser, The influence of second phase Ti_3Al on the deformation mechanisms in TiAl, *Philos. Mag. Lett.* 59 (1989) 299–307.
<https://doi.org/10.1080/09500838908206358>.
- [63] D. Holec, R.K. Reddy, T. Klein, H. Clemens, Preferential site occupancy of alloying elements in TiAl-based phases, *J. Appl. Phys.* 119 (2016) 205104.
<https://doi.org/10.1063/1.4951009>.
- [64] H. Clemens, W. Wallgram, S. Kremmer, V. Güther, A. Otto, A. Bartels, Design of novel β -solidifying TiAl alloys with adjustable $\beta/B2$ -phase fraction and excellent hot-workability, *Adv. Eng. Mater.* 10 (2008) 707–713.
<https://doi.org/10.1002/adem.200800164>.
- [65] E. Schwaighofer, H. Clemens, S. Mayer, J. Lindemann, J. Klose, W. Smarsly, V. Güther, Microstructural design and mechanical properties of a cast and heat-treated intermetallic multi-phase γ -TiAl based alloy, *Intermetallics.* 44 (2014) 128–140.
<https://doi.org/10.1016/j.intermet.2013.09.010>.
- [66] H. Clemens, S. Mayer, Design, processing, microstructure, properties, and applications of advanced intermetallic TiAl alloys, *Adv. Eng. Mater.* 15 (2013) 191–215. <https://doi.org/10.1002/adem.201200231>.
- [67] T. Tetsui, A newly developed hot worked TiAl alloy for blades and structural components, *Scr. Mater.* 47 (2002) 399–403. [https://doi.org/10.1016/S1359-6462\(02\)00158-6](https://doi.org/10.1016/S1359-6462(02)00158-6).
- [68] Q. Wang, R. Chen, Y. Yang, S. Wu, J. Guo, H. Ding, Y. Su, H. Fu, Effects of lamellar spacing on microstructural stability and creep properties in β -solidifying γ -TiAl alloy by directional solidification, *Mater. Sci. Eng. A.* 711 (2018) 508–514.
<https://doi.org/10.1016/j.msea.2017.11.080>.
- [69] H. Jiang, S. Zeng, A. Zhao, X. Ding, P. Dong, Hot deformation behavior of β phase

- containing γ -TiAl alloy, *Mater. Sci. Eng. A.* 661 (2016) 160–167. <https://doi.org/10.1016/j.msea.2016.03.005>.
- [70] T. Li, G. Liu, M. Xu, B. Wang, T. Fu, Z. Wang, R.D.K. Misra, Flow stress prediction and hot deformation mechanisms in Ti-44Al-5Nb-(Mo, V, B) alloy, *Materials (Basel)*. 11 (2018). <https://doi.org/10.3390/ma11102044>.
- [71] F. Appel, H. Clemens, F.D. Fischer, Modeling concepts for intermetallic titanium aluminides, *Prog. Mater. Sci.* 81 (2016) 55–124. <https://doi.org/10.1016/j.pmatsci.2016.01.001>.
- [72] G. Molénat, B. Galy, M. Musi, L. Toualbi, M. Thomas, H. Clemens, J.P. Monchoux, A. Couret, Plasticity and brittleness of the ordered β_0 phase in a TNM-TiAl alloy, *Intermetallics*. 151 (2022). <https://doi.org/10.1016/j.intermet.2022.107653>.
- [73] F. Appel, H. Clemens, F.D. Fischer, Modeling concepts for intermetallic titanium aluminides, *Prog. Mater. Sci.* 81 (2016) 55–124. <https://doi.org/10.1016/j.pmatsci.2016.01.001>.
- [74] M. Kasthuber, B. Rashkova, H. Clemens, S. Mayer, Enhancement of creep properties and microstructural stability of intermetallic β -solidifying γ -TiAl based alloys, *Intermetallics*. 63 (2015) 19–26. <https://doi.org/10.1016/j.intermet.2015.03.017>.
- [75] I.J. Watson, K.D. Liss, H. Clemens, W. Wallgram, T. Schmoelzer, T.C. Hansen, M. Reid, In situ characterization of a Nb and Mo containing γ -TiAl based alloy using neutron diffraction and high-temperature microscopy, *Adv. Eng. Mater.* 11 (2009) 932–937. <https://doi.org/10.1002/adem.200900169>.
- [76] F. Appel, R. Wagner, Microstructure and deformation of two-phase γ -titanium aluminides, *Mater. Sci. Eng. R Reports*. 22 (1998) 187–268. [https://doi.org/10.1016/S0927-796X\(97\)00018-1](https://doi.org/10.1016/S0927-796X(97)00018-1).
- [77] T. Sakai, A. Belyakov, R. Kaibyshev, H. Miura, J.J. Jonas, Dynamic and post-dynamic recrystallization under hot, cold and severe plastic deformation conditions, *Prog. Mater. Sci.* 60 (2014) 130–207. <https://doi.org/10.1016/j.pmatsci.2013.09.002>.
- [78] A. Dehghan-Manshadi, M.R. Barnett, P.D. Hodgson, Recrystallization in AISI 304 austenitic stainless steel during and after hot deformation, *Mater. Sci. Eng. A.* 485 (2008) 664–672. <https://doi.org/10.1016/j.msea.2007.08.026>.
- [79] M.H. Maghsoudi, A. Zarei-Hanzaki, P. Changizian, A. Marandi, Metadynamic recrystallization behavior of AZ61 magnesium alloy, *Mater. Des.* 57 (2014) 487–493. <https://doi.org/10.1016/j.matdes.2013.12.051>.
- [80] X. Chen, B. Tang, W. Chen, Y. Yang, G. Zheng, Z. Fan, J. Li, Effect of inter-pass annealing on the deformation microstructure of Ti-48Al-2Cr-2Nb alloy, *J. Alloys Compd.* 934 (2023) 167751. <https://doi.org/10.1016/j.jallcom.2022.167751>.
- [81] F. Kong, Y. Chen, F. Yang, Effect of heat treatment on microstructures and tensile properties of as-forged Ti-45Al-5Nb-0.3Y alloy, *Intermetallics*. 19 (2011) 212–216. <https://doi.org/10.1016/j.intermet.2010.08.012>.
- [82] J. Li, B. Song, H. Nurly, P.J. Xue, S. Wen, Q. Wei, Y. Shi, Microstructure evolution and a new mechanism of B2 phase on room temperature mechanical properties of Ti-47Al-2Cr-2Nb alloy prepared by hot isostatic pressing, *Mater. Charact.* 140 (2018) 64–71. <https://doi.org/10.1016/j.matchar.2018.03.043>.
- [83] R. Lebensohn, H. Uhlenhut, C. Hartig, H. Mecking, Plastic flow of γ -TiAl-Based polysynthetically twinned crystals: Micromechanical modeling and experimental validation, *Acta Mater.* 46 (1998) 4701–4709. [https://doi.org/10.1016/S1359-6454\(98\)00132-3](https://doi.org/10.1016/S1359-6454(98)00132-3).
- [84] M.U. Ilyas, M.R. Kabir, Modelling high temperature deformation of lamellar TiAl crystal using strain-rate enhanced crystal plasticity, *Mater. Sci. Eng. A.* 788 (2020)

139524. <https://doi.org/10.1016/j.msea.2020.139524>.
- [85] A.J. Palomares-García, M.T. Pérez-Prado, J.M. Molina-Aldareguia, Effect of lamellar orientation on the strength and operating deformation mechanisms of fully lamellar TiAl alloys determined by micropillar compression, *Acta Mater.* 123 (2017) 102–114. <https://doi.org/10.1016/j.actamat.2016.10.034>.
- [86] M. Yamaguchi, H. Inui, S. Yokoshima, K. Kishida, D.R. Johnson, Recent progress in our understanding of deformation and fracture of two-phase and single-phase TiAl alloys, *Transition.* 213 (1996) 25–31.
- [87] J.P. Monchoux, J. Luo, T. Voisin, A. Couret, Deformation modes and size effect in near- γ TiAl alloys, *Mater. Sci. Eng. A.* 679 (2017) 123–132. <https://doi.org/10.1016/j.msea.2016.09.092>.
- [88] Y.W. Kim, Strength and ductility in TiAl alloys, *Intermetallics.* 6 (1998) 623–628.
- [89] Y.W. Kim, Effects of microstructure on the deformation and fracture of γ -TiAl alloys, *Mater. Sci. Eng. A.* 192–193 (1995) 519–533. [https://doi.org/10.1016/0921-5093\(94\)03271-8](https://doi.org/10.1016/0921-5093(94)03271-8).
- [90] A.J. Palomares-García, I. Sabirov, M.T. Pérez-Prado, J.M. Molina-Aldareguia, Effect of nanoscale thick lamellae on the micromechanical response of a TiAl alloy, *Scr. Mater.* 139 (2017) 17–21. <https://doi.org/10.1016/j.scriptamat.2017.06.002>.
- [91] D.X. Wei, Y. Koizumi, M. Nagasako, A. Chiba, Refinement of lamellar structures in Ti-Al alloy, *Acta Mater.* 125 (2017) 81–97. <https://doi.org/10.1016/j.actamat.2016.11.045>.
- [92] G. Cao, L. Fu, J. Lin, Y. Zhang, C. Chen, The relationships of microstructure and properties of a fully lamellar TiAl alloy, *Intermetallics.* 8 (2000) 647–653. [https://doi.org/10.1016/s0966-9795\(99\)00128-4](https://doi.org/10.1016/s0966-9795(99)00128-4).
- [93] R. Muñoz-Moreno, C.J. Boehlert, M. Teresa Pérez-Prado, E.M. Ruiz-Navas, J. Llorca, In situ observations of the deformation behavior and fracture mechanisms of Ti-45Al-2Nb-2Mn + 0.8 vol pct TiB₂, *Metall. Mater. Trans. A Phys. Metall. Mater. Sci.* 43 (2012) 1198–1208. <https://doi.org/10.1007/s11661-011-1022-3>.
- [94] H. Zhu, D.Y. Seo, K. Maruyama, P. Au, Microstructural stability of fine-grained fully lamellar XD TiAl alloys by step aging, *Metall. Mater. Trans. A Phys. Metall. Mater. Sci.* 36 (2005) 1339–1351. <https://doi.org/10.1007/s11661-005-0225-x>.
- [95] K. Zhu, H., Seo, D.Y., Maruyama, Effect of heat treatment on microstructure and mechanical property of 45/47XD TiAl alloys, *Mater. Sci. Forum.* 475–479 (2005) 581–584. <https://doi.org/10.4028/www.scientific.net/MSF.475-479.581>.
- [96] H. Zhu, D.Y. Seo, K. Maruyama, P. Au, Effect of initial microstructure on microstructural instability and creep resistance of XD TiAl alloys, *Metall. Mater. Trans. A Phys. Metall. Mater. Sci.* 37 (2006) 3149–3159. <https://doi.org/10.1007/s11661-006-0195-7>.
- [97] H. Zhu, D.Y. Seo, K. Maruyama, P. Au, Effect of lamellar spacing on microstructural instability and creep behavior of a lamellar TiAl alloy, *Scr. Mater.* 54 (2006) 1979–1984. <https://doi.org/10.1016/j.scriptamat.2006.03.023>.
- [98] H. Zhu, D.Y. Seo, K. Maruyama, P. Au, Effect of microstructure on creep deformation of 45XD TiAl alloy at low and high stresses, *Mater. Sci. Eng. A.* 483–484 (2008) 533–536. <https://doi.org/10.1016/j.msea.2006.09.137>.
- [99] K.S. Chan, Y.W. Kim, Effects of lamellae spacing and colony size on the fracture resistance of a fully-lamellar TiAl alloy, *Acta Metall. Mater.* 43 (1995) 439–451. [https://doi.org/10.1016/0956-7151\(94\)00278-P](https://doi.org/10.1016/0956-7151(94)00278-P).
- [100] K. Maruyama, R. Yamamoto, H. Nakakuki, N. Fujitsuna, Effects of lamellar spacing, volume fraction and grain size on creep strength of fully lamellar TiAl alloys, *Mater. Sci. Eng. A.* 239–240 (1997) 419–428. <https://doi.org/10.1016/s0921->

5093(97)00612-6.

- [101] C.E. Wen, K. Yasue, J.G. Lin, Y.G. Zhang, C.Q. Chen, The effect of lamellar spacing on the creep behavior of a fully lamellar TiAl alloy, *Intermetallics*. 8 (2000) 525–529. [https://doi.org/10.1016/S0966-9795\(99\)00131-4](https://doi.org/10.1016/S0966-9795(99)00131-4).
- [102] Y. Mine, K. Takashima, P. Bowen, Effect of lamellar spacing on fatigue crack growth behaviour of a TiAl-based aluminide with lamellar microstructure, *Mater. Sci. Eng. A*. 532 (2012) 13–20. <https://doi.org/10.1016/j.msea.2011.10.055>.
- [103] T. Zhang, D. Wang, J. Zhu, H. Xiao, C.T. Liu, Y. Wang, Non-conventional transformation pathways and ultrafine lamellar structures in γ -TiAl alloys, *Acta Mater.* 189 (2020) 25–34. <https://doi.org/10.1016/j.actamat.2020.02.053>.
- [104] J. Lapin, T. Pelachová, M. Dománková, Long-term creep behaviour of cast TiAl-Ta alloy, *Intermetallics*. 95 (2018) 24–32. <https://doi.org/10.1016/j.intermet.2018.01.013>.
- [105] J. Bresler, S. Neumeier, M. Ziener, F. Pyczak, M. Göken, The influence of niobium, tantalum and zirconium on the microstructure and creep strength of fully lamellar γ/α 2 titanium aluminides, *Mater. Sci. Eng. A*. 744 (2019) 46–53. <https://doi.org/10.1016/j.msea.2018.11.152>.
- [106] J.N. Wang, K. Xie, Refining of coarse lamellar microstructure of TiAl alloys by rapid heat treatment, *Intermetallics*. 8 (2000) 545–548. [https://doi.org/10.1016/S0966-9795\(99\)00153-3](https://doi.org/10.1016/S0966-9795(99)00153-3).
- [107] J.N. Wang, J. Yang, Q. Xia, Y. Wang, On the grain size refinement of TiAl alloys by cyclic heat treatment, *Mater. Sci. Eng. A*. 329–331 (2002) 118–123. [https://doi.org/10.1016/S0921-5093\(01\)01543-X](https://doi.org/10.1016/S0921-5093(01)01543-X).
- [108] J. Yang, J.N. Wang, Y. Wang, Q. Xia, Refining grain size of a TiAl alloy by cyclic heat treatment through discontinuous coarsening, *Intermetallics*. 11 (2003) 971–974. [https://doi.org/10.1016/S0966-9795\(02\)00126-7](https://doi.org/10.1016/S0966-9795(02)00126-7).
- [109] A. Szkliniarz, Grain refinement of Ti-48Al-2Cr-2Nb alloy by heat treatment method, *Solid State Phenom.* 191 (2012) 221–234. <https://doi.org/10.4028/www.scientific.net/SSP.191.221>.
- [110] A. Kościelna, W. Szkliniarz, Effect of cyclic heat treatment parameters on the grain refinement of Ti-48Al-2Cr-2Nb alloy, *Mater. Charact.* 60 (2009) 1158–1162. <https://doi.org/10.1016/j.matchar.2009.03.008>.
- [111] K. Kamyshnykova, J. Lapin, Grain refinement of cast peritectic TiAl-based alloy by solid-state phase transformations, *Kov. Mater.* 56 (2018) 277–287. https://doi.org/10.4149/km_2018_5_277.
- [112] S. Yim, H. Bian, K. Aoyagi, A. Chiba, Materials Science & Engineering A Effect of multi-stage heat treatment on mechanical properties and microstructure transformation of Ti – 48Al – 2Cr – 2Nb alloy, *Mater. Sci. Eng. A*. 816 (2021) 141321. <https://doi.org/10.1016/j.msea.2021.141321>.
- [113] J.K. Kim, J.H. Kim, J.Y. Kim, S.H. Park, S.W. Kim, M.H. Oh, S.E. Kim, Producing fine fully lamellar microstructure for cast γ -TiAl without hot working, *Intermetallics*. 120 (2020) 106728. <https://doi.org/10.1016/j.intermet.2020.106728>.
- [114] S.L. Semiatin, A. Force, M. Directorate, *ASM Handbook: Metalworking: Bulk Forming*, 14A (2005) 888.
- [115] G.E. Dieter, H.A. Kuhn, S.L. Semiatin, Workability theory and application in bulk forming processes, *Handb. Work. Process Des.* (2003) 172–187. <https://doi.org/10.1361/h>.
- [116] C. Herzig, T. Przeorski, M. Friesel, F. Hisker, S. Divinski, Tracer solute diffusion of Nb, Zr, Cr, Fe, and Ni in γ -TiAl: Effect of preferential site occupation, *Intermetallics*. 9 (2001) 461–472. [https://doi.org/10.1016/S0966-9795\(01\)00025-5](https://doi.org/10.1016/S0966-9795(01)00025-5).

- [117] N. Bibhanshu, A. Bhattacharjee, S. Suwas, Influence of Temperature and Strain Rate on Microstructural Evolution During Hot Compression of Ti-45Al-xNb-0.2C-0.2B Titanium Aluminide Alloys, *Jom.* 71 (2019) 3552–3564. <https://doi.org/10.1007/s11837-019-03722-2>.
- [118] S.L. Semiatin, V. Seetharaman, A.K. Ghosh, Plastic flow, microstructure evolution, and defect formation during primary hot working of titanium and titanium aluminide alloys with lamellar colony microstructures, *Philos. Trans. R. Soc. A Math. Phys. Eng. Sci.* 357 (1999) 1487–1512. <https://doi.org/10.1098/rsta.1999.0386>.
- [119] I.W. S.L. Semiatin, V. Seetharaman, Hot workability of titanium and titanium aluminide alloys—an overview, *Mater. Sci. Eng. A.* 243 (1998) 1–24.
- [120] J.J. Jonas, C.M. Sellars, W.J.M. Tegart, Strength and structure under hot-working conditions, *Metall. Rev.* 14 (1969) 1–24. <https://doi.org/10.1179/mtlr.1969.14.1.1>.
- [121] H.J. McQueen, J.J. Jonas, Recent advances in hot working: Fundamental dynamic softening mechanisms, *J. Appl. Metalwork.* 1984 33. 3 (1984) 233–241. <https://doi.org/10.1007/BF02833651>.
- [122] M. Nobuki, T. Tsujimoto, Influence of alloy composition on hot deformation properties of TiAl intermetallics, *ISIJ Int.* 31 (1991) 931–937.
- [123] S.L. Semiatin, V. Seetharaman, A criterion for intergranular failure during hot working of a near-gamma titanium aluminide alloy, *Scr. Mater.* 36 (1997) 291–297. [https://doi.org/10.1016/S1359-6462\(96\)00386-7](https://doi.org/10.1016/S1359-6462(96)00386-7).
- [124] V. Seetharaman, S.L. Semiatin, Intergranular fracture of gamma titanium aluminides under hot working conditions, *Metall. Mater. Trans. A Phys. Metall. Mater. Sci.* 29 (1998) 1991–1999. <https://doi.org/10.1007/s11661-998-0025-1>.
- [125] D.J.L. M. G. Cockcroft, A Simple Criterion of Fracture for Ductile Metals, *Natl. Eng. Lab.* 240 (1966).
- [126] P. Groche, C. Müller, J. Stahlmann, S. Zang, Mechanical conditions in bulk metal forming tribometers - Part one, *Tribol. Int.* 62 (2013) 223–231. <https://doi.org/10.1016/j.triboint.2012.12.008>.
- [127] E. Schwaighofer, H. Clemens, J. Lindemann, A. Stark, S. Mayer, Hot-working behavior of an advanced intermetallic multi-phase γ -TiAl based alloy, *Mater. Sci. Eng. A.* 614 (2014) 297–310. <https://doi.org/10.1016/j.msea.2014.07.040>.
- [128] J.S. Luo, T. Voisin, J.P. Monchoux, A. Couret, Refinement of lamellar microstructures by boron incorporation in GE-TiAl alloys processed by Spark Plasma Sintering, *Intermetallics.* 36 (2013) 12–20. <https://doi.org/10.1016/j.intermet.2012.12.006>.
- [129] C. Yang, D. Hu, X. Wu, A. Huang, M. Dixon, Microstructures and tensile properties of hot isostatic pressed Ti4522XD powders, *Mater. Sci. Eng. A.* 534 (2012) 268–276. <https://doi.org/10.1016/j.msea.2011.11.068>.
- [130] D. Hu, Effect of boron addition on tensile ductility in lamellar TiAl alloys, *Intermetallics.* 10 (2002) 851–858. [https://doi.org/10.1016/S0966-9795\(02\)00087-0](https://doi.org/10.1016/S0966-9795(02)00087-0).
- [131] G.E. Fuchs, Supertransus processing of TiAl-based alloys, *Metall. Mater. Trans. A Phys. Metall. Mater. Sci.* 29 (1998) 27–36. <https://doi.org/10.1007/s11661-998-0156-4>.
- [132] W. Xu, X. Jin, K. Huang, Y. Zong, S. Wu, X. Zhong, F. Kong, D. Shan, S. Nutt, Improvement of microstructure, mechanical properties and hot workability of a TiAl-Nb-Mo alloy through hot extrusion, *Mater. Sci. Eng. A.* 705 (2017) 200–209. <https://doi.org/10.1016/j.msea.2017.08.082>.
- [133] G. Çm, H. Clemens, R. Gerling, M. Koçak, Diffusion bonding of γ -TiAl sheets, *Intermetallics.* 7 (1999) 1025–1031. [https://doi.org/10.1016/S0966-9795\(99\)00012-6](https://doi.org/10.1016/S0966-9795(99)00012-6).
- [134] S.L. Semiatin, B.W. Shanahan, F. Meisenkothen, Hot rolling of gamma titanium

- aluminide foil, *Acta Mater.* 58 (2010) 4446–4457.
<https://doi.org/10.1016/j.actamat.2010.04.042>.
- [135] J. Tang, B. Huang, W. Liu, Y. He, K. Zhou, A. Wu, K. Peng, W. Qin, Y. Du, A high ductility TiAl alloy made by two-step heat treatment, *Mater. Res. Bull.* 38 (2003) 2019–2024. <https://doi.org/10.1016/j.materresbull.2003.07.014>.
- [136] A.P. Mouritz, Titanium alloys for aerospace structures and engines, in: *Introd. to Aersp. Mater.*, Elsevier, 2012: pp. 202–223.
<https://doi.org/10.1533/9780857095152.202>.
- [137] D.E. Larsen, Status of investment cast gamma titanium aluminides in the USA, *Mater. Sci. Eng. A.* 213 (1996) 128–133. [https://doi.org/10.1016/0921-5093\(96\)10234-3](https://doi.org/10.1016/0921-5093(96)10234-3).
- [138] C. Yang, D. Hu, A. Huang, M. Dixon, Solidification and grain refinement in Ti45Al2Mn2Nb1B subjected to fast cooling, *Intermetallics.* 32 (2013) 64–71.
<https://doi.org/10.1016/j.intermet.2012.08.023>.
- [139] Lance T. Gant, Airworthiness Directives; International Aero Engines LLC, Turbofan Engines, *Fed. Regist.* 85 (2020) 1–9. <https://doi.org/10.11693/hyhz20181000233>.
- [140] P. Janschek, Wrought TiAl Blades, *Mater. Today Proc.* 2 (2015) S92–S97.
<https://doi.org/10.1016/j.matpr.2015.05.024>.
- [141] T. Tetsui, Development of a TiAl turbocharger for passenger vehicles, *Mater. Sci. Eng. A.* 329–331 (2002) 582–588. [https://doi.org/10.1016/S0921-5093\(01\)01584-2](https://doi.org/10.1016/S0921-5093(01)01584-2).
- [142] S. Yim, H. Bian, K. Aoyagi, A. Chiba, Effect of multi-stage heat treatment on mechanical properties and microstructure transformation of Ti–48Al–2Cr–2Nb alloy, *Mater. Sci. Eng. A.* 816 (2021) 141321. <https://doi.org/10.1016/j.msea.2021.141321>.
- [143] L. Chen, L. Zhu, Y. Guan, B. Zhang, J. Li, Tougher TiAl alloy via integration of hot isostatic pressing and heat treatment, *Mater. Sci. Eng. A.* 688 (2017) 371–377.
<https://doi.org/10.1016/j.msea.2017.02.028>.
- [144] W.J. Zhang, U. Lorenz, F. Appel, Recovery, recrystallization and phase transformations during thermomechanical processing and treatment of TiAl-based alloys, *Acta Mater.* 48 (2000) 2803–2813. [https://doi.org/10.1016/S1359-6454\(00\)00093-8](https://doi.org/10.1016/S1359-6454(00)00093-8).
- [145] A. Hadadzadeh, F. Mokdad, M.A. Wells, D.L. Chen, A new grain orientation spread approach to analyze the dynamic recrystallization behavior of a cast-homogenized Mg-Zn-Zr alloy using electron backscattered diffraction, *Mater. Sci. Eng. A.* 709 (2018) 285–289. <https://doi.org/10.1016/j.msea.2017.10.062>.
- [146] Z. Wan, Y. Sun, L. Hu, H. Yu, Dynamic softening behavior and microstructural characterization of TiAl-based alloy during hot deformation, *Mater. Charact.* 130 (2017) 25–32. <https://doi.org/10.1016/j.matchar.2017.05.022>.
- [147] X. Chen, B. Tang, D. Liu, B. Wei, L. Zhu, R. Liu, H. Kou, J. Li, Dynamic recrystallization and hot processing map of Ti-48Al-2Cr-2Nb alloy during the hot deformation, *Mater. Charact.* 179 (2021) 111332. <https://doi.org/10.1016/j.matchar.2021.111332>.
- [148] S.L. Semiatin, V. Seetharaman, I. Weiss, Flow behavior and globularization kinetics during hot working of Ti-6Al-4V with a colony alpha microstructure, *Mater. Sci. Eng. A.* 263 (1999) 257–271. [https://doi.org/10.1016/S0921-5093\(98\)01156-3](https://doi.org/10.1016/S0921-5093(98)01156-3).
- [149] S.L. Semiatin, V. Seetharaman, V.K. Jain, Microstructure development during conventional and isothermal hot forging of a near-gamma titanium aluminide, *Metall. Mater. Trans. A.* 25 (1994) 2753–2768. <https://doi.org/10.1007/BF02649227>.
- [150] J.C.F. Millett, J.W. Brooks, I.P. Jones, Assessment and modelling of isothermal forging of intermetallic compounds Part 1 - TiAl, *Mater. Sci. Technol.* 15 (1999) 697–704. <https://doi.org/10.1179/026708399101506292>.
- [151] S. Tian, H. Jiang, W. Guo, G. Zhang, S. Zeng, Hot deformation and dynamic

- recrystallization behavior of TiAl-based alloy, *Intermetallics*. 112 (2019) 106521. <https://doi.org/10.1016/j.intermet.2019.106521>.
- [152] J. Bresler, S. Neumeier, M. Ziener, F. Pyczak, M. Göken, The influence of niobium, tantalum and zirconium on the microstructure and creep strength of fully lamellar γ/α 2 titanium aluminides, *Mater. Sci. Eng. A*. 744 (2019) 46–53. <https://doi.org/10.1016/j.msea.2018.11.152>.
- [153] Y. Lin, G. Zhang, J. Chen, G. Yang, J. Deng, Effects of heat treatment on the microstructures and mechanical properties of β c titanium alloy, *Xiyou Jinshu Cailiao Yu Gongcheng/Rare Met. Mater. Eng.* 27 (2023) 78. <https://doi.org/10.1016/j.jallcom.2023.169420>.
- [154] Q. Wang, H. Ding, H. Zhang, R. Chen, J. Guo, H. Fu, Influence of Mn addition on the microstructure and mechanical properties of a directionally solidified γ -TiAl alloy, *Mater. Charact.* 137 (2018) 133–141. <https://doi.org/10.1016/j.matchar.2018.01.029>.
- [155] L. Cheng, X. Xue, B. Tang, H. Kou, J. Li, Flow characteristics and constitutive modeling for elevated temperature deformation of a high Nb containing TiAl alloy, *Intermetallics*. 49 (2014) 23–28. <https://doi.org/10.1016/j.intermet.2014.01.007>.
- [156] H.Z. Niu, Y.Y. Chen, S.L. Xiao, F.T. Kong, C.J. Zhang, High temperature deformation behaviors of Ti-45Al-2Nb-1.5V-1Mo-Y alloy, *Intermetallics*. 19 (2011) 1767–1774. <https://doi.org/10.1016/j.intermet.2011.07.025>.
- [157] B. Tang, W.Y. Wang, L. Xiang, Y. Liu, L. Zhu, S. Ji, J. He, J. Li, Metadynamic recrystallization behavior of β -solidified TiAl alloy during post-annealing after hot deformation, *Intermetallics*. 117 (2020) 106679. <https://doi.org/10.1016/j.intermet.2019.106679>.
- [158] X.G. Fan, H. Yang, P.F. Gao, R. Zuo, P.H. Lei, The role of dynamic and post dynamic recrystallization on microstructure refinement in primary working of a coarse grained two-phase titanium alloy, *J. Mater. Process. Technol.* 234 (2016) 290–299. <https://doi.org/10.1016/j.jmatprotec.2016.03.031>.
- [159] L. Cheng, H. Chang, B. Tang, H. Kou, J. Li, Characteristics of metadynamic recrystallization of a high Nb containing TiAl alloy, *Mater. Lett.* 92 (2013) 430–432. <https://doi.org/10.1016/j.matlet.2012.11.026>.
- [160] Q. Wang, L. Zeng, H. Ding, R. Chen, J. Guo, H. Fu, On the high temperature deformation of a directionally solidified γ -TiAl alloy, *Mater. Sci. Eng. A*. 758 (2019) 19–27. <https://doi.org/10.1016/j.msea.2019.04.072>.
- [161] Y. Liu, X. Xue, H. Fang, Y. Tan, R. Chen, Y. Su, J. Guo, The growth behavior of columnar grains in a TiAl alloy during directional induction heat treatments, *CrystEngComm*. 22 (2020) 1188–1196. <https://doi.org/10.1039/c9ce01631g>.
- [162] S.L. Semiatin, V. Seetharaman, D.M. Dimiduk, K.H.G. Ashbee, Phase transformation behavior of gamma titanium aluminide alloys during supertransus heat treatment, *Metall. Mater. Trans. A Phys. Metall. Mater. Sci.* 29 (1998) 7–18. <https://doi.org/10.1007/s11661-998-0154-6>.
- [163] R.M. Imayev, V.M. Imayev, M. Oehring, F. Appel, Microstructural evolution during hot working of Ti aluminide alloys: Influence of phase constitution and initial casting texture, *Metall. Mater. Trans. A*. 36 (2005) 859–867. <https://doi.org/10.1007/s11661-005-0199-8>.
- [164] A.J. Palomares-García, M.T. Pérez-Prado, J.M. Molina-Aldareguia, Effect of lamellar orientation on the strength and operating deformation mechanisms of fully lamellar TiAl alloys determined by micropillar compression, *Acta Mater.* 123 (2017) 102–114. <https://doi.org/10.1016/j.actamat.2016.10.034>.
- [165] D.. Seo, L. Zhao, J. Beddoes, Microstructural evolution during heat treatments in Ti-

- 45 and 47Al–2Nb–2Mn+0.8vol.%TiB₂ XDTM alloys, *Mater. Sci. Eng. A.* 329–331 (2002) 130–140. [https://doi.org/10.1016/S0921-5093\(01\)01546-5](https://doi.org/10.1016/S0921-5093(01)01546-5).
- [166] F. Qiang, E. Bouzy, H. Kou, Y. Zhang, L. Wang, J. Li, Grain fragmentation associated continuous dynamic recrystallization (CDRX) of hexagonal structure during uniaxial isothermal compression: High-temperature α phase in TiAl alloys, *Intermetallics*. 129 (2021) 107028. <https://doi.org/10.1016/j.intermet.2020.107028>.
- [167] P. Gao, M. Fu, M. Zhan, Z. Lei, Y. Li, Deformation behavior and microstructure evolution of titanium alloys with lamellar microstructure in hot working process: A review, *J. Mater. Sci. Technol.* (2019). <https://doi.org/10.1016/j.jmst.2019.07.052>.
- [168] V. Rudnev, D. Loveless, R.L. Cook, *Handbook of Induction Heating*, Second Edition, 2017. <https://doi.org/10.1201/9781315117485>.
- [169] H.-J. Fecht, M. Mohr, *Metallurgy in Space The Minerals, Metals & Materials Series*, n.d. <http://www.springer.com/series/15240>.
- [170] Y.Y. Chen, B.H. Li, F.T. Kong, Microstructural refinement and mechanical properties of Y-bearing TiAl alloys, *J. Alloys Compd.* 457 (2008) 265–269. <https://doi.org/10.1016/j.jallcom.2007.03.050>.
- [171] R. Hu, Y. Wu, J. Yang, Z. Gao, J. Li, Phase transformation pathway and microstructural refinement by feathery transformation of Ru-containing γ -TiAl alloy, *J. Mater. Res. Technol.* 18 (2022) 5290–5300. <https://doi.org/10.1016/j.jmrt.2022.04.160>.
- [172] P.M. Souza, G. Sivaswamy, A. Andreu, S. Rahimi, A novel cyclic thermal treatment for enhanced globularisation kinetics in Ti-6Al-4V alloy: Experimental, constitutive and FE based analyses, *J. Alloys Compd.* 898 (2022) 162859. <https://doi.org/10.1016/j.jallcom.2021.162859>.
- [173] H. Li, Y. Long, X. Liang, Y. Che, Z. Liu, Y. Liu, H. Xu, L. Wang, Effects of multiaxial forging on microstructure and high temperature mechanical properties of powder metallurgy Ti-45Al-7Nb-0.3W alloy, *Intermetallics*. 116 (2020) 106647. <https://doi.org/10.1016/j.intermet.2019.106647>.

8 Appendix

All data that is present in this document and supports it is available on PURE with the DOI:

[10.15129/e6d4d4fc-9f6d-4943-bcd4-d7096e90be7e](https://doi.org/10.15129/e6d4d4fc-9f6d-4943-bcd4-d7096e90be7e)

The dataset is to be read together with the thesis "Development of alternative thermomechanical processing techniques to improve forging outcomes of cast peritectic TiAl alloys"

This dataset includes.

- Calculated phase diagram (CALPHAD) for 45XD and 4822 alloy from PANDAT commercial software.
- SEM/BSE images using Scanning electron microscopy (SEM) using an FEI Quanta-250 with field-emission gun, with back-scattered electron (BSE) detector fitted, using an accelerating voltage of 20 kV and a working height of 10 mm for imaging -EBSD data, as CTF files, collected with the above SEM setup, a NordlysNano electron back-scattered diffraction (EBSD) system acquired crystallographic data. The EBSD was setup with an acquisition time of 120mS, 0.5 μm step size, with 90% of scanned areas indexed as a minimum.
- Energy dispersion spectroscopy (EDS) mapping for elemental analysis using the same set up for SEM as above but in EDS mode.
- MATLAB code for reading EBSD data.
- Cyclic heat treatment pyrometer temperature monitoring data.
- Compression data from Zwick-Roell Z150 material testing rig. Together with a record of dimensions and images of compression samples, as well as temperature monitoring during compression.